Machine Learning Applied to Electrical Impedance Tomography for the Improved Management of Nocturnal Enuresis

Presented by:

Eoghan Dunne

to:

Electrical and Electronic Engineering,

College of Engineering and Informatics,

National University of Ireland Galway,

In fulfilment of the requirements for the degree of

Doctor of Philosophy.

Supervised by:

Martin O'Halloran and Emily Porter

December 2020

Contents

Declaration of Originality

I, the Candidate Eoghan Dunne, certify that this thesis entitled “Machine Learning Applied to Electrical Impedance Tomography for the Improved Management of Nocturnal Enuresis”:

- is all my own work;
- has not been previously submitted for any degree or qualification at this University or any other institution;
- and where any work in this thesis was conducted in collaboration, appropriate reference to published work by my collaborators has been made and the nature and extent of my contribution has been clearly stated.

Name: Eoghan Dunne

Eoghan Dunne

Abstract

Nocturnal Enuresis (or bedwetting) is a condition that commonly affects children but can continue into adulthood. The condition can have serious implications on the quality of a child's life. The current first-line medical treatment options are limited and none alert the user before voiding occurs. Electrical Impedance Tomography (EIT) is a low-cost, wearable and safe imaging modality that is investigated in this thesis as a potential proactive bedwetting alarm technology for nocturnal enuresis.

In the literature, methods to estimate the bladder volume have been established in EIT. However, no research has been performed to determine when to alert the user in time to void their bladder. Consequently, this thesis investigates classification of bladder fullness in terms of not-full and full states using machine learning. After reviewing the literature, numerical forward models were critically investigated. Using anatomical information, a novel three-dimensional EIT pelvic numerical forward model was devised. Bladder state classification using machine learning was employed with both EIT measurement data and images. The classifiers were tested against varying noise sources previously established in the literature. A novel child pelvic numerical forward model (with realistic anatomical and electrical conductivity information) was then designed and implemented for bladder monitoring studies. Bladder state classification was then tested on child EIT data for the first time. Feature processing and classifier optimisation were also examined to improve classification performance and memory storage. Finally, the classifiers were investigated against the electrode misplacement noise source using EIT measurement data from the numerical child model.

The overall findings indicated that high performance can be achieved with EIT bladder state classification using machine learning in the presence of established sources of error. Electrical impedance tomography measurement data was found to be the best input to the classifiers. Feature processing and classifier optimisation were found to improve the performance of an EIT-based bedwetting alarm solution. Electrode misplacement was found to greatly reduce classification performance. However, it has been shown that this error can be reduced by including data from varying electrode misplacements in the training dataset. Overall, this thesis has made significant strides towards the design and development of a non-invasive, proactive bladder monitor for children with nocturnal enuresis based on EIT.

Acknowledgements

I would like to take this opportunity to acknowledge the people who supported me during this Ph.D. and who made this thesis possible. This support came in many forms: collaboration, guidance, direction, advice, discussion and meetings, outings, and essential daily banter and camaraderie.

Firstly, I would like to thank my supervisors, Prof. Martin O'Halloran and Prof. Emily Porter, for all their support, advice, and guidance throughout the Ph.D. They have been readily available both in person and remotely to answer queries, to clarify ideas, to offer advice, suggestions, and moral support. I am grateful for the opportunity to have pursued a Ph.D. with the Translational Medical Device Lab (TMD Lab), and in so doing, gained invaluable experience in research, collaboration, public speaking, attended national and international conferences, and have availed of funding opportunities. It has been a pleasant and stimulating work environment.

To my colleagues in the TMD Lab (past and present), I wish to thank you for sharing your expertise and experience with me. Within the lab, many contacts have been made and friendships have been formed (too numerous to name). These friendships have helped sustain me during demanding times, such as COVID-19 pandemic restrictions that disrupted our work practices and limited our movement and social interactions.

As well as support from the TMD Lab, my work has benefitted from consulting with others in the Department of Electrical and Electronic Engineering in National University of Ireland Galway (NUI Galway) including those who have been on my Graduate Research Committee (Prof. Gearóid Ó Laighin, Prof. Edward Jones, Dr. Fearghal Morgan, and Dr. Maeve Duffy) and fellow research students (in particular, Ashkan Parsi for insights into Machine Learning).

I would also like to thank the staff of the Department of Psychology and the College of Medicine, Nursing & Health Sciences at NUI Galway and the Department of Radiology in University Hospital Galway for any expertise and access to facilities that they provided.

During the course of the Ph.D., I was hosted by the Electromagnetics Research Group at the University of Malta. This opportunity broadened my research skill set and areas of expertise, provided experience of working abroad and I made new contacts and friends. In particular, I wish to acknowledge Prof. Charles V. Sammut and Dr. Lourdes Farrugia who oversaw my

research in Malta and Prof. Pierre Schembri-Wismayer who provided medical expertise for the project. Thank you to my co-worker and friend Julian Bonello who ensured my visit to Malta was active and enjoyable. I look forward to visiting you all again!

To my immediate family and friends who never signed up for this Ph.D., but still found themselves involved in it: thank you for all the affirmation and encouragement, many acts of kindness, and the odd reminder that life outside the Ph.D. does exist! I have many happy memories of times spent with you, including conversations, walks, travel, and activities (climbing, hiking, and boxing to name a few!).

The Ph.D. is known to be a challenging process, but all of the above have made it an enjoyable and transformative experience for me. Thank you!

List of Figures

List of Tables

Abbreviations

2D	two-dimensional
3D	three-dimensional
BVM	bladder volume monitoring
CAD	computer-aided design
CM	continual monitoring (abbreviation used in regard to naming dataset)
CT	computed tomography
EBC	expected bladder capacity
EIDORS	Electrical Impedance Tomography and Diffuse Optical Tomography Reconstruction Software
EIT	electrical impedance tomography
FEM	finite element model
GI	global impedance
IMU	inertial motion unit
KNN	*k*-nearest neighbours
L2COCV	leave-2-conditions-out cross-validation
LOCOCV	leave-one-condition-out cross-validation
LPCOCV	leave-p-conditions-out cross-validation
MRI	magnetic resonance imaging
NICE	National Institute for Health and Care Excellence
PCA	principal component analysis
RBF	radial basis function
ROI	region of interest
RTT	realistic train-test (abbreviation used in regard to naming dataset)
SNR	signal-to-noise ratio
STL	stereolithography
SVM	support vector machines
TC	test-case (abbreviation used in regard to naming investigations)

VAT	value-added tax
VHP®	Visible Human Project®

1 Introduction

1.1 Social Context and Thesis Motivation

Nocturnal enuresis (or 'bedwetting' and abbreviated to 'NE') is the loss of bladder control during sleep. The condition commonly occurs in children, where prevalence decreases with age, e.g., prevalence of about 10% at age seven to 3.1% for ages eleven to twelve [1]. Nocturnal enuresis can negatively impact the child by poorer self-image, social-exclusion, and being bullied [2], [3]. Families are also burdened with increased work and concern [4], [5]. The family can become intolerant of an enuretic child when NE persists long-term [4]. Therefore, it is important to treat the condition as soon as possible for the well-being of the child and their family.

Behavioural changes are first attempted when treating NE [6]. If behavioural changes are unsuccessful, first-line medical treatments for NE are employed [6]. These treatments include enuresis alarms or the medication Desmopressin. The enuresis alarms seeks to wake the user at the start of the bedwetting event, but it can often take weeks of continued use before a child will show a significant reduction in bedwetting [7], [8]. Desmopressin alters the function of the kidneys during sleep by reducing the water excreted by the kidneys to the bladder [9]. Desmopressin has an immediate response to resolving bedwetting [7]. However, the medication has a high rate of bedwetting reoccurring directly after the treatment is ended [10].

These first-line medical treatment options are reactive or invasive. Such treatment options have either a slow response time to ceasing bedwetting, or a poor long-term success rate of dry nights after treatment ends. An ideal treatment option would be proactive and would have a high long-term success rate. A proactive solution would also have a quick response rate. The solution also needs to be affordable for parents and health systems. Therefore, a low-cost, proactive and safe technology needs to be developed for better treatment of NE.

Electrical Impedance Tomography (EIT) is an imaging modality based on the measurement of electrical impedance of biological tissue. Electrical impedance tomography is particularly well suited for scenarios where bodily impedances vary with time, such as monitoring lung ventilation and bladder filling [11], [12]. Electrical impedance tomography has shown promise to monitor bladder volume on healthy adult volunteers and paraplegic patients [12], [13]. However, no investigations have been performed for child-specific applications of bladder

monitoring, such as a bedwetting alarm for NE. Bladder fullness monitoring has primarily focused on the estimation of bladder volume rather than the fullness state of the bladder (e.g., ‘not-full’ or ‘full’). Therefore, this thesis investigates EIT as a potential proactive bedwetting alarm solution for NE. In the next section, the contributions of this thesis are presented.

1.2 Thesis Contributions

This thesis presents several novel and significant contributions to the field of bladder fullness monitoring using EIT. These contributions are:

- the proposal of a new clinical application for EIT and a novel proactive bedwetting alarm system design using EIT;
- the design and implementation of a numerical pelvic forward model for adults that integrates anatomically derived information;
- the investigation of the feasibility of bladder state classification and the best input to the classifiers of EIT measurement data and EIT images;
- the development of a novel child pelvic forward model for EIT bladder monitoring;
- bladder state classification on EIT measurement data from a child model for the first time and validation of adult bladder state classification findings;
- the proposal and development of feature processing methods for bladder state classification using EIT measurement data for the first time in the EIT bladder monitoring field;
- the novel investigation of tolerance of bladder state classification with the additional noise of misaligned electrode positions, and demonstration of the ability to cater for these errors with machine learning.

The work on this thesis draws from three first-author journal papers and one first-author conference paper. These publications are listed below.

Journal Publications

1. **E. Dunne**, B. McGinley, M. O’Halloran, and E. Porter, “A Realistic Pelvic Phantom for Electrical Impedance Measurement”, *Phys. Meas.*, vol. 39, no. 3, pp. 1-10, Mar. 2018, doi: 10.1088/1361-6579/aaa3c0.

2. **E. Dunne**, A. Santorelli, G. Leader, B. McGinley, M. O'Halloran and E. Porter, "Supervised Learning Classifiers for Electrical Impedance-based Bladder State Detection", *Sci. Rep.*, vol. 8, no. 1, Art. no. 5363, pp. 1-12, Mar. 2018, doi: 10.1038/s41598-018-23786-5.
3. **E. Dunne**, A. Santorelli, B. McGinley, G. Leader, M. O'Halloran and E. Porter, "Image-based Classification of Bladder State using Electrical Impedance Tomography", *Phys. Meas.*, vol. 39, no. 12, Art. no. 124001, pp. 1-13, Dec. 2018, doi: 10.1088/1361-6579/aae6ed.

Conference Publications

1. **E. Dunne**, A. Santorelli, B. McGinley, M. O. Halloran, G. Leader, and E. Porter, "EIT Image-Based Bladder State Classification for Nocturnal Enuresis," in *19th Int. Conf. Biomed. Appl. Electr. Impedance Tomography*, Edinburgh, Scotland, Jun. 11-13, 2018, pp. 40.

Each contribution and relevant publication are highlighted in the appropriate chapter. An overview of each chapter is given in the next section.

1.3 Thesis Outline

In Chapter 2, the thesis is set in the context of the literature. The relevant anatomy is presented along with the clinical need of NE. Current treatment options for NE are also discussed. Next, proactive options for treating NE currently under development are critically examined. Electrical impedance tomography is identified as a potentially promising technology for supporting the treatment of NE. Next, the background of bioimpedance and EIT are reviewed. Finally, the EIT-based bedwetting alarm concept using machine learning is presented.

In Chapter 3, numerical forward models in the bladder monitoring EIT field are discussed. A new numerical forward model of a male human pelvic region is created for EIT measurement data (also referred to as raw EIT voltage data) generation and image reconstruction. The forward model contains a novel dynamically filling bladder model for EIT bladder monitoring. Electrical impedance tomography measurement data and image data are then generated to determine whether either one is a better input for bladder state classification.

In Chapter 4, bladder state classification using machine learning is investigated using image data as input to the classifiers. The classifiers are evaluated with EIT data and conditions of

varying bladder volumes, varying urine conductivities and added noise. Tolerances are determined for each condition. Realistic training and testing scenarios are then examined.

In Chapter 5, EIT measurement data used as the input to the classifiers is investigated for bladder state classification. This investigation is performed to alleviate some of the difficulties posed by image reconstruction. A similar testing scenario to Chapter 4 is performed for a fair comparison of the classifiers using the two data input sources of EIT images and EIT measurement data.

In Chapter 6, a realistic child numerical forward model is designed and developed to evaluate bladder state classification, specifically on child EIT data. An accurate boundary of the pelvic region is extracted from a medical imaging data source. The pelvic bone, the lower spine and the upper femur are also extracted. A finite element model (FEM) for use in EIT simulations is formed from the computer-aided design (CAD) model of the pelvic region. Measurement data using this child model is generated and analysed in terms of the effect of the added bone, varying bladder volumes and varying urine conductivities.

In Chapter 7, bladder state classification is investigated on child EIT measurement data. Findings from previous chapters are validated. In parallel, classifier optimisation and feature processing techniques are examined to improve the overall performance of the classification and memory required for storing data. The best performing classifier is then tested against another realistic noise source of misplaced electrode positions. Tolerance of the classifiers is analysed and a method to overcome the noise sources is devised.

In Chapter 8, the thesis is summarised in terms of the findings and conclusions of each chapter. The future work for the fields of bladder monitoring using EIT and EIT bladder state classification are also outlined.

2 Background

In this chapter, the motivation for the thesis and background information is presented. Specifically, the fundamentals of the urinary bladder and bladder control are first discussed in Section 2.1. Next, the difficulty of maintaining bladder control at night (nocturnal enuresis) is discussed in Section 2.2. This section also includes how the condition affects the child, close family and the health system. Medical treatment options including devices used to help remedy bedwetting are discussed in Section 2.3, and the motivation is developed for a proactive alarm solution that could help children with NE. Possible technologies to proactively monitor the bladder are also presented in Section 2.3. Next, the fundamental principles of bioimpedance and EIT are discussed in Section 2.4. Then, a bioimpedance-based alarm solution using EIT. The chapter is then summarised in Section 2.5.

The application of EIT bladder state classification for NE examined in this chapter was first introduced to the EIT imaging field in the conference paper:

E. Dunne, A. Santorelli, B. McGinley, M. O. Halloran, G. Leader, and E. Porter, "EIT Image-Based Bladder State Classification for Nocturnal Enuresis," in *19th Int. Conf. Biomed. Appl. Electr. Impedance Tomography*, Edinburgh, Scotland, Jun. 11-13, 2018, pp. 40.

2.1 The Urinary Bladder and Bladder Control

In this section, the anatomy of the urinary bladder within the urinary system is discussed. Also discussed in this section is the development of bladder control at childhood and how the operation of the bladder changes at night-time.

2.1.1 The Urinary System and The Urinary Bladder

The urinary system is an essential system within the human body with the responsibility for removing waste from the blood, assisting in maintaining the acid-base balance, as well as regulating the fluid and the electrolyte balance within the body [14]. The kidneys, the ureters, the bladder, and the urethra form the urinary system [14], as shown in Figure 2.1. The kidneys filter the blood and extract the waste products that combine to form urine. Urine is composed of water, urea, uric acid, electrolytes (e.g., sodium, potassium, chloride), creatinine, and ammonia [14], [15]. Urine can also contain leukocytes, red blood cells, and medication [14].

After production, the urine flows from the kidneys to the bladder by two thin tubes known as the ureters [16]. The ureters enter the bladder at the upper part of the angled base of the bladder [16], and urine is drip-fed into the bladder continuously [15]. When urine leaves the bladder, urine flows through the urethra passage out of the body [16], as shown in Figure 2.2.

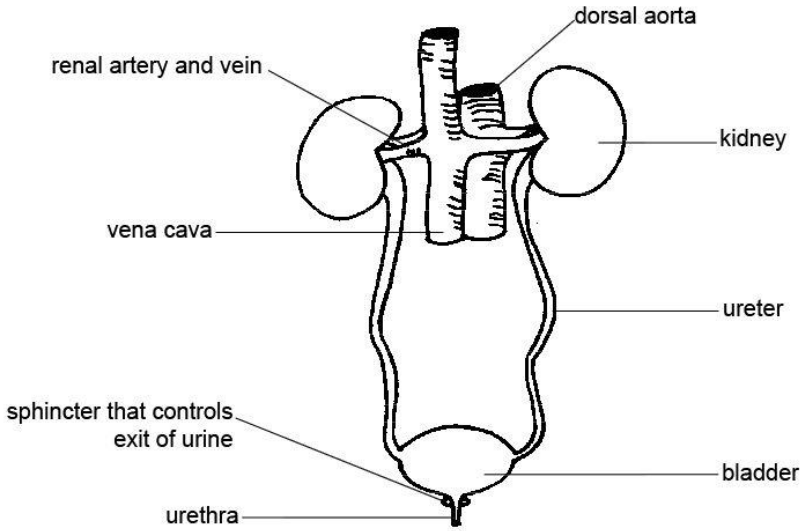

Figure 2.1: Illustration of the urinary system containing the bladder. Urine is produced in the kidneys and flows to the bladder through the ureters. Urine is held in the bladder until the urine is voided from the body through the urethra. The urethral sphincter prevents the urine leaving the bladder until voiding. The blood vessels (artery and vein) connecting to the kidney are also shown. Image source: 'Anatomy and physiology of animals Urinary system.jpg' [17] *by Ruth Lawson, Otago Polytechnic, uploaded by Sunshineconnelly and is licensed under CC BY-3.0* [18].

To hold urine in the bladder, the sphincter muscles of the bladder contract and close the urethra passageway [15]. Men have two sphincters (internal and external) whereas women only have one (external) [16]. For males, the internal sphincter is located at the bladder-urethra junction, and the second sphincter is inferior to the prostate [16]. In women, the sphincter is inferior to the bladder [16]. To allow urine out of the bladder, the urethral sphincter relaxes [15].

The bladder is an organ with the purpose of temporarily storing urine before urine is expelled from the human body [14]. The organ is hollow and has a wall that can expand on filling [15]. Within the bladder wall is the detrusor muscle. The detrusor muscle relaxes as the bladder fills and the muscle contracts to push urine out of the bladder on urination [15].

In terms of location in the human body, the base position of the bladder changes from neonates to adulthood [16]. In neonates, the bladder is almost entirely in the abdominal region. The base of the bladder descends into the pelvic cavity during childhood until the base is in the pelvic

cavity (adult position) after puberty [16]. The bladder is in the anterior of the pelvic cavity [16]. As the bladder fills, the bladder expands upwards into the abdominal region [16]. The bladder is surrounded by elements of the gastrointestinal system and the reproductivity system [16], e.g., the rectum, and the prostate (males) or the uterus (females) as shown in Figure 2.3. The bladder is also surrounded by the pelvic girdle bone and sits behind the pubic symphysis (a cartilage joint where the two pelvic bones meet) [16].

Surrounding tissues can interact with the bladder (discussed later in the chapter). For example, constipation of the rectum placing additional pressure on the bladder. Surrounding muscles can assist the bladder to void, e.g., by increasing intra-abdominal pressure [16].

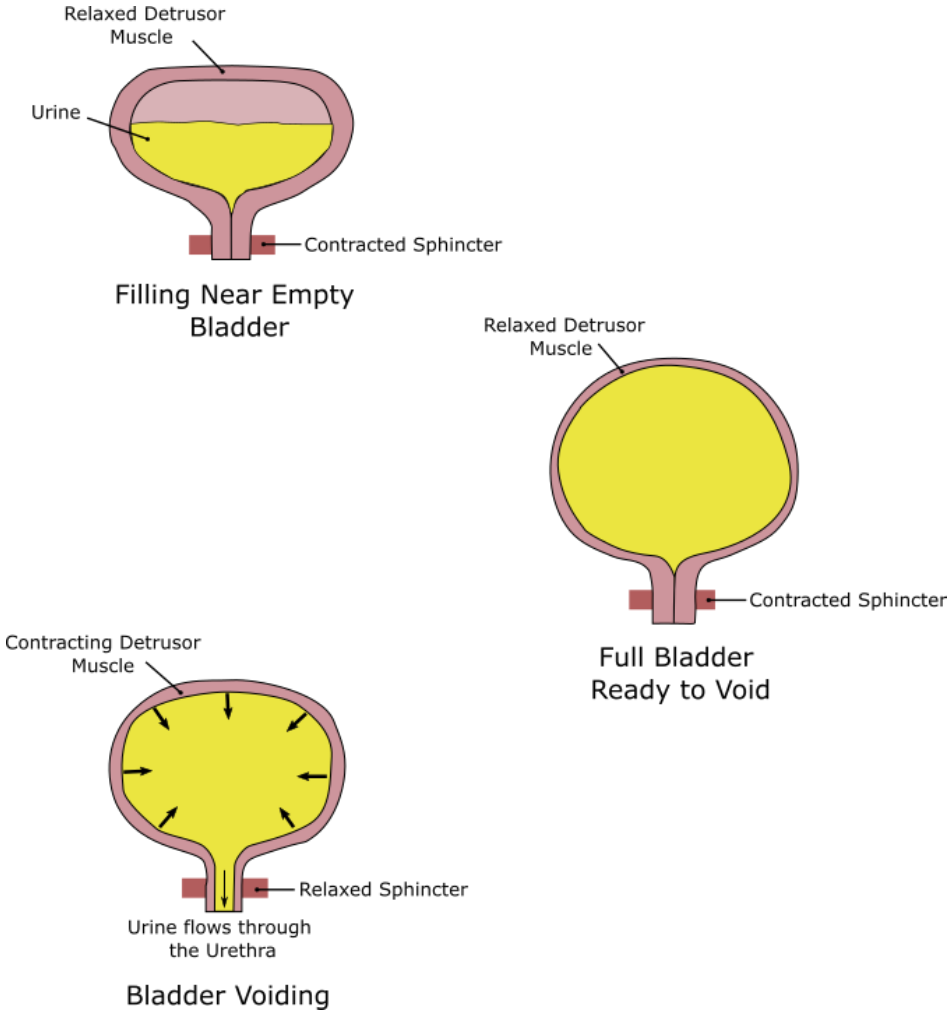

Figure 2.2: Illustration of the bladder cycle (involuntary): filling to voiding. As the bladder fills, the bladder wall including the detrusor muscle relaxes and stretches allowing the bladder to grow superiorly into the abdominal region, while the base of bladder remains connected to the urethra in the pelvic cavity. The urethral sphincter remains contracted to hold urine in the bladder during filling. To void the bladder, the detrusor muscle contracts while the urethral sphincter relaxes and the urine flows from the bladder through the urethra out of the body.

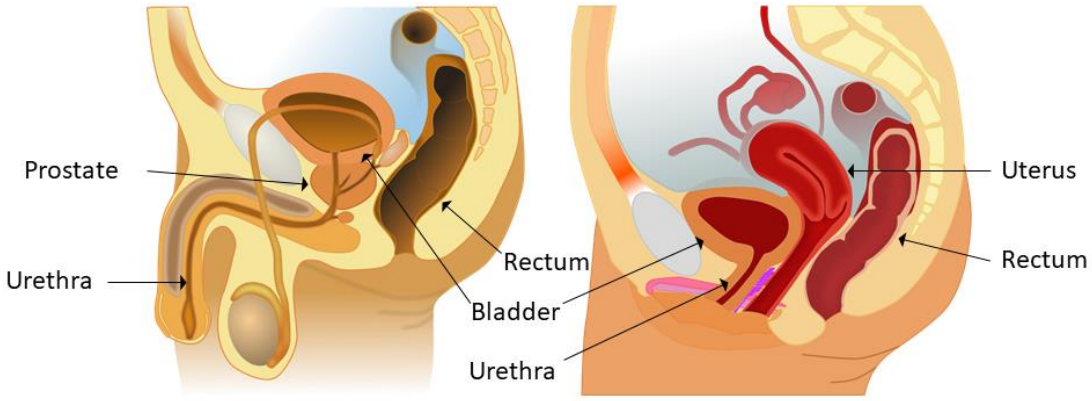

Figure 2.3: Lower urinary tract for both male (left) and female (right). For the male, the bladder sits superior to the prostate while the female bladder sits superior to the pelvic floor. Urine flows from the bladder through the urethra to the outside world on voiding. This modified image is sourced from 'Male and female anatomy.svg' [19], *formed by andrybak and is licensed under CC BY-SA 3.0* [20]. *Modified image is under the same licence* [20].

2.1.2 Bladder Urination Control when Awake and Asleep

To urinate (also referred to as 'to void'), the detrusor muscle needs to contract, and the urethral sphincter muscles needs to relax [15]. The process is termed 'the micturition reflex' [15]. Until continence is achieved (e.g., between 3-5 years of age [21]), urination is under involuntary control of the sympathetic nervous system and the micturition reflex [15]. Timing of urination is determined based on signals sent from stretch receptor nerves in the bladder wall [15].

When a child is about 3-5 years of age, the muscles and nerves have matured sufficiently so that the brain can control the bladder voluntarily [15]. Involuntary micturition responses are overridden by the brain and voluntary muscle control is established by the pelvic floor pubococcygeal muscle [15]. The altered process for voluntary urination becomes: contracting the abdominal muscles; contacting the detrusor muscle; and relaxing of the pubococcygeal and sphincter muscles [15].

Urination frequency depends on both the individual and fluid consumption [15]. The total volume voided per day also depends on the amount of fluid consumed and the climate conditions [14]. Bladder capacities are dependent on age [22]–[24]. For example, expected bladder capacities can range between 150-390 ml for children aged between 4-12 years old [22]. For adults, the literature has reported adult bladder capacities of 300-600 ml [14], [15], [24], [25]. However, the sensation to void may occur earlier, such as between 200-400 ml [15], [26].

During sleep, the normal bladder operation is altered. The body reduces the amount of urine being produced by secreting regulatory hormones [27]–[29], reducing the need to wake at night to void. The need to void may cause the individual to awaken. However, waking frequently from sleep to urinate is a condition called “nocturia” and consequently, nocturia can have negative impact on an individual [30]–[32]. Impacts of nocturia include sleep disruption and subsequently, a potentially higher risk of mood disorders, hypertension, obesity, and mortality [32]. Nocturia can be caused by any of a number of factors, including the level of fluid consumption, urological disorders, and other health conditions such as diabetes [31].

This section has provided a fundamental understanding of the role of the bladder in the urinary system, including how the bladder functions and how bladder control is established. Next, the condition of NE is discussed.

2.2 Nocturnal Enuresis: What is it? Prevalence, Impacts, Pathogenesis and Evaluation

Nocturnal enuresis (NE) is defined as the involuntary loss of urine in discrete episodes during sleep [22]. The condition is applicable when children are aged five years and older and where NE occurs greater than once a month for at least three months [22]. Nocturnal enuresis can be subdivided into the categories of monosymptomatic or non-monosymptomatic, and primary or secondary. Monosymptomatic enuresis occurs without any other lower urinary tract symptoms (LUTS) or bladder dysfunction (e.g., daytime incontinence) [22]. Non-monosymptomatic enuresis includes LUTS such as hesitancy and straining to void, LUT pain, dribbling after urination, daytime incontinence, abnormal voiding frequency [22], [33]. Primary NE refers to NE in a child who has never had six months of dry nights, whereas secondary NE refers to NE where there has previously been night-time continence for at least six months [22].

The prevalence of NE decreases with age, e.g., about 10% at age seven, 3.1% for ages eleven to twelve and 1.3% for ages sixteen to seventeen, where children have either monosymptomatic or non-monosymptomatic NE [1]. The condition is more common in boys than girls [1], [34]–[36]. Nocturnal enuresis can continue from young adult to adulthood and is considered to affect at least 2% of adults [37]. For young adults and adults who have never achieved night-time continence for longer than six months [38], their lives can be negatively impacted psychologically and socially, as well as affecting their family life and their job selection.

A child's quality of life can also be negatively impacted by having NE [39]. A child with NE can have a lower self-image along with a higher tendency towards depression than their peers without NE [2], [40]. These children can fear their bedwetting being discovered and avoid over-night events such as sleepovers [41], [42]. Enuretic children can also be bullied because of their bedwetting by other children, including their own brothers/sisters [3], [6], [42]. The smell and sensations accompanying bedwetting can also bother the child, along with dealing with the aftermath of bedwetting, i.e., changing bedsheets and cleaning themselves [42]. These factors contribute to the child with NE feeling isolated and different [43].

The family of the enuretic child can also be burdened by the condition. Having an enuretic child can severely impact a family by increased concern and worry, financial costs, as well as negatively impacting them socially [4], [5]. Beyond day-to-day tasks, the family have to deal with an increased workload and cost from washing and drying of bedding and night-clothes [4]. It is not only the quality of life of an enuretic child that is affected. A study focused on mothers with enuretic children showed that mothers had a lower quality of life to those in the control group [44]. Family intolerance can grow for a child who has had prolonged NE [4], [6]. Earlier treatment of the condition can bring great relief for the family [4].

Nocturnal enuresis also has an impact on the health system. Many resources may be needed to help with treating and managing the condition such as nurses, paediatricians, psychologists, and specialists for investigation of underlying conditions [6], [9], [41], [45], [46]. Multiple follow ups may also be required for continual monitoring of progress [6], [46]. In particular, referral to further investigation may be needed if the condition is not resolving [6]. Recently, a 2019 paper [47] estimated the annual economic cost of treating NE for one enuretic child to be £3000 with at least a doubling effect for two or more children in the same family.

Therefore, the condition has many implications and consequences for the child, their family, and the health system. To determine which children are particularly affected, the pathogenesis is examined in the following subsection.

2.2.1 Aetiology/Pathogenesis

In the literature, NE has been highlighted as a multifaceted condition [48]. The main predictors for the development of NE include a genetic history of NE; abnormal detrusor activity, sleep-arousal problems; and high urine production at night [48]–[50].

It has been found that many children presenting with NE have parents who also had NE [48], [51], [52]. Data drawn from a large scale British epidemiology study for a 2011 paper indicates that a child has 3.63 times or 1.85 times likelihood of having severe NE if there was maternal or paternal NE history, respectively [52]. The hereditary factor has also been demonstrated in twin studies [53], [54] and formal genetic studies have analysed chromosomes for the NE genes [55], [56].

In a portion of children with NE, abnormally high urine production at night can occur [48]. This occurrence can be due to irregular behaviour of the antidiuretic hormone that is produced by the body to reduce urine production at night-time [48], [49], [57].

Detrusor overactivity is another common pathogenesis presented in the literature [58]. This uncontrolled triggering of the detrusor muscle to contract can lead to voiding of the bladder during sleep [58]. Detrusor overactivity also occurs in daytime urinary incontinence [59].

Crucially, sleep arousal difficulties play a key role in the pathogenesis of NE [58]. The child does not awaken to void and thus, bed wets. However, the child may be continent during the day [58]. Children with NE have a high sleep arousal threshold [60] and bedwetting can occur in any of the sleep stages [58].

Children with NE can suffer psychologically as highlighted previously. However, research indicates that many psychological problems seem to arise due to having NE rather than as the source of NE [48]. However, stressful events may be a source of psychological issues that leads to NE in a small group of children [58].

Other causes/co-occurring conditions include constipation, urinary tract infections and sleep apnoea [8], [61]. Relieving some of these conditions can reduce NE symptoms [61], [62].

The pathogeneses of NE are complex. The current understanding of the pathogeneses of NE is under consideration and refinement [58]. Certain pathogenesis may be connected, e.g., constipation and detrusor overactivity [58], [63]. However, more investigation and analysis are needed. More details on the current state of these investigations and the future work for the area can be found in [58].

After a child experiences NE, the parents may seek medical support to identify the cause and seek out potential solutions. During the initial clinical investigation, the pathogeneses are examined to determine the most suitable treatment options. The evaluation procedure and patient pathway are discussed in the following subsection.

2.2.2 Evaluation of Nocturnal Enuresis and Patient Pathway

Clinical evaluation starts with gathering a detailed history on the child [6], [46], [64]. Questions will investigate: bedwetting frequency; family history of NE; any dry periods; voiding and fluid intake; daytime symptoms; LUTS; stooling and previous medical history; and any underlying medical problems [6], [64]. Developmental and behavioural difficulties may also be investigated [6]. Voiding diaries for both daytime and night-time may be used to gather information such as when daytime voiding occurred, the bladder capacity, frequency of bedwetting [64]. Bowel movements may be journaled too [64].

The physician will also perform a physical examination. The examination performed may include palpation of the stool in the abdominal region to identify any constipation, and inspection of the spine for malformation symptoms [48], [49], [64]. Urine tests may be carried out if necessary for investigations of diabetes and urinary tract infections [6], [48], [64].

If an ultrasound device is available, post-residual urine and bladder thickness may be investigated for signs of other conditions beyond NE [46], [48]. Further medical imaging such as X-rays may be carried out when referred for specialist observation [64]. However, treatment of underlying conditions is prioritised over NE.

Children and parents/guardians may obtain this clinical evaluation by attending their primary care medical practitioner [46], [64]. Then after initial investigation, the child may be prescribed non-medical treatment/management of the condition (examined in Section 2.3) or referred for further investigation, particularly in the case of non-monosymptomatic NE. In the case of monosymptomatic NE, a follow up of 2-3 months can occur after prescription of initial management strategies [9]. If initial management strategies fail, medical treatment options examined in Section 2.3 may be prescribed, along with the associated follow up and evaluation procedure [9].

After medical evaluation, NE management and treatment strategies can be prescribed. Treatment is interdisciplinary [48] and the child may be referred to specialists in the cases of non-monosymptomatic NE (not covered in this thesis due to different treatment strategies for the underlying problems that are beyond treatment for NE). The treatments specifically for NE are discussed in Section 2.3.

2.3 Management and Medical Treatment of Nocturnal Enuresis and Potential Alternatives

Before any specific treatment is applied for NE, it is recommended that constipation, faecal incontinence as well as daytime incontinence or LUTS should be treated first [48], [64]. Initial management of NE [6], [9] includes:

- informing the child and parents/guardians about the condition;
- making lifestyle changes such as toileting and minimising fluid intake before bed;
- implementing a positive reward system e.g., a star or sticker for going to the toilet before bedtime.

If the initial management stage is not successful, the medical treatment options of alarm and/or drug therapies may be used [6], [49]. These options are detailed in the following sections.

2.3.1 Alarm Therapy

Enuresis alarms are a device-based medical option for treating NE. Enuresis alarms fundamentally work by detecting the moisture at the start of urination and triggering an alarm to wake the child [8]. The aim of the alarm is to reduce/prevent bedwetting by waking the child and to help the child pre-empt the alarm and awake before loss of bladder control, preventing any bedwetting [9], [65].

Different alarm versions [50], [65], [66] have been devised over the years but can be categorised into a moisture sensor, either:

- under the bed sheet that the child lies on (pad-and-bell); or
- placed in the pants of the child that may be wired or wirelessly connected to the alarm source (can be referred to as body-worn and this alarm type is more recent than the pad-and-bell).

An illustration of the modern body-worn alarm design is given in Figure 2.4. The alarm can make a certain noise or vibrate (recommended to those with hearing difficulties) to wake the child from sleep [6].

A variant of an enuresis alarm that has been investigated is called the code-word alarm [66]. The code-word alarm alerts the child first. Then, a pre-recorded personalised message (termed ‘code-word’) is delivered after the child wakes and stops the alarm [66]. The child is asked to remember the code-word in the morning, and the code-word is changed daily by the parents

[66]. A reward is given for remembering the code word to incentivise the child being more responsive [66]. This alarm variant attempts to overcome situations where the child does not sufficiently react to the alarm on wetting. Recalling the code-word attempts to promote a higher sleep arousal [66].

Alarms have been shown to be a strong treatment option for NE. Approximately 65% of children were shown to become dry (14 consecutive dry nights) after using alarm therapy when compared to only 13% with no treatment [65]. For the trials that followed up after treatment, approximately 43% of children remained dry compared to only about 2% of children in the control [65].

Compared to the control alarm, the code-word alarm improved waking to the bedwetting alarm control (by approximately 11%) in a randomised control trial (353 children total, 177 children in the control group) [66]. But, there was no significant difference in the six month relapse rate (more than one wet night per month over the six month period after treatment) between the code-word alarm and alarm control [66]. The discontinuation rate (the proportion of subjects who stop using the therapy during treatment) was lower for the code-word alarm by approximately 10% when compared to the control alarm [66].

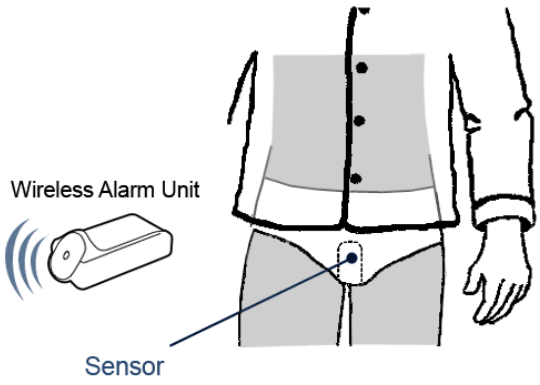

Figure 2.4: Illustration of body-worn alarm with a wireless alarm unit. The moisture sensor is placed in the underwear and when the child starts-to-void, the moisture is detected, and the alarm is sounded. Image source: 'DRIsleeper-Wireless-Alarm.gif' [67] *by Kiwianaa licensed under CC BY-SA 3.0* [20].

Alarms may not be suitable in the cases of where a lot of urine is being produced (where the pharmaceutical option of Desmopressin may be more suitable [46]) or where a quick resolution of bedwetting is desired/needed [6], e.g., the family shows intolerance. The alarm therapy gradually reduces bedwetting symptoms [7]. Underwear and bedsheets still need to be changed on bedwetting during this time, which can continue the burden and sleep disruption on the child

and parents/guardians. In these cases, or where the alarm therapy has not shown signs of relieving NE, pharmaceutical options may be investigated.

2.3.2 Desmopressin Therapy and Other Pharmaceutical Options

Desmopressin is the primary pharmacological option for treating NE [48]. Desmopressin is a medication that causes the kidneys to reabsorb water, reducing the amount of water excreted from the kidney to the bladder and increasing the concentration of the urine [9]. The treatment is particularly suited where the alarm therapy has been unsuccessful, was unsuitable to be used, or where a rapid improvement in bedwetting symptoms is required [6], [46]. The drug can be taken in oral form and is recommended to be taken between 30 minutes to 2 hours before bedtime [6], [48].

After prescribing the treatment, the National Institute for Health and Care Excellence (NICE) guidelines recommend checking the response to the treatment at four weeks and continuation of the treatment for three months on positive response signs (e.g., smaller bedwetting patches, fewer bedwetting episodes per night and fewer bedwetting nights) [6]. Treatment can be withdrawn for at least a week every three-months to evaluate the response and to determine the next steps, e.g., to start the treatment withdrawal process or to continue Desmopressin for another three months on partial response [6]. On relapses of bedwetting, the drug can be prescribed again [6].

In a systematic review, Desmopressin was found to give around 1-2 wet nights per week fewer than a placebo [10]. During treatment, more children became dry (e.g., 19% for Desmopressin vs. 2% for Placebo with a 20 µg dose) [10]. However, the review found there was no difference in results between the Desmopressin and placebo groups after treatment [10]. This finding leads to doubts on the long-term effectiveness of the treatment.

Desmopressin has a good safety profile [46], [68]. Adverse effects are uncommon but do include water intoxication [68], [69]. To reduce the possibility of overhydration, water intake before and after Desmopressin intake is limited [68], [69].

Other pharmaceutical options include anticholinergics and tricyclics antidepressions [6]. Anticholinergics are a group of medications that help inhibit the detrusor muscle, reducing the urge to void and helping increase the amount of urine stored in the bladder [69]. Anticholinergics are not recommended by NICE to be used by themselves [6], but are used in combination with Desmopressin [6]. Anticholinergics can have side-effects such as

constipation, increased post-void residual urine volume, and can cause nightmares [33], [69], [70].

Tricyclic antidepressions can also be prescribed but are not recommended for first-line medical intervention like Desmopressin [6]. Tricyclic antidepressions do have similar effective performance to Desmopressin, with the caveat of more side effects, e.g., seizures [71], [72]. More detail on tricyclic antidepressants for NE can be found in the systematic review in [71], along with details on the poorer effective performance of antidepressants compared to alarms.

At this stage, insight into the medical options for NE that are both medical device-based and pharmaceutical-based has been provided, as well as their placement along the treatment pathway. In the next subsection, both the first-line treatments of alarm and Desmopressin therapies are compared.

2.3.3 Comparison of First-Line Treatments

In this section, the alarm and Desmopressin therapies are directly compared based on the literature available. Both treatments are typically the first-line medical therapies for treating NE [6], [48], [73] and systematic reviews have been performed that compare the two treatment options.

In a 2015 systematic review by Perrin et al. [74] comparing effectiveness of alarm and Desmopressin therapy for primary mono-symptomatic NE, seven of the eight trial studies investigated showed that there was no statistical difference between the level of dryness achieved using the alarm and Desmopressin therapy at the end of treatment. But in the studies with follow ups, alarm therapy had statistically significant lower relapse rates than Desmopressin. A higher discontinuation rate was found for alarms when compared to Desmopressin treatment (two studies only with discontinuation rates for alarms vs. Desmopressin of: 58% vs 44% in [75] and 20% vs 5% in [76]). Reasons reported by Perrin et al. [74] for the discontinuation of the alarm were anxiety due to the alarm noise at night, false alarms or no alert when bedwetting occurred, and the alarms disturbing others but not waking the child [74].

A systematic review in 2018 by Peng et al. [73] comparing effectiveness of alarm and Desmopressin therapy for monosymptomatic NE found there was no significant difference between the two therapies for the amount of children who achieved a 90% reduction of bedwetting symptoms or greater. Again, alarms had a higher likelihood of discontinuation than

Desmopressin [73]. However, the alarm therapy was indicated as the better long-term strategy over Desmopressin due to lower relapse rates [73].

Recently, a 2020 Cochrane systematic review was performed on the effectiveness of alarms [65]. The results suggest alarms may improve bedwetting compared to no therapy or a control [65]. The level of the certainty is poor due to low-quality evidence [65]. For comparison of alarms and Desmopressin, the findings indicated that alarms increase (''slightly'' [65], estimated likelihood of about 7.6% more [65]) the number of children staying dry after treatment [65].

The 2020 Cochrane study looked at comparisons that may not be clinically relevant based on the treatment pathway discussed previously. For example, they summarised comparisons between alarm and behavioural methods that include rewards. A reward system can be implemented before alarm treatment begins or alongside. The review highlighted the need for stronger randomised controlled trials to compare alarms against other treatment options [65]. Stronger randomised controlled trials would help determine with more certainty the effectiveness of alarms compared against other NE interventions [65]. The quality of trials in the literature has also been commented on by other systematic reviews over the years [74], [77]. Despite the uncertainty about the exact level of impact that alarm therapy has, the current evidence indicates that alarm therapy does work and is an effective long-term strategy, as discussed previously.

From this section, the preference of alarm therapy in the literature and medical guidelines as the preferred initial medical treatment for NE has been shown. However, proactively monitoring the bladder to alert the child could overcome practical challenges that moisture alarm faces. Proactive monitoring of the bladder is further discussed in Section 2.3.4.

2.3.4 Potential Proactive Alarm Technologies

As described in the literature, the first-line medical treatment for NE has often been the use of the alarm-based therapies. However, the current moisture alarm is reactive by alerting only at the start of urination. Proactively monitoring the bladder during filling could overcome weaknesses of the moisture alarm. These weaknesses include the time taken for the alarm to reduce bedwetting symptoms and the resultant changing of underwear or bedsheets by the child and/or the parents while the child is still bedwetting. Proactively monitoring the bladder could also make the alarm preferable in certain cases where Desmopressin would otherwise be selected, such as a short-term resolution to wetting the bed. To date and to the knowledge of

the author, no proactive alarm has been used as part of common practice. A number of technologies have the potential for proactively monitoring the bladder non-invasively, such as ultrasound and ultra-wideband (UWB) radar. These technologies are further discussed in the following subsections.

2.3.4.1 Ultrasound

Ultrasound is an existing medical device technology that works by sending acoustic waves from a probe into the body. The waves can be absorbed, scattered, refracted, diffracted or reflected (echoed) as the wave travels and encounters tissues [47]. The reflected waves can be captured by the probe and used to image or measure a target of interest, such as the bladder volume.

Ultrasound is used in routine bladder volume measurements in clinics and hospitals, and devices have evolved over the years from being large and difficult-to-move to hand-held ultrasound devices. In research, the use of ultrasound has been investigated for continuous bladder volume monitoring (BVM) in applications like urinary incontinence and NE [47], [78]–[82]. The research has crossed over at least two decades.

In the device designs for bladder volume measurements, the ultrasound probe or a small wearable ultrasound device is placed on the skin just above the pubic symphysis [78], [79]. The sound beam is then angled directly across the anterior-posterior of body or angled down into the pelvic cavity [78], [79]. The reflections captured can be related to penetration depth [83]. Thus, the presence of the posterior bladder wall may be detected, or the anterior-posterior bladder dimension determined from the collected data [78], [79]. An example of a wearable ultrasound for BVM as well as an example waveform is given in Figure 2.5.

Ultrasound prototypes have been developed and tested with children in clinical settings or in their homes [47], [79], [84]. For one device [79], the potential of bladder state classification of not-full and full states was highlighted by using a threshold in post-analysis of urodynamic clinical data [79]. This study was validated in [85] where notifications at 80% and 100% of the maximum bladder volume were tested on children undergoing a one-day in-patient bladder training in a clinical scenario [85]. The median notification rate (the amount of successful full bladder notifications received) was 92.9% for 56 urinations between 14 children [85]. However, challenges were noted including sensor positioning errors limiting detection [79], [85], lack of detection or exclusion of obese participants [79], [85], and lack of sensor contact [84]. Each of these studies was conducted over a single day or single night.

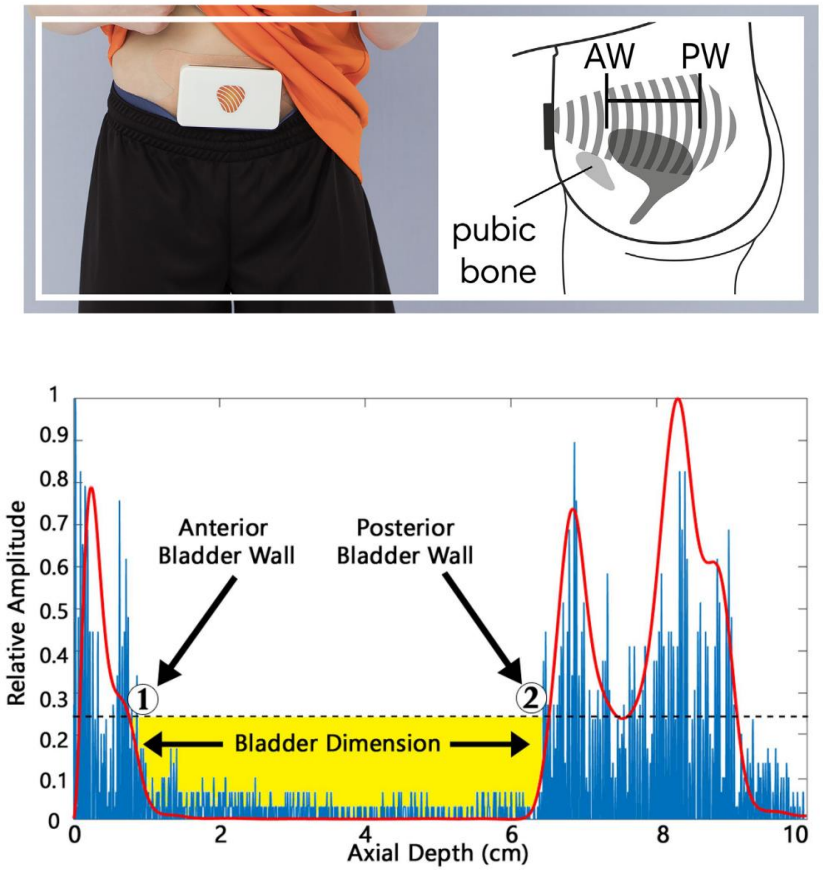

Figure 2.5: (top) An ultrasound bladder monitor developed by a commercial company on a child alongside an illustration of the ultrasound sound waves being transmitted into the pelvis [79]*; Image is a reprint from* [79] *with permission from Elsevier. (bottom) A reflected ultrasound signal in raw and processed format from bladder monitoring with the bladder monitor in* [86] *(a different bladder monitor to the one shown on top). The bladder anterior-posterior dimension can be estimated from the echoes as a function of penetration depth of the ultrasound sound wave. Image is a reprint from* [86]*, © IOP Publishing. Reproduced with permission. All rights reserved*.

More powerful tools have been used for classifying bladder state over multiple days. Kuru et al. [47] used machine learning and ultrasound to determine the plausibility of an intelligent wearable ultrasound bladder monitor (wearable ultrasound device and a mobile phone application). Data was collected from two male children volunteers in their home environment over multiple days for training and testing with machine learning algorithms [47]. The data from both children were combined into one dataset. Four classes describing the bladder state were used: empty; half full; three quarters full; and full [47]. Using the data collected, machine learning algorithms on a smartphone were used to fit the data with 10-fold cross-validation [47]. The three-quarters full class was considered a potential alert class [47]. The sensitivity and specificity of the three-quarter full class was 89% and 93%, respectively [47].

Therefore, an ultrasound solution is promising for NE to proactively monitor the bladder. However, these solutions still have some limitations. The ultrasound transducer has a fixed orientation to scan the bladder that may be ineffective with varying body mass indexes. Refinement of the ultrasound devices may be needed to allow for obesity and sensor misplacement [85]. Any movement limitations may also need to be identified.

While ultrasound is one option, another possible bladder monitoring technology is UWB radar. This technology is discussed in the next subsection.

2.3.4.2 Ultra-Wideband Radar

Another technology that has been considered for BVM is based on UWB radar. This technology is still at an early stage, with pilot studies on animals or humans yet to be completed. The technology is a form of microwave imaging. It works by emitting a radio pulse into the body within the designated UWB frequency range of 3.1-10.6 GHz (the range can vary between regulation bodies) [87] and recording reflected and/or transmitted signals. Different tissues have different dielectric properties, which determine how electromagnetic waves are reflected and transmitted through a material. Antennas are used to record the reflections and/or transmissions. Urine has a high-water content and consequently, a larger relative permittivity (stored energy) than surrounding tissues in the pelvic region [88]. This contrast in relative permittivity highlights the reason UWB has been investigated as an option to proactively monitor the bladder. An illustration of an UWB radar device for bladder monitoring is given in Figure 2.6.

The technology has been examined in both simulations and with experimental phantoms of varying complexity [88]–[92]. Machine learning algorithms have been used to classify bladder states as small, medium and full. In the study by O'Halloran et al. [91], the classes corresponded to the anterior-posterior distance of the bladder model. Two bladder sets were used. For Set 1, anterior-posterior distances were 10 mm for small; 20 mm for medium and 30 mm for full. For Set 2, anterior-posterior distances were 20 mm for small; 30 mm for medium and 40 mm for full. In simplified phantom models constructed as flat, three-layered models of the bladder (two layers of muscle and one layer of urine), classification average accuracies of over 87% were achieved [91]. The effect of classification performance with varying conditions of sampling rates and number of antenna array elements was also analysed [91]. Lower sampling rates were achieved by down sampling the recorded signals from 50 GHz. For accuracies over 70%, a

sampling rate of 10 GHz was needed [91]. The study also found that only two of four antenna elements were needed to obtain classification accuracies of approximately 80% or higher [91].

Anatomically and dielectrically realistic simulation models for a man and women were further developed in Krewer et al. [92] and machine learning was performed again for small (40-130 ml), medium (130-200 ml), and large (210-300 ml) bladder classes. Results were promising in ideal conditions with classification accuracies over 80% when SNR levels were 80 dB or above [92]. However, the performance of the classifier degraded greatly to between 28.20-57% when the classifier was tested in the condition of added noise (signal-to-noise ratio of below 80 dB for the male model and below 60 dB for the female model) [92]. Antenna position error of ± 1 cm also caused performance degradation to an accuracy as low as 30% [92]. Thus, further work is needed in this field to determine if UWB radar can monitor bladder volume and to make a robust solution for a proactive bladder monitor.

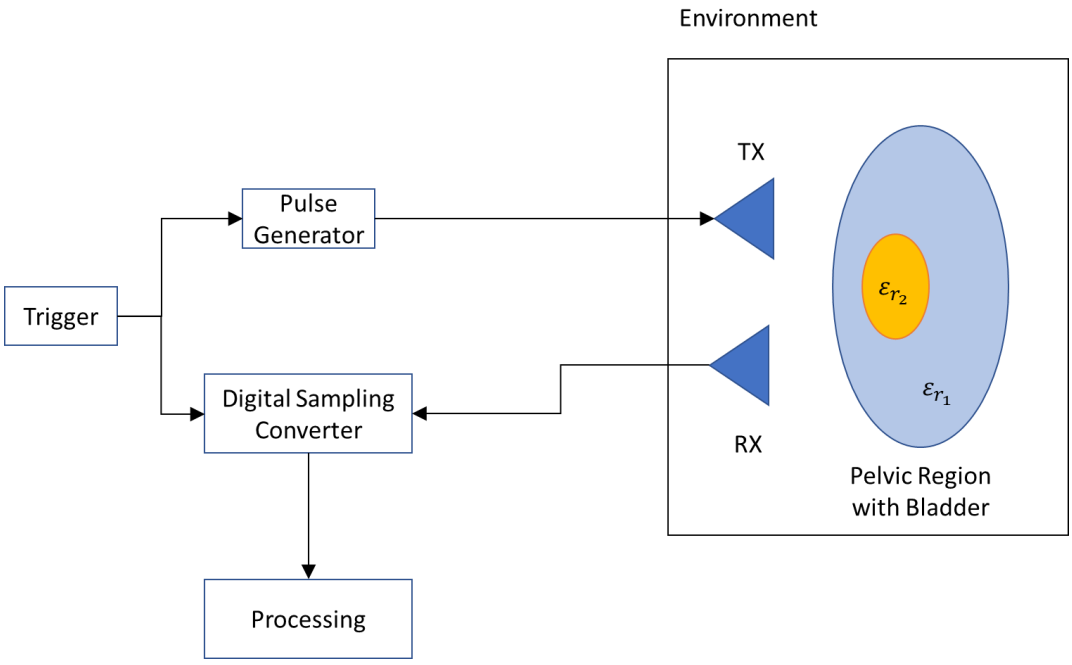

Figure 2.6: Illustration of a microwave system where on a trigger event, an electromagnetic pulse is generated and transmitted from an antenna into the body. The reflected/transmitted wave is then captured at a receiving antenna as a voltage waveform, and the data is sent for further processing.

2.3.4.3 Potential Proactive Alarm Technologies Summary

Both technologies discussed above (Ultrasound and UWB Radar) offer the potential to monitor the bladder but differ in terms of their approach and development stage. Ultrasound has been a proven medical imaging technology in the urology field and a number of feasibility studies using the technology as a wearable monitor have been performed. Challenges such as obesity

and sensor misplacement are potential difficulties for an ultrasound bladder monitor [85]. An UWB-based bladder monitor has been researched through numerical simulations and experimental studies with phantoms. However, no feasibility has been shown in humans to date to monitor bladder volume. Thus, more work is needed to demonstrate the feasibility of this technology in a real-life scenario.

These technologies show promise as a bladder monitor, with ultrasound currently the furthest in the research and development process. However, they have not yet reached common use with children, despite both being around for several years. Lack of up take is likely due to the amount of time taken to develop medical devices and the challenges with varying human bodies, particularly in children whose bodies vary and change with time. In addition, current device design limitations are problematic, e.g., the fixed transducer angle. Medical ultrasound devices are also quite costly such as those in hospitals (thousands of Euro). The wearable SENS-U ultrasound (a published version shown in Figure 2.5) starter kit[1] by the Netherlands-based company Novioscan (novioscan.com) was quoted as €900.00[2], but excludes value-added tax (VAT) and shipment. This device is reported in the technical sheet [93] as 94x55x16 mm in size and 55 grams in mass. In comparison, microwave devices have been designed in research for breast cancer applications and can be quite bulky, consisting of costly switching matrices and vector network analysers that can both cost thousands of euros. Research has been performed to reduce the cost and the size of a microwave system by integrating the switching matrix [94]. However, these microwave devices are still under clinical evaluation and have not become standard-of-care. Thus, room exists for a low-cost, small, wearable, and non-invasive solution.

Another proactive bladder monitoring candidate has been identified as having potential to overcome challenges and will be the focus of this thesis. This candidate technology is based on bioimpedance measurements (electrical impedance measurements of biological tissues), the foundations of which will be discussed in the next section.

[1] Starter Kit contains: the Sens-U device along with instructions; 35 adhesive patches (€55.00 excluding VAT) [226]); 1 bottle of ultrasound gel (€2.50 excluding VAT [227]); Alcohol Swaps (€3.00 excl. VAT [228]) and Spray for skin protection. All prices from the website were recorded on the 21st September 2020.

[2] Quote obtained by the author (in Ireland) through the website (novioscan.com) and by subsequent email with the sales team at Novioscan (21st September 2020). Price for direct purchase of the device from the company.

2.4 Bioimpedance Fundamentals and an EIT Nocturnal Enuresis Alarm

In this section, the fundamentals of bioimpedance are first studied. Next, technologies that harness the phenomenon of electrical current flowing through tissue are examined. Then, the use of bioimpedance in BVM is reviewed. And finally, the proposed proactive bedwetting alarm using bioimpedance-based images is presented.

2.4.1 Fundamentals of Bioimpedance

When current flows through an electrical circuit, the current is subject to an impedance that hinders current flow and creates a voltage difference. This impedance consists of resistance and reactance. The resistance acts for both direct and alternating current, while reactance only acts with alternating current. The fundamental relationship of voltage, current and impedance is given by Ohm's Law. Using the phenomenon of impedance and Ohm's Law, devices can be used to capture electrical properties of different materials.

When electrodes are connected to a biological tissue, an electrical circuit can be created. The circuit can then be used to capture information on the body of interest. Each tissue has its own ability to conduct electrical current, which is referred to as conductivity. Conductivity is inversely proportional to the resistivity of a material and hence, conductivity is also inversely proportional to the resistance. The conductivity of a material may be reported as a single value for a given frequency and temperature, when homogeneity of the body of interest is assumed.

At different current frequencies, the electrical properties of tissues can vary. A tissue is composed of many cells that influence current flow based on frequency [95]. The reason for varying impedance values with frequency can be explained by considering a cell as an electrical circuit of three components: a resistor R_e representing the extracellular fluid, a resistor R_i representing the intracellular fluid and a capacitor C_m representing the low conducting membrane [95]. The equivalent circuit for the cell is shown in Figure 2.7.

The impedance of the circuit, Z, as a function of the angular frequency ω is defined as:

$$Z(\omega) = \frac{R_e R_i + \frac{R_e}{j\omega C_m}}{R_e + R_i + \frac{1}{j\omega C_m}}. \tag{2.1}$$

At low frequency, most of the current flows through the extracellular fluid as the current cannot pass through the membrane [95]. Thus, the impedance is equivalent to the resistance R_e. At higher frequencies, most of the current flows through both the extra- and intracellular fluid and the capacitor becomes closer to a closed-circuit element [95]. Thus, the impedance is mostly

resistive again, composing of both R_e and R_i in a parallel resistor circuit. In between low and high frequencies, the impedance is complex [95]. As the phase increases, the resistance and reactance map to an approximate semi-circle when plotted on a Cole-Cole plot as shown in Figure 2.8 [95]. The plot also shows the impedance being primarily resistive at low and high frequencies.

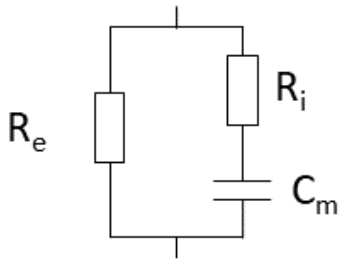

Figure 2.7: Three circuit elements model of a cell containing resistive elements and a capacitive element that affects the impedance in terms of the phase. A resistor R_e represents the extracellular fluid, a resistor R_i represents the intracellular fluid and a capacitor C_m represents the cell membrane, which acts as an insulator between two conductors.

Temperature also affect the electrical properties of material, e.g., dielectric properties of tissue [96], [97]. Thus, conductivity is temperature dependent. Experiments typically control the temperature or the tissue temperature may be assumed, e.g., body temperature or standard room temperature.

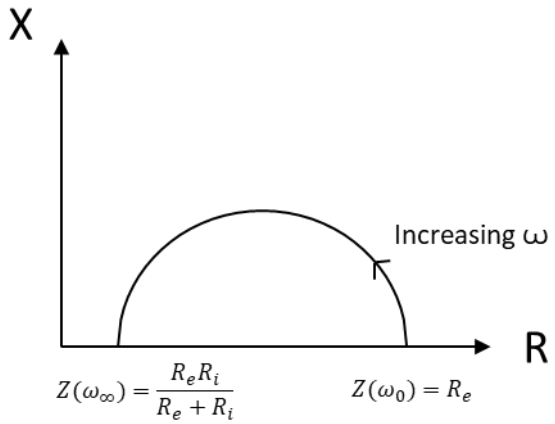

Figure 2.8: Cole-Cole model describing how the impedance changes in terms of resistance R and the reactance X. As the angular frequency ω increases from low (direct current) to high (infinite), the impedance changes from being entirely resistive to complex and then back to resistive again based on how current flows through the extra- and intracellular fluid and the capacitor acting membrane.

This section has provided insight into the fundamentals of impedance and how the impedance of tissue is affected under different conditions. Now, the measurement of bioimpedance can be discussed.

2.4.2 Fundamental Bioimpedance Measurement

Bioimpedance measurement involves the injection of small alternating-current (milliamps or less) into a body of interest and the measurement of the resultant voltages. Two electrodes can be used for injection and measurement. This system is referred to as the two-electrode method. An alternative system involves two electrodes for injection of current and two different electrodes for measurement of voltage, termed the four-electrode method. The systems are illustrated in Figure 2.9.

During injection of current into the human body, the electrode-skin impedance (contact impedance) is observed. This impedance is captured in the two-electrode method as both electrodes are injecting current and measuring voltage. The four-electrode method removes the measurement of electrode-skin impedance at the injection electrodes by measuring with two different electrodes [98].

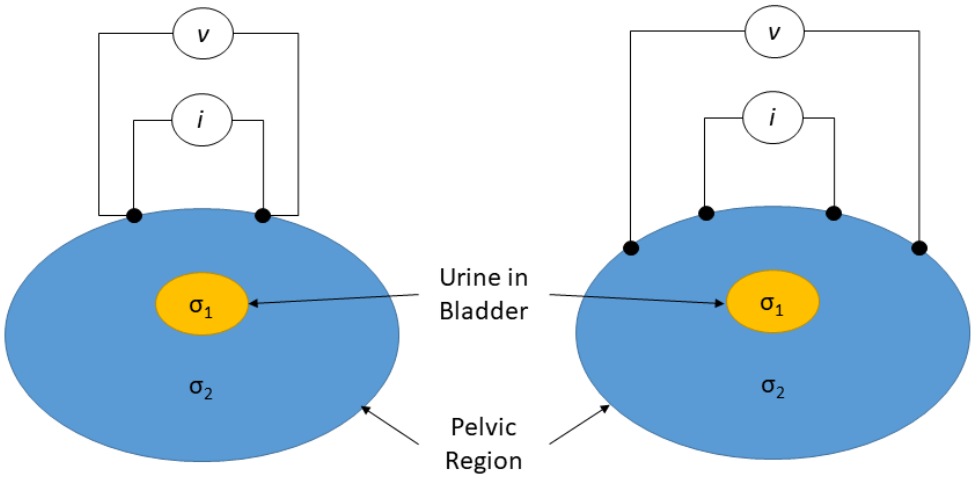

Figure 2.9: Illustration of the two-electrode method (left) and the four-electrode method (right) for the injection of current and measuring of the resultant voltage from the pelvic region containing the bladder of urine. The four-electrode eliminates the effect of measuring skin-electrode impedance resulting at the injection electrodes that is present in the two-electrode method.

Following measurement of the voltage from the bioimpedance circuit, the impedance can be calculated using Ohm's Law, or an image reconstructed to determine the observed conductivity

distributions from the given measurement data. Bioimpedance imaging is referred to as EIT and is discussed in the next subsection.

2.4.3 Electrical Impedance Tomography

Electrical Impedance Tomography involves two main parts: 1) collection of measurement data, and 2) image reconstruction. To collect measurement data, multiple electrodes (generally 8 or more) are placed around the ROI (e.g., the pelvis for bladder monitoring and the chest for breathing). For a given injection pair of electrodes, measurements are recorded at all the electrode measurement pairs. Stimulation and measurement patterns control which electrodes inject and which electrodes measure at any given time. A gap of a number of electrodes between the injection electrodes as well as between the measurement electrodes may be used to help capture changes deeper within the body of interest. This gap is referred to as a 'Skip' and is illustrated in Figure 2.10. The exact current amplitude injected is determined under international guidelines and varies with frequency [99]. Frequencies used in EIT are dependent on the application and hardware design but the range includes frequencies as low as Hz to as high as around 1 MHz [95], [100], [101].

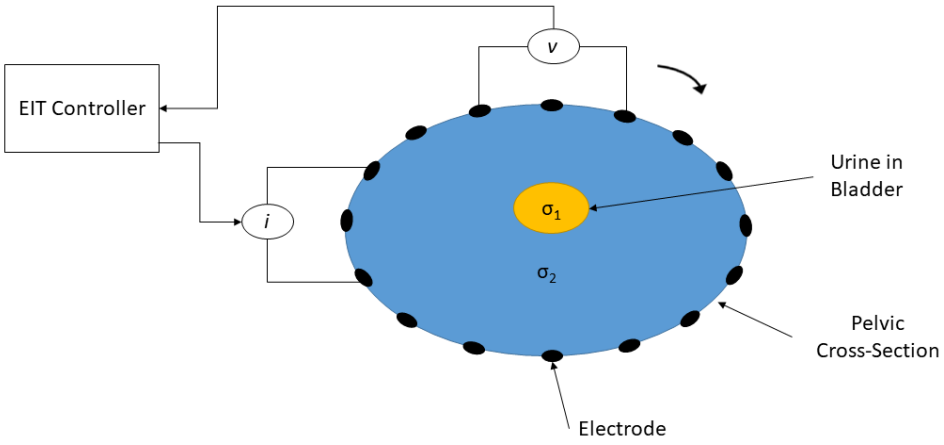

Figure 2.10: Illustration of collecting data from a region with a fixed electrode gap between the pair of injection electrodes as well as the pair of measuring electrodes. The illustration shows a Skip of one, where there is one electrode between a pair of injection electrodes as well as one electrode between the pair of measuring electrodes.

At data collection, the measured voltage data is gathered from a region of interest (ROI) with a given conductivity distribution (called 'the Forward Problem'). Next, the data is transferred for processing and storage to a computer from the EIT system. Then, an image can be reconstructed by giving the data to a reconstruction algorithm. The reconstruction algorithm is

performed to reconstruct the conductivity distribution observed by the given set of measurements (this is called ‘the Inverse Problem’).

Electrical impedance tomography is an ill-posed problem [95], which leads to any small noise greatly impacting the resultant image [102]. Thus, *a priori* information is often used in the reconstruction algorithm to help constrain the problem. The *a priori* information is typically described in the form of a FEM that can describe the electrodes and their location, the boundary of the region-of-interest (ROI) and any known approximate conductivity distributions within the model. An example of a cylindrical FEM of a ball in a cylinder is shown in Figure 2.11. This example was generated using the open-source EIT framework EIDORS [103], which includes algorithms to solve both the inverse and forward problems. After image creation, the images can be used for visual interpretation or further processed to give a single metric value (e.g., the sum of all the pixel values) that can be related to some quantity of interest.

Electrical impedance tomography imaging approaches includes absolute, frequency-difference and time-difference modalities. Absolute imaging involves capturing all the information at one instance of time and at a single frequency. Absolute imaging in EIT is often subject to high error as the imaging modality requires highly accurate *a priori* information that may be difficult to obtain in reality, e.g., the well-defined geometry of the boundary and electrodes in the situation being recorded [99]. Frequency-difference involves capturing data for the region-of-interest at multiple frequencies. The data frames are subtracted, capturing frequency-dependent information of the tissues within the region-of-interest. However, time-difference imaging is the most common imaging modality of EIT, as EIT has a high temporal resolution and many EIT noise sources are common across time [99]. With time-difference EIT, measurement data is recorded at two different instances in time. The data frames are subtracted, removing the common and constant noise between the two measurement instances. The resultant image then captures only information on the time varying quantities, e.g., breathing and bladder volume changes [11], [12].

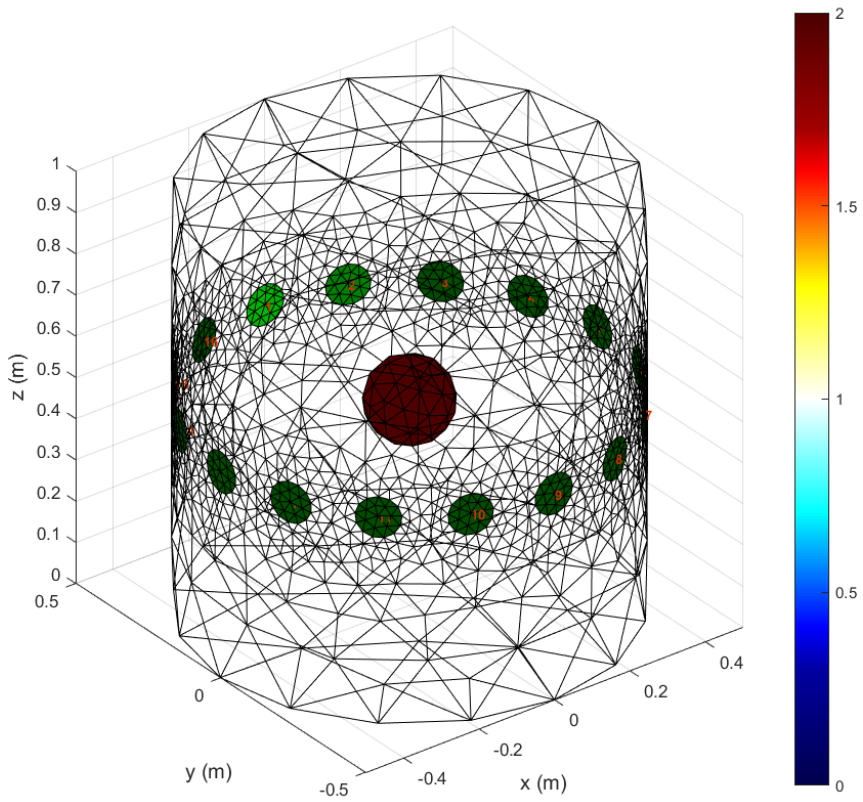

Figure 2.11: Cylindrical FEM with a sphere in the centre of conductivity 2 S/m (conductivity given by colour in FEM as per the colourbar). All the space outside the sphere is referred to as the background and has a conductivity of 1 S/m. The FEM is made up of 9565 tetrahedral elements. The circular electrodes on the boundary are marked in green. This FEM can be used to generate voltage measurement data at the electrodes, or to aid in image reconstruction as a priori information.

Bioimpedance measurements techniques including EIT have been investigated for BVM. Reasons for using bioimpedance to monitor bladder volume include: 1) urine can be the most conductivity substance in the pelvic region (dependent on the composition of urine from fluid intake and diet) as shown in Figure 2.12; 2) the bladder can change greatly in size from empty to full (bladder capacities previously discussed in Section 2.1.2). Based on these facts of large volume changes over time and a large contrast of the conductivity of urine from the surrounding tissues, bioimpedance measurement techniques have substantial promise in being able to measure changes in the bladder volume.

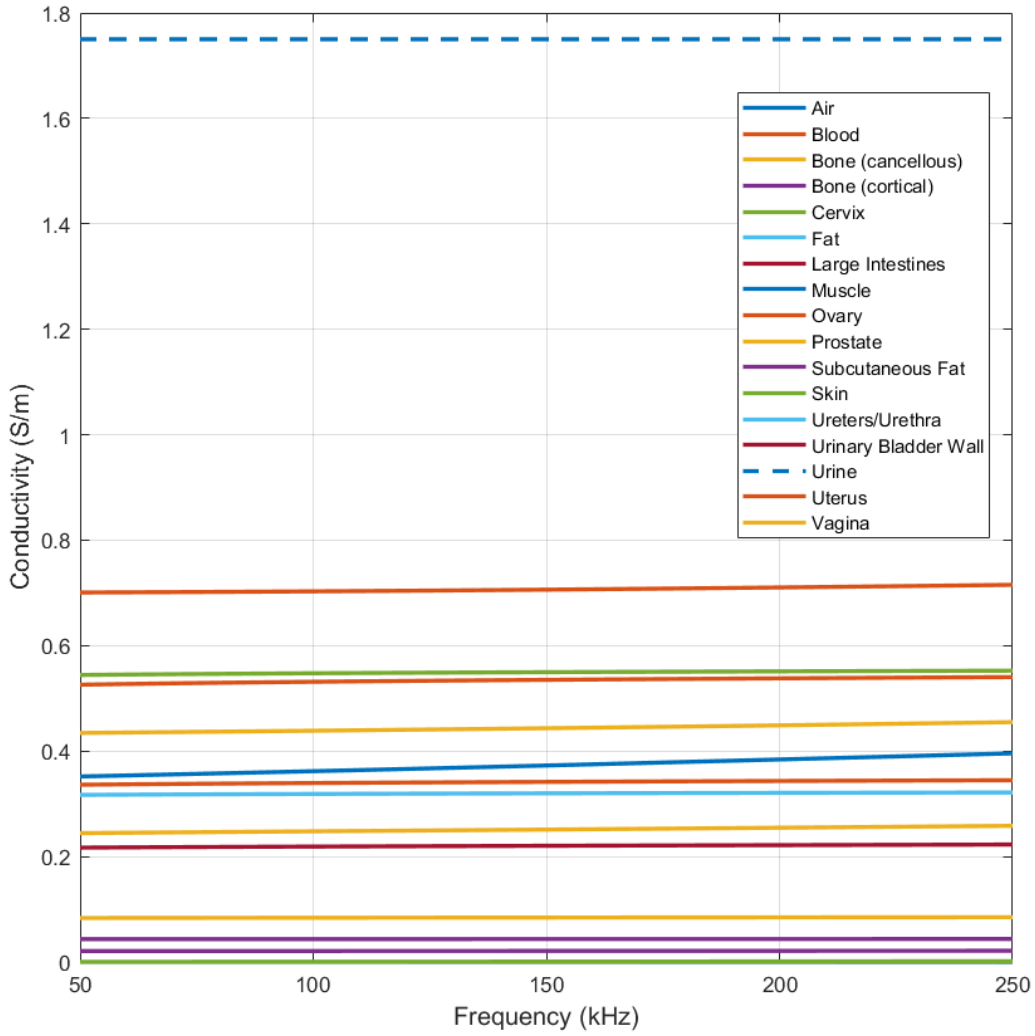

Figure 2.12: Electrical conductivities of tissues in the pelvic region including urine from the database of Hasgall et al. [104]. *Compared to most tissues, urine (highlighted by dash lines) has a high conductivity over this frequency range.*

Bioimpedance measurements for bladder monitoring have included using impedance data, voltage data, and image data to monitor the bladder volume. The state-of-the-art in these research areas are discussed in the following subsection.

2.4.4 Feasibility of Bioimpedance for Bladder Volume Monitoring

Studies have demonstrated that bladder volume can be monitored non-invasively using electrical impedance over the years [12], [13], [105]–[112]. These studies have investigated tracking bladder volume changes in animals or humans using electrical impedance devices. The studies have been performed in controlled scenarios of infused solution into the bladder and in normal bladder filling/emptying controlled testing scenarios. These studies are documented further in Table 2.1.

Most notably, the bladder volume has been found to correlate approximately linearly with the voltage or the impedance measured and the metrics using time-difference EIT image pixel values in the controlled testing scenarios. The linear correlation has been found to be either negative and positive in slope for voltage data, impedance data and image data. In the case of injecting a fixed-current amplitude, a negative correlation between the increasing bladder volume and the impedance-based measurement would be expected. However, one possible reason for why opposing correlations occurred is the bladder moving out of the measuring range of the electrodes during filling, e.g., because of electrode location and/or body mass index [12]. Thus, the system measures the increase in impedance by the bladder leaving the measured ROI rather than the accumulating bladder volume. Multiple electrodes around the pelvis and in different planes may add additional information by enabling measurements at different heights to occur, thereby monitoring the bladder as it fills more effectively. Findings from the literature demonstrate that bladder volume changes can be tracked using electrical impedance measurement methods such as the four-electrode method and EIT.

Building on these studies, a number of studies examined refining electrical impedance systems for both the four-electrode method and EIT. These studies included electrode placements investigations, combining reconstruction algorithms to overcome weaknesses of individual algorithms, and investigating/reducing noise from motion and variable urine conductivity [113]–[120]. This work has been carried out in simulation, in phantoms and in pilot studies. In particular, the EIT electrode placements have been tested on pilot adult volunteer data and comparisons of EIT against ultrasound have been performed for bladder volume estimation [120]. Electrical impedance tomography was found to be slightly more effective than ultrasound in estimating the maximum bladder volume. The error increased for both ultrasound and EIT when estimating the residual urine. However, ultrasound devices were found to be more effective at estimating the residual bladder volume. Thus, more work is needed to improve the mapping of the measured data and/or images reconstructed to a level of bladder fullness for EIT. Previously researched bladder state classification and bladder volume estimation methods are discussed in the next subsection.

Table 2.1: Summary of bioimpedance studies that have investigated the feasibility to monitor bladder volume non-invasively. The abbreviations: yrs, Neg., Pos. RMS, r, TD, $\Delta\sigma$, ΔZ stand for years, negative, positive, root mean squared, the Pearson correlation coefficient, time-difference, the conductivity change, and the impedance change, respectively.

Reference	**Volunteer or Species Description**	**Volunteer Condition**	**Body Position**	**Bladder Filling/Voiding Type**	**Measurement System**	**Injection Current†**	**Freq.**	**Data Form**	**Trend Observed**
Denniston & Baker [105] (1975)	6 Dogs, 15-25 kg	Healthy, Sedated	Lying*	Catheterised Bladder Filling	Four-Electrode Method	4 mA	100 kHz	Impedance	Linear Neg. Trend with Volume
Doyle & Hill [106] (1975)	10 Adults	Incontinence Patients, 3 Sedated	Supine, Sitting	Catheterised Bladder Filling	Four-Electrode Method	4 mA_{rms}	100 kHz	Impedance	Linear Neg. Trend with Volume
Abbey & Close [107] (1983)	20 males, 20 females, 18-43 yrs	Healthy	Supine	Self-Bladder Filling	Four-Electrode Method	0.2 mA	75 kHz	Impedance	Neg. Trend with Time
Yamada et al.[#] [109] (1994)	7 males, 3 females, 46-80 yrs	Patient, Impaired Bladder Function but no Urinary Incontinence	Not Stated	Catheterised Bladder Filling	Four-Electrode Method	1 mA_{peak}	50 kHz	Impedance	Neg. Trend with Volume and Time
Kim et al. [108] (1998)	12 males, 1 female, 24-48 yrs	Spinal Cord Injuries	Not Stated	Catheterised Bladder Filling	Two-Electrode Method	1 mA	60 kHz	Impedance	Neg. Correlation with Volume (r = -0.7988)

Table 2.1 continued

Reference	**Volunteer or Species Description**	**Volunteer Condition**	**Body Position**	**Bladder Filling/Voiding Type**	**Measurement System**	**Injection Current†**	**Freq.**	**Data Form**	**Trend Observed**
Shida & Yogami [112] (2006)	1 Male, Mid. 20's, 64 kg	Not Stated	Lying (Supine*)	Self-Bladder Filling	Four-Electrode Method	Not Stated	100 kHz	Impedance	Neg. Trend with Time
Leonhardt et al. [12] (2011)	9, Males, 23-63 yrs, 59-105 kg	Paraplegics	Supine*	Catheterised Bladder Filling	16-electrode EIT, single ring belt	5 mA_{rms}	50 kHz	TD Images (Representing ΔZ)	4 Neg. Correlations with Volume ($r = -0.8776$ to -0.9796 5 Pos. Correlations with Volume ($r = 0.5319$ to 0.8313)
Liao & Jaw [110] (2011)	3 Females, 43-55 yrs, 52-62 kg	Not Stated	Not Stated	Catheterised Bladder Filling	Two-Electrode Method	0.2 mA	115 Hz	Voltage	Pos. Linear Trend with Volume
Li et al. [121] (2013)	1 male ('college student' [121])	Healthy	Lying	Self-Bladder Filling	Four-Electrode Method	1 mA_p	50 kHz	Impedance	Neg. Trend with Time

Table 2.1 continued

Reference	Volunteer or Species Description	Volunteer Condition	Body Position	Bladder Filling/Voiding Type	Measurement System	Injection Current†	Freq.	Data Form	Trend Observed
Palla et al. [111] (2015)	1 Subject	Healthy	Sitting	Self-Bladder Filling	Four-Electrode Method	100 uA	50 kHz	Impedance	Neg. Trend with Time
Li et al. [13] (2016)	6 Males, 23-26, 55-70 kg	Healthy	Lying (Supine*)	Self-Bladder Filling	1) Four-Electrode Method 2) 16-electrode EIT, single ring belt	0.5 mA_{peak}	50 kHz	1) Impedance 2) TD Images (representing $\Delta\sigma$)	1) Neg. Correlation with Time in 4/6 cases for 4-Electrode Method ($r = -0.3592$ to -0.9753) 2) Pos. Correlation with Time for $\Delta\sigma$-based images ($r = 0.9694$ to 0.9913)

†Some papers did not report the measure of current, i.e., RMS, Peak, Peak-Peak. In these cases, this information is absent in the table
#Information based on the available partial Japanese [122] and full English versions of this study.
*Not stated in text but demonstrated in figures.

2.4.5 Bladder Fullness Prediction and Bladder Volume Estimation

Bladder fullness monitoring has been examined based on both bladder state classification and bladder volume estimation. The research in this field is summarised in Table 2.2.

At the time of starting this research, the state-of-the-art in the area of bladder state classification was limited. Previous work suggested thresholds with certain values may work for alerting when to go to the toilet based on analysis of the data gathered, e.g., 60-70% of the maximum desire to void volume [109]. A study by Abbey and Close [107] used the four-electrode method and a cumulative sum test to determine large increases in bladder volume and then to alert of bladder fullness (defined in the study as the urge to void). A decision rule to class as 'void' (classes: 'void' and 'no void') was equivalent to void volumes of greater than 300 ml. The prediction algorithm to classify voiding had an accuracy of 74.6%, a sensitivity of 78.9% and a specificity of 66.8%. This result showed strong potential for bladder state classification.

However, the main focus of the field at the time of starting this research was on estimating the bladder volume, as can be seen in the summary in Table 2.2. The bladder volume estimation approach has largely been performed using regression methods. For example, prediction of bladder volume based on metrics from images such as global impedance (sum of all the pixel intensity values in an EIT resistive image) or the use of neural networks to predict the exact bladder volume based on the voltage data collected from an EIT system [115], [123], [124]. In ideal scenarios of no-noise and no-other varying conditions beyond bladder volume, the algorithms devised in these studies performed well (relative volume errors as low as 0%). However, the estimation performance of the devised algorithms was susceptible to conditions of high added noise, geometry mismatch and varying urine conductivity. Performance degraded in these scenarios and errors in bladder volume estimation could be beyond 300 ml in certain cases (e.g., testing the effect of varying urine in neural network bladder volume estimation in simulation [115][3]).

A metric specifically for overcoming variations in urine conductivity was proposed by Schlebusch et al. in [117]. After fitting to the training bladder volumes at a fixed urinary conductivity, test scenarios included varying conductivity and varying noise in simulation as well as phantom experiments. In simulation, the bladder volume could be estimated approximately independently of the tested urine conductivities ({0.40, 1.22, 2.00, 2.80} S/m).

[3] Translation and interpretation for the thesis [115] (in all referenced cases) based on using Google Translate (https://translate.google.com/) for the text as well as visual interpretation for graphics. E&OE.

For this finding, the algorithm was applied to the reactance-based component when data was generated at a single frequency and the absolute impedance for frequency difference data (over the range of approximately 100-500 ml). Noise greatly affected the algorithm with errors ranging[4] from 0 ml to approximately 390 ml in estimation of bladder volume at the signal-to-noise ratio (SNR) of 40 dB. In phantom experiments, the performance of the metric to remove the influence of urine conductivity on measurements observed in simulation was not shown as strongly. However, bladder volume estimation errors were below 50 ml in the case of applying the algorithm to the single frequency reactance data. Further quantification is needed as well as comparison to other metrics to determine the exact improvement of the algorithm.

Another EIT bladder fullness monitoring method is the estimation of the bladder shape first, before estimating the volume. In a preliminary simulation study by Khambampati et al. [125], the shape of the bladder was estimated for a two-dimensional (2D) numerical forward model. The volume can then be estimated by determining the area of the reconstructed shape [125]. However, this method increases the number of steps required to determine the resultant bladder volume leading to potential of error propagation at each step.

Both thresholding and bladder volume estimation have limitations. The thresholding performed in bioimpedance is similar to that in the ultrasound bladder monitoring field discussed in Subsection 2.3.4.1. Thresholding is suitable in controlled scenarios but may face challenges of inter- and intra-individual differences e.g., obesity and sensor misplacement. Estimating bladder volume requires initial input of bladder volume to help fit algorithms to the data. This procedure may be too complex at night-time in home scenarios of children bedwetting their bed, and where alertness of the child may be questionable. Estimating the bladder volume and then introducing a method to determine whether the bladder volume is full or not is also increasing the risk of error propagation. Thus, room exists to improve the bladder fullness prediction for an alarm solution.

[4] Exact upper value dependent on which data type (single frequency absolute impedance measurement, single frequency reactance-based measurement; frequency-difference absolute impedance measurement).

Table 2.2: Summary of studies translating bioimpedance measurements into quantifications of bladder fullness

Reference	Analysis Type	Intended Application	Test Scenario	Measurement System	Conditions Tested
Abbey & Close [107](1983)	Bladder State Classification	Predicting bladder fullness for individuals with spinal cord injury	40 Healthy Adult Volunteers	Four-Electrode Method	Self-bladder filling of volunteers in supine position over twelve four-hour periods
Yamada et al. [109](1994)	Bladder State Classification	Alternative to diapers for urinary incontinence	10 Adult Patients (Catheterised)	Four-Electrode Method	Electrical Impedance Measurement during Controlled Infused Saline
Schlebusch et al. [123] (2013)	Bladder Volume Estimation	Determine when to void in paraplegic patients and individuals with impaired bladder sensation, e.g., age-related diabetic neuropathy	Simulation	16 Electrode Single Ring EIT System	Varying Bladder Volumes Varying Added Noise
Schlebusch et al. [126] (2014)	Bladder Volume Estimation	Preventing kidney reflux and overflow incontinence	Simulation	2x32 Electrode Rings EIT System	Varying Bladder Volumes Varying Urine Conductivities Varying Added Noise
Schlebusch et al. [124] (2014)	Bladder Volume Estimation	Determine when to void in paraplegics and individuals with impaired bladder sensation	Simulation	16 Electrode Single Ring EIT System	Varying Bladder Volumes Varying Urine Conductivities Varying Added Noise

Table 2.2. continued

Reference	Analysis Type	Intended Application	Test Scenario	Measurement System	Conditions Tested
Schlebusch et al. [117] (2014)	Bladder Volume Estimation	Determine when to void in individuals with impaired bladder sensation e.g. overactive bladder syndrome	Simulation & Phantom	8 and 16 Electrode Single Ring EIT Systems	Varying Bladder Volumes Varying Urine Conductivities Varying Added Noise EIT Hardware using Cylindrical Tank
Schlebusch [115] (2015)	Bladder Volume Estimation	Determine when to void in patients with impaired bladder sensation, e.g., paraplegics	Simulation & Phantom & 4 Neurologically Impaired Volunteers	16 Electrode Single Ring EIT System	Varying Bladder Volumes Varying Urine Conductivities Varying Added Noise Boundary Mismatch EIT Hardware using Cylindrical Tank Electrical Impedance Measurement during Controlled Infused Saline
Leonhäuser et al. [120] (2018)	Bladder Volume Estimation	Determine when to void in spinal cord injury & neuropathic bladder	10 Healthy Adults Sitting on Commode	16 Electrode EIT System with 4 Electrode Configurations Tested	Electrical Impedance Measurement during Voiding of Sitting Volunteers

.

2.4.6 Previous Work of Bioimpedance Bladder Monitoring for NE

Nocturnal Enuresis (NE) is a relatively new clinical application for bioimpedance. Patient cohorts referred to in the literature for monitoring of bladder fullness include those with urological diseases, spinal cord injury or the elderly [12], [13], [107], [123]. In feasibility and pilot studies discussed in Subsection 2.4.3, healthy volunteers consisted of adults. However, one bioimpedance-based study performed research for an alarm for the cause of NE [127].

Shin et al. [127] employed a system-on-chip approach with bioimpedance measuring capabilities to form a three-electrode bioimpedance device for an NE application. In the work, the hardware was assembled along with a multi-frequency motion noise reducing algorithm for postural changes. The algorithm was assessed on three adult volunteers during the daytime before being tested on one volunteer for seven nights. Feasibility for a bioimpedance enuresis alarm was shown. An impedance change captured during the day was suggested as the impedance change threshold. However, a three-electrode measurement is uncommon in this field and a system with more electrodes is likely to provide more information.

While much work in the bioimpedance bladder monitoring field has been performed in optimising hardware and handling noise, there is room to improve the level and robustness of research in predicting the bladder fullness after data collection. For example, research to establish what data source is best to use in bladder state classification, voltage or image, and what specific challenges related to child-based measurements are needed. These questions will be investigated through this thesis based on the proposed EIT-based bladder fullness monitor for NE that is discussed in the next section.

2.4.7 Proposed EIT-based Bedwetting Alarm for NE

Work in the bioimpedance field to date has highlighted the potential of the technology to monitor bladder volume. Research has examined the potential of bioimpedance for alarms and bladder volume estimation. However, methods such as bladder volume estimation require reference bladder volumes and measurement data as input. Bladder volume input may be difficult in real life as children can wet the bed or may not be fully awake to measure the bladder volume. As discussed in Section 2.2, parents/guardians are already burdened by the condition without adding an extra level of workload. Thus, a prediction method with easy input is needed. Also needed are adaptive methods of learning the optimum level at which to alert rather than a pre-set or user-defined threshold.

A powerful set of tools is now available for learning a specific task based on a collection of data in the form of machine learning. In fact, machine learning has already been employed in this field in the form of neural networks for bladder volume estimation at the date of starting this research [115], [124]. However, a more direct solution for determining whether to alert the user or not would be classification, e.g., 'not-full' and 'full'. In this application, a means to accurately alert the child to the toilet before they bed wet is required rather than knowledge of the precise bladder volume. When the classifier predicts full, the alarm can sound to alert the child. These labels can be assigned during data gathering based on labelling a number of recordings before a voiding episode. If incorrect, the number of recordings before the episode marked as full can be increased to give an earlier alarm. This design would enable a proactive enuresis alarm, potentially overcoming some of the limitations of the current alarm design, e.g., alerting after bedwetting has begun and the long response time.

Importantly, these labels only rely on detection of a voiding episode. Two methods are proposed: 1) detection of rapid change in the direction of the bladder filling signal trend indicating voiding; 2) input from the child to inform the device the child has voided. In the input from the child scenario, a happy and sad face ('emojis') could be used to indicate successfully waking up to go to the toilet event or a bedwetting event, respectively. The early alert may be delayed over time, to help the child to become more independent of the device, i.e., waking to go to the toilet by themselves.

Preliminary research has indicated that an EIT system is better for monitoring bladder volume than the four-electrode method by Li et al. [13]. Li et al. showed that the EIT method provided a more consistent correlation of bladder volume with image data when compared to the four-electrode method (100% positive linear correlations for images of conductivity change with EIT, compared to 66.67% for negative correlations for impedance changes with the 4-electrode method, 6 male volunteers in total, further details in terms of Pearson Correlation Coefficients in Table 2.1) [13]. Also, EIT had several advantages over the four-electrode method, such as more measurements from around the body and the visualisation of the bladder volume change and the conductivity change spatially in terms of pixel intensity [13]. Problems arising from the bladder filling moving out of the measuring region (which were discussed in Section 2.4.4 for both bioimpedance measurement methods) may be overcome with an EIT system using more than four electrodes and spreading the electrodes over the bladder filling region. Also, an EIT system can capture two- and four-electrode measurements on data collection.

Along with being non-invasive, EIT can be low-cost and can be miniaturised for wearable applications such as hand gesture recognition on smart watches [128]–[130]. A wearable hand gesture recognition EIT system for smart watches operating at 40 kHz was made in by Zhang et al [130] for a total hardware cost of $80 in their 2016 study [130]. Zhang et al. [130] highlighted that the device could be made more compact and for lower cost when produced in mass in commercial applications. The low-cost of parts for EIT could make the technology an attractive alternative to ultrasound approaches, previously discussed in Section 2.3.4. Both technologies can have difficulties in terms of sensor/electrode positioning and contact. However, electrical impedance tomography offers the potential to suppress these errors by time-difference imaging as well as providing more data channels from multiple electrode combinations to overcome noise in the system. Therefore, an EIT system is examined as the bioimpedance measurement technology for this alarm proposal. Illustrations of the alarm concept is given in Figure 2.13 and Figure 2.14.

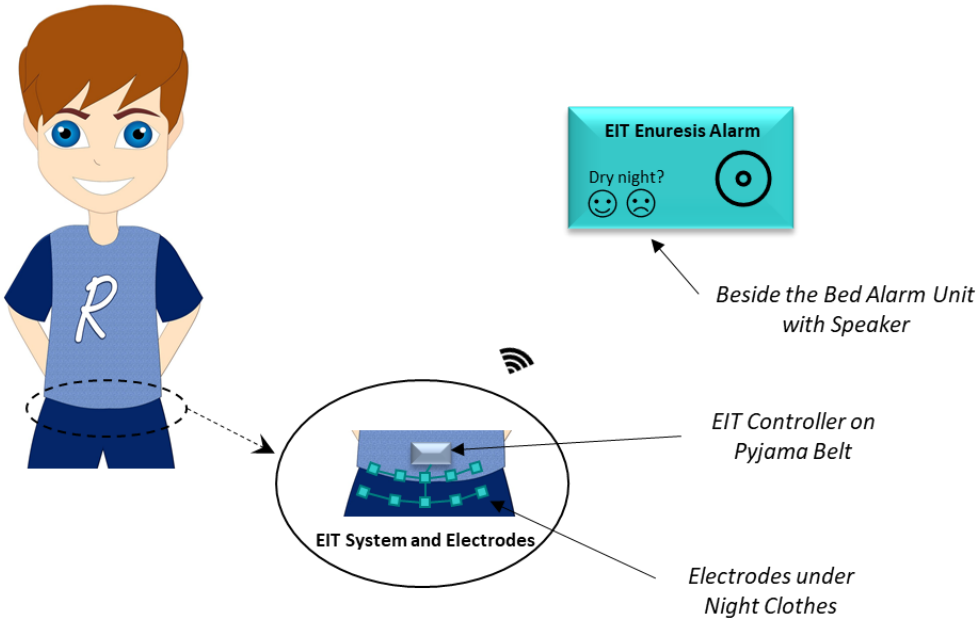

Figure 2.13: Illustration of an enuresis alarm using an EIT electrode array. The alarm unit can be positioned beside the bed to wake the child on detection of a 'full' state bladder.

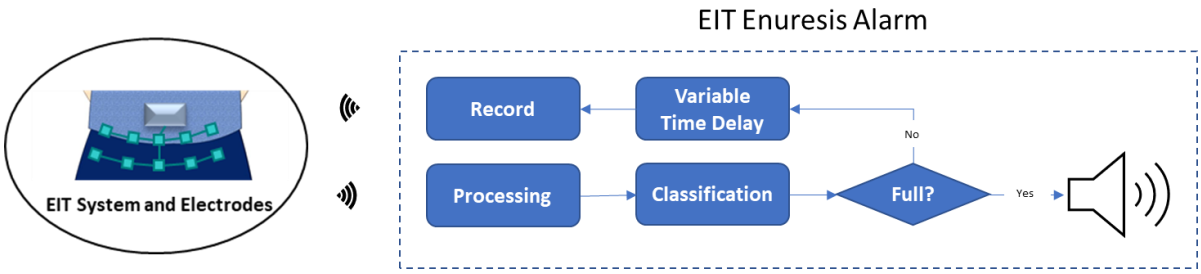

Figure 2.14: Simplified EIT monitoring system with a machine learning classifier to determine whether the processed frame is for a not-full or full bladder. The alarm box communicates back and forth with the EIT recording system wirelessly. A variable delay can be employed where the recording should be infrequent just after voiding, but more frequent as time passes. On classification of a 'full' state, the alarm sounds.

The chapter can now be concluded having critically reviewed the state-of-the-art literature in this field and identified key gaps and limitations.

2.5 Summary

In this chapter, the background for the thesis was presented. The background included an overview of the urinary bladder, including the role of the bladder in the urinary system, the process of voiding and developing and maintaining bladder control in Section 2.1. Voluntary bladder control develops as the nerve and muscle systems of a child matures. However, some children can have difficulty establishing or maintaining bladder control, particularly at night.

In Section 2.2, the medical condition of NE where children involuntary void during sleep was presented. Research of the condition highlighted that NE is a common childhood condition with significant consequences for the child, the surrounding family, and the health system. Evaluation guidelines exist to eliminate potential underlying causes and identify children who truly have only NE. Then management and treatment options can be examined for remedying the condition.

In Section 2.3, the management and medical treatment options for NE were discussed. The first-line medical options were alarm and Desmopressin-based therapies. The selection of a particular therapy is dependent on the suitability for the child and the family. The alarm has been shown to produce better long-term NE outcomes than Desmopressin therapy. However, alarm therapy has a higher discontinuation rate than Desmopressin for reasons such as false alarms, waking the family but not the child with NE, as well as taking a longer time to show a bedwetting reduction when compared to Desmopressin. Current enuresis alarms are also reactive in operation rather than proactive, requiring the start of urination in order to alert the

child. Thus, a proactive solution to monitor the bladder and to alert before bedwetting is needed that may reduce some of the downsides of the alarm device. Proactive options to monitor the bladder currently under research include Ultrasound and UWB radar. These technologies have been present for a number of years but have not reached common usage. Potential reasons include financial cost and size. However, bioimpedance measurement is another promising potential avenue with the need for further research.

In Section 2.4, the fundamentals of bioimpedance were discussed. Research in the field was presented for the feasibility to monitor bladder volume; translating impedance measurements to measures of bladder fullness; and the previous use of bioimpedance methods in NE applications. Research into child-focused applications like NE is limited to one paper and no studies have performed numerical simulations with child models or pilot studies with child volunteers in the field. The current state-of-art of bladder fullness monitoring using EIT has focused primarily on bladder volume estimating. However, improvements such as direct prediction of the bladder state (e.g., ‘not-full’ and ‘full’) for an alarm solution can be made using machine learning. These improvements may eliminate the need to record bladder volume measurements and eliminate error propagation over the multiple stages required for estimating bladder volume followed by classifying bladder state. A proposal of an EIT-based enuresis alarm using machine learning was then presented to improve on these limitations of current research. This proposal may further the field to a low-cost and proactive enuresis alarm solution. However, this proposed solution has yet to be investigated to assess the feasibility of the approach over some of the conditions that are challenging for bladder volume bioimpedance measurement.

In this chapter, it was found that the primary test platforms used to investigate new approaches and algorithms in the literature for EIT bladder applications were mainly simulation and small pilot studies. The studies examined scenarios involving varying bladder volumes, urine conductivities and added noise. This thesis makes advances towards the proposed solution presented in Figure 2.13 and Figure 2.14 by each successive chapter taking a step forward in the investigation of using machine learning for bladder state classification. Numerical simulation is used to investigate the approach and to determine tolerances of the classification algorithms with different conditions for a future bedwetting alarm device design using EIT. However, numerical forward models are needed to generate the measurement data. Thus, a numerical forward model for early-stage investigation with plausible measurement data is developed in the next chapter.

3 Numerical Modelling of the Adult Pelvic Region

In Chapter 2, the need for bladder state classification was presented for children suffering from NE. The technology of EIT showed fundamental promise for BVM as urine has a high contrast in terms of electrical conductivity compared to the large surrounding tissues in the pelvic region. Further, previous studies have shown potential of the four-electrode method and EIT to monitor electrical impedance changes due to the bladder filling, as discussed in Section 2.4.4.

Numerical simulations can be performed to test EIT bladder state classification before real-world testing. Simulations can be performed with the use of numerical forward models that represent the pelvic region boundary and the bladder. Thus, a numerical forward model is designed and developed in this chapter to enable initial investigation of bladder state classification. The numerical forward model is informed by anatomical information from the pelvic region.

The forward model designed and developed in this chapter is adult size and is used for initial testing before tailoring the system for children. Using an adult model is in keeping with the literature, previously discussed in Section 2.4.5 and Section 2.4.6. Also, it would be expected that the findings for any new medical device would have to be verified on healthy adult volunteers before ethically assessing the EIT bedwetting device with enuretic children. Therefore, it would be important to know how bladder state classification performs on an adult model that has wider girth and a bladder deeper within the pelvic cavity than a child. After development of the forward model, the forward model is used to generate example raw voltage data (also call measurement data) and time-difference images to validate the functionality of the model. Then, the forward model can be used for bladder state classification studies that are performed later in the following chapters.

Specifically, this chapter is divided as follows: a general overview of numerical forward models for BVM using EIT is presented in Section 3.1; then, the design of the boundary of the model is discussed in Section 3.2; the selected conductivity of the forward model excluding the bladder region is discussed in Section 3.3; the bladder model design is presented in Section

3.4; the resultant anatomical model is presented and the main characteristics summarised in Section 3.5; measurement voltage and reconstructed image data is generated from the model in Section 3.6; the limitations with the model are discussed in Section 3.7; and the chapter is concluded in Section 3.8.

This chapter draws from earlier research work in the following publications:

1. E. Dunne, B. McGinley, M. O'Halloran, and E. Porter, "A Realistic Pelvic Phantom for Electrical Impedance Measurement", *Phys. Meas.*, vol. 39, no. 3, pp. 1-10, Mar. 2018, doi: 10.1088/1361-6579/aaa3c0.
2. E. Dunne, A. Santorelli, G. Leader, B. McGinley, M. O'Halloran and E. Porter, "Supervised Learning Classifiers for Electrical Impedance-based Bladder State Detection", *Sci. Rep.*, vol. 8, no. 1, Art. no. 5363, pp. 1-12, Mar. 2018, doi: 10.1038/s41598-018-23786-5.

3.1 Overview of Numerical Forward Model Complexity in EIT-Based Bladder Volume Monitoring

In EIT, simulations can involve using 2D or three-dimensional (3D) FEMs to describe a particular region in the body, such as the pelvis, with varying physical complexity. Using the finite element method, outer object dimensions, shape, and electrical properties can be described along with embedded objects or layers such as different tissue groups or organs (e.g., bladder). Typically, the outer-most object defines the external boundary of the FEM. Therefore, the outer-most object is often referred to just as the 'boundary'. The resulting models can then include a number of tissue types and structures. Once the models are developed, they are then used to generate relevant numerical measurement data.

For BVM using EIT, forward models have varied from 2D circular FEMs [113] to more commonly used 3D cylindrical FEMs [114], [115], [117], [124], [126] to represent the boundary of the pelvis. Some exceptions to these models include the use of a single computed tomography (CT) slice for 2D simulations [125] and a full body model in propriety software [115]. However, the use of 2D models may not allow for accurate modelling of the dispersion of current in 3D. The use of complex full body models may be time and resource consuming, particularly in early-stage testing of a novel approach. Also, incorrectly matching accurate models such as using the model of one person to represent another may provide additional error. This problem may be particularly relevant where it would be difficult to gather CT or

Magnetic Resonance Imaging (MRI) data of the individuals who will be using the EIT bedwetting alarm.

Further to the 2D or 3D boundary models, the bladder may be represented internally with a number of elements in 2D, or cylinders or spheres in 3D that can vary in locations from the centre of the FEM to the anterior [113]–[115], [117], [124], [126].

In this thesis, the early-stage testing makes use of cylindrical 3D FEMs as is common in the literature to date. Simplified models are also used to represent the bladder, especially the highly conductive urine. To advance these simplified models, key properties can be informed by anatomical information from the literature such as the dimensions of the boundary and of the bladder, and the conductivities of the background tissue and the urine. The generated data can be more representative of the real-world scenario by incorporating this anatomical data into the simple forward model.

Within each of the next three sections, the current state of the literature in boundary models and bladder models is discussed in more detail and various models are compared. Then, derived anatomical information is used to design improved forward models of the pelvic region. The anatomical information used includes appropriate boundary and bladder shape dimensions, and electrical properties of the actual tissues.

3.2 Modelling of the Pelvic Outer Boundary

In this section, the simplified numerical forward model excluding the bladder is devised. The work is based on previous literature in the field and anatomical information. The parameters examined in this section are the dimensions and shape of the boundary of the forward model.

3.2.1 Existing Simplified Numerical Forward Models of the Pelvic Boundary in the Literature

A number of similar cylindrical numerical forward models have been used in EIT-based bladder monitoring literature to date to model the exterior of the pelvis region [114], [115], [117], [123], [124], [126]. These models have mainly differed by the exact shapes of the cylinder used and the dimensions of the cylinder.

The primary cylindrical shape has been circular [114], [115], [117], [124], [126] with the exception of an elliptical cylinder in [123]. Where stated in the literature, the circular cylinder has had a radius of 15 cm [114], [115], [117], [124], [126], and heights of 3.9 cm [117] or

30 cm [114], [115], [124]. When a justification for these sizes was provided, the shape and dimensions employed were assumed to represent the abdomen [124] or to match the phantom setup later used in the same work [117]. The dimensions of such a cylinder as those previously described in terms of radius and height are demonstrated in Figure 3.1.

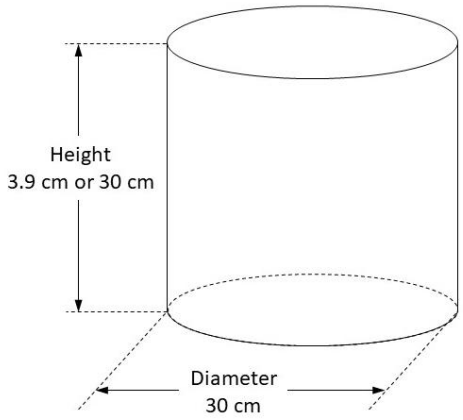

Figure 3.1: Sketch illustration of the main cylindrical boundary of the FEMs used in BVM using electrical impedance to date. The forward models are quite similar in terms of the diameter [114], [115], [117], [124], [126] *and the majority of the forward models are 30 cm in height* [114], [115], [124].

Following on from the literature, more dimensions can be specified in the simple model if an elliptical cylinder is used. Having more dimensions that can be specified is particularly useful as the human body is not a perfect circular cylinder. Therefore, an elliptical cylinder is used in this work as the basis of the simplified model for proof-of-concept testing of bladder state classification in simulation.

In the majority of cases of the forward models employed in the literature, the models make no reference to anatomical information for the boundary dimensions or shape (except where the model is assumed to represent the abdomen [124]). To make the forward model more relatable to the real-world case, more information from human data (e.g., CT scans and previous dielectric measurement research) can be employed to better inform the dimensions of the forward model. This topic is discussed in the following subsections.

3.2.2 Dimensions for the Boundary of the Numerical Forward Model

In the previous section, an elliptical cylinder model was chosen for the basic shape of the forward model. The dimensions of this boundary can be further informed by using anatomical information.

Medical image scans of the body such as those from CT can provide valuable information such as dimensions of the body itself, along with other anatomical information such as shape and location of organs or tissues. The United States National Library of Medicine Visible Human Project® (VHP®) [131] is a publicly available CT dataset for research that includes CT data for a whole body of an adult male cadaver (courtesy of the United States National Library of Medicine). In this work, the CT data for this adult male cadaver (specifically sourced from [132][5]) is used, with the pelvic region as the ROI. This ROI includes the pelvis and the abdomen from above the genitals to and including the navel (a distance of approximately 20 cm). This ROI allows the model to capture the bladder filling and facilitates usage of strong anatomical reference points such as the pubic symphysis employed in pilot studies to date [13], [120] for comparison with existing bladder EIT literature. Examples of scans in two different views are given from the CT database in Figure 3.2 with the bladder labelled. Having defined the ROI, dimensions can now be established along the anatomical planes and axes. Before detailing the dimensions, the anatomical planes and axes are defined for clarity and completeness.

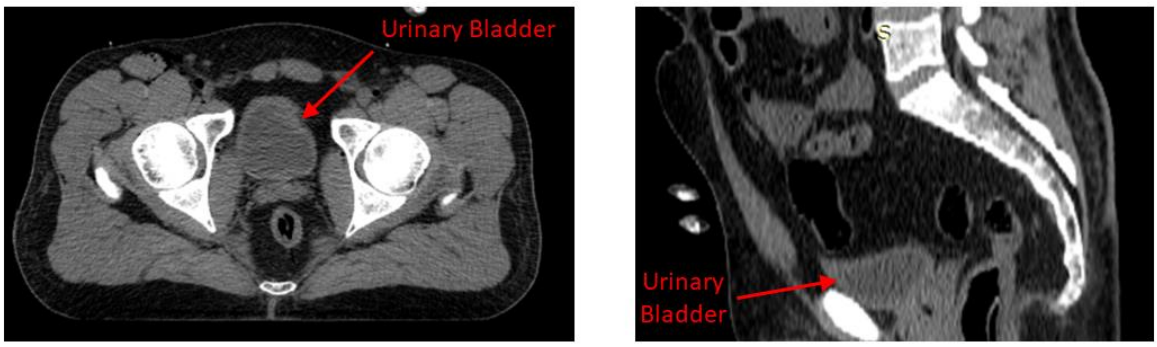

Figure 3.2: Example cross-section slices from the CT database of the male cadaver from the VHP® [131] *(courtesy of the United States National Library of Medicine). The CT data was specifically sourced from* [132][5]*. The urinary bladder is marked in both images. The bladder is nested in the anterior of the pelvic region of the human body.*

The anatomical planes in the body are the axial, coronal, and sagittal planes. These planes are at right angles to each other and are used to divide the human body in the 3D world. The planes are shown in Figure 3.3. A coordinate system for the body in terms of the anteroposterior, the left-right/transverse, and the craniocaudal axes is also given in Figure 3.3. Having clear planes and axes allows for more clear communication of the dimensions and orientations presented in this chapter. The measurements along the axial plane are first determined for the forward model.

[5] More up-to-date file formats for the data can be found on the VHP® [131] website [229].

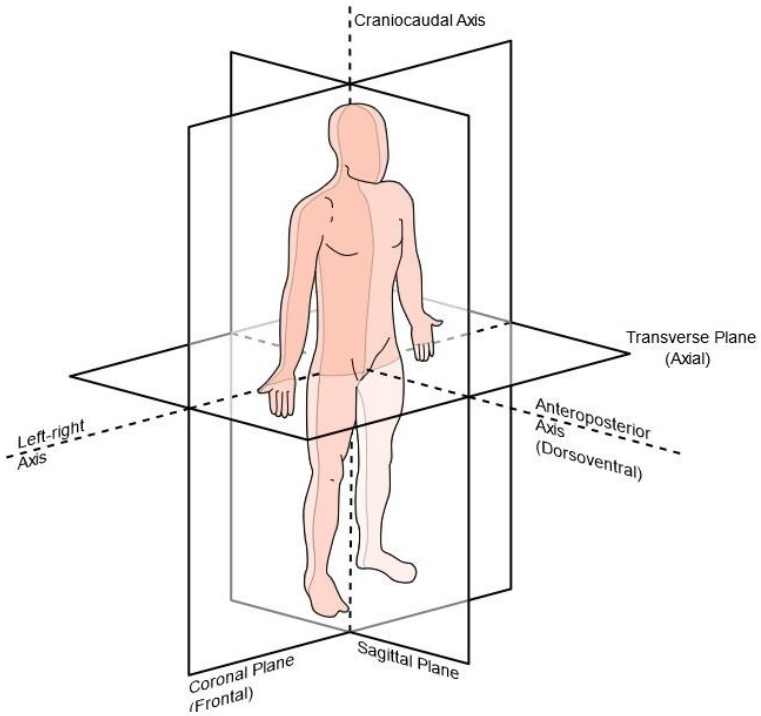

Figure 3.3: Illustration of anatomical planes and axes. The body can be divided into three planes and three axes. These planes and axes will be used to describe locations in the human body and in the model. Image sourced from "Anatomical Planes-en.svg" [133] *by Edoarado is licensed under CC BY-SA 3.0* [20] .

The height of the electrodes (along the craniocaudal axis) is the most relevant height for selecting which axial scan should boundary measurements be taken. The height of the electrodes is important because the forward model will assume electrodes are on the boundary (i.e., electrodes placed on the surface of the body). Previous EIT pilot studies have used distances from just above the pubic symphysis, the approximate midway between the pubic symphysis and the navel (approx. 8 cm below the navel), and at the waist for placing electrodes [12], [13], [120]. In ultrasound imaging of the bladder, the recommended heights for placing the probe in some National Health Service (NHS) hospitals is 2.54-3 cm above the pubic symphysis [134], [135]. Therefore, a slice of approximately 3 cm above the pubic symphysis is used in this work as the boundary of the slice is suitable for electrode placement. A bounding box was placed around the single slice from the adult male CT scans and the dimensions were measured manually. The resulting dimensions are illustrated in Figure 3.4.

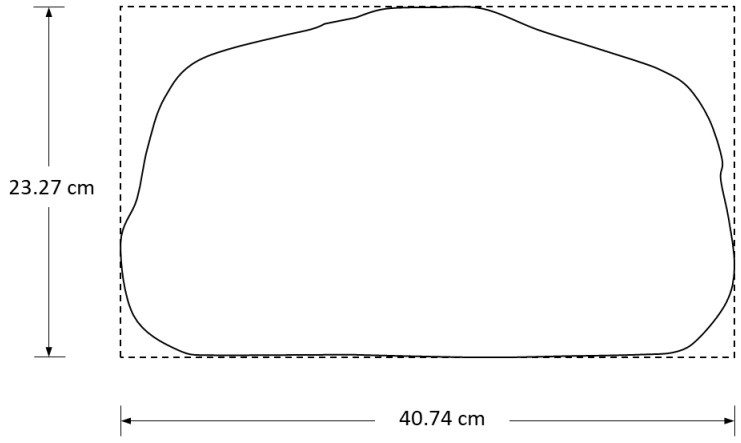

Figure 3.4: Sketch illustrating how the cross-sectional lengths of the simplified numerical forward model were determined using a CT slice approximately 3 cm above the pubic symphysis. A bounding box was placed around the boundary and the lengths of the box were measured and taken as the anterior-posterior length and the transverse length. These dimensions can be then fitted to the major and minor axes of the elliptical cylinder (the simplified numerical forward model).

The resultant axial dimensions were anterior-posterior length of 23.27 cm and a transverse length of 40.74 cm. To match the ROI selected, the height of the cylinder was defined as 20 cm (which is within height range of previous EIT BVM studies, 3.9-30 cm as discussed in Section 3.2.1).

3.3 Modelling of the Pelvic Region Background Conductivity

In this section, the background conductivity of the forward model is devised. The background conductivity is considered the conductivity assigned to the overall forward model, excluding regions of differently defined conductivity like the bladder. This work is based on previous literature in the field and available anatomical information.

3.3.1 Background Conductivities of Simplified Forward Models Previously used in the Literature

In the literature to date, homogeneous background conductivities outside the region of the bladder have been mainly used for numerical forward models [114], [117], [123], [124], [126], [136], of which a variety of different estimates have been used. Specifically, these background values have included 1 S/m [114], unit conductivity (where the conductivity units where specified in terms of ‘units’) [124], [126], the conductivity of the intestines [123], or the complex conductivity of muscles at different frequencies [117], [136].

Following on from the literature, an anatomically-informed background conductivity will be used in this work.

3.3.2 Selection of the Background Conductivity for the Forward Model

Anatomically-informed conductivities previously used in the literature include those of muscle and the intestines [117], [123], [136]. As discussed in Chapter 2, the pelvic and abdominal region consist of many other tissues, including fat and bone from the femur and the pelvic bone. These tissues are poor electrical conductors relative to muscle and the small and large intestines at low frequencies (conductivities for these tissues at different frequencies can be found at [104]). These tissues can be directly embedded into the forward model. For example, Schlebusch et al. [123] added a CT segmented pelvic bone to their forward model. However, the bladder model is the only individual anatomy part that is added within the boundary of the forward model for the initial investigations of bladder state classification

One way to determine the background conductivity would be to include these tissues from the ROI in a volume weighted average. However, a weighted average is only based on one circumstance (for instance, a cadaver of one single individual from a CT scan) and the conductivities and volumes may vary on a number of factors including tissue deformation, the presence of intestinal gas, the age and sex of the individual, and based on how fit an individual is (quantity of muscle and fat). Over time, the overall conductivity of the ROI for any given individual may also vary due to changing of lifestyle or diet. Therefore, no single conductivity value may be sufficient in representing all possible scenarios, particularly as the ROI is full of complex and dynamic processes including the urine filling the bladder, the digestive actions of the small intestines, and faecal matter moving in the large intestines and the rectum. However, defining each tissue may be too complex and resource consuming in a proof-of-concept.

For initial investigation, the conductivity of muscle is used in this work, similar to [117], [136]. The background conductivity error should be suppressed by time-difference imaging. Future models may incorporate more regions of different conductivity for the improved modelling. The conductivity value of 0.352 S/m for muscle was gathered from IT'IS database [104] at the frequency of 50 kHz. The frequency of 50 kHz is one of the main frequencies used in the literature to date for monitoring the bladder with electrical impedance (Table 2.1) and is within the hardware frequency capabilities as Sentec (formally Swisstom) Pioneer Set (SenTec AG, Switzerland, sentec.com) [137], research EIT hardware that could be used for data collection.

3.4 Bladder & Urine Modelling

In this subsection, bladder modelling in the literature is examined. Then, anatomical information regarding the bladder sizes and urine conductivities is presented along with the developed models.

3.4.1 Previous Bladder Models in the Field

As previously discussed, the bladder consists of a thin muscle within the bladder wall, and a cavity to store urine (Section 2.1.1). When modelling the bladder for EIT, the thin bladder wall is typically neglected in the literature and the volume and the conductivity are based solely on the urine, e.g., [114], [115], [117], [124]. Table 3.1 provides information on previous bladder models used in the literature.

As shown in Table 3.1, the model for most commonly representing the bladder was found to be a sphere. However, two studies used a cylinder to represent the bladder. The locations of the bladder models were either placed in the centre or touching the boundary wall (demonstrated in Figure 3.5), where the location was stated in the literature. In certain cases [114], [115], [124], the bottom of the bladder model in the craniocaudal axis was fixed in the FEM. This bottom position allowed the bladder model to extend upwards from a fixed craniocaudal height at the base, which may be considered more physiological [114]. In the studies documented in Table 3.1, the bladder shapes were mainly spherical and bladder locations were constrained to two common locations. In the next sections of the thesis, these bladder model features will be examined in more detail and improved upon.

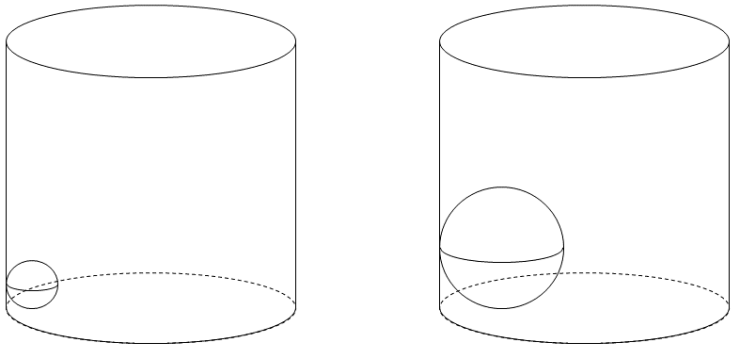

(a) (b)

Figure 3.5: Sketch interpretation based on one set of bladder positions in the literature [114], [115], [124]. *The bottom of the bladder model is on the base of the cylindrical model and in contact with the boundary wall: (a) a small bladder volume; (b) a fuller bladder volume than in (a) that has extended towards the centre of the FEM as the bladder filled.*

Aside from the bladder model shape and location, the bladder volumes and the urine conductivity values are also key parameters in the numerical modelling of the pelvic region. To date, a large variation of bladder volumes or dimensions have been employed in the literature, as summarized in Table 3.1. Across these studies, the urine volumes ranged from 10 ml to 11.49 L (including calculated volumes where dimensions of the bladders were given in the studies and the bladder model type is also given or assumed as a sphere based on the single radius dimensions for each bladder given). Thus, further information is needed to constrain the exact bladder volumes that would be expected in reality.

Table 3.1: Property summary of the simplified 3D bladder models previously used in EIT bladder monitoring. Bladder models vary in terms of dimensions, urine conductivity and location. Any specific anatomical reference of the bladder location was also captured. Please note: for values not stated, the entry is marked NS; where dimensions are given for a bladder model rather than volume, the volume is also given in the table and the volume is calculated under the assumption the model is a sphere.

Reference	**Bladder Model**	**Volumes/ Dimensions** [a]	**Location**	**Urine Conductivity**
Schlebusch et. al. [114] (2013)	Sphere	1-14 cm (radius) 4.19 ml – 11490 ml	Case 1: Centre of FEM Case 2: Bladder model in contact with the bottom of the Cylinder and touching a boundary wall	2 S/m
Schlebusch et. al. [123] (2013)	Parametrizable ellipsoid (Assumed Sphere)[b]	Approx. 1-9 cm (radius) 4.19 ml – 3050 ml	NS	3 S/m
Schlebusch et. al. [115], [124] (2014, 2015)	Sphere	Approx. 10-410 ml	Bladder model in contact with the bottom of the Cylinder and touching a boundary wall	1.5-5 units [c]
Schlebusch et. al. [117] (2014)	Cylinder	Approx. 10-500 ml	NS	{0.4, 1.2, 2, 2.8} S/m
Schlebusch et. al. [126] (2014)	Sphere	50-550 ml	‘eccentrically’ [126]	Other[d]
Orschulik et al. [136] (2014)	Cylinder	NS	NS	1.2–2.8 S/m

[a] Volumes calculated by author based on the bladder shape and radii when no volumes given in the papers

[b] Single radius value given for each entry

[c] Conductivity specified in “units” rather than “S/m”

[d] Levels of conductivity contrast relative to the unit conductivity background given. Contrast was between 1-3.

Similarly, further information is needed to confirm the range of urine conductivities possible. A discussion related to urine conductivities is provided in Subsection 3.4.2.4.

3.4.2 Modelling the Bladder for Simulation

This subsection builds on the research presented in Subsection 3.4.1 and examines improvements for the bladder modelling design based on anatomical information. The modelling aspects covered are: the bladder shape and dimensions during filling; the bladder location and orientation; and the appropriate ranges to be used for urine volume and the urine conductivity.

3.4.2.1 Bladder Shape and Dimensions within the Forward Model

Previous EIT work has modelled the bladder as a sphere. The ellipsoid is a model often used in ultrasound measurements to measure the bladder volume, as in [138]. An ellipsoid is similar to spherical models used previously in the literature [114], [115], [123], [124], but allows for specifying radii in three dimensions rather than just one radii with the sphere. Thus, the bladder is assumed to be ellipsoidal in this work.

To determine how radii of the bladder model vary, information from Hirahara et al. [139] was used. Hirahara et al. recorded bladder volume information of fifteen healthy male adult volunteers voiding using 4D Ultrasound. Specifically, the axial, coronal, and sagittal diameters were recorded over time in graphical format. In this study, a regression line is fitted to the data from the study of Hirahara et al., similar to Krewer et al. [92]. The minimum and maximum data points of the fifteen healthy volunteers at each recording instance were manually read from the graphs and used in the formulation of the bladder dimensions. The minimum and maximum points are used instead of using the data from just one patient. This procedure was used as the data for each volunteer were interspersed among each other in the plots, making it difficult to discern the data for a single volunteer. Thus, the minimum and maximum values were averaged for recording instances between 0 s and 9.3 s of voiding. Linear regression lines were formed relating the axial diameters to the coronal and sagittal diameters. Figure 3.6 illustrates the collected points and regression lines relating the coronal diameter and the sagittal diameter to the axial diameter.

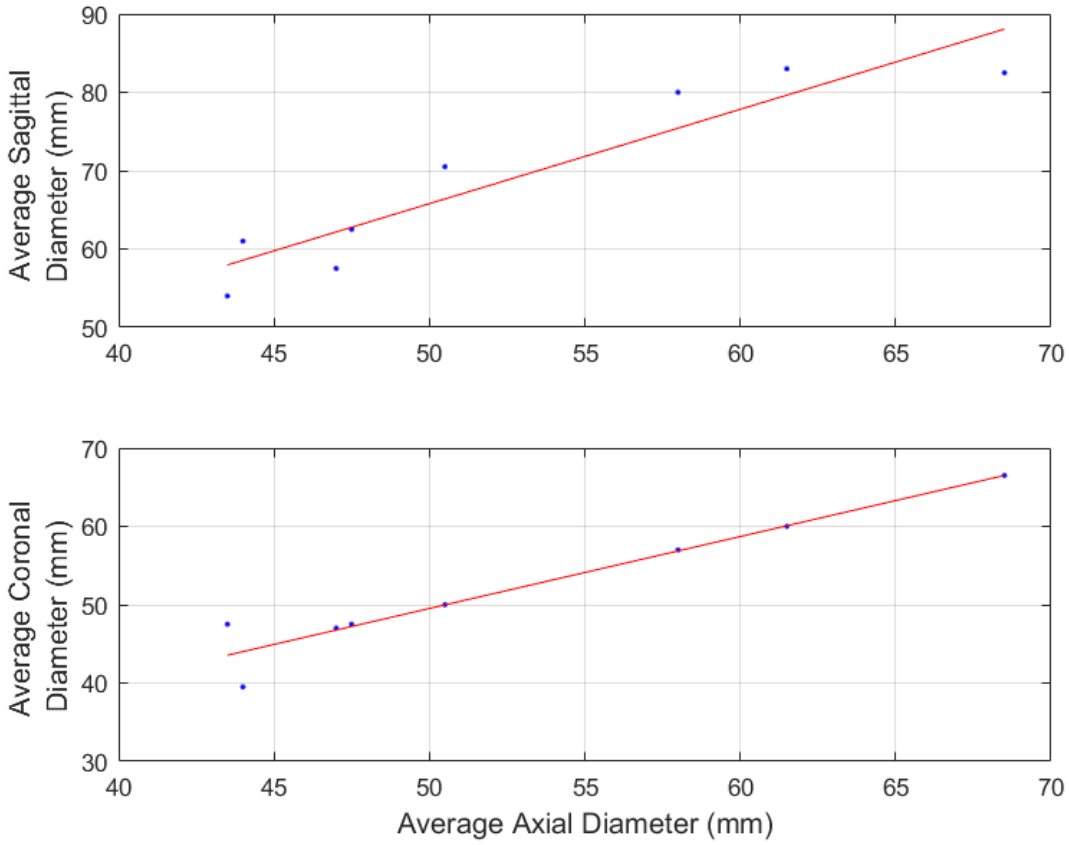

Figure 3.6: Average of the minimum and maximum values of the axial, coronal and sagittal diameters at voiding, based on the data reported in Hirahara et al. [139]. *Regression lines relating the sagittal (top graph), and coronal (bottom graph) diameters to the axial diameter were fitted. Using the equations for these lines, bladder dimensions could be formed for desired bladder volumes. The mean squared errors for each regression line from the top graph to the bottom graph are 4.541 mm, and 2.453 mm, respectively.*

The defining ellipsoid model equations (based on Figure 3.6) to four-decimal places are:

$$d_{sagittal} = 5.5597 + 1.2046 * d_{axial}, \quad (3.1)$$

$$d_{coronal} = 3.6108 + 0.9182 * d_{axial}, \quad (3.2)$$

where d is the diameter in mm. The mean squared errors are 4.541 mm and 2.453 mm for $d_{sagittal}$ and $d_{coronal}$. These equations translate into the following radii equations (to four-decimal places):

$$r_{sagittal} = 2.7799 + 1.2046 * r_{axial}, \quad (3.3)$$

$$r_{coronal} = 1.8054 + 0.9182 * r_{axial}, \quad (3.4)$$

where r is the radius in mm. These radii are then used along with the volume equation for an ellipsoid to get specific values for the three ellipsoid radii based on the desired volume. This calculation is done by finding the root of each cubic function of the axial radius based on the

desired volume, for r_{axial} within {-100, 100} mm. Having determined the appropriate bladder model shape and how the bladder should increase with volume, the location and the orientation are established next.

3.4.2.2 Bladder Location and Orientation within the Forward Model

Anatomically, the bladder rests in the pelvic cavity just posteriorly to the pubic symphysis, i.e., in the anterior of the pelvic cavity [16]. As the bladder fills with urine, the bladder ascends from the pelvic cavity towards the abdominal region. Similarly, the bottom location of the ellipsoid model in this work is fixed so that the ellipsoid extends upwards and outwards as the volume increases (as demonstrated in Figure 3.7).

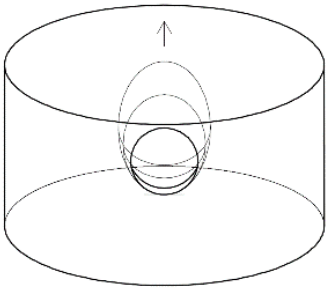

Figure 3.7: Demonstration of how the bladder changes with increasing volume (Figure 1a in E. Dunne et al. [140]*, licenced under CC BY 4.0* [141]*). The bottom of the bladder is fixed, and the bladder ascends upwards and outwards as the bladder volume increases.*

In the literature to date, the location of the bladder model has varied from two main positions in forward models: resting against the one face of the FEM [114], [115], [124] or placed in the centre of the FEM [114]. One difficulty with placing the bladder model in the correct anterior location is related to the movement of the bladder. The bottom of the bladder is in the pelvic cavity. But as the bladder fills, the overall volume displaces the bladder in different directions. In particular, the bladder displaces anteriorly and superiorly, deforming over the pubic symphysis bone. Thus, this filling of the bladder is difficult to model with an ellipsoid or regular geometrical shape.

Another option includes fixing the bottom of the bladder at the connection of the urethra. While the bladder is always connected to the urethra, the exact connection location may be difficult to determine from CT data. Also, the exact location inter-individually may vary due to conditions causing enlargement of the prostate in adult males [142]. While these problems may not happen in children, the forward model in this chapter is being developed for an adult using

publicly available data and further refinement for a child should be made in a child specific model.

Further, the exact position of the bladder from the boundary may vary potentially due to the bladder filling and body fat composition. The bladder position may also vary with sex [143] and age, e.g., from childhood to adulthood [16]. Thus, no single location will be ideal to place the bottom of the bladder.

For these reasons, the anterior-posterior midpoint of the bladder (measured at the midpoint slice of the bladder in the image data) at one instance in time is used in this work. This decision results in the vertical midline of the ellipsoid bladder model near the pubic symphysis and in the anterior region of the FEM. Specifically, the bladder location taken is 14.03 cm from the posterior and 1.3 cm down from the top of the pubic symphysis. This location means that the height from the boundary slice (and the electrode height) in Section 3.2.2 to the slice of the bottom of the bladder is approximately 4.3 cm. In terms of the position of the bladder in the left-right axis, the bladder model is assumed to be centred on the left-right axis.

For orientation of the elliptical bladder, the dimensions outlined in Subsection 3.4.2.1 were from data gathered in the sagittal, coronal, and axial planes. The relation between these dimensions and the body axes are not specified. Thus, the orientation employed in this work is: the dimensions from the sagittal plane are fitted to the anteroposterior axis; the dimensions from the axial plane are fitted to the left-right/traverse axis; and the dimensions from the coronal plane are fitted to the craniocaudal axis.

At this stage, the bladder shape, how the bladder shape changes with volume, and the bladder location and the bladder orientation have been determined. More analysis is needed to determine the exact volume and urine conductivity ranges. These parameters are investigated in the next sections.

3.4.2.3 Bladder Volume Range for Simulation

The aim of this section is to determine the appropriate range of bladder volumes for the adult model. The bladder has two extreme states: empty and full. However, in the real world the bladder may not become entirely empty, retaining some small amounts of urine called residual urine. The low range of abdominal residual urine is considered between 50-100 ml [144]. For the full state, normal adult bladder capacity has been reported from approximately 300-400 ml [24] but larger bladder capacities have been reported, see Section 2.1.2.

It is important to note that the sensation to void may occur earlier, for example, between 200-400 ml [26]. However, these values may be individual specific. Consequently, empty bladder volumes are considered from 0-50 ml and bladder volumes classed as full are considered starting at 300 ml in this work. Having considered an appropriate range for the urine volumes used in the study, an appropriate range for the urine conductivities also needs to be established.

3.4.2.4 Urine Conductivity for Simulation

Urine is composed of water, urea, uric acid, electrolytes (e.g., sodium, potassium, chloride), creatinine, and ammonia [14], [15]. Notably, the conductivity of the urine varies on food and fluid intake of the individual and their renal activity [117]. Literature has subsequently reported a wide range of conductivity values of urine. A summary of studies that have reported these values is given in Table 3.2.

As can be seen from Table 3.2, the conductivity of urine ranges from 0.5-3.33 S/m. Thus, conductivities of urine in this work cover a wide range of approximately 0.5-3.33 S/m to ensure valid simulation. Having defined aspects of the adult male model, the model can now be formed, and the properties summarised.

Table 3.2: Examples of the different values of urine conductivities in the literature. The abbreviation NS refers to 'Not Stated'.

Reference	Frequency	Urine Conductivity
Hasgall et al. [104]	1-1000 kHz	1.75 S/m
Gabriel et al. [145]	10-1000 kHz	Order of 2 S/m
Grimnes and Martinsen [97]	1 Hz-10 kHz and at ca. 1 MHz	0.5-2.6 S/m
Li et al. [13]	NS[a]	0.64-1.78 S/m
Schlebusch et al. [117]	NS[b]	0.59-3.22 S/m
Duck [146]	0-10 kHz	3.33 S/m

[a] Frequency or measurement method not stated

[b] Using a conductivity meter

3.5 Anatomically-Informed Numerical Forward Model of the Adult Pelvic Region

The designed and developed anatomically-informed numerical forward model from Section 3.2, Section 3.3, and Section 3.4 for adult pelvic region is presented in Figure 3.8 in solid form with an empty classified bladder of 50 ml. The main properties determined in Section 3.2,

Section 3.3, and Section 3.4 are summarised in Table 3.3. Following discretization, the model can be used to generate raw EIT data and images as is discussed in Section 3.6.

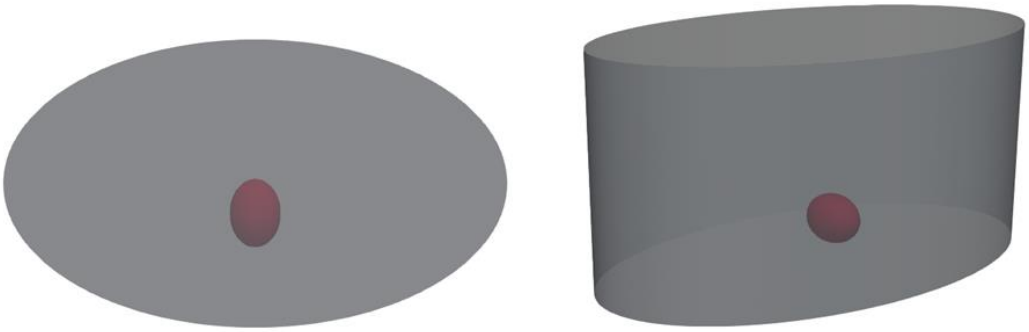

Figure 3.8: Solid format of the designed anatomically-informed forward model. The model is shown from a 2D top view (left) and a 3D perspective view (right). Similar to bladder in the example CT scans in Figure 3.2, the bladder is situated off-centre to the anterior of the model.

Table 3.3: Property summary of the designed and developed anatomically-informed numerical pelvic model.

Property	Value
Boundary Shape	Elliptical Cylinder
Boundary Dimensions	40.74 cm along the left-right axis 23.27 cm along the anteroposterior axis 20 cm along the craniocaudal axis
FEM Background Conductivity	0.352 S/m (at 50 kHz)
Bladder Shape	Ellipsoidal
Bladder Location	Centred on the left-right axis; 14.03 cm from the posterior of the model; 2.2 cm from the base of the model;
Realistic Bladder Volume Range	0-600 ml
Realistic Urine Conductivity Range	0.5-3.33 S/m

3.6 Example Data Generation with the Adult Simplified Forward Model

In this section, the designed numerical forward model is used to generate example voltage and image data to demonstrate functionality of the model. First, simulation parameter settings such as the injection pattern and current levels are discussed along with the electrode configuration. Then, the procedure for adding noise to the simulated data is presented. Lastly, the data generation and image reconstruction methods are described, and sample results presented.

3.6.1 Demonstration of the Developed Forward Model

The discretised forward model based on the design considerations from Section 3.2, Section 3.3, and Section 3.4 is shown in Figure 3.9 with both an empty and full bladder volume of 50 ml and 400 ml, respectively. The FEM is used for forward solving to obtain simulated raw EIT data. The FEM includes 32 electrodes. For each bladder volume, the mesh is regenerated to correctly model the bladder shape and the resultant volume change. To potentially minimise meshing errors outlined in [147], the number of elements in the FEM is in the order of 1.6 million elements (similar to [124]). Additionally, electrode mesh refinement is performed to better model current flow at the electrodes as recommended in [148].

Using the open source EIT software, EIDORS, data can be generated for specific measurements settings such as the injection current and the electrode gaps between injection electrodes and/or measurement electrodes. Research EIT devices such as the Sentec Pioneer sets [137] allow adjustment of the electrode gap between the injection/measurement electrodes. In the Sentec Pioneer device, the electrode gap ('Skip') used is equal between the injection electrodes as well as between the measurement electrodes as illustrated in an example in Figure 2.10. For generation of simulated data, the default Skip of 4 from the Pioneer set is used. The injection current used is 6 $mA_{p\text{-}p}$ (approx. 2.12 mA_{rms}), which is in line with the Patient Auxiliary currents in the standard IEC-60601 [149], [150] (the safety standard for injected current into the body, which is used by the EIT community [99]) at the operating frequencies in this thesis.

The electrodes used are in a ring formation, which is a configuration that has been very common in EIT for 2D imaging, e.g., [124], [151]. This ring configuration would be feasible in the real-world for this bladder monitoring application by placing the electrodes on a belt or embedding electrodes in underwear that the user could wear. The electrodes are on the boundary surface and are circular with a diameter of 1.7 cm. This electrode size is within the dimensions and resultant surface area of electrodes modelled previously for EIT [151].

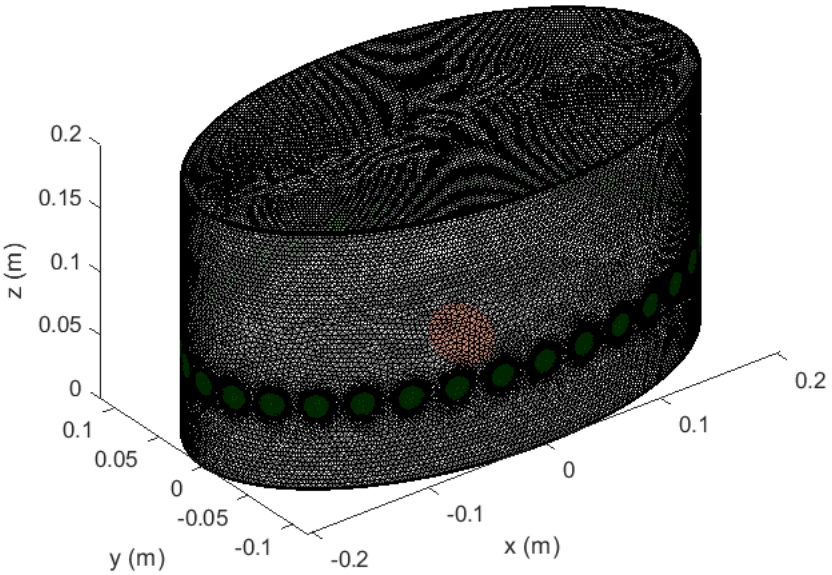

(a)

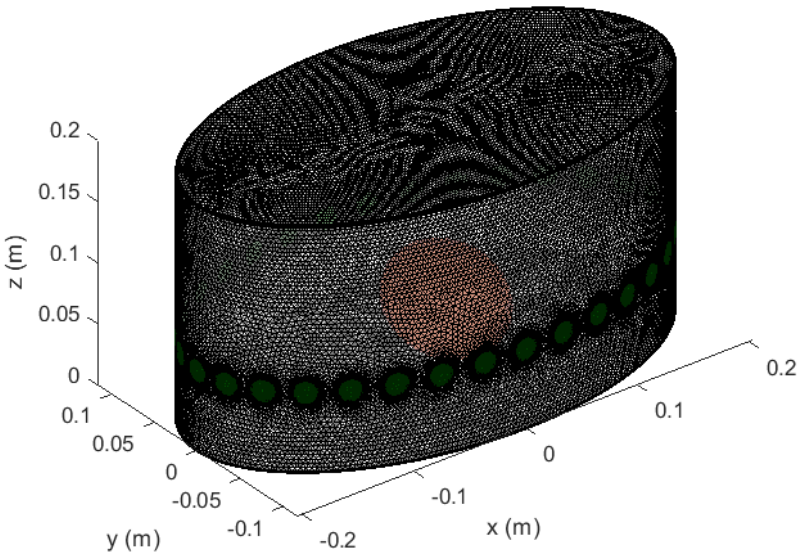

(b)

Figure 3.9: The designed anatomically-informed numerical FEM of the adult pelvic region. The FEM has 32 circular electrodes on the boundary for stimulation and a background conductivity of 0.352 S/m (white region embedded with the black lines of the elements). Each electrode (shown in green) has additional mesh refinement as recommended in [148] *to improve modelling of current distributions at the electrodes. For demonstration, the FEM is shown with two different bladder volumes and urine conductivities: (a) 50 ml bladder volume of urine conductivity 0.5 S/m (pink region); and (b) with 400 ml bladder volume with urine conductivity of 3.33 S/m (pink region).*

3.6.2 Additive Simulation Noise Model

In the real world, many factors affect the measured voltage values and impact the quality of the desired signal (i.e., any interference to the desired signal). Such factors are generally referred to as 'noise', and noise is usually considered as any signal differing from the desired signal. Sources of noise in the real world could include interference from equipment and electrode-skin contact, environmental factors, and movement [95], [99], [152]. Movement noise is particularly problematic for EIT data collection [95].

When simulated voltage data is generated, the data is noiseless (ideal), i.e., the voltage data shows only the signal changes due to the changing of the FEM (e.g., bladder filling). This data is not affected by any real-world interference. Therefore, noise is generally added to the voltages after generation to make the simulation approach the real-world situation.

In EIT, noise applied to the data is commonly in the form of additive noise [103], [117], [123], [124], [153], [154] such as additive Gaussian noise [103], [153], [154]. In this work, additive random Gaussian noise from [155] is used. The function scales the Gaussian probability density function using the Euclidian norms of the signal and of the generated random noise. The function also scales the Gaussian probability density function by the user supplied signal-to-noise ratio (SNR). In this work, the SNR is defined as:

$$SNR = \frac{V_S}{V_N} = 10^{\frac{SNR_{dB}}{20}}, \tag{3.5}$$

where V_S and V_N are the voltages for the signal and noise respectively, and SNR_{dB} is the SNR in decibels.

As there are many sources of noise mentioned (and potentially more unknown), it is difficult to design a model to cater for each source of noise. Thus, no model of noise may fully represent real-world data collection. However, modelling the noise can provide more realistic trends such as degradation of system performance with increasing noise levels (decreasing SNR).

In regard to specific noise levels for this application, EIT hardware has been reported to have a wide range of SNRs. For example, a number of modern EIT hardware have reported SNRs of around 80 dB or higher [100] (e.g., up to 120 dB SNR). However, Schlebusch et al. [124] reported noise level of 42-156 dB with the EIT hardware they employed (Goe MF II EIT device) in their bladder volume studies. Noise levels of the order of 40 dB SNR are also reported in EIT literature [156]. Thus, a reasonable SNR range for simulation is between 40-156 dB. Subsequently, SNR values from 40 dB and upwards will be considered in this work.

Having obtained a method to create data and make the data more realistic by the addition of noise, example data can be generated for initial analysis.

3.6.3 Data Generation and Image Reconstruction

In this subsection, raw EIT voltage data is first generated using the forward model introduced in the previous sections. Then, images are reconstructed based on this voltage data. For image reconstruction, the effect of prior knowledge of background conductivity is also examined.

3.6.3.1 Voltage Data Generation with the Adult Model

The data collected from an EIT system is the voltage from each electrode measurement pair (fixed current injection amplitude). Specifically, this voltage data consists of multiple channels. For 32 electrodes, voltages are recorded at the 32 measurement pairs for each of the 32 injection electrode pairs. These measurements result in 1024 voltages compiled into a single data frame. Typically, measurements at the injection electrodes are not used in processing as the measurements from these electrodes suffer especially from a high voltage drop due to the impedance of the electrode and the large impedance of the skin [95] (discussed in Section 2.4.2). Thus, removal of these injection electrode measurements reduces the number of measurements for a 32-electrode system from 1024 measurements/frame to 928 measurements/fame. This reduction is because three measurements are taken with either one or both of the individual electrodes in the injection electrode pair. Therefore, the number of measurements considered in each frame is given by the equation $N_{electrodes}(N_{electrodes} - 3)$, where $N_{electrodes}$ is the number of electrodes.

In cases where there are no mismatches within the instrumentation or differences between contact impedances for combinations of injection-measurement electrode pairs, the frame can be further reduced by half due to reciprocity of the EIT data collection [95]. In initial studies the full frame size will be kept, similar to previous bladder volumes estimation studies [115], [124]. Thus, simulated data is generated for 928 real voltages and the noise is added after the forward solve. Figure 3.10 shows the mean magnitude of the voltage frames (where the mean was taken across all the measurement channels in the frame, ignoring the sign) for eight bladder volumes and two urine conductivities. The magnitude is taken, as the sign of the voltage values refers to the polarity.

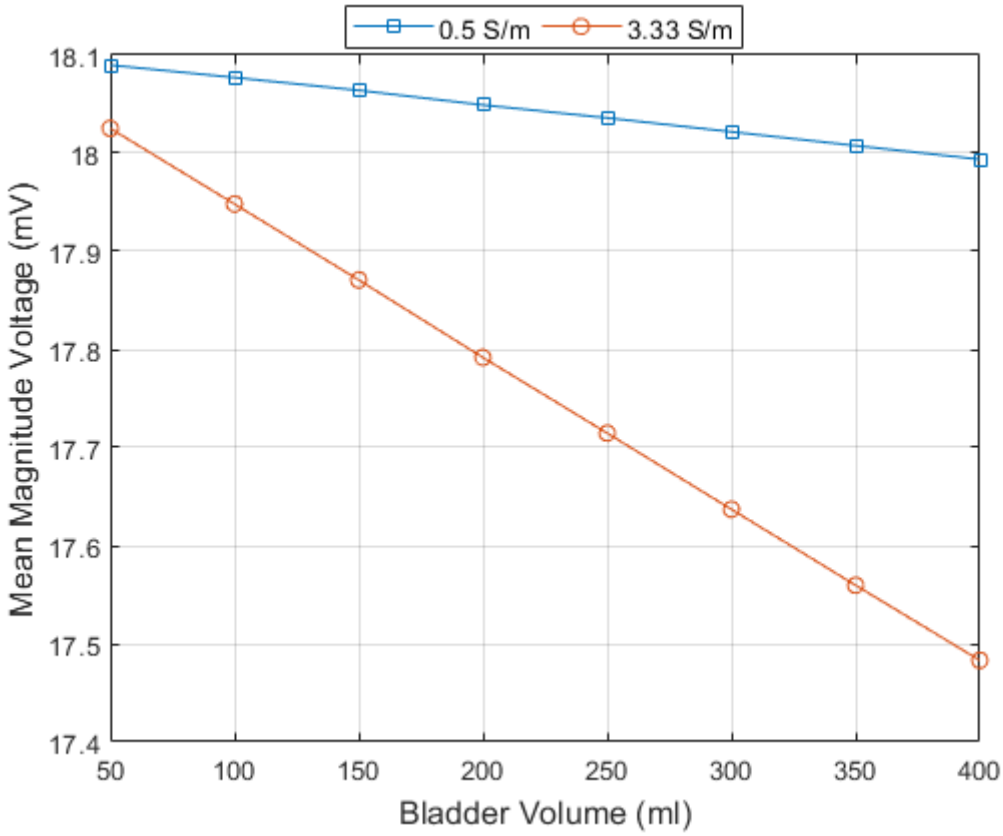

Figure 3.10: Mean magnitude of the ideal simulation voltage frames for the bladder volumes ranging from 50-400 ml in steps of 50 ml and for the urine conductivities 0.5 S/m and 3.33 S/m with a background conductivity of 0.352 S/m. By observation, there is separability between each of the bladder volumes and each of the two different conductivities.

As can be seen from Figure 3.10, the data is visibly separable both by bladder volume and the urine conductivity. This finding suggests feasibility to perform classification of bladder state. Analysing the data in Figure 3.10 quantitatively, the average percentage difference between the mean magnitude voltages for the two conductivities curves is 1.62 ± 0.88%. The percentage difference of the mean magnitude voltages of 50 ml (i.e., classed as the upper end of the empty bladder volume range) and 300 ml (i.e., classed as the start of the full bladder range) for the 0.5 S/m and 3.33 S/m curves was 0.38% and 2.18%, respectively. The 300 ml is used for comparison as the volume is the start point of full bladder region as discussed in Subsection 3.4.2.3. To put the voltage percentage difference in perspective, the volume change between the 50 ml and 300 ml bladder volume (i.e., 250 ml) within the overall volume of the cylinder is approximately 1.68%. While the voltage differences are around the same order of magnitude as the volume change, the percentage difference is considered small as the calculation was on non-noisy data. The contrast between the signals could greatly decrease when system and environmental noise is added. Therefore, the small percentage difference values could indicate

the need for more powerful methods than high level descriptive statistics to separate the data for bladder state classification.

To show the effect of noise, 1000 noisy frames were created for a single bladder volume of 400 ml and urine conductivity of 3.33 S/m. Then two channels (a channel is considered an individual entry in a frame for a specific set of measurement and injection electrode pairs), one near the injection electrode and one furthest away from the injection electrodes were used to show the degradation of the channel due to decreasing SNR. This data is shown in Figure 3.11. From Figure 3.11, the effect of adding noise clearly impacts the signal quality. Further, this added noise may hinder the bladder state classification and the exact performance effect will need to be investigated.

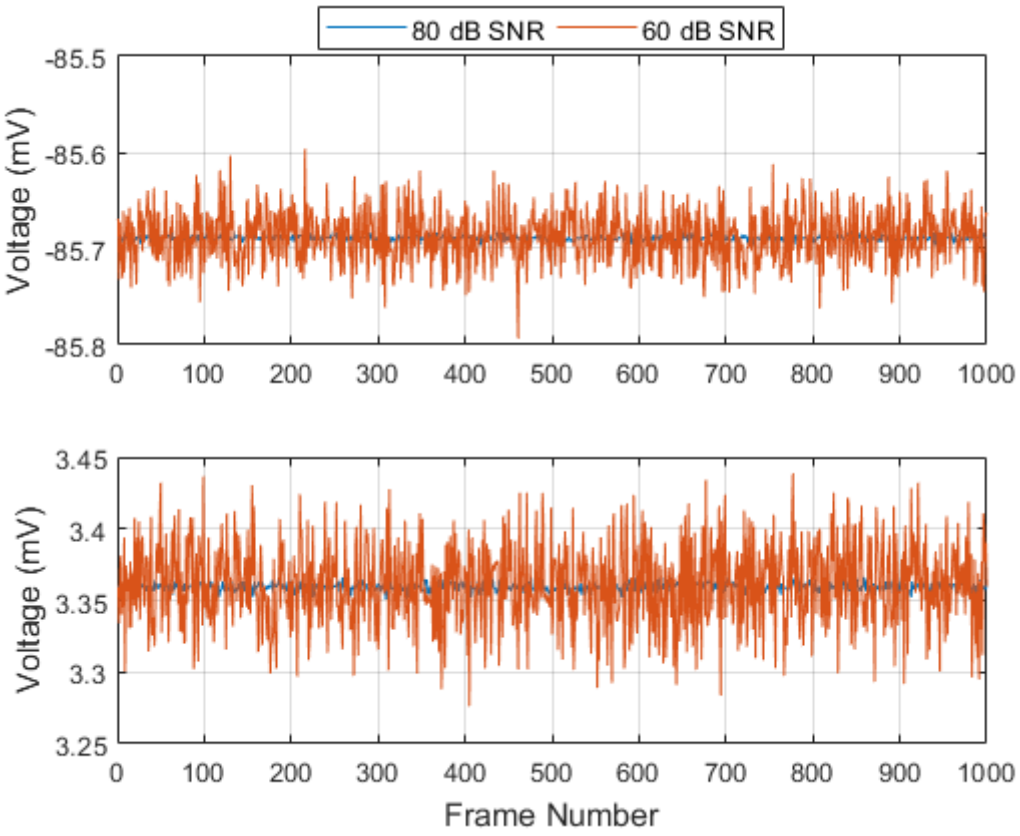

Figure 3.11: Illustration of the effect of two different noise levels (80 dB SNR and 60 dB SNR) on two channels, one right beside the injection electrodes where the 'strong' voltages are (top plot) and one on the opposite side of the ring to the injection electrodes where the 'weak' voltages are (bottom plot). Decreasing the SNR distorts the signal. Please note: negative voltage refers to the polarity of the voltages on that channel. Also, these graphs do not represent each channel or the channel at all times but only for one set of 1000 noisy frames.

In this subsection, initial analysis on voltage data was performed and it was shown that empty and full states are separable by descriptive statistics alone. Now, the voltage data can be further transformed to images for further investigation.

3.6.3.2 Image Data Generation with the Adult Model

In EIT, images are primarily examined as opposed to the raw voltages alone, as they are more human readable. Images also provide another way to process the data before classification. As outlined in Section 2.4.3, EIT works best with difference imaging, particularly in the temporal case. Numerous studies have shown the feasibility to monitor bladder filling or the difference between full and empty with electrical impedance on humans in controlled scenarios (see Section 2.4.4) and a small set specifically with imaging [12], [13], [120]. The advantage of imaging is its ability to enhance the interpretation of the data by showing spatial changes that are more easily understood by humans. Image reconstruction with time-difference EIT may allow for removal or suppression of some sources of error that are present in both 'before' and 'after' captured signals (where the 'after' signal is subtracted from the 'before' signal).

In this work, the commonly used time-difference EIT image reconstruction Graz consensus Reconstruction algorithm for EIT (GREIT) [151] is employed. The 2D linear image reconstruction algorithm is based on optimisation for the reconstruction matrix rather than for the reconstruction image (the normal process for regularized image reconstruction algorithms) [151], [157]. The matrix is optimised under performance metrics that are termed Figures of Merit. These performance metrics quantify within the image: the position error of the targets; how consistent pixel values are for the targets with the same conductivity in different regions of the image; the resolution of the targets; the effect of the linear filtering ringing artefact; and how deformed the shape of the target is in the image reconstruction image [151]. The targets in the desired image are circular and have diameters less than 5% of the boundary diameter [151].

The default settings of GREIT and EIDORS are used and the noise figure (quantifies the amplification of measurement frame noise in the reconstruction image) for GREIT is set to 0.5 as recommended in [151]. This noise figure can be tailored specifically to the noise level of the hardware in later work. For the image reconstruction, prior knowledge of the body is in the form of a coarse reconstruction FEM (fixed at 186350 elements), i.e., coarser than the FEM used to generate simulation data. In real-life, knowledge of the exact boundary may be difficult to maintain, particularly where the wearer of the device is moving. Research is being pursued

to detect the boundary with accelerometers and bend sensors [158], which could potentially aid in reducing boundary mismatch artefacts. A fixed background homogenous conductivity of 0.352 S/m is used in image reconstruction, which matches that of the numerical generation model.

To demonstrate image reconstruction, the non-noisy frames of the 50 ml and 400 ml bladder volumes with a urine conductivity of 3.33 S/m were reconstructed with a non-noisy voltage reference frame of 30 ml bladder volume of 0.5 S/m in Figure 3.12. Visually there is a strong contrast between the pixel intensities for both images. However, it is difficult to discern the shape differences. This result may be due to poor spatial resolution of EIT, as well as having the empty and full bladder volume images on the same pixel intensity colour bar scaling.

Quantitively, summary statistics based on the image data were performed for between 50 ml and 300 ml bladders (similar to the mean magnitude voltage comparison in Subsection 3.6.3.1). The percentage difference between the maximum pixel intensity of the non-noisy 50 ml and 300 ml bladder volume images was determined to be 134.67%. This large contrast based on image amplitude alone suggests image reconstruction as a strong starting point for bladder state classification.

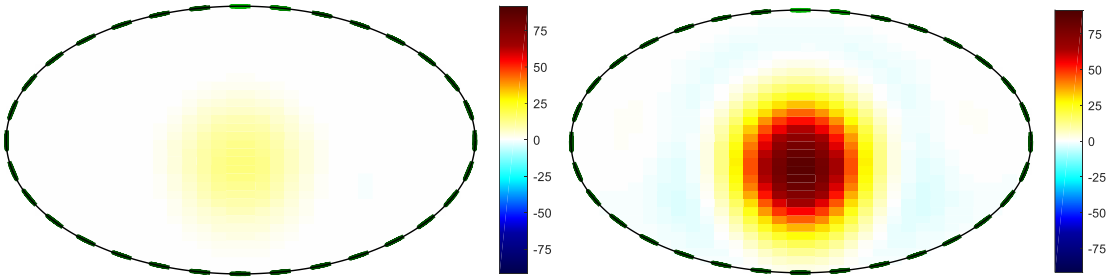

Figure 3.12: Demonstration of imaging with non-noisy data of a 50 ml bladder volume (left) and a 400 ml bladder volume (right) with a urine conductivity of 3.33 S/m. Both images have been assigned the same colour bar range. A black line marks the boundary and the electrodes are marked by the green line segments. There is a strong contrast in the two volumes by pixel intensity alone. Spatially, it is difficult to visually discern the bladder shape for a small bladder. Note: the pixel intensities have arbitrary units, the values are related to the conductivity change and may require calibration for the application (e.g., [99]*).*

The non-noisy images greatly change when noise is added. For example, the quality of the image degrades with increasing noise levels (decreasing SNR) using the 50 ml and 400 ml full bladder with urine conductivity of 3.33 S/m in Figure 3.13. Visually, the degradation is minimal for the 400 ml bladder with only some image artefacts introduced. However, the effect of noise is stronger for this example of images on the smaller bladder with distortion of the

shape at 40 dB SNR. This result is expected since the data from the reference frame is more similar to the data of the smaller bladder, than to the data for the larger bladder. These are just two example cases illustrating some effects of noise. The images will be examined in further detail in the next chapter as inputs to classification algorithms, particularly as a function of conductivity and with smaller bladder volumes.

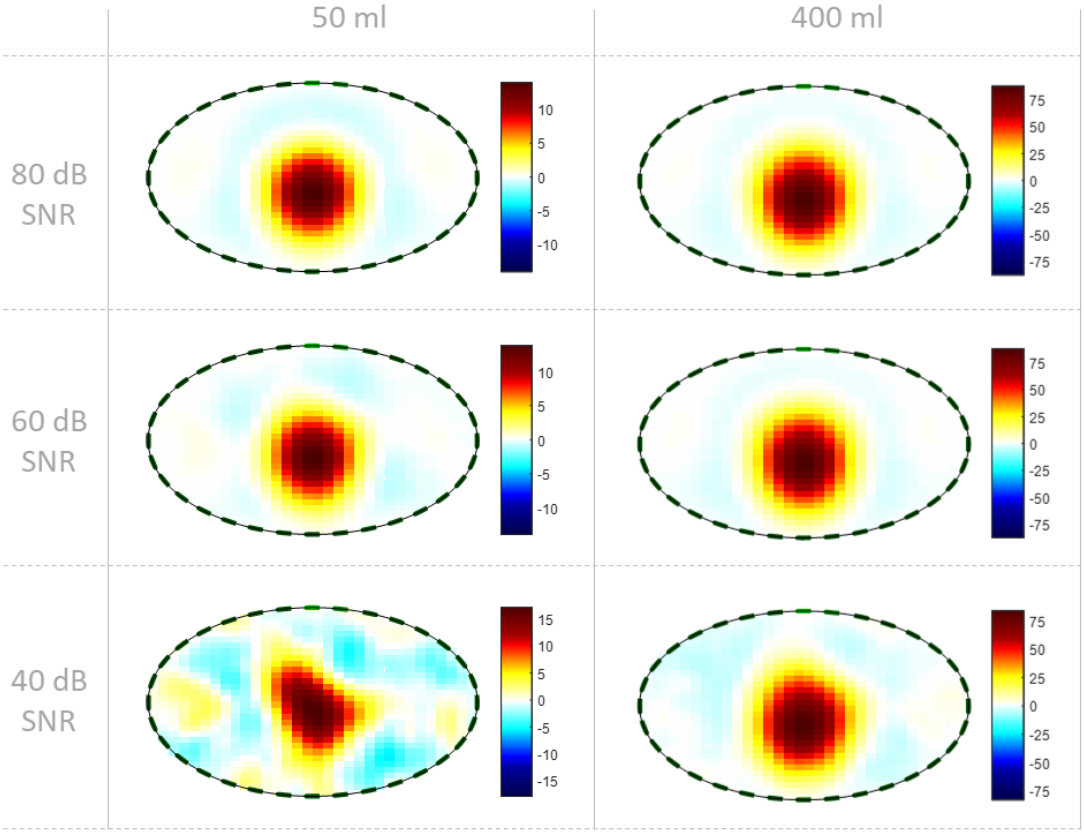

Figure 3.13: Demonstration of imaging with noisy data at {40, 60, 80} dB SNR of a 50 ml bladder volume (left) and a 400 ml bladder volume (right) with a urine conductivity of 3.33 S/m. The images were reconstructed with the same non-noisy reference frame of a 30 ml bladder volume with a urine conductivity of 0.5 S/m. To show the effect of noise at each SNR level and on the two bladder volumes, each image has its own colour bar with arbitrary units that are related to the conductivity change. As the noise level increases (decreasing SNR), the image quality degrades, particularly for the small bladder volume. Please note: these are sample noisy images generated at one time and these images are not representative of all possibilities of bladder volume, urine conductivity or noise value.

In this section, a numerical forward model representing an adult male has been used to demonstrate data generation and image reconstruction for the bladder monitoring using EIT. Differences in empty and full bladders have been shown along with the potential to separate the empty and full sets using high-level descriptive measures on non-noisy data. The large

contrast calculated on the image amplitude alone between the images for non-noisy empty and full bladders suggests image inputs as a strong starting point for bladder state classification.

3.7 Limitations of the Adult Pelvic Forward Model

In this chapter, a numerical forward model was designed to allow for modelling of changes in size and conductivity of an inclusion (mimicking a human bladder) within a cylinder (approximation of a boundary of a human pelvic region). In general, numerical forward models of the anatomy region in EIT are inherently inaccurate as each model makes some assumptions about the real-scenario, e.g., the body can be discretised into millions of elements. Thus, no model is entirely representative and at best, can provide an identification or suggestion of what would be expected in the real world. Importantly, the outputs of the forward model should match the expected trend that have been shown true in the real world. For example, the overall voltage decreases with a conductivity increase when current is fixed (as in a system injecting a fixed current amplitude), obeying Ohm's Law.

In the numerical forward model created in this chapter, some of the main assumptions include:

- The boundary of a human body can be approximated by a simplified cylinder and that the bladder can be approximated by an ellipsoid with a fixed bottom;
- The conductivities of the bladder and the background are homogeneous;
- That the only noise is from the random Gaussian noise added to each frame.

However, these conditions are much more complex in the real-world. Therefore, the best testing ground for assessing the effect of these factors is in real-world scenarios. Some of the conditions may be assessed in controlled settings, such as phantoms, while others such as the exact filling and deformation of the bladder as well as noise may require controlled test scenarios with animals or people.

Other identifiable limitations include modelling errors such as remeshing, which has been shown to give image artefacts even when there are high number of elements in the forward solve mesh [147]. However, meshing is flawed in itself. The model is discretized into millions of elements that may not exactly replicate the original structure. Further, to model shapes in the mesh with small changes would require a highly fine mesh. This approach has the drawbacks of increased computation cost for both meshing and for solving the forward problem, particularly in adult size 3D models. Therefore, no method for constructing numerical

forward models is without limitations. Despite meshing limitations, meshing is an inevitable step in performing numerical simulations, and is a widely used and a well-accepted technique.

However, the forward model generated has the overall benefit of assessing a range of parameters such as different bladder volumes, tissue conductivities, electrode configurations, Skips and other hardware settings such as frequency and injection current. Importantly, it provides a method to initially gather large quantities of data and assess whether bladder monitoring with classification is feasible and to determine potentially suitable methods to employ.

3.8 Summary

In this chapter, a simplified forward model for bladder fullness monitoring was designed and its functionality demonstrated. The forward model mimics a male adult in proportion and was anatomically informed. The anatomical information used in the model included: defining the sizing of the model; the bottom location of the bladder; the dimensions of the bladder as the bladder fills; and the ranges of bladder volume and urine conductivity used in the work. This information could help to give more realistic results at the early stage of prototyping a bladder monitoring solution. The specific content described by each section is summarized below.

In Section 3.1, a literature review of numerical forward models in BVM with EIT was presented, and it was found that different levels of complexities have been used. The most common models are 3D cylindrical models that enable rapid testing. However, these simple 3D models can be improved by enhancing the 3D models by adding anatomical information.

In Section 3.2, the boundary of the forward model representing the boundary of the pelvic region was defined. Existing research from EIT and anatomical literature formed the foundation for the model. By simply quantifying information from available public medical image data, rapid models for simulation can be made more realistic while still not requiring patient-specific image segmentation at an early-stage in testing.

In Section 3.3, the conductivity outside the bladder in the forward model was designed. Similar to existing research, a single-value conductivity (referred to as the ‘background conductivity’) was defined. While no single-value conductivity may fully represent the pelvic region, other potential methods also have limitations due to the dynamically changing nature of processes in this pelvic region. Thus, exact modelling of the pelvic region may not be needed at this early stage in prototyping.

In Section 3.4, the bladder model for the forward model was defined. Similar to Section 3.2, existing research from EIT and anatomical literature formed the foundation for the model. By gathering medical image data available, the bladder dimensions and the bladder location can be better informed.

In Section 3.5, the pelvic model designed in the previous sections was presented in solid format and the main properties from Section 3.2, Section 3.3, and Section 3.4 were summarised. The designed model could be used in discretised form for simulation.

In Section 3.6, the designed forward model was used to form simulation data of both raw EIT measurement data and image data. It was found that images offered a strong potential of separating empty and full bladder volumes by descriptive statistics alone. This result suggests that images as the input source for a classifier would be a strong starting point for bladder state classification.

In Section 3.7, the limitations of the designed forward model were discussed. While no numerical forward models can be exactly representative of the body they are modelling, the forward models enable simulation of bladder filling before real-world testing of basic test scenarios. These test scenarios include classification of bladder state with different types of input data, moving of electrodes and the changing of simulation parameters through EIDORS such as the amount of current injected and the Skip.

Thus, a numerical forward model was designed and developed that will now facilitate initial studies of bladder state classification in simulation. The forward model is simple, yet anatomically informed. The use of the forward model to generate voltage data and reconstructed images has shown that the forward model works as expected and can be used in future studies. Building on the results from this chapter, the developed numerical forward model is used in Chapter 4 to examine the potential of EIT of bladder state classification with image data.

4 Bladder State Classification with EIT Images

In Chapter 2, the concept of bladder state classification with EIT was presented as an alternative to the state-of-the-art of estimating the exact bladder volume. A key advantage of predicting the bladder fullness by classification is that the user is given a clear and conclusive alert to which they can respond immediately by proactively voiding their bladder. In Chapter 3, a numerical forward model of an adult pelvic region was designed and developed. This forward model was used to generate EIT measurement data and images. Image data was shown as the best potential input based on the separability of ideal empty and full bladder volume images using descriptive statistics. This chapter now advances work on the EIT-based bedwetting alarm by the investigation of bladder state classification using simulated EIT image data. Machine learning classification of not-full and full bladder states is performed with the objectives of establishing:

1. whether bladder state classification is possible using EIT image data;
2. how classification with EIT image data performs under the conditions of varying bladder volumes, urine conductivities, and measurement frame noise, which are all key conditions for bladder monitoring as previously established in the literature [124];
3. how the classifiers perform when all conditions in the dataset are varied;
4. the advantages and disadvantages of using reconstructed EIT images for bladder state classification.

This chapter is divided as follows: datasets of varying conditions are formed in Section 4.1 using simulated data from the adult numerical forward model developed in Chapter 3; the machine learning classifiers are designed in Section 4.2; the machine learning evaluation architectures and the data pre-processing are discussed in Section 4.3; the evaluation metrics used to determine the performance of the classifiers are described in Section 4.4; the data is classified in Section 4.5 to observe the effect of each condition (bladder volume, urine conductivity and measurement frame noise) on bladder state classification with images; and then a more realistic scenario of training and testing of all the conditions varying in the dataset is performed in Section 4.6. Finally, the advantages and disadvantages of using EIT image data

for bladder state classification are discussed in Section 4.7 and the chapter is summarised in Section 4.8.

The content of this chapter draws from earlier published work:

E. Dunne, A. Santorelli, B. McGinley, G. Leader, M. O'Halloran and E. Porter, "Image-based Classification of Bladder State using Electrical Impedance Tomography", *Phys. Meas.*, vol. 39, no. 12, Art. no. 124001, pp. 1-13, Dec. 2018, doi: 10.1088/1361-6579/aae6ed.

4.1 Formation of Simulated Datasets for Image Bladder State Classification

In this section, previous datasets that have been used in the field are discussed, and the formation of new datasets is detailed for each of the different test-cases needed to answer the research questions posed in this chapter. The test-cases are: 1) testing if untrained bladder volumes can be accurately classified as not-full or full; 2) testing the effect of untrained urine conductivities; and 3) testing the effect of untrained measurement frame noise levels. The structuring of the images in the dataset before pre-processing and classification is also discussed.

4.1.1 Previous Dataset Design for Bladder Volume Monitoring using EIT images in Simulation

In the literature to date, studies have primarily focused on estimating the bladder volume rather than determining the bladder state as information to report to the device wearer. Thus, the studies that have estimated bladder volume are discussed in this section. The algorithms using EIT images employed in these studies have been trained and tested on either simulated, phantom, or human voiding data. However, in this section the focus is on simulated data based on the scope of this chapter.

For the studies by Schlebusch [115] and Schlebusch et al. [124] (some of the formulations of which were introduced and demonstrated in [123]), the bladder volume regression models involved extracting data from the images and then relating the extracted information to the bladder volume on non-noisy data. Finally, testing of the developed regression models was performed on varying cases of non-noisy bladder volume data, increasing noisy bladder volume data, and a single bladder with varying urine conductivity. Two forms of data extraction were performed: 1) the summation of all the pixel intensities from a given reconstructed image to form the Global Impedance (GI) metric; and 2) filtration and segmentation of the bladder from the image to obtain the bladder pixel area and to calculate the equivalent circular diameter of

the bladder for relating to the bladder volume. Testing in simulation was performed at bladder volumes of between approximately 10-410 ml, urine conductivities from 1.5 to 5 conductivity units (with algorithms trained/calibrated at 2 units when studying the influence of urine conductivity), and SNRs of {40, 80, 120, ∞}.

In [126], Schlebusch et al. adapted an image reconstruction algorithm to solve for the parameters of the urine conductivity (referred to as conductivity contrast) and the radius of a single spherical target when the background was known. The bladder volume range was 50-550 ml with conductivity contrast of 1-3 units and SNR levels in the range of 10^1 to 10^4. The specific conductivity contrast of 2 units and a SNR level of 10^4 was used for training.

In [117], Schlebusch et al. formed a metric that aimed to minimise the influence of different urine conductivities on images in order to predict the bladder volume. The metric was fitted to bladder volumes at a urine conductivity of 2 S/m. Bladder volumes between approximately 10-500 ml; urine conductivities of {0.4, 1.2, 2, 2.8} S/m and SNR levels of {40, 50, 60, ∞} were employed in simulation in the study.

While these datasets allow for testing of the conditions affecting BVM using EIT, in a real application it would be unlikely to have ideal data to train the classifiers on, as in [124]. Thus, datasets in this work will use urine conductivities with the units of Siemens per meter (S/m) and will be trained and be tested on a variety of different bladder volumes, urine conductivities and measurement frame noise levels. These datasets will increase in difficulty from test-case 1 to 3, with each test-case adding another varying condition. A test-case having all conditions varying during train-test will then be examined. Importantly to note, the noise and SNR levels used in this work will refer to that noise added to the measurement frames before time-difference image reconstruction.

4.1.2 Dataset Properties for Test-Case 1: Investigating the Effect of Varying Bladder Volumes on Pixel-wise Image Bladder State Classification

Test-Case 1 (TC1) is comprised of testing on unseen bladder volumes, while holding the amount of noise (measured by the SNR level) and urine conductivity constant. Twenty-six bladder volumes are used in the range of {40, 420} ml with an equal number of bladder volumes per class. In real-life use, a similar number of observations per class could be obtained by increasing the sampling rate as the rate of the bladder filling increases or as the time since voiding increases. Also, it may be possible to observe a high number of bladder volumes with repeated voiding cycles in real-life use. However, the exact number of different bladder

volumes and conditions would be difficult to model in simulation or phantom without prior knowledge. Thus, 120 observations per bladder volume were used to increase the dataset size to a number greater than the number of input features. Each of the 120 observations varied from each other by the random Gaussian noise added to the measurement voltage frames. This number of observations would be equivalent to collecting multiple seconds of data for a single bladder volume using a frame rate, which is within the capability of the EIT hardware, e.g., Sentec EIT Pioneer Set (up to 50 frame/s).

In order to form time-difference EIT images, a single reference frame (also called a 'baseline') for image reconstruction of a dataset is used. It is assumed a system will try to find the minimum relevant reference data measured after voiding. This approach is similar to other EIT applications where the reference data may be taken when the stomach is empty for gastric EIT or for a partially emptied lung at the end of expiration in lung EIT [95]. In this work, the baseline is based on the average of ten noisy frames (each frame at the same SNR as the test case data) to mimic a more realistic situation where the reference may be the average of multiple frames [151], [159]. More frames could be used in the averaging. However, having fewer frames to average could make the testing harder, as less noise may be filtered out.

The reference bladder volume of 30 ml is used, which assumes there is some urine left after voiding when a baseline was established. Further validation is needed to determine what actual residual volume would occur during the operation of the system. However, a normal residual urine volume is considered between 0-50 ml as discussed in Section 3.4.2.3. The urine conductivity used is 2 S/m for all the bladder volume models, including the baseline. The 2 S/m urine conductivity value is near to the average of the range (approximately 1.91 S/m) and is far from both extreme ends of urine conductivity range.

For initial analysis, the algorithms are trained and tested at specific SNR levels since noiseless data is not possible to achieve in real-life. Thus, three datasets differing by the three SNR levels ({40, 60, 80} dB) are trained and tested. Figure 4.1 shows images for six bladder volumes at the 60 dB SNR level of TC1.

From Figure 4.1, it is evident that the contrast in both the pixel intensity and the shape of the bladder increases with the increased bladder volume.

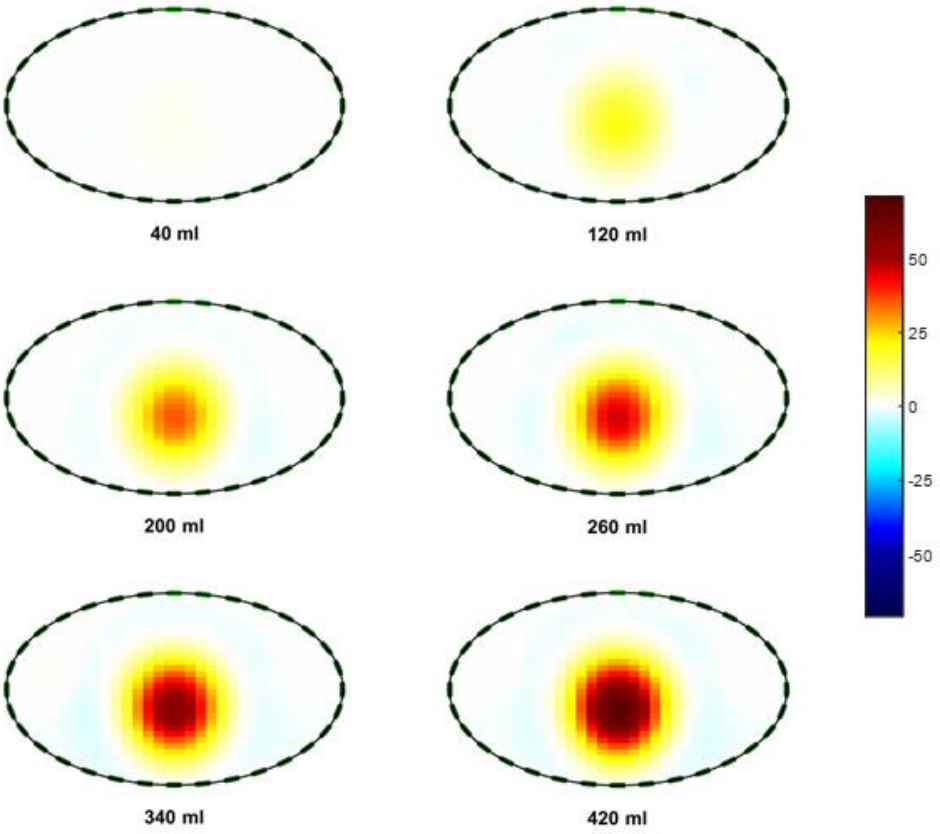

Figure 4.1: Sample images in the 60 dB TC1 dataset of six different bladder volumes. Going across then down, the images correspond to increasing bladder volumes of {40, 120, 200, 260, 340, 420} ml at a urine conductivity of 2 S/m and 60 dB SNR. Spatial changes can be seen with volume change along with a strong contrast between the pixel intensities in the location of the bladder. Note: The colour bar is in arbitrary units and indicates the change in conductivity between the test data and the reference data.

4.1.3 Dataset Properties for Test-Case 2: Investigating the Effect of Varying Urine Conductivities on Pixel-wise Image Bladder State Classification

Test-Case 2 (TC2) builds on TC1 by increasing the number of urine conductivities in each SNR dataset. Also, the testing is performed in order to observe the effect of testing on unseen urine conductivities with 'seen' bladder volumes. Twelve urine conductivities were simulated between 0.5 S/m and 3.25 S/m, inclusively, as this range approximately covers the expected range of urine conductivity over the EIT frequency range that was established in Section 3.4.2.4.

The addition of these urine conductivities can impact how the dataset is designed. The dataset design from TC1 is used as a template here. Reducing the number of similar bladder volume observations in TC1 has potentially higher variance in the dataset. Thus, TC2 has

120 observations per bladder volume but 12 urine conductivities per bladder volume in the dataset.

The baseline of a 30 ml bladder volume, urine conductivity of 0.6 S/m and the average of 10 noisy frames (at the particular SNR) was used. The urine conductivity of 0.6 S/m ensures that none of the urine conductivities to be held out are seen in any way.

Figure 4.2 demonstrates a sample of three different urine conductivities for three different bladder volumes at 60 dB SNR. The effect of a lower urine conductivity results in lower pixel intensity values for the same bladder volume. Spatial changes are visible for the sample bladder volumes at 0.5 S/m when the colour scaling is based on the minimum and maximum pixels intensities across all images.

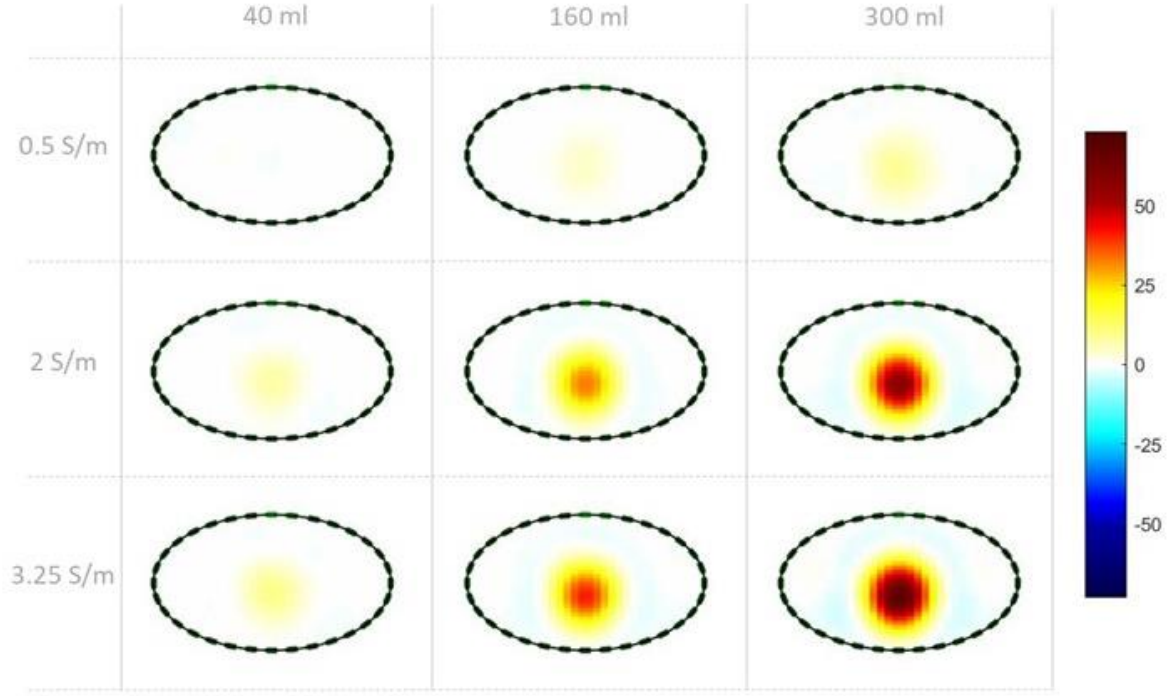

Figure 4.2: Effect of urine conductivity on sample bladder volumes (40 ml, 160 ml, and 300 ml) images in the 60 dB TC2 dataset. Spatial changes are more difficult to discern at lower urine conductivities due to a decrease in pixel intensities values when compared to the same bladder volumes at higher urine conductivities. Note: The colour bar is in arbitrary units and indicates the change in conductivity between the test data and the reference data.

4.1.4 Dataset Properties for Test-Case 3: Investigating the Effect of Varying the Measurement Frame Noise on Pixel-wise Image Bladder State Classification

Test-Case 3 (TC3) examines the effect of the measurement frame noise on bladder state classification. The dataset design in TC2 was modified here. The ten observations per bladder volume and per urine conductivity in TC2 dataset design were assigned a different SNR level in the TC3 dataset. The noise levels were varied between {40, 76} dB in steps of 4 dB. These SNR levels are within the previously investigated SNR range used in Section 4.1.2 and Section 4.1.3. The baseline used was the average of ten frames at the SNR of 80 dB with a 30 ml bladder volume and 0.5 S/m urine conductivity (i.e., the lowest urine conductivity in the dataset). Figure 4.3 presents sample images from this dataset.

As can be seen in Figure 4.3, the effect of measurement frame noise is mainly seen at lower SNR levels with the introduction of image artefacts as well as distortion of the bladder in the image.

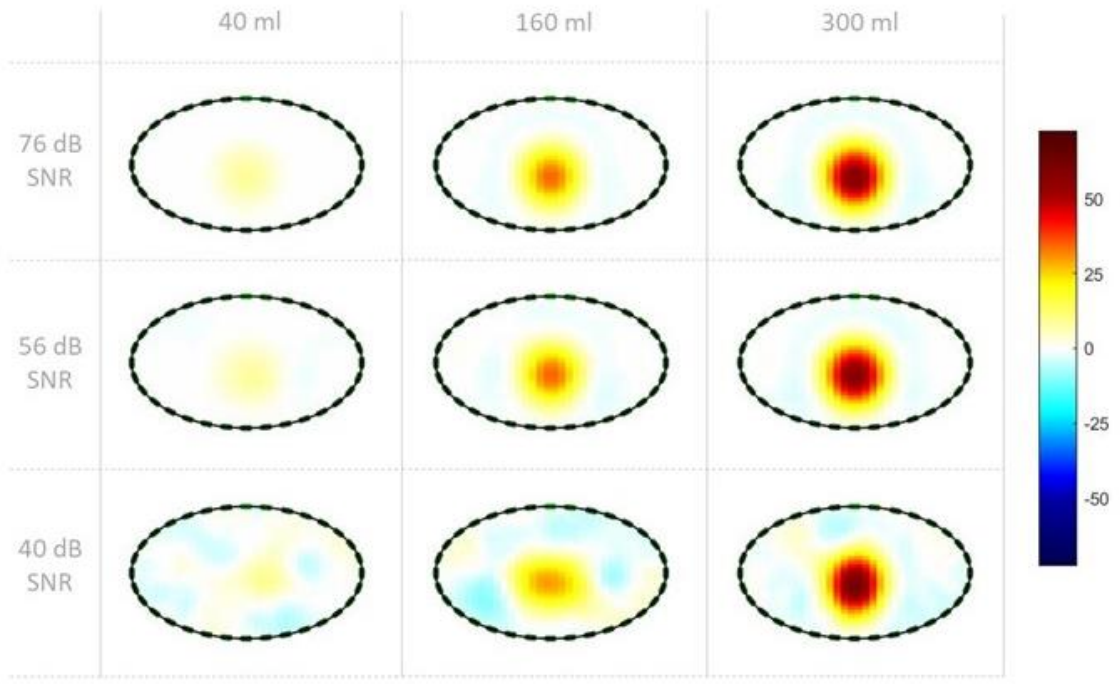

Figure 4.3: Sample images from the TC3 dataset with a urine conductivity of 2 S/m. From this selection of images, the noise seems to affect smaller bladder volumes in terms of spatial information in the image. The main difference between the bladder volumes in the images seems to be pixel intensity and the size of the highest-pixel intensity region, as before. Please note: The colour bar is in arbitrary units and indicates the change in the conductivity between the test data and the reference data.

4.1.5 Dataset Properties for the Realistic Test Scenarios

In this section, two remaining test cases are described, both of which are more representative of a real-world scenario than TC1-TC3.

Firstly, a more realistic assessment is performed where the conditions of bladder volumes and different urine conductivities are unknown and some of the noise in the images has not been filtered out. The classifiers are trained with approaches that would be used in reality (further outlined in Section 4.3.1). The dataset consists of all 26 bladder volumes, 12 urine conductivities and 10 SNR levels previously used in TC3. Each observation differs by a combination of these three conditions. This test differs from TC3 in that no set of observations is excluded based on one of the three conditions of bladder volume, urine conductivity or measurement frame noise. Thus, this test-case is called the 'Realistic Learning Test Case'. The dataset used in this test-case is summarised in Table 4.1 and Table 4.2.

Secondly, another variant on the realistic scenario is examined. Specifically, the classifier could be trained on the whole dataset after a sufficient testing performance has been obtained for deployment. Maintenance could be performed to ensure the classifier is working as intended [160]. If the classifier is not working, modifications may have to be made such as refining the data collection process, increasing the variety of observations, modifying the features used, and examining the assumptions made. To observe the effect of completely new data on the classifier trained with the full dataset, 6 new bladder volumes, 12 new urine conductivities, and 11 new SNRs are used to show the classifier functionality when evaluated on new data. This test case is referred to as the Continual Monitoring (CM) test-case and the dataset is referred to the CM1 dataset.

4.1.6 Overall Summary of the Datasets for each Test-Case

Table 4.1 summarises the overall makeup of each of the datasets in each test-case and Table 4.2 summarises the number of observations for each factor in each test-case.

Table 4.1: Characteristics of each condition in the datasets for each test-case used in Chapter 4.

Test case	SNRs	Bladder Volumes	Urine Conductivity
TC1	{40, 60, 80} dB	Not-Full: {40 + 20*n} ml Full: {300 + 10*n} ml where n = 0, 1, 2, 3, …, 12	2 S/m
TC2	{40, 60, 80} dB	Not-Full: {40 + 20*n} ml Full: {300 + 10*n} ml where n = 0, 1, 2, 3, …, 12	{0.5 + 0.25*p} S/m, where p = 0, 1, 2, 3, …, 11
TC3 & Realistic Learning	{40 + 4*a} dB where a = 1, 2, 3, …, 9	Not-Full: {40 + 20*n} ml Full: {300 + 10*n} ml where n = 0, 1, 2, 3, …, 12	{0.5 + 0.25*p} S/m, where p = 0, 1, 2, 3, …, 11
CM	{38, 42, 46, … 78} dB	Not-Full: {20, 190, 290} Full: {305, 365, 430}	{0.63 + 0.25*p, 3.33}, where p = 0, 1, 2, 3, …, 10

Table 4.2: Number of datasets, observations and observations per factor in each test-case (TC). For brevity, bladder volume is represented by BV and urine conductivity by UC in the table.

Test-case	Number of Datasets	Number of Observations per Dataset	Number of Observations per BV	Number of Observations per single BV and UC
TC1	3	3120	120	120
TC2	3	3120	120	10
TC3 & Realistic Learning	1	3120	120	10
CM	1	792	72	1

4.1.7 Structuring of the Images in the Dataset for Machine Learning Classification

In the literature to date, information from images was extracted in order to estimate the bladder volume, such as the metrics of GI and the Equivalent Circular Diameter [124]. Different methods can be used to compile images into a form suitable for machine learning algorithms. From Section 3.6.3.2, the pixel intensity values of the EIT images showed strong promise to separate empty and full bladder volumes. Hence, pixel-intensities are given to the classifiers to classify not-full and full states for initial investigation of bladder state classification and the

classification is referred to as pixel-wise classification. Each pixel value is considered a feature in the dataset. The basis of the classification is then primarily dependent on the pixel intensity. The pixel-wise classification approach is used to gather a baseline performance in this chapter, before the addition of spatial information to the classifiers (e.g., by feature detection in images [161], [162] and by feature engineering).

To form the dataset, each unprocessed image is translated into 1x1024 vector. This transformation is done by transforming all the image columns into one single row vector. Further pre-processing may be needed as the elliptical boundary of the FEM does not fill each of the pixels in the 32x32 square array. Thus, some pixel intensities will not be relevant.

The selection of certain classification algorithms may influence the pre-processing required. Hence, the selected classification algorithms and designed classifiers are discussed in the next section.

4.2 Design of the Classifiers

In this section, the selection of different classifiers is discussed. Two different classifiers are used in the initial study to ensure that the results and trends observed are not classifier dependent. For this work, *k*-Nearest-Neighbours (KNN) and Support Vector Machines (SVM) are employed. These machine learning algorithms have been previously used in BVM studies for Microwave Imaging [92]. Both algorithms are outlined in the following subsections.

4.2.1 k-Nearest-Neighbours Classifier Design

k-Nearest Neighbours is a machine learning algorithm that works fundamentally by first storing all the training data and then performing classification by comparing a new observation to the trained data. The algorithm initiates the comparison by calculating some distance measure (e.g., Euclidean distance) from the new observation to each trained observation and finding the trained observations with the closest distance [163]. The label of the new observation can then be decided by voting of the *k*-nearest trained observations (e.g., $k = 9$) whose labels are known.

In this study, the algorithm is employed with 9 nearest neighbours and using Euclidean distance as the distance metric. In later work, these hyperparameters could be further optimised to find the most optimum fit for the data.

4.2.2 Support Vector Machines Classifier Design

Support Vector Machines are powerful classifiers used in many classification tasks including medical imaging [164]. The classifier works by separating the data by a hyperplane for two classes and chooses the best hyperplane fit by maximising the margin of the hyperplane between the closest datapoints (support vectors) [163]. A soft margin may be needed where the data is not linearly separable and some datapoints may be required to be misclassified [165], [166]. Further, SVMs can use the 'Kernel Trick' to transform non-linear data to a higher dimensional space where a hyperplane can be fitted [163], [167]. More information on SVMs and the formulation can be found in [163], [167].

In this chapter, a linear SVM is employed with the box constraint (regularisation hyperparameter for the soft margin) of one. The hyperparameters for SVM (e.g., most optimum kernel) can be later optimised on a more realistic dataset.

4.3 Classification Architecture and Data Pre-processing for Machine Learning

In this section, the classification architectures employed to answer each research question are discussed along with the methodology used to pre-process the observation data before training and testing.

4.3.1 Employed Machine Learning Train-Test Architectures

In machine learning, it is important to assess fairly the generated model in order to report the expected performance for cases not in the trained data. A number of options exist for evaluating models that can be divided into two stages: 1) a training stage where a classification model is fitted to a training set; and 2) a testing stage where the fitted classification model is evaluated on a test set previously unseen to the model (i.e., a test set composed of data that was not part of the training set). However, these evaluation options may vary depending on the scale of the data [167]. For small dataset sizes, resampling methods are commonly used that involve training and testing on the same dataset multiple times, with different train-test sets used each time [167]. These methods reduce the bias from just picking one train-test set that could be unrepresentative of the actual dataset and allow for determination of the average error and variance of the model [167]. The evaluation methods can also help identify over-fitting.

In this chapter, two different evaluation architectures are used in order to best answer the posed research questions. First, the leave-p-candidate-out cross-validation (LPCOCV) architecture is

discussed for use in the bladder volume classification, and for testing the effect of new conductivities and new measurement frame noise levels. Then, the *k*-fold validation architecture is presented for use in test cases where the bladder volumes and conductivity values are unknown.

The first main architecture used is the LPCOCV, a subtype of which is the leave-one-candidate-out cross-validation (LOCOCV, also sometimes referred to as 'leave-one-subject-out [168], [169] and leave-one-user-out' [170]). The LOCOCV has been used in gender recognition with biometric data [170] and functional MRI analysis [168], [169]. The LPCOCV and LOCOCV architectures are discussed in more detail below, along with the type of scenarios that each is used for in this work.

First, to determine whether bladder state classification is possible with unseen bladder volumes or new urine conductivities, LPCOCV is used. In LPCOCV, a candidate is considered as a condition in the dataset such as a bladder volume, a urine conductivity, or a SNR, along with the observations associated with that candidate. In this evaluation method, p-candidates are left out for testing on while the remaining candidates are used for training. Specifically, leave-two-candidate-out cross-validation with the condition of one not-full and one full bladder volume in each test set is used in this chapter to determine if new bladder volumes can be classified into not-full and full bladder states. The evaluation architecture is referred to as 'stratified L2COCV' in this chapter as this method ensures that the classifiers are trained and tested on an equal number of bladder volumes in each category, i.e., stratified. The number of folds is equal to the number of not-full bladder volumes multiplied by the number of full bladder volumes, i.e., no repeated test combinations are used in the evaluation.

Next, for classifying new conductivities and new measurement frame noise levels, LOCOCV is used ($p = 1$). The LOCOCV involves leaving out a candidate (e.g., data with a given value of urine conductivity) to be tested on after training the classifier on the remaining candidates.

To summarise, both stratified L2COCV and LOCOCV methods test on all the possible candidates in the dataset (i.e., the methods are exhaustive). All observations for the candidate are grouped together and are not seen in training. The stratified L2COCV method is built on LPCOCV but is specifically tailored to the test case in this chapter.

The L2COCV and LOCOCV methods are suitable where the underlying condition, such as bladder volume or urine conductivity, is known. However, there is typically no additional information available when recording bladder EIT data from a human subject. In other words,

the bladder volume and urine conductivity will not be definitively known for any observation. Thus, a more realistic case for classification would involve a dataset of EIT measurements with labels of not-full and full (where full is the label assigned to a specific set of measurements, e.g., such as the 10 recordings before a voiding episode). In this case, the exact bladder volumes and urine conductivities would not be known, and all the conditions are scrambled within the dataset unmarked.

Hence, a more applicable testing architecture would be *k*-fold validation, which is the second main architecture used in the chapter. The *k*-fold validation architecture works by:

1. dividing the dataset into *k* blocks ('folds'), each block of approximately equal number of samples;
2. fitting the model to *k*-1 blocks;
3. testing the classification model on the remain block;
4. and repeating *k* times until each block has been trained on *k*-1 times and tested on only once.

A common selection for the value of *k* in *k*-fold cross-validation is 10 [163]. An illustration describing *k*-fold cross-validation is shown in Figure 4.4.

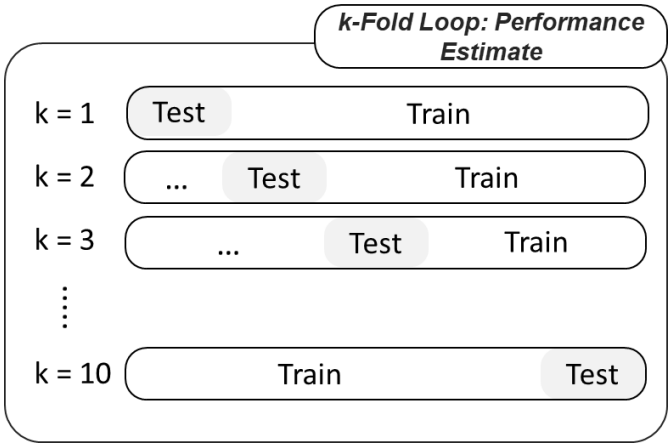

Figure 4.4: Illustration of 10-fold cross-validation for performance estimation. K-fold cross-validation can be used to get a generalised performance for dataset and reduce the bias of just picking one train-test set from a dataset. This image has been adapted from Figure 5 in Oliveira et al. [171] *that is licensed under CC BY 4.0* [141].

Similar to other resampling methods, *k*-fold cross-validation reduces the bias of the classifier and the variance of just randomly sampling a single test set [167]. An improvement on *k*-fold cross-validation is to run repeated *k*-fold cross-validation where multiple sets of *k*-folds are

generated and trained and tested upon. By training and testing on multiple *k*-folds, the bias of selecting one set of *k*-folds is reduced [167]. Therefore, 5-times repeated stratified 10-fold cross validation is used on the realistic test-case to determine the average performance of the classifier.

If the aim was to compare machine learning algorithms or to optimise machine learning models by tuning hyperparameters, modifications to the evaluation architecture may be required and/or statistical tests performed. Thus, the architecture of evaluating performance is case dependent.

4.3.2 Pre-Processing of Image Observations for Bladder State Classification

In Section 4.1.7, the images were converted into row vectors of 1x1024 pixels. However, the elliptical boundary of the FEM does not cover the whole original 32x32 pixel image. Thus, there are redundant pixel intensities in the observation for the image. Pixel intensities outside the FEM are removed from the observation, resulting in a row vector of length 812 pixels, i.e., 812 features.

For the classifiers chosen, feature scaling is required to prevent any one feature(s) dominating the class selection when a feature has values much larger than the other features. However, information sharing from the test set can occur by just applying feature scaling, such as standardising, to the entire dataset as observations in the test may be used to calculate the mean and standardisation for each feature. It is therefore important to ensure that the training set is independent of the test set in order to ensure reliable results. Thus, for each train-test pair in cross-validation, the standardisation (centring by the mean and dividing by the standard deviation) is calculated only on the training set and then the means and standard deviations calculated in training are applied to each observation in the test set.

4.4 Evaluation Metrics for Bladder State Classification

To evaluate a classifier, quantitative assessment is required. This quantitative assessment can be completed based on the predicted results from an evaluation dataset (such as the test set). One summary method is to calculate the true positive (*TP*), false positive (*FP*), false negative (*FN*) and true negative (*TN*) values by comparing the true and predicted classes in the test set. The true positive and true negative are the total number of observations correctly classified by the classifiers as positive and negative classes, respectively. The false positive is the number of observations misclassified by the classifier as the positive class when the correct classification is the negative class (e.g., the classifier indicates a person should go to the toilet

when they do not need to go). The false negative is the number of observations misclassified by the classifier as the negative class when the correct classification is the positive class (e.g., indicating a person should not go to the toilet when actually they should go). The confusion matrix is a tabulated form of these values and is illustrated in Figure 4.5 in the context of this application. The confusion matrix can be used to determine performance metrics such as the accuracy, the sensitivity and the specificity.

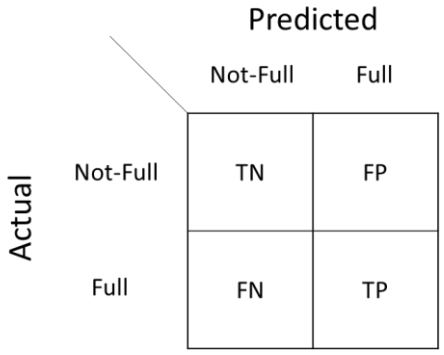

Figure 4.5: Illustration of the confusion matrix in the context of this application with binary classification. The confusion matrix can summarise the results from classification and enable calculation of many classification performance metrics.

The accuracy is the total correctly classified observations divided by the total number of observations and can be expressed in the form:

$$Accuracy = \frac{TP+TN}{TP+FN+FP+TN}. \tag{4.1}$$

Accuracy is an easy and quick-to-interpret metric that provides high-level information on the overall performance of the classifier. However, the accuracy value does not provide any indication of where the classifier is failing, i.e., what types of errors occurred [167]. For this reason, other methods may be needed to supplement the accuracy metric. In the context of this work, the clinical need is to alert the user to go toilet before they void. Thus, the worst error is to tell the user they do not need to go to the toilet when they should, i.e., a false negative. The sensitivity performance metric can help in capturing the false negative information in relation to the correctly predicted positive classes by the classifier. The metric is defined as:

$$Sensitivity = \frac{TP}{TP+FN}. \tag{4.2}$$

However, it is also important to not alert the user too early (for example, just after voiding) as this may lead to frustration on behalf of the user and potentially, to the discontinuation of use

of the device. Information on the false positive is captured with the specificity performance metric, and the metric is defined as:

$$Specificity = \frac{TN}{TN+FP}. \tag{4.3}$$

These metrics are just some of the standard performance metrics available for classification [167]. Custom performance metrics may be developed to be application specific [167]. Some bounding conditions for such a metric in this application would be higher penalties for predicting too early (e.g., just after voiding) or after missing a voiding event could be defined. However, an exact implementation custom metric may depend on what feedback the device gets (such as time since voiding, observing rapid emptying of the bladder or a user input of successful alert or an episode missed) and is therefore best left until after user feasibility testing.

In this work, the accuracy, sensitivity and specificity will be reported to summarise the performance of classifiers. With cross-validation, the accuracy, sensitivity and specificity will be presented as an average of the performance on the specific test set along with the standard deviation (i.e., average ± 1 standard deviation).

4.5 Investigating the Effect of Bladder Volume, Urine Conductivity, and Measurement Frame Noise on Pixel-Wise Image Bladder State Classification

In this section, a number of the research questions posed in the introduction are addressed. Bladder volume, urine conductivity, and measurement frame noise are investigated in separate test-cases. Each test-case is a controlled scenario to allow error-analysis to be performed.

4.5.1 Test-Case 1: Investigating the Effect of Varying Bladder Volumes on Pixel-Wise Image Bladder State Classification

The stratified L2COCV was used to determine if new bladder volumes could be classified using EIT image data. Specifically, the pixel intensities from the reconstructed images were used as input features to the classifiers. Three datasets were run, where each dataset has a different SNR. Table 4.3 shows the results for the average performance metrics for 169 test sets, each with a not-full and full bladder combination (that was not repeated) from the total 26 bladder volumes (13 not-full and 13 full bladder volumes). The lowest accuracy observed was 94.51%, indicating classification is possible based on bladder volume alone when trained on noisy data. The performance of the classification degrades with increasing measurement frame noise, e.g.,

the accuracy drops by approximately 3.35% for KNN and 1.56% for Linear SVM as the measurement frame noise changes from 80 dB to 40 dB.

The sensitivity and specificity metrics show that the main loss in classification accuracy occurs due to having more false positives than false negatives, as the specificity is lower than the sensitivity for each of the datasets. Figure 4.6 shows the misclassification error for each tested bladder volume for the 40 dB data set.

The data provided in Figure 4.6 indicates that the most influential bladder volumes on the classification accuracy rates are those near the bladder separation volume of 300 ml. The highest misclassified bladder volume was 280 ml for both classifiers (at least 40% of the observations for the 280 ml were misclassified on average), which contributes to the overall high specificity. A possible reason why the 280 ml bladder volume was the most misclassified was due to the larger gaps in bladder volumes in the not-full class compared to the full class. Thus, more bladder volumes near the bladder state separation could be needed on data collection to better inform the classifier and the type of kernel used.

Table 4.3: Average performance of the classifiers for classifying new bladder volumes on three different noisy image-based datasets.

SNR	Classifier	Accuracy (%)	Sensitivity (%)	Specificity (%)
80 dB	KNN	97.86 ± 7.60	99.92 ± 0.32	95.79 ± 15.22
	Linear SVM	98.44 ± 5.66	100.00 ± 0.00	96.88 ± 11.32
60 dB	KNN	96.82 ± 8.92	99.16 ± 3.07	94.48 ± 17.84
	Linear SVM	98.28 ± 5.83	99.79 ± 0.79	96.77 ± 11.70
40 dB	KNN	94.51 ± 10.25	98.49 ± 3.66	90.53 ± 20.50
	Linear SVM	96.88 ± 7.43	97.51 ±7.97	96.24 ± 13.16

To demonstrate that the results are not specific to one urine conductivity level, TC1 was run at different urine conductivities (specifically, at the same twelve urine conductivities as TC2 in Table 4.1). The results are shown in Figure 4.7. High classification accuracies of above 85% are observed for each urine conductivity with the lowest accuracy occurring at 0.5 S/m. The reason for this noticeable drop in performance at 0.5 S/m may be answered by analysing the results of TC2, which examines the effect of unseen urine conductivities on bladder state classification.

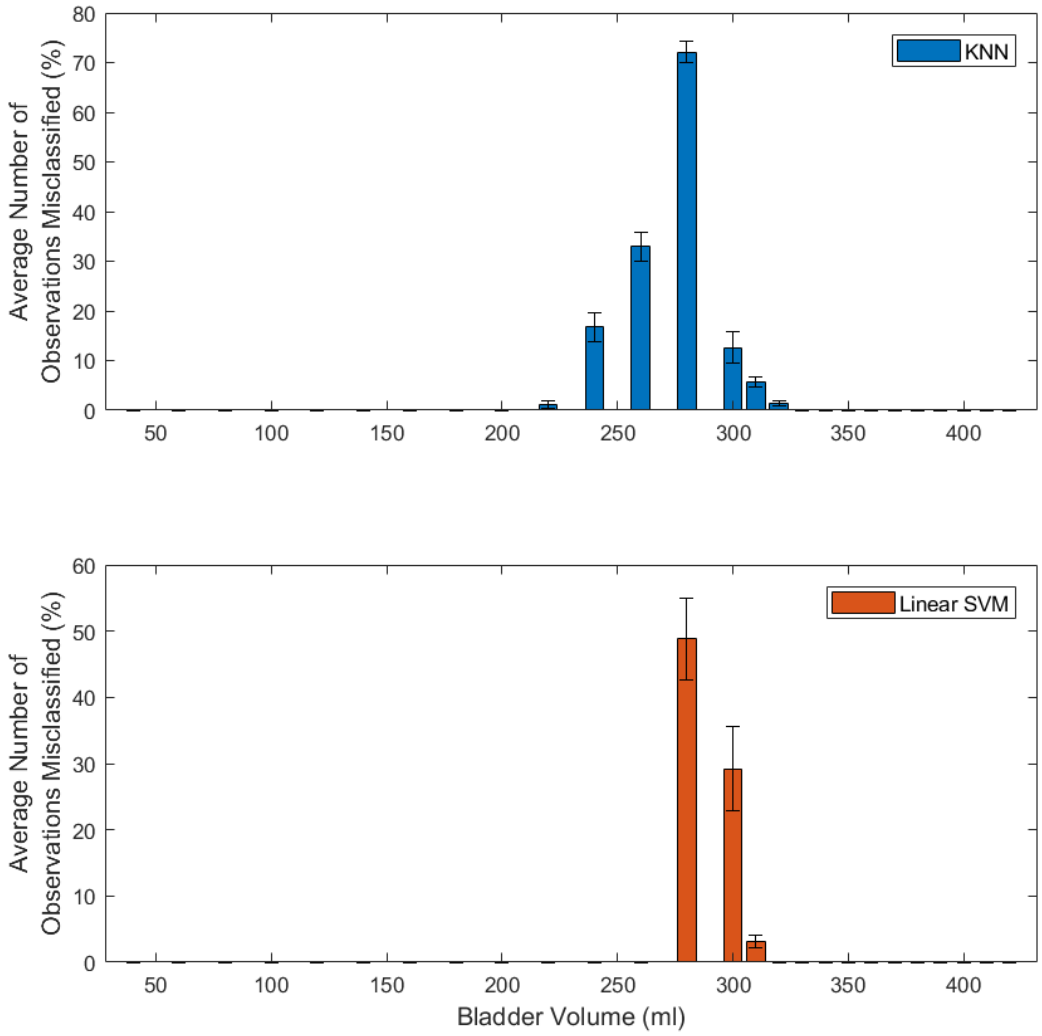

Figure 4.6: Percent of observations misclassified for each bladder volume by the classifiers using the 40 dB SNR TC1 dataset. Most misclassification occurs around the separation volume of 300 ml with the most misclassified bladder volume being 280 ml.

To illustrate that this level of performance can be achieved with bladder volume separation volumes other than 300 ml, the bladder volume classification performed at a urine conductivity of 2 S/m was repeated for bladder separation of 360 ml (i.e., all volumes in the dataset were shifted by 60 ml) and the results were calculated. The average of each performance metric was found to be in agreement with the values shown in Table 4.3 to within 1% for the 80 dB SNR and 60 dB SNR datasets and within 2% at 40 dB dataset.

In this subsection, it has been shown that the classification performs well on data of unseen bladder volumes when trained on a fixed urine conductivity and a fixed SNR level. In the next subsection, the effect of variation in urine conductivity on the not-full and full classification will be examined.

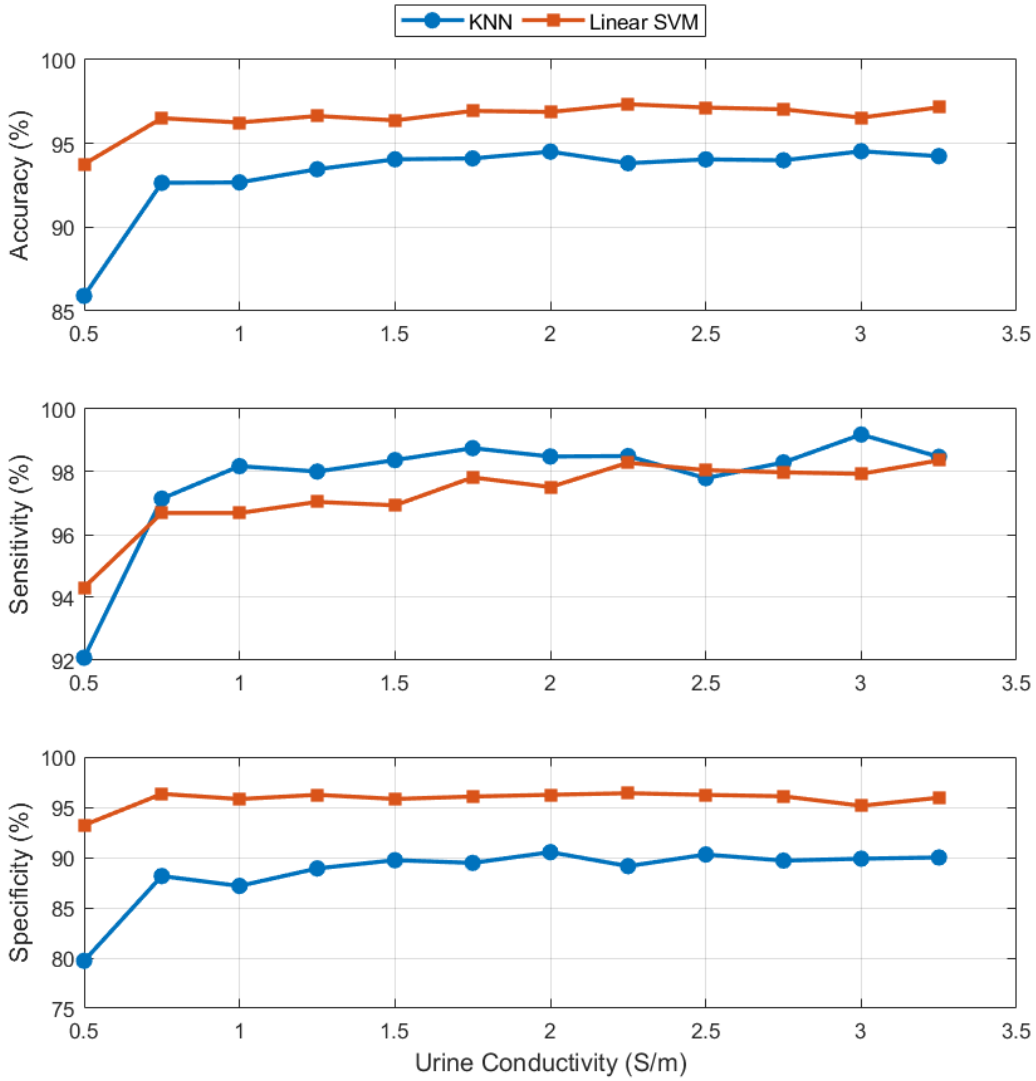

Figure 4.7: Average performance for classifying not-full and full bladder volumes at 40 dB SNR across each conductivity. High classification performance (e.g., accuracy > 85%) is observed. However, a deterioration of classification performance is seen at the lower conductivity value of 0.5 S/m.

4.5.2 Test-Case 2: Investigating the Effect of Varying Urine Conductivities on Pixel-wise Image Bladder State Classification

In Section 4.5.1, it was demonstrated that unseen bladder volumes could be classified using classifiers trained on a fixed urine conductivity and a fixed SNR at {40, 60, 80} dB. The bladder volume dictates the fullness level. However, the urine conductivity contrast is essential for the detection of bladder fullness using EIT. Bladder monitoring with EIT relies on the principle that urine has a different conductivity from that of the surrounding tissues. Thus, urine conductivity is an important condition to isolate in order to determine what effect variations in urine conductivity have on bladder state classification.

To isolate the urine conductivity, constant 'seen' bladder volumes were used for each simulated urine conductivity. The method LOCOCV was used to isolate a urine conductivity to test on while the other eleven urine conductivities used for training (dataset outlined in Section 4.1.3). The overall performance metrics for LOCOCV at the SNR levels of {40, 60, 80} dB are summarised in Table 4.4. A further breakdown of the performance metrics as a function of urine conductivity is given in Figure 4.8 for the 40 dB SNR dataset where both the KNN and the SVM classifiers showed a large breakdown in performance.

Table 4.4 shows that new urine conductivities can be classified. However, there is a high variance in the classification accuracy. Examining the data more closely in Figure 4.8, it is evident that the classifiers break down severely when they have not seen extremely low urine conductivities. For example, KNN performance drops to circa 50% when bladder volumes from the unseen urine conductivity of 0.5 S/m and 0.75 S/m are tested upon. Notably, the sensitivity is poorer for low urine conductivities than for high urine conductivities while the specificity degrades as new increasingly higher urine conductivities are tested upon, particularly in the case of the KNN classifier. One reason for this result is that the classification has a high dependency on the image pixel intensity values, which in turn are related to both the conductivity of the bladder in the test scenario and the conductivity of the reference bladder used in the image reconstruction.

Looking at sample images presented earlier in the chapter in Figure 4.2 (EIT bladder images with different urine conductivities), the pixel intensities in the images for the same bladder volumes were much lower for lower urine conductivities than their higher urine conductivity counterparts. In particular, the contrast between different bladder volumes in Figure 4.2 was smaller at 0.5 S/m than at 2 S/m or 3.25 S/m. Importantly, the contrast between the background conductivity of the FEM (0.352 S/m) and the urine conductivity is at the smallest (as defined in Chapter 3, Section 3.4.2.4), when the urine conductivity is 0.5 S/m. This lack of contrast from the background and other urine conductivities could explain why there is poorer performance at the lowest conductivity. As described in Section 4.1.7, the pixel-wise based classification is primarily dependent on the image pixel intensities. So, when the urine conductivity is low and is not part of the training set, the new full bladder volumes will have lower pixel intensities than corresponding full bladders with higher urine conductivities (e.g., at 3.25 S/m) that were trained on (see example images for Figure 4.2). This situation could lead to the incorrect classification of full bladder volumes and result in high false negatives (lower

sensitivity). The inverse situation can also occur, causing the degradation of specificity at high urine conductivities.

Table 4.4: Average performance of the classifiers for classifying new bladder states with unseen urine conductivities on three different noisy image-based datasets.

SNR	Classifier	Accuracy (%)	Sensitivity (%)	Specificity (%)
80 dB	KNN	90.71 ± 15.07	82.24 ± 30.55	99.17 ± 1.11
	Linear SVM	99.62 ± 1.22	99.29 ± 2.44	99.94 ± 0.22
60 dB	KNN	89.49 ± 14.65	83.65 ± 30.15	95.32 ± 2.53
	Linear SVM	94.71 ± 8.21	92.95 ± 17.50	96.47 ± 3.03
40 dB	KNN	76.35 ± 14.23	69.74 ± 39.60	82.95 ± 13.04
	Linear SVM	86.86 ± 11.83	84.68 ± 27.51	89.04 ± 4.77

The results shown here illustrate that the classifiers were able to classify bladder state for urine conductivities within the range of the trained urine conductivities. Further, urine conductivities outside the trained range can be classified with high accuracy when the test conductivities are higher (3.25 S/m). However, this is not the case when the lowest urine conductivity was excluded and the accuracies drop to circa 50%. Therefore, it is important when data collecting to try to collect low conductivity samples (e.g., over hydrated) in order to ensure better classification performance.

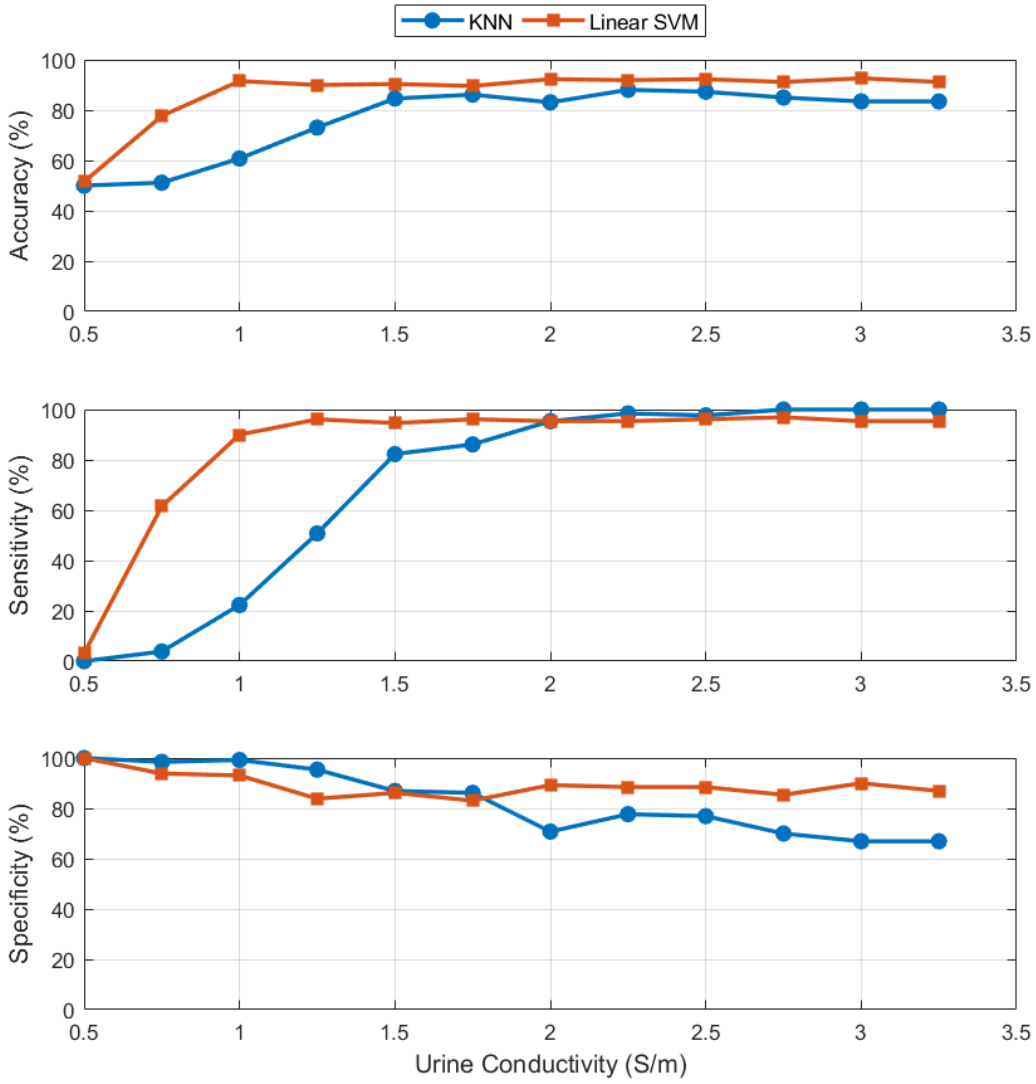

Figure 4.8: Performance of the classifiers for unseen urine conductivity values for the TC2 40 dB SNR dataset. Classification is possible with unseen urine conductivities except at extreme lower urine conductivities of 0.5 S/m, where the classifiers had accuracies near 50%.

4.5.3 Test-Case 3: Investigating the Effect of Varying Measurement Frame Noise on Pixel-Wise Image Bladder State Classification

Previous subsections in Section 4.5 showed the effects of training and testing on the same measurement frame noise level. However, having consistent SNR levels is unlikely in a real-world scenario as noise can be introduced into the recordings from sources such as electronic noise, variable electrode contact over time and body movement. Thus, the effect of unseen SNRs on bladder state classification is evaluated in this section using the LOCOCV architecture. Twelve different noise levels were used on the measurement frames before image

reconstruction to form the observations, as summarised in Table 4.1. The overall classification results are shown in Table 4.5.

Table 4.5: Average performance of the classifiers for classifying bladder states using image data with unseen SNR levels.

Classifier	Accuracy (%)	Sensitivity (%)	Specificity (%)
KNN	92.85 ± 7.73	92.50 ± 9.63	93.21 ± 5.94
Linear SVM	92.24 ± 7.00	92.50 ± 6.81	91.99 ± 7.37

From the overall results, the classifiers perform well on unseen measurement frame noise levels, with accuracies of circa 92%. However, there is a high variance (maximum standard deviation of 7.73%) that is further explained by analysing the performance at the held-out SNRs, presented in Figure 4.9. The performance of the classifiers continually degrades as the held-out SNR decreases. Linear SVM degraded the most with the unseen measurement frame noise levels. The sensitivity, specificity, and accuracy all decrease as the SNR decreases as shown in Figure 4.9.

Unlike the urine conductivity, the worst tested SNR did not result in the classifier having accuracies circa 50%, indicating that the classification may be more robust to variations in measurement frame noise levels than to variations in urine conductivity. It is important to note that the implementation of the noise function results in changes to the raw EIT signal that are quite different from the changes caused by different urine conductivity values. With varying measurement frame noise levels, there is no increase in the mean amplitude of the average frame (over many noisy frames at the same SNR as approaches infinite, small sample in Figure 3.11) at the same measurement frame noise level. This effect is unlike the effect of urine conductivity, which changes the mean amplitude of a frame for the given bladder volume and urine conductivity. Thus, the effect of the low unseen SNRs tested in this work seems to be less problematic than the effect of low unseen urine conductivities.

The results from Table 4.5 and Figure 4.9 indicate that training on a diverse range of noisy data does enable classification with minimal degradation in the classifier accuracy. This result gives validity to having observations not only differing in bladder volume and urine conductivity, but also in terms of the noise levels as implemented here in the form of simple additive random Gaussian noise.

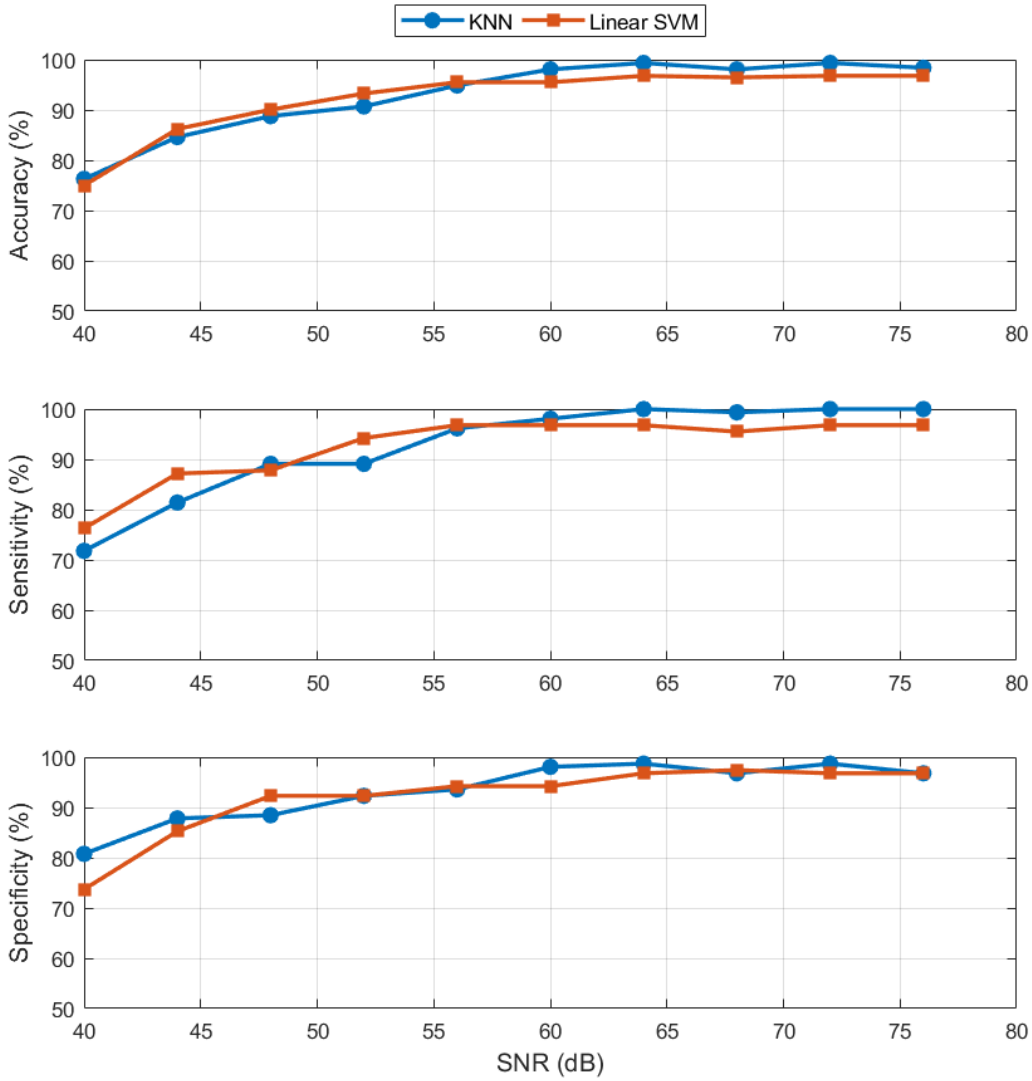

Figure 4.9: Performance degradation of the classifiers as the SNR level is decreased. As expected, the performance of the classifiers degrades with decreasing SNR. However, the accuracy was greater than 70% even at the lowest tested SNR level of 40 dB. This result suggests that the classifiers may be able to handle noise, even when the noise persists after signal pre-processing or noise-reduction methods.

4.6 A More Realistic Learning Test-Case of All Conditions in the Dataset Varying

In Section 4.5, the effects of unseen bladder volume, urine conductivity and SNR were investigated in a controlled way. In a more realistic case, the exact values of these conditions may not be known unless being directly tested for during recording, or by some sort of explicit input. Thus, recordings will only have time information (collection of frames one after the other) as well as some feedback from a successful/not-successful emptying.

To demonstrate classification with a more realistic dataset, and corresponding train-test setup, the dataset from TC3 was used along with a 5-repeat stratified 10-fold cross-validation evaluation architecture. This TC3 dataset includes a wide range of different bladder volumes, different urine conductivities, and different SNR levels, as summarised in Table 4.1. The average results across the test folds for this scenario, called Realistic Learning Test-Case, are given in Table 4.6.

Table 4.6: Average performance of the classifiers on the Realistic Learning Test-Case.

Classifier	Accuracy (%)	Sensitivity (%)	Specificity (%)
KNN	92.89 ± 1.32	92.36 ± 1.86	93.42 ± 1.98
Linear SVM	92.53 ± 1.42	92.97 ± 1.86	92.08 ± 2.28

It was found the classifiers that misclassifications were greatest around the bladder volume separation value, at low urine conductivities, and at low SNRs. This result is consistent with the analysis found in Section 4.6, which considered each of these three conditions individually.

Assuming that the performance of the classifiers is sufficient for this application of bladder fullness detection, the classifiers were retrained on the whole dataset and used to classify new, previously unseen data for the CM test case, as outlined in Section 4.1.5. The exact composition of the dataset is outlined in Table 4.1 and Table 4.2. The overall performances are given in Table 4.7 and the misclassification rates across bladder volume, urine conductivity, and SNR, are presented in Figure 4.10.

Table 4.7: Average performance of the classifiers on the CM1 dataset of six new bladder volumes, eleven new urine conductivities and twelve new SNRs.

Classifier	Accuracy (%)	Sensitivity (%)	Specificity (%)
KNN	83.59%	91.16%	76.01%
Linear SVM	84.97%	93.69%	76.26%

As can be seen in Figure 4.10, the classifier behaves as expected based on the results in Section 4.5, i.e., high numbers of misclassifications around the bladder separation; and higher misclassifications at lower urine conductivities and lower SNRs. For urine conductivity, the lowest urine conductivity did not have the highest number of misclassifications for the SVM. This result could be because the lowest urine conductivity in the CM1 dataset was 0.63 S/m

and a lower urine conductivity of 0.5 S/m is seen in the training phase, which may have supported the learning for SVM and not KNN.

From the new CM1 dataset, it is seen that the classifier works overall as expected with high classification accuracies. From the misclassification rates over each condition in Figure 4.10, the performance is similar to what has been demonstrated in previous sections.

Overall, the classifier has been shown to work when trained and tested on a variety of possible combinations of bladder volume, urine conductivity and measurement frame noise. Now that images have been shown to have potential in bladder state classification with EIT, some of the advantages and disadvantages of images need to be considered.

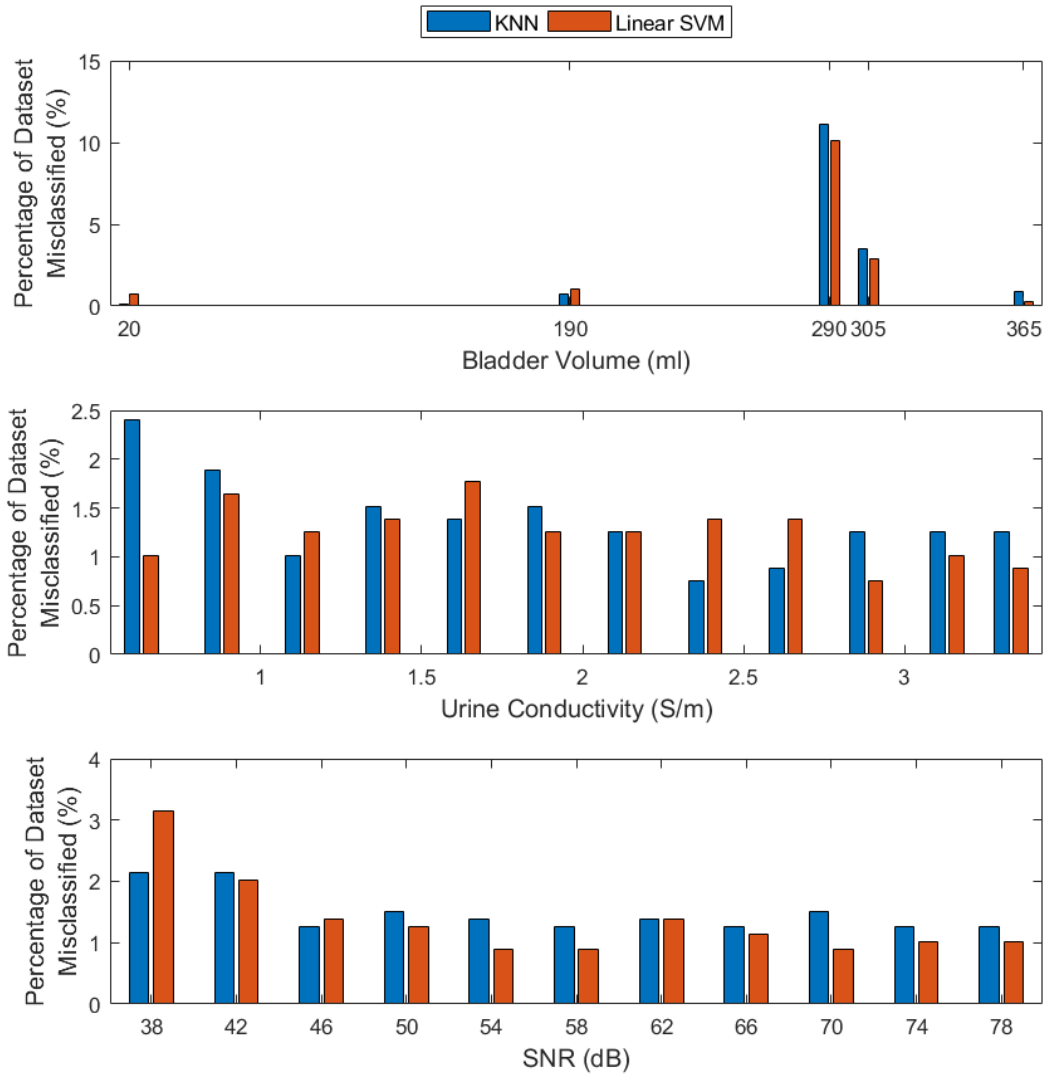

Figure 4.10: Performance of the dataset-trained classifiers on a CM1 dataset. The classifiers greatly degrade around the bladder separation volume, lower urine conductivities and lower SNR levels. These results are similar to the findings from previous sections in this chapter.

4.7 Advantages and Disadvantages of EIT Image Data for Bladder State Classification

Images offer the benefit of being more easily interpretable for users than raw EIT voltage data, and they can convey spatial information that is not as readily evident from a collection of raw EIT voltage data. Electrical impedance tomography imaging has a particularly strong temporal resolution [99] and is used in continuous monitoring applications such as continual monitoring of patients using mechanical ventilation [11].

However, EIT imaging has some disadvantages. EIT images have low spatial resolution [95]. The low spatial resolution is partly due to the fact that current flows in a 3D space, leading to the ill-posed nature of EIT [95]. To help with image reconstruction *a priori* information is provided [95]. The *a priori* information includes the geometry of the boundary and the electrodes, and the location of the electrodes. This information can be difficult to obtain in reality and mismatches between the assumed and the actual situation may introduce error [99]. Time-difference EIT image reconstruction requires a reference/references to correct for *a priori* information mismatch and artefact removal. The use of the reference is particularly effective where the noise interference is more stable in time [99], e.g., a mismatch in the expected and real boundary in a resting body.

Realistic geometric FEMs may better inform image reconstruction [172]. However, more realistic geometric forward models of a child are difficult to access to inform the image reconstruction. In fact, these FEMs would be hard to obtain for each child using the device as the anatomically-informed models used in EIT are based on scans from CT or MRI [173], [174].

In applications with large amounts of body movement noise, tracking the boundary and deforming FEMs may be needed to minimise boundary and electrode location errors in real-time. This processing can increase the complexity and computational cost of image reconstruction [175].

Many problems arise before image reconstruction at the data collection process, e.g., body movement and electronic drift [95]. However, the addition of *a priori* information may not actually sufficiently mitigate the problems from data collection and may introduce new and unexpected artefacts. Lastly, the image reconstruction algorithm and generating the *a priori* information for the FEM (in particular, if the FEM is of high element resolution) may also lead to increased computational demands of a bladder monitoring system. The exact noise sources

in this application for EIT imaging requires further analysis and quantifying to first determine if: 1) they apply and 2) how serious of an effect they may have. This research may be achieved in future work.

The use of EIT images has strong potential for bladder state classification as shown in this chapter. However, there are still many challenges to overcome from the data collection process that image reconstruction may not solve. Image reconstruction also requires high quality and accurate *a priori* information to be provided, increasing the complexity and computation resources of an EIT-based enuresis alarm.

4.8 Summary

In this chapter, bladder state classification of not-full and full classes was investigated. The main finding from this chapter was that accurate bladder state classification of not-full and full is possible using noisy image data varying in complexity, with different bladder volumes, urine conductivities and measurement frame noise levels. The specific findings of each section are summarised below.

In Section 4.5, the effect of conditions of unseen bladder volumes, unseen urine conductivities and unseen measurement frame noise levels on bladder state classification were individually evaluated. The classifiers struggled to classify bladder volumes at the boundary of the not-full and full classes, suggesting the need to collect data more frequently as the time from the last voiding increases. The classifiers employed also resulted in accuracies circa 50% when tested on the lowest urine conductivity (i.e., when tested on a conductivity that is lower than the range of conductivities included in the training set). In this scenario, the classifiers had to extrapolate for the lowest urine conductivity. This result suggests the need to collect as many of different urine conductivities as possible during the training period, particularly at low urine conductivities. Another way of handling this noise source is to include some method for determining urine conductivity to provide urine conductivity information explicitly to the classifier. Lastly, it was found that an increase of measurement frame noise will result in a degradation in classification performance, as expected. Thus, it is important to employ strategies to minimise noise where possible, and where not, to include more samples in the dataset for the classifier to overcome the noise.

In Section 4.6, a realistic learning test case was presented where the classifiers were trained and tested on all three variable conditions of bladder volume, urine conductivity and

measurement frame noise. High performance was achieved (average accuracies of 92.53% for Linear SVM and 92.89% for KNN on the test set) and a continual monitoring example mimicking real-life deployment was presented where the classifiers were trained on the whole dataset and given completely new bladder volumes, urine conductivities and measurement frame noise levels. From this section, an indication is given that a classifier can be initially trained on a small number of recordings and provide reasonable performance (e.g., classifying the correct state with an accuracy of 80% or greater).

In Section 4.7, the advantages and disadvantages of using EIT images for bladder state classification were discussed. While many challenges with images exist, the need for *a priori* information to help with the ill-posed problem of EIT may impact the use of images negatively. Achieving high-quality *a priori* information would be very difficult and cumbersome to do for each child in the NE application. A way of mitigating the need of providing *a priori* information for image reconstruction could be by using the raw EIT measurement data (i.e., the measured voltages) directly as the main data source for classification.

In summary, this chapter has shown that bladder state classification of not-full and full classes is possible on noisy simulated data. Future research on EIT images can be performed to investigate the full effect of the use of *a priori* image reconstruction information and the selection of the reference on the accuracy of bladder state classification. Further research to avoid *a priori* image reconstruction information by simply avoiding the image reconstruction step could be possible by using the EIT measurement data as input for bladder state classification rather than EIT images. This idea of using the EIT measurement data as input to the classifiers in this application is investigated in Chapter 5.

5 Bladder State Classification with EIT measurement Data

In Chapter 4, the concept of bladder state classification was evaluated. Specifically, bladder state classification using EIT images was found to be viable under conditions of varying bladder volumes, urine conductivities and measurement frame noise. However, reconstructing EIT images requires significant *a priori* information (e.g., boundary shape and size) that could potentially cause unintended error if the *a priori* information is inaccurate. Thus, an alternative to images as input to bladder state classification would be the EIT voltage measurement. Using the collected measurement data as the input avoids the need for EIT-related *a priori* information and could therefore allow for classification with fewer assumptions and reduced error.

Thus, the work from the previous chapters is advanced upon in this chapter through the investigation of bladder state classification using simulated raw EIT voltage data. Binary classification of not-full and full bladder states is performed with the objectives of establishing:

5. whether bladder state classification is possible using raw EIT voltage data;
6. how classification with EIT image data performs under the individual conditions of varying bladder volumes, varying urine conductivities, and measurement frame noise, which are all key conditions for bladder monitoring, as previously established in the literature [124];
7. how the classifiers perform when conditions in the dataset are varied;
8. the advantages and disadvantages of using raw EIT voltage data for bladder state classification.

This chapter is divided as follows: datasets of varying conditions are formed in Section 5.1 using the simulated data from the adult numerical forward model developed in Chapter 3; the methods used in this chapter for pre-processing and classification are described in Section 5.2; classification results are presented in Section 5.3, examining the effect of each condition (bladder volume, urine conductivity and noise) on bladder state classification with raw EIT voltage data; and then a more realistic scenario of training and testing of all the conditions

varying in the dataset is performed in Section 5.4. Finally, the advantages and disadvantages of using raw EIT voltage data are discussed in Section 5.5 and the chapter is concluded in Section 5.6.

The content of this chapter draws from earlier published work:

E. Dunne, A. Santorelli, G. Leader, B. McGinley, M. O'Halloran and E. Porter, "Supervised Learning Classifiers for Electrical Impedance-based Bladder State Detection", *Sci. Rep.*, vol. 8, no. 1, Art. no. 5363, pp. 1-12, Mar. 2018, doi: 10.1038/s41598-018-23786-5.

5.1 Formation of Simulated Datasets for Voltage-based Bladder State Classification

This section describes the design and formation of datasets to help answer the research questions posed in this chapter. First, previous datasets that have been used in the literature for voltage-based classification of bladder state are discussed; then the formation of new datasets is presented for each of the different research questions posed in this chapter. The test-cases are: 1) testing of the effect of unseen bladder volumes; 2) testing the effect of unseen urine conductivities; and 3) testing the effect of unseen SNR levels. Each test-case is studied to examine the extent to which the bladder state can be accurately classified as not-full or full. The structuring of the raw EIT voltage data in the dataset before pre-processing and classification is also discussed. The dataset formation utilises similar dataset design as in Section 4.1, in which a similar investigation was performed for the bladder state classification using EIT image data. These similarities between conditions in the datasets facilitates better comparisons between image-based and voltage-based classification methods.

5.1.1 Dataset Design using EIT Measurement Data for Bladder State Classification

In the literature to date, the research on BVM using raw EIT voltage data has been focused around bladder volume estimation [123], [124]. Thus, the existing work associated with bladder volume estimation is discussed here. In these works, the algorithms for estimating bladder volume using raw EIT voltage data (voltage data comprising each measurement frame) have been trained and tested first on simulated data [115], [123], [124].

For the studies by Schlebusch [115] and Schlebusch et al. [124], bladder volume estimation algorithms were designed for the raw EIT voltage data rather than reconstructed images as a means to overcoming the effect of noise in the images and to remove the need of regularisation commonly employed in image reconstruction. Two approaches were used: a neural network

and singular value decomposition-based method. The two methods differed by the use of reference data or not. For the neural network estimation of bladder volume, simulated noiseless measurement frame data was given to a neural network to be trained, tested, and validated upon. For the singular value decomposition-based approach (first introduced in [123]), each noiseless measurement frame was transformed into a 2D array. The reference data was added to this 2D array in the form of an additional column. Singular value decomposition was then applied to the 2D array before fitting the difference of the first two resultant singular values for each singular value decomposition to the bladder volume data. In both bladder volume estimation methods, different tests were performed with bladder volumes between approximately 10-410 ml, at SNRs of {40, 80, 120, ∞} and on urine conductivities from 1.5 to 5 conductivity units (with algorithms trained/calibrated at 2 units when studying the influence of urine conductivity).

In this work, measurement frames without a reference will be used as observations in the dataset, as used in the neural network bladder volume estimation approach in Schlebusch et al. [124]. References are used in EIT difference images to help correct for modelling mismatches and noise sources that are common between the reference and the observed data [99]. Using the raw EIT voltage data, image reconstruction and the modelling of parameters required are avoided. Also, reference data that does not share the same noise as the observed data could potentially lead to increased error in the input data for the classifiers. Thus, measurement frames without a reference correction are used as observations in the datasets.

Similar to Chapter 4, the datasets in this work will use urine conductivities with the units of Siemens per meter (S/m). The datasets will also vary in terms of different bladder volumes, urine conductivities and SNR levels. These datasets will increase in difficulty from Test-Case (TC) 1 to 3 by the addition of varying each condition.

The next three sections discuss the three test-cases considered in this chapter.

5.1.2 Dataset Properties for Test-Case 1: Investigating the Effect of Varying Bladder Volume on Voltage-Based Bladder State Classification

Similar to the test-case developed in Section 4.1.2 for pixel-wise image-based classification, TC1 in this chapter comprises of testing on unseen bladder volumes while holding the values of noise (measured by the SNR level) and urine conductivity constant. Twenty-six bladder volumes are used in the range of {40, 420} ml with an equal number of bladder volumes per class. Each observation in the dataset is a measurement frame. In order to increase the dataset

size to a number greater than the number of input features, 120 observations per bladder volume are used. Each of the 120 observations vary from each other by additive random Gaussian noise. In all cases, the input to the classifier is the raw EIT voltage frame data and each feature is a location in the measurement frame (also called a channel). Figure 5.1 illustrates the relation of channel to the injection and measurement protocols. Specifically, each channel refers to data from one injection pair and one measurement pair. The protocol includes a Skip of 4, as outlined in Section 3.6.1. Twenty-nine measurements are collected for each injection pattern when the injection electrode measurements are excluded. For a 32-electrode system, there are 32 injection patterns in total leading to a measurement frame of 928 channels. A non-rotational measurement scheme is used that involves measurements always starting at either Electrode 1, or Electrode 2 for the first injection pattern.

For initial analysis of classifying bladder volumes into not-full and full classes, the classification algorithms are trained and tested at specific SNR levels, since noiseless data is not possible to achieve in a real-world scenario. Thus, three datasets with the three different SNR levels of {40, 60, 80} dB are trained and tested upon.

Having obtained more insight into how the data collection functions and the terminology used in this section, the data from the TC1 datasets can be analysed. Figure 5.2 shows example observations for three bladder volumes of {40, 300, 420} ml from the 60 dB SNR TC1 dataset.

From Figure 5.2, the example observations for the three bladder volumes overlap greatly. However, there are small voltage differences between the waveforms at different measurement locations, i.e., at different channels. The voltage differences are particularly noticeable between the ranges of the {280, 500} channels and the {800, 928} channels. These locations include voltage differences at measurements near the injection electrodes for each injection pattern, as well as for measurements away from the injection electrodes. These voltage differences can be better seen in Figure 5.3, a zoomed in version of Figure 5.2, for measurements in injection patterns at the anterior and posterior of the FEM.

This subsection has established datasets of raw EIT voltage data for classifying bladder volume into not-full and full classes and provided insights into how the classifier might use the data to classify the bladder fullness with varying bladder volumes in the datasets. In the next section, the datasets for analysing the effect of urine conductivity on bladder state classification are established.

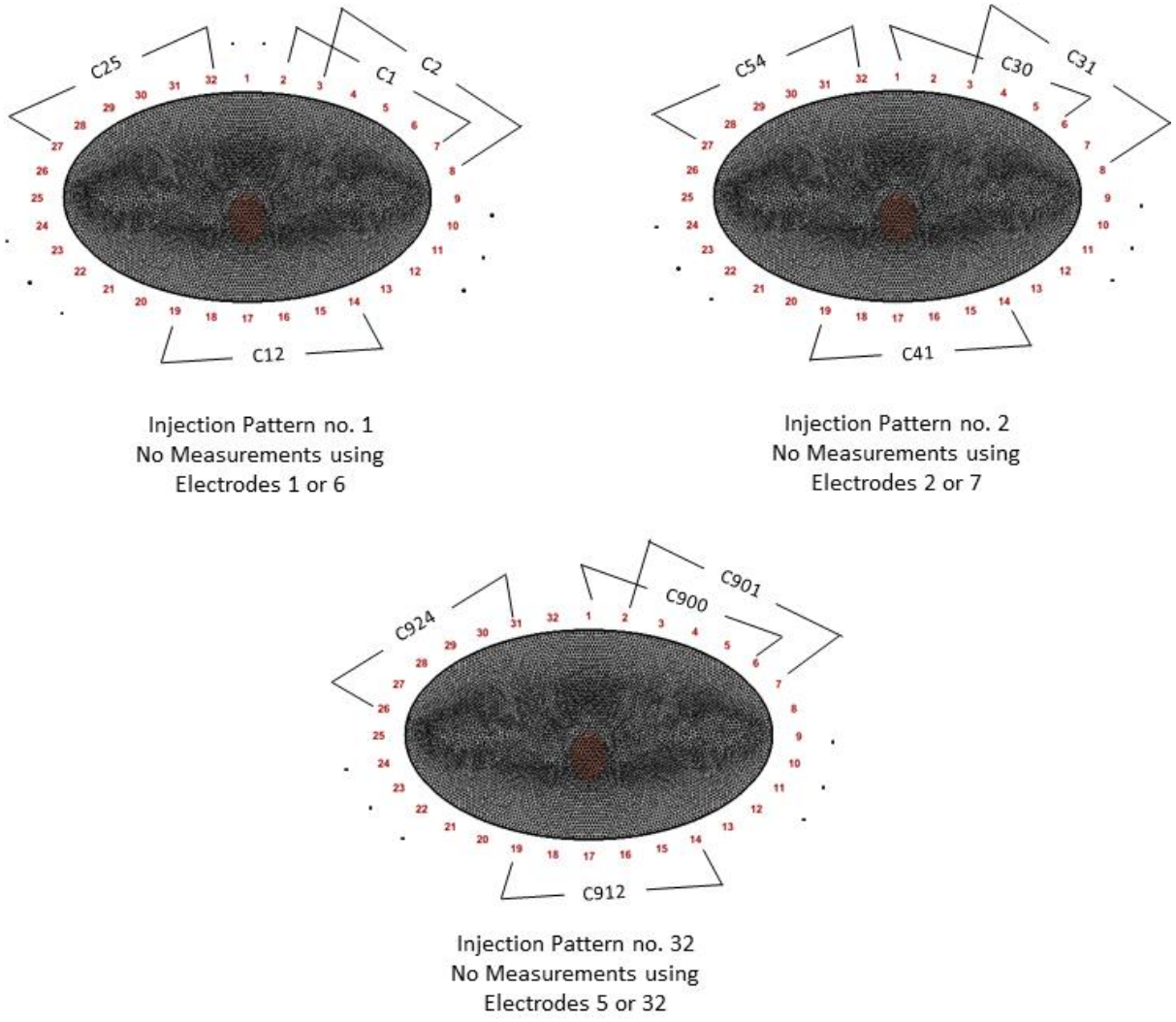

Figure 5.1: Example injection patterns and associated locations in the measurement frame, i.e., channels (abbreviated to 'C' in the diagram) from the data collection protocol using the 32-electrode EIT system outlined in Section 3.6.1. Three measurements are removed in each injection pattern as no measurements at the injection electrodes are used. This removal of measurements results in a measurement frame of 928 channels rather than 1024 channels. A non-rotational measurement scheme is used, which involves measurements always starting at either Electrode 1, or Electrode 2 for the first injection pattern.

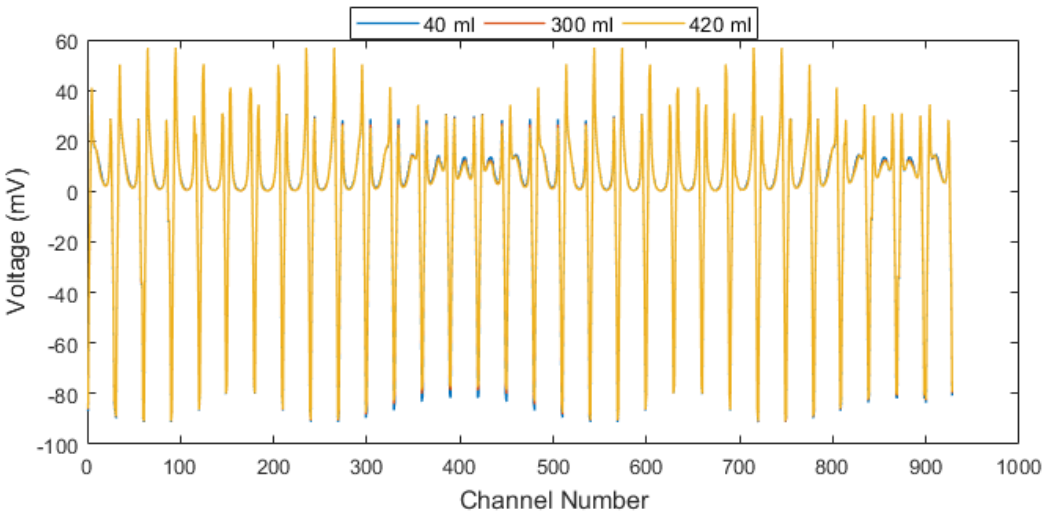

Figure 5.2: Example observations (measurement frames) in the 60 dB SNR TC1 dataset of noisy raw EIT voltage data for the bladder volumes {40, 300, 420} ml. Between the observation for each bladder volume, there is separation in terms of the voltage at distinct channels showing potential for the classifier to be able to separate the bladder volumes into the not-full and full classes.

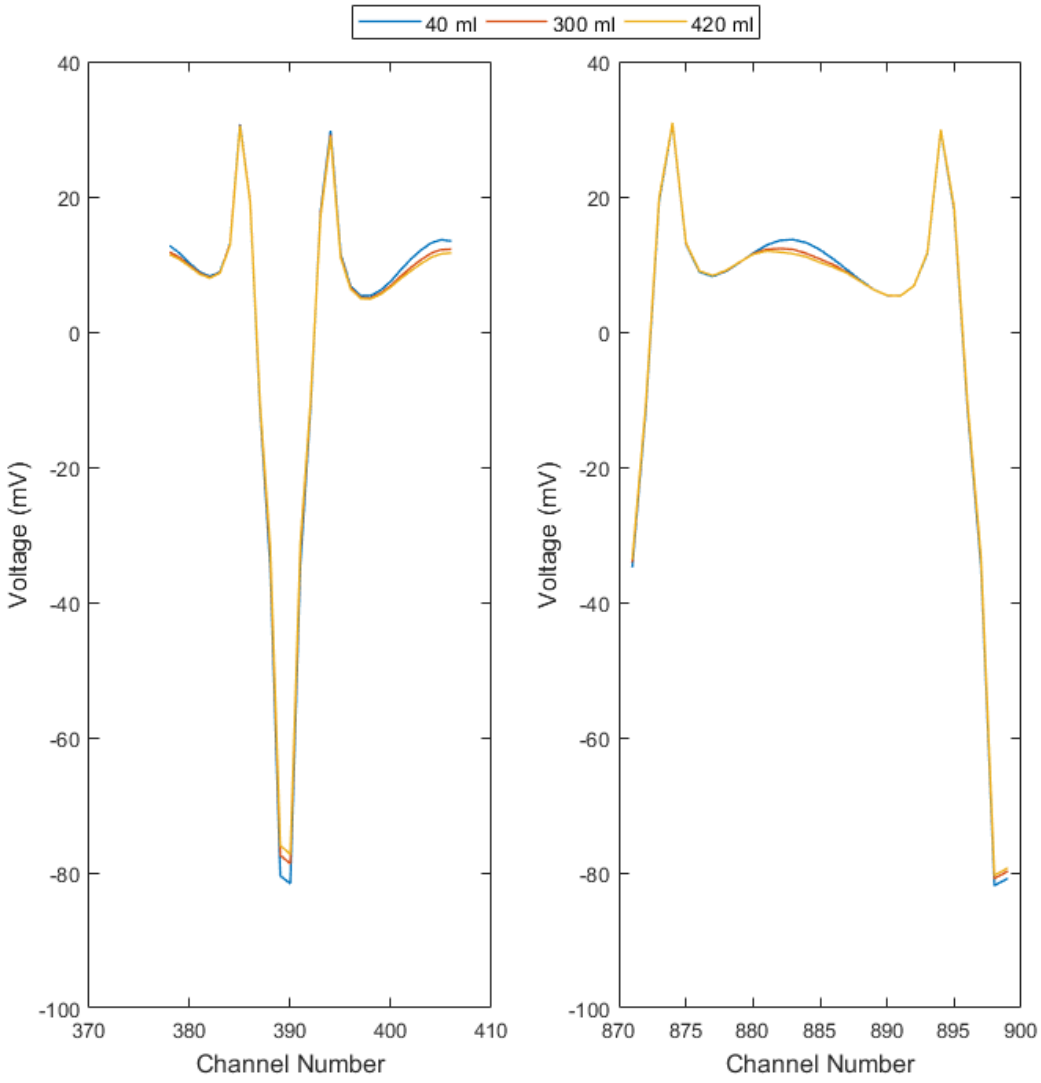

Figure 5.3: Measurements associated with two injection patterns from example frames in Figure 5.2: (left) measurements from an injection pattern at the anterior of the FEM (injection electrodes 14 and 19), near the bladder; (right) measurements from the position of the FEM (injection Electrodes 31 and 4). The voltage differences between the data for the three bladder volumes of {40, 300, 420} ml can be clearly seen at certain channels and may be used by the classifier to help classify the not-full and full classes.

5.1.3 Dataset Properties for Test-Case 2: Investigating the Effect of Varying Urine Conductivities on Voltage-Based Bladder State Classification

In this test-case, the effect of urine conductivity is examined by controlling the bladder volume and noise in the dataset. The dataset from TC1 is changed by adding more distinct observations per bladder volume. Specifically, twelve urine conductivities are used with ten observations each. These ten observations differ from each other by the added noise, similar to TC1 in Section 5.1.2. Thus, the total size of each dataset in TC2 is the same as in TC1, except that the datasets of TC2 have more complexity due to the varying urine conductivity. The twelve urine

conductivities ranged from 0.5 S/m to 3.25 S/m, inclusively. This range covers the range of expected urine conductivity values in humans, as previously discussed in Section 3.4.2.4. Figure 5.4 shows frames from the dataset for three different urine conductivities for a 300 ml bladder volume.

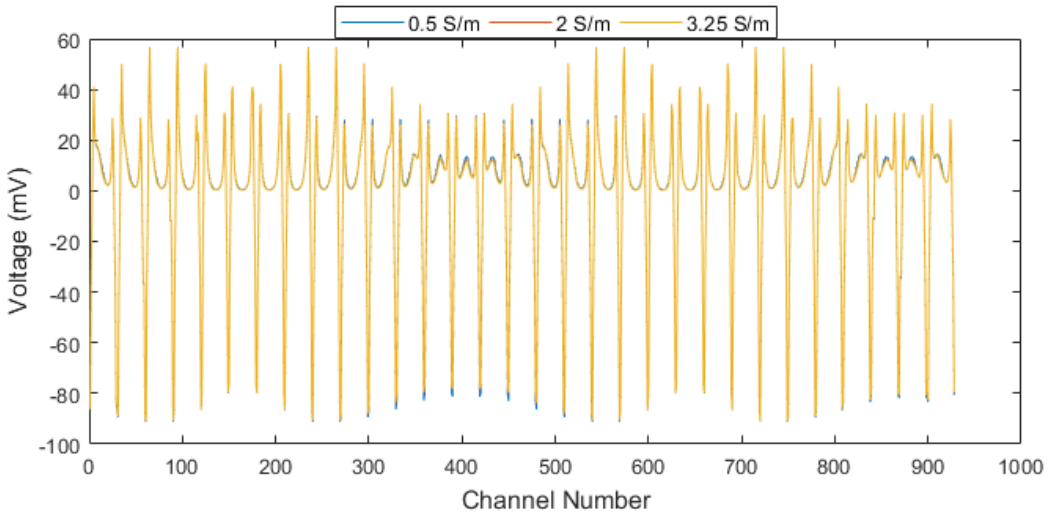

Figure 5.4: Example observations of noisy raw EIT voltage data for the urine conductivities of {0.5, 2, 3.25} S/m, with bladder volume of 300 ml and at 60 dB SNR. Between the observation for each urine conductivity, there is separation in terms of the voltage at distinct channels. The contrast of urine conductivity to the background tissues enables EIT measurements to record changes in urine conductivity and bladder volume, but the effect of different urine conductivities seems similar to that of bladder volume changes in Figure 5.2. The additional complexity of urine conductivity needs to be determined and handled sufficiently to minimise misclassifications in bladder state classification using raw EIT voltage data.

Similar to Figure 5.2 for varying bladder volumes, small voltage differences are evident at different channels throughout the frame in Figure 5.4. An examination of measurements from certain injection patterns is given in Figure 5.5. Comparing Figure 5.2 and Figure 5.3 to Figure 5.4 and Figure 5.5, there are similar trends to how the traces are affected due to varying bladder volumes and varying urine conductivity. For example, the percentage difference at channel 883 between the 40 ml and 420 ml voltage trace is found to be 16.70% in Figure 5.2. While the percentage difference at channel 883 between the 0.5 S/m and 3.25 S/m voltage trace for a 300 ml bladder volume is 12.95% in Figure 5.4. Although this is just an arbitrary example, the similarities in voltage differences due to varying bladder volumes and varying urine conductivities could make it challenging to isolate changes in bladder volume from changes in urine conductivity. This observation further motivates the use of powerful tools such as machine learning for discriminating unseen observations into classes.

Having prepared datasets for investigating both varying bladder volumes and urine conductivities, the datasets for varying noise will be formed in the next subsection.

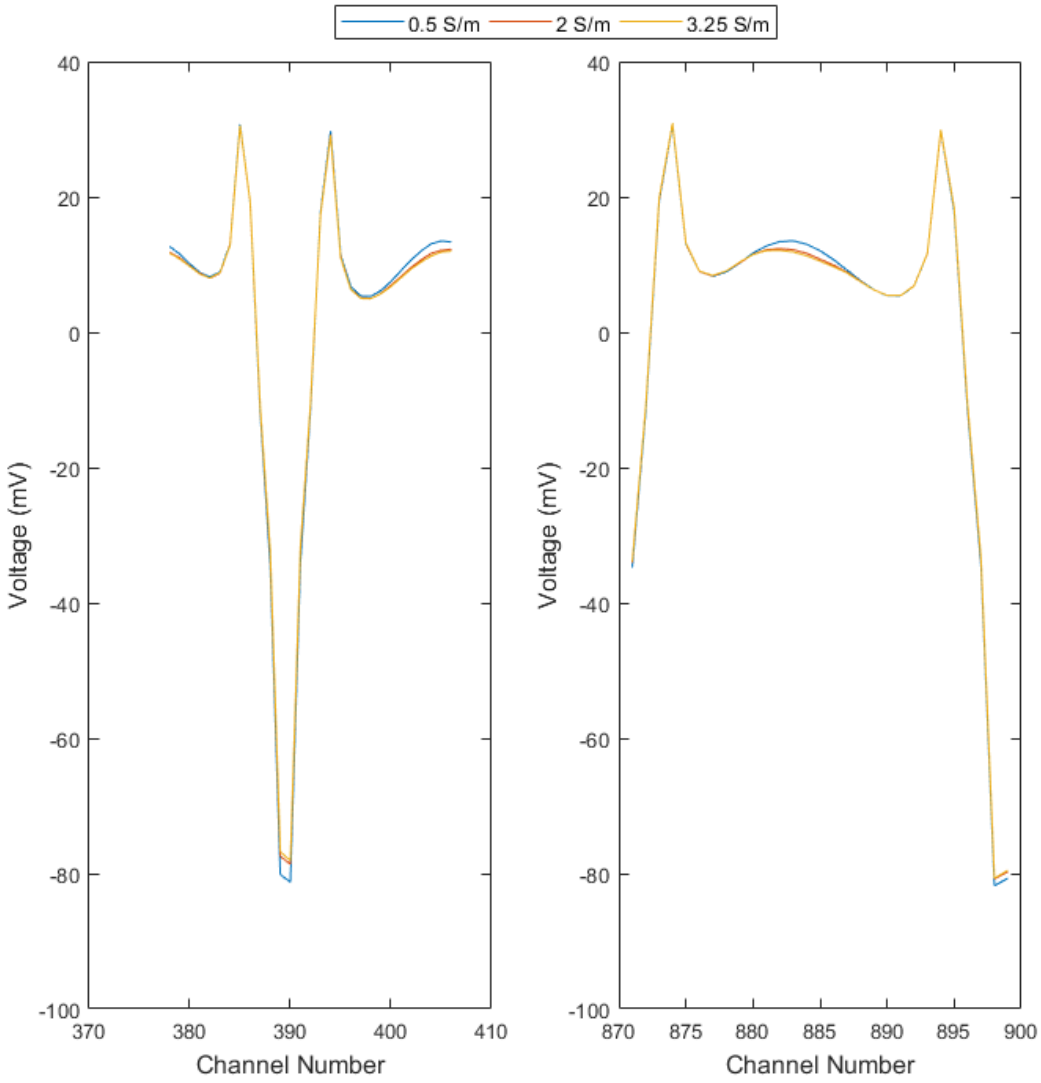

Figure 5.5: Measurement associated with two injection patterns of the example frames in Figure 5.4: (left) measurements from an injection pattern at the anterior of the FEM (Injection Electrodes 14 and 19), near the bladder; (right) measurements from the position of the FEM (Injection Electrodes 31 and 4). The voltage differences between the data for the three urine conductivities of {0.5, 2, 3.25} S/m at certain channels can be clearly seen and may affect the performance of the classifiers.

5.1.4 Dataset Properties for Test-Case 3: Investigating the Effect of Varying Noise on Voltage-Based Bladder State Classification

The final condition investigated for bladder state classification with raw EIT voltage data in this chapter is the effect of the added measurement frame noise. In both TC1 and TC2, common noise levels were used during training and testing. In these test-cases, multiple datasets were

formed to allow training and testing performance to be established on different noise levels. In this investigation, one dataset is formed with ten distinct SNR levels between {40, 76} dB, inclusively. These ten noise levels are applied to the ten noisy frames per bladder and per urine conductivity that were at a constant noise level in TC1 and TC2. Thus, the dataset size is the same as TC1 and TC2. Figure 5.6 shows the effect of three different SNR levels on the same bladder volume and urine conductivity. From Figure 5.6, it is evident that there is distortion in the voltage traces, but the distortion is less noticeable than the effect of changing bladder volume or urine conductivity as was shown in Figure 5.2 and Figure 5.4. The distortion can be better observed in isolated injection patterns as in Figure 5.7.

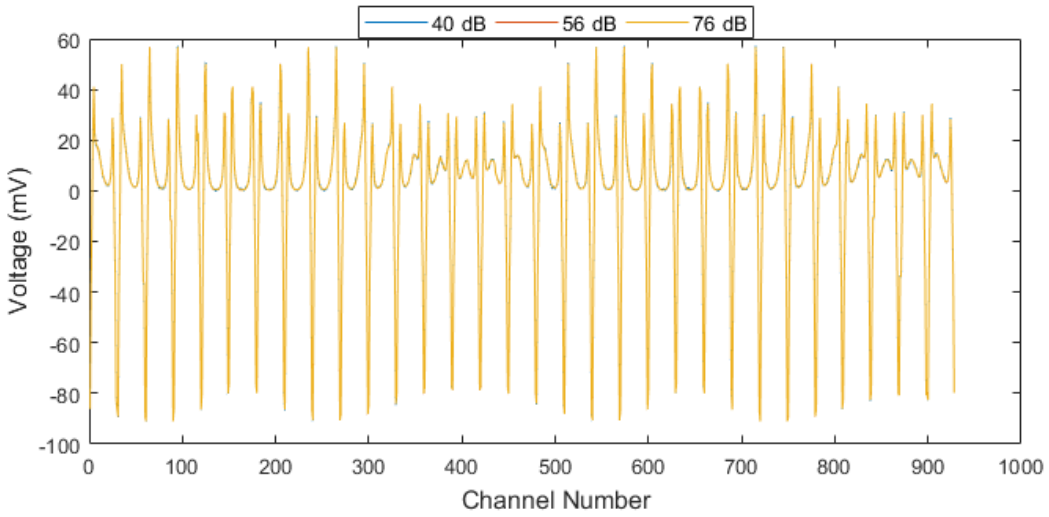

Figure 5.6: Example observations of different noise levels on raw EIT voltage data for the bladder volume of 300 ml and urine conductivity of 2 S/m. The added noise causes some distortion on the voltage traces, but the effect of added noise seems to be less problematic than the effect of different bladder volumes and urine conductivity on EIT measurement traces as given in Figure 5.1 and Figure 5.3.

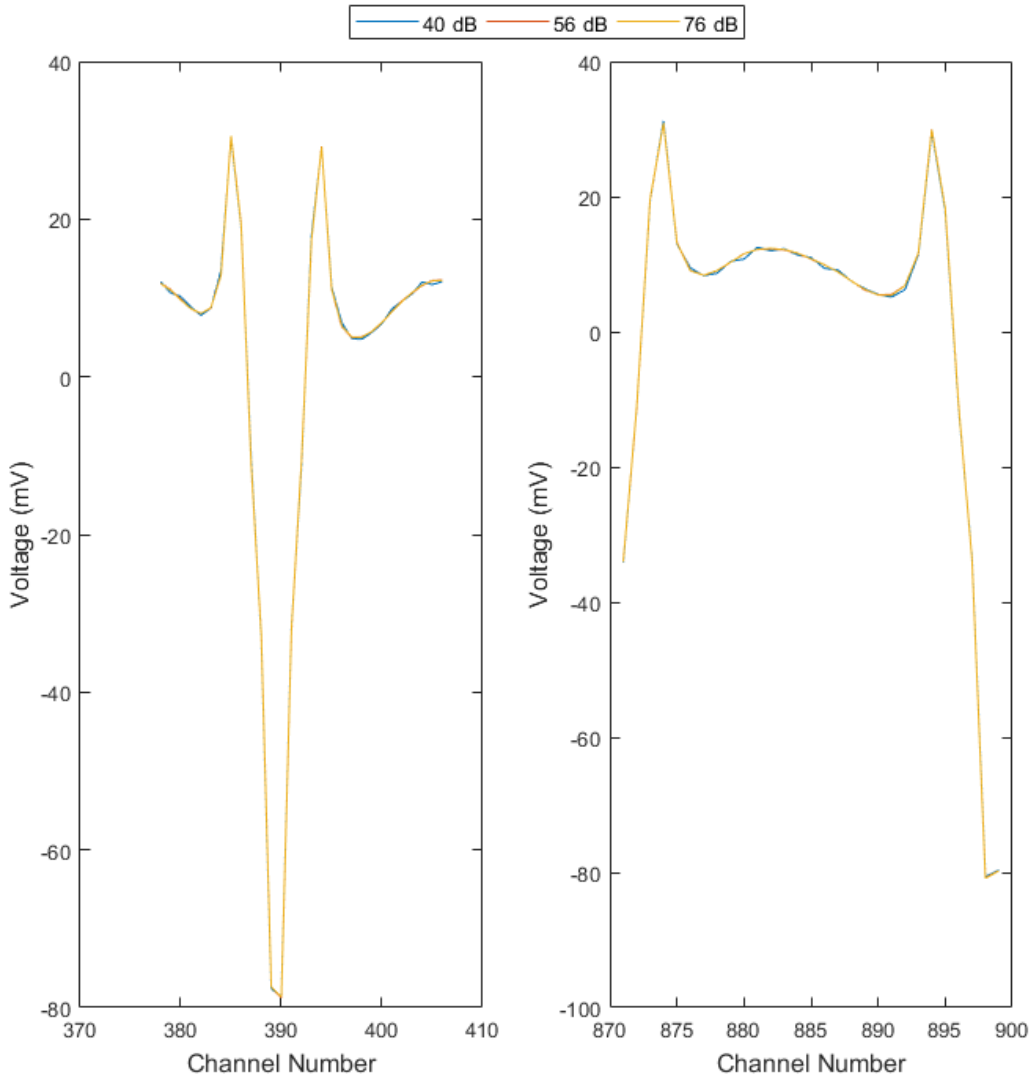

Figure 5.7: Measurements associated with two injection patterns from the example frames in Figure 5.6: (left) measurements from an injection pattern at the anterior of the FEM (Injection Electrodes 14 and 19), near the bladder; (right) measurements from the position of the FEM (Injection Electrodes 31 and 4). The distortion from the added noise is evident at certain channels and may affect the performance of the classifiers.

5.1.5 Dataset Properties for Realistic Test Scenarios

In this section, the two remaining test cases are described, both of which are more representative of a real-world scenario. First, a train-test situation is considered that has only observations and labels and does not isolate a condition. Second, a continual-monitoring test-case is performed that mimics testing the classifiers after deployment.

The dataset for training and testing consists of all 26 bladder volumes, 12 urine conductivities and 10 SNR levels previously used in TC3. Each observation differs by a combination of these three conditions. This test differs from TC3 in that no set of observations is excluded based on

one of the three conditions of bladder volume, urine conductivity or measurement frame noise. Thus, this test-case is called the 'Realistic Learning Test-Case' and is equivalent to the Realistic Learning Test-Case in Section 4.1.5 for image classification. Table 5.1 and Table 5.2 summarise the data set used in this test-case.

The second test-case in this section is another variant on the realistic scenario. Specifically, the classifier can be trained on the whole dataset after a sufficient testing performance has been obtained for deployment. This test-case is referred to as the CM test-case. To observe the effect of completely new data on the classifier trained with the full dataset, 6 unseen bladder volumes, 12 unseen urine conductivities, and 11 unseen SNRs are used to show the classifier functionality when evaluated on new data. The exact values of each condition are given in Table 5.1. This test-case is equivalent to the CM test-case described in Section 4.1.4 for image classification. Further details about how such monitoring might work in real life are provided in Section 4.1.4.

5.1.6 Overall Summary of the Datasets for each Test-Case

The main difference between the datasets in Section 4.1.2 to Section 4.1.5 in Chapter 4 and the datasets in Section 5.1.2 to Section 5.1.5 is the form of data (raw EIT voltage data or EIT image data), the processing (image reconstruction and time-difference subtraction instead of using the noisy observed raw EIT voltage data frame), and the number of features per observations (812 pixels instead of 928 voltages). In both Section 4.1 and Section 5.1, the same conditions and the same values of each condition are used for consistency of approach. Thus, Table 4.1 and Table 4.2 summarise the image datasets for each test-case, while similar tables are provided in this section for Chapter 5 as Table 5.1 and Table 5.2. Specifically, Table 5.1 summarises the overall makeup of the datasets in each test-case and Table 5.2 summarises the number of observations for each condition in each test-case.

Table 5.1: Characteristics of each condition the datasets for each test-case used in Chapter 5.

Test case	SNRs	Bladder Volumes	Urine Conductivity
TC1	{40, 60, 80} dB	Not-Full: {40 + 20*n} ml Full: {300 + 10*n} ml where n = 0, 1, 2, 3, …, 12	2 S/m
TC2	{40, 60, 80} dB	Not-Full: {40 + 20*n} ml Full: {300 + 10*n} ml where n = 0, 1, 2, 3, …, 12	{0.5 + 0.25*p} S/m, where p = 0, 1, 2, 3, …, 11
TC3 & Realistic Learning	{40 + 4*a} dB where a = 1, 2, 3, …, 9	Not-Full: {40 + 20*n} ml Full: {300 + 10*n} ml where n = 0, 1, 2, 3, …, 12	{0.5 + 0.25*p} S/m, where p = 0, 1, 2, 3, …, 11
CM	{38, 42, 46, … 78} dB	Not-Full: {20, 190, 290} Full: {305, 365, 430}	{0.63 + 0.25*p, 3.33} where p = 0, 1, 2, 3, …, 10

Table 5.2: Number of datasets, observations and observations per condition in each test-case (TC). For brevity, bladder volume is represented by BV and urine conductivity by UC in the table.

Test-case	Number of Datasets	Number of Observations per Dataset	Number of Observations per BV	Number of Observations per single BV and UC
TC1	3	3120	120	120
TC2	3	3120	120	10
TC3 & Realistic Learning	1	3120	120	10
CM	1	792	72	1

5.1.7 Structuring of the EIT Measurement Data in the Dataset for Machine Learning Classification

For bladder state classification using raw EIT voltage data, single noisy measurement frames are used as observations for the classifiers to both train and test. No structural transformation is applied to data before any additional pre-processing for classification (as discussed in Section 5.2). The structure of each observation in the dataset is a one-dimensional frame with length of 928 voltages. Similar to the datasets for the image classification work in Section 4.1, each

observation has a label associating the observation with not-full or full bladder states for supervised machine learning.

5.2 Machine Learning Methodology: Classifiers, Architectures, Pre-processing and Evaluation Metrics

For bladder estimation using raw EIT voltage data, machine learning in the form of neural networks has been previously performed by Schlebusch [115] and Schlebusch et al. [124] to estimate the exact bladder volume. The five-layer neural network used had 208 input neurons that corresponded to the number of voltage channels from a sixteen-electrode system, when the measurements from the injection electrodes were removed. The neural network had one output neuron for the bladder volume estimation. The neural network was trained with noiseless data and the architecture of a 70% train set, 15% validation set and 15% test set was used. Testing was performed in simulation at bladder volumes of between approximately 10-410 ml, urine conductivities from 1.5 to 5 conductivity units (with algorithms trained/calibrated at 2 units when studying the influence of urine conductivity), and SNRs of $\{40, 80, 120, \infty\}$. The neural network showed promise for bladder volume estimation on noiseless data. However, Schlebusch et al. [124] reported that the noiseless data trained neural network suffered poor performance when estimating outside or around the training data borders on noisy data.

Estimating the exact bladder volume is not necessary for bladder monitoring applications like an

EIT-based enuresis alarm. Instead, identification of a full bladder is key for an alert. Therefore, this chapter builds upon the bladder state classification work in Chapter 4 by investigating raw EIT voltage data as input for bladder state classification. Specifically, the classifiers and their design are the same as employed in Section 4.2, enabling comparison across results from pixel-based image classification (Chapter 4) and voltage-based classification (this chapter).

Also, the train-test architectures employed in Section 4.3.1 are the same as those used in Section 5.3 to classify the bladder states of not-full and full using the raw EIT voltage data. These train-test architectures (LOCOCV, stratified L2COCV and 5-times repeated stratified 10-fold cross-validation) are suited for the dataset sizes from Section 4.1 and Section 5.1, as discussed in detail in Section 4.3.1.

The standardisation pre-processing required for the classifiers that was outlined in Section 4.3.2 is also used in Section 5.3 and Section 5.4. To assess fairly the performance of the classifiers,

the evaluation metrics for classification as outlined in Section 4.4 are also employed in Section 5.3 and Section 5.4.

Having established the methodology for classification of bladder state classification with raw EIT voltage data as input, the impact of the conditions of bladder volume, urine conductivity and noise on classification can now be studied.

5.3 Investigating the Effect of Bladder Volume, Urine Conductivity, and Noise on Raw EIT Voltage Data Classification

In this section, the effect of the conditions: bladder volume (TC1), urine conductivity (TC2) and measurement frame noise (TC3) are determined and analysed individually to determine their impact on bladder state classification using raw EIT voltage data.

5.3.1 Test-Case 1: Investigating the Effect of Varying Bladder Volumes on Raw EIT Voltage Data Bladder State Classification

The stratified L2COCV train-test architecture was used to determine the performance of classifying unseen bladder volumes with an equal number of classes in both the train and test sets, similar to Section 4.5.1. The TC1 datasets outlined in Section 5.1.2 and Table 5.1 and Table 5.2 were used that had a urine conductivity of 2 S/m. The performance metrics at the three SNR levels of {40, 60, 80} dB SNR are reported in Table 5.3.

Table 5.3: Average performance of the classifiers for classifying unseen bladder volumes on three different noisy voltage-based datasets.

SNR	Classifier	Accuracy (%)	Sensitivity (%)	Specificity (%)
80 dB	KNN	96.45 ± 12.88	100.00 ± 0.00	92.90 ± 25.76
	Linear SVM	96.45 ± 12.88	100.00 ± 0.00	92.90 ± 25.76
60 dB	KNN	98.01 ± 7.16	99.97 ± 0.17	96.05 ± 14.33
	Linear SVM	97.92 ± 7.55	100.00 ± 0.00	95.84 ± 15.10
40 dB	KNN	96.43 ± 10.77	99.44 ± 1.85	93.42 ± 21.63
	Linear SVM	96.84 ± 7.74	97.76 ± 7.15	95.92 ± 14.39

The minimum accuracy observed from Table 5.3 was 96.43%, indicating that bladder state classification is possible based on voltage data. Unexpectedly, the second minimum accuracy occurred on the highest SNR (least noisy) dataset for both KNN and linear SVM classifiers. Analysis of the misclassifications from Figure 5.8 shows that the majority of 280 ml bladder

volume voltages were misclassified. Further, twelve of the thirteen combinations of not-full and full bladder volumes that had 280 ml as a not-full bladder volume in the test set were classified with an accuracy of 50% by both classifiers, a sensitivity of 100% (correctly classed the full bladder volumes), and a specificity of 0%. The only test set where the observations for the 280 ml bladder volume were not all misclassified (and in fact each observation in the test set were all correctly classified) was for the test set with the observations for the 280 ml and 300 ml bladder volumes.

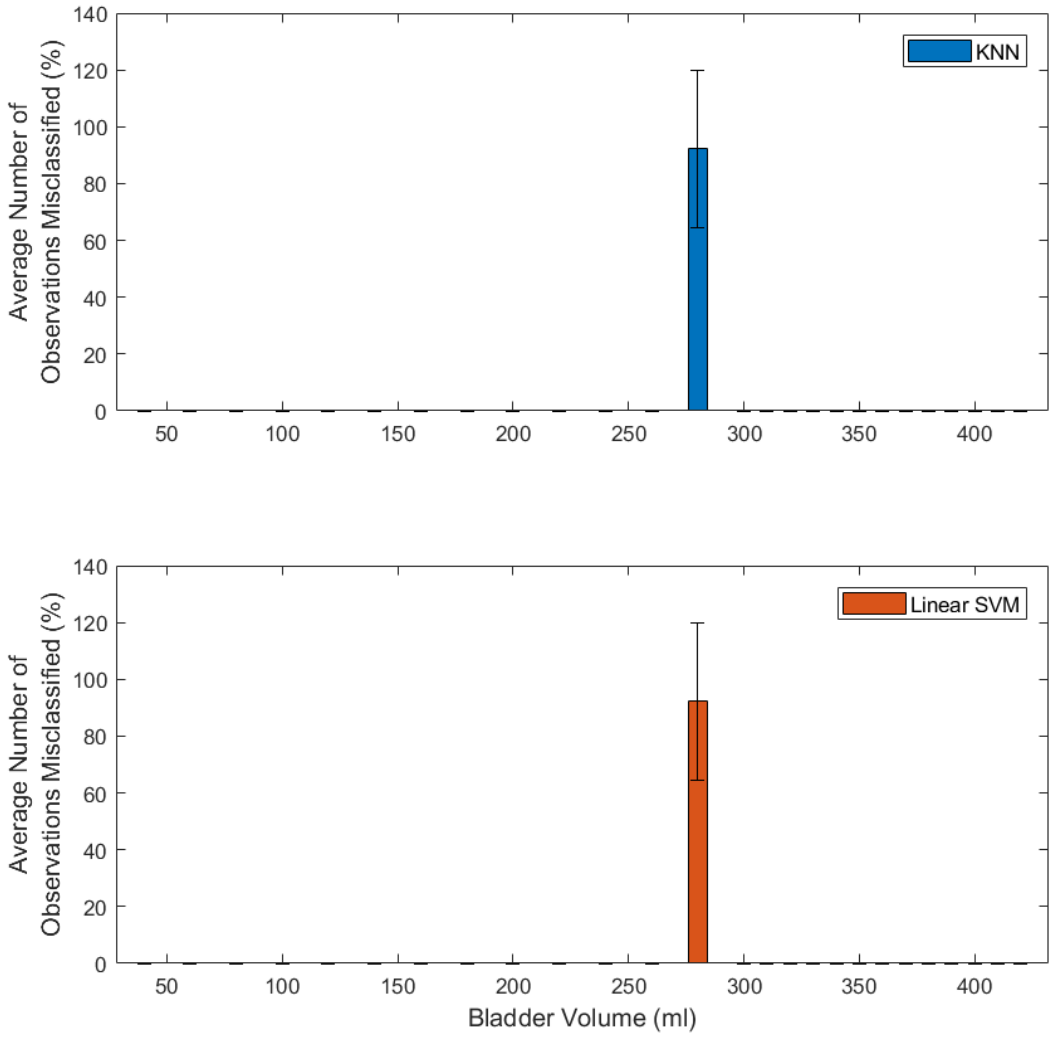

Figure 5.8: The misclassifications per bladder volume of the classifiers on the 80 dB TC1 dataset. The KNN and linear SVM classifiers both misclassify only observations from the 280 ml bladder volume.

To explain this result, a more detailed analysis of the dataset and the train-test architecture design was completed. The largest gap between the not-full and the full labels occurs when observations from the 280 ml bladder volume are excluded. This result is most noticeable in the 80 dB SNR dataset as shown in Figure 5.9, where the observations per bladder are clustered

together due to the low noise in the dataset. Using linear SVM as an example, the linear decision boundary should be between the observations for the 260 ml bladder volume and the next full bladder volume in the training set, which is either the 300 ml or the 310 ml bladder volume, depending on the train-test run. The bladder volumes in each training set are due to the stratified L2COCV train-test architecture used and outlined in Section 4.3.1. Thus, the decision boundary can occur near where the observations for the 280 ml bladder volume are located. If the observations for the 280 ml bladder volume are on the wrong side of the decision boundary, this can lead to misclassification of these observations and can explain why specifically the 280 ml bladder volume is misclassified so frequently by the classifiers in TC1.

As to why fewer of the observations for the 280 ml are misclassified for the noisier data, the higher amount of noise could provide more variation between the observations in the noisier datasets; which in turn could better spread datapoints in the not-full and full regions, as illustrated in Figure 5.9. Thus, some additive random Gaussian noise may help in better fitting the decision boundary when there are large gaps between not-full and full bladder volumes as in the TC1 datasets.

To further validate the effect of the 280 ml bladder volume observations on the 80 dB SNR dataset, the results from test sets that had 280 ml were removed (as in Table 5.3) and the accuracy of each classifier on the difference noisy datasets was re-evaluated. It was found that the accuracy for the KNN classifier on the {80, 60, 40} dB SNR datasets was 100 ± 0%, 99.98 ± 0.09%, and 99.50 ± 1.14% respectively. The accuracy for the linear SVM classifier on the {80, 60, 40} dB SNR datasets was 100 ± 0%, 100 ± 0%, 98.79 ± 3.71%, respectively. These results show the expected trend of the performance of the classifiers decreasing as more noise is present in the train-test datasets.

The misclassifications of observations per bladder volume for the 40 dB SNR TC1 dataset is given in Figure 5.10. Both Figure 5.8 and Figure 5.10 show the expected trend for a bladder state classifier, in which the accuracy degrades around the bladder separation volume of 300 ml as previously demonstrated in Section 4.5.1 of Chapter 4.

To further determine whether the performance achieved in Table 5.3 occurs for training and testing just on one urine conductivity, or all urine conductivities, the TC1 methodology was applied to the 40 dB SNR TC1 dataset (similar to Section 4.5.1 in Chapter 4) at the twelve urine conductivities that are used in TC2. The results are given in Figure 5.10. The findings are similar to those from Section 4.5.1 and Section 4.5.2 of Chapter 4. Specifically, the

performance of the classifiers decreases as the contrast between urine conductivity and the background conductivity of the FEM decreases. The exact effect of urine conductivity in bladder state classification on raw EIT voltage data is analysed in the next section.

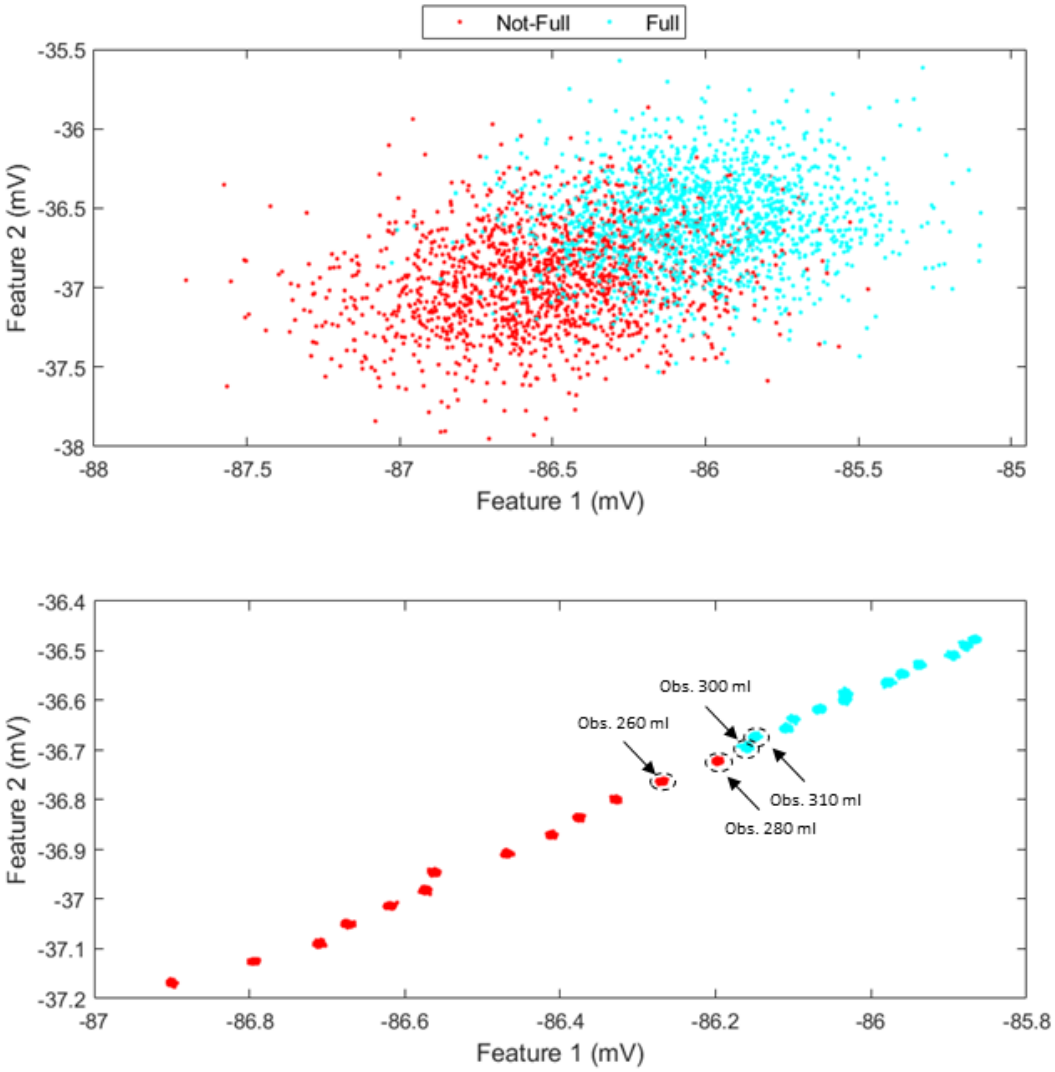

Figure 5.9: Plots of feature 2 as a function of feature 1 in the 40 dB SNR (top graph) and the 80 dB SNR (bottom graph) TC1 datasets. For the 80 dB SNR TC1 dataset, the clustered observations for the {260, 280, 300, 310} ml bladder volumes are also labelled with 'Obs.' (for observation) and the bladder volume in millilitres. While a separating line may be placed by eye more easily in the 80 dB SNR dataset plot than the 40 dB SNR dataset plot, the exact placement of this line may lead to misclassifications if certain observations for a bladder volume near the bladder separation volume of 300 ml are excluded from the training data, e.g., 280 ml. The datapoints for both not-full and full classes in the 40 dB dataset are more interspersed than in the 80 dB dataset, which may have contributed to the better fitting of the classifiers on average and overall better performance of the classifiers on the noisy datasets in TC1 as given in Table 5.3.

Lastly, to verify that the results from Table 5.3 are not just confined to the bladder separation volume of 300 ml, the TC1 methodology with a urine conductivity of 2 S/m was repeated with

a bladder separation of 360 ml, i.e., each bladder volume in the dataset was shifted by 60 ml. With a 360 ml bladder separation volume, the average performance metrics of both classifiers agree within 0%, 1.6% and 1% of the results in Table 5.3 for the 80 dB, 60 dB and 40 dB SNR TC1 datasets, respectively.

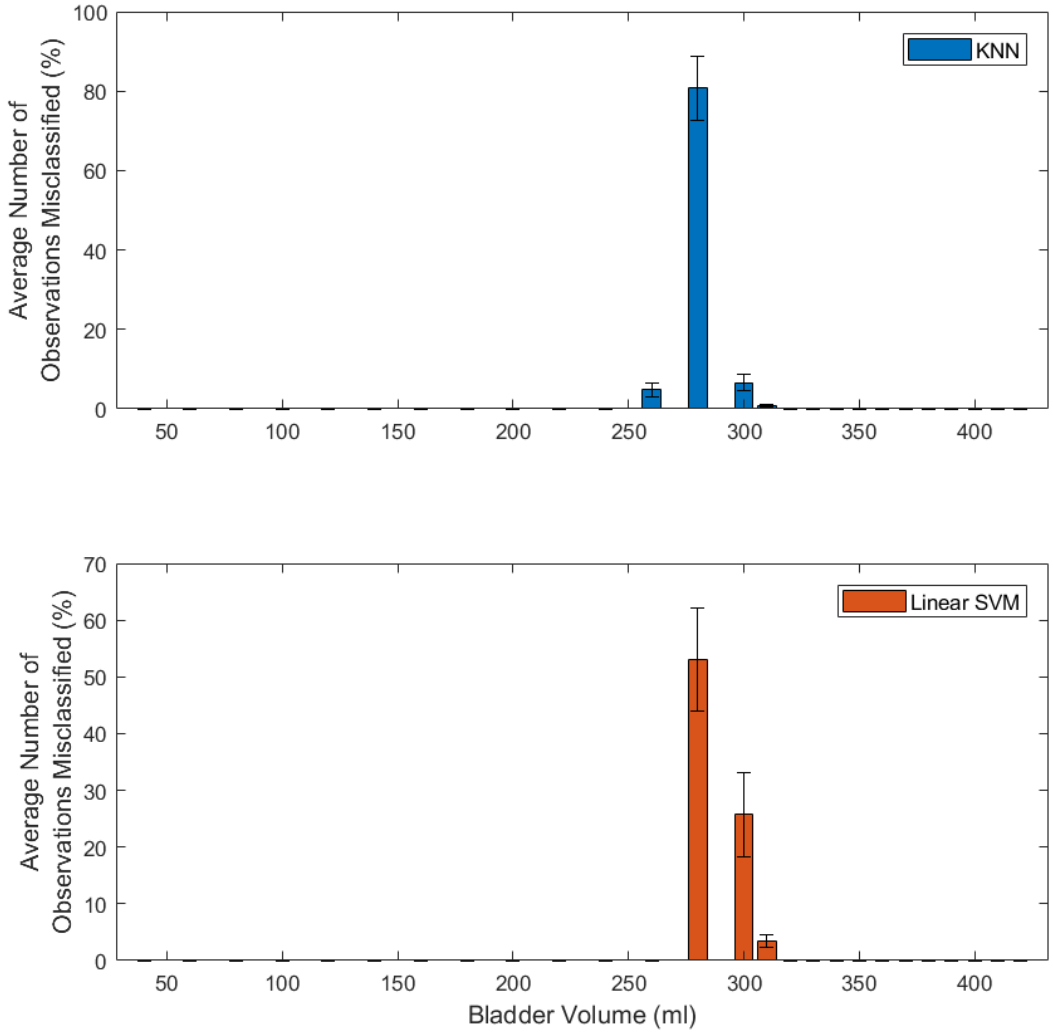

Figure 5.10: The misclassifications per bladder volume of the classifiers on the 40 dB TC1 dataset. The KNN and linear SVM classifiers both misclassify observations around the 300 ml bladder separation volume, as is expected.

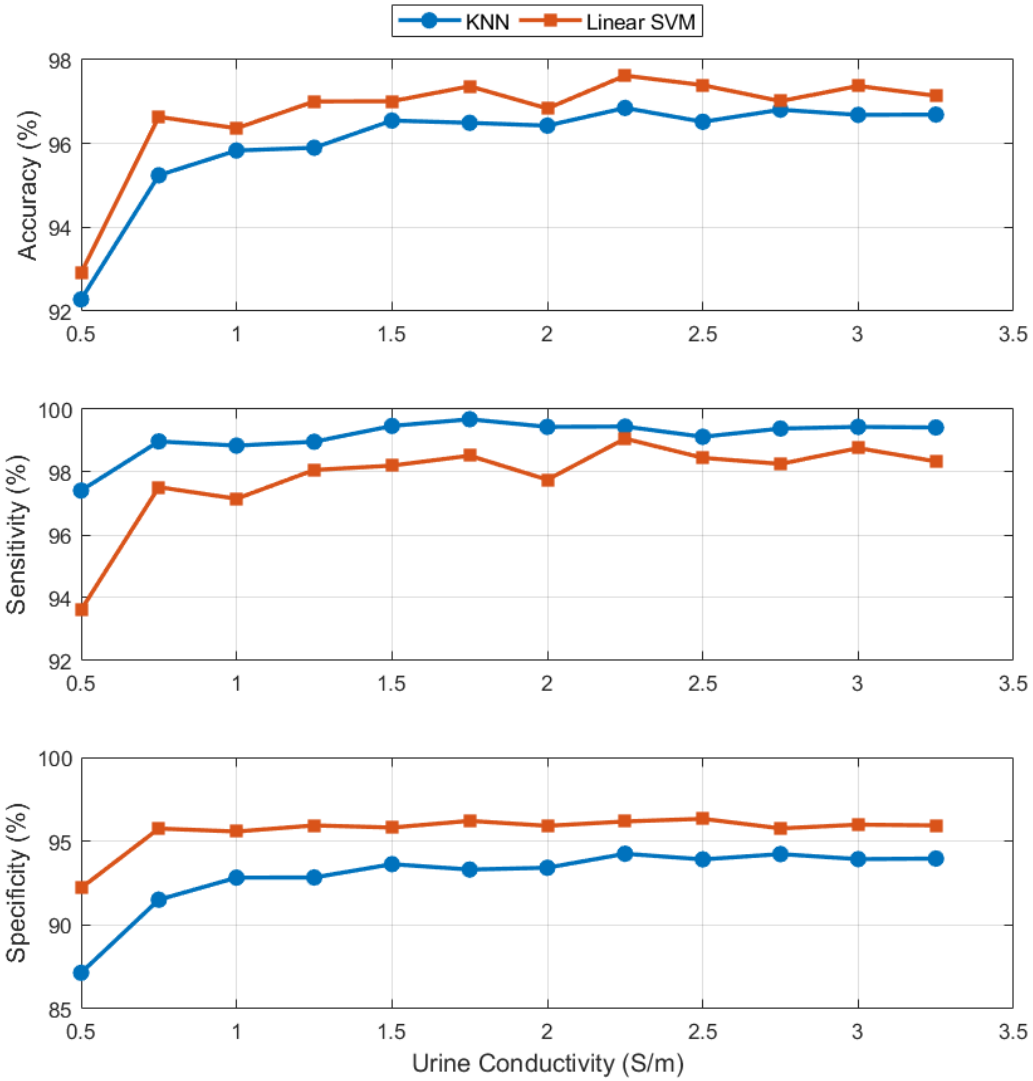

Figure 5.11: Average performance of the classifiers for varying bladder volumes when trained and tested on 40 dB SNR datasets with different urine conductivities between the datasets. The accuracies for the classifiers at the different urine conductivities is greater than 90%, with a drop off in performance as the contrast between urine conductivity and the background conductivity of the FEM decreases (i.e., as the urine conductivity decreases).

5.3.2 Test-Case 2: Investigating the Effect of Varying Urine Conductivities on Raw EIT Voltage Data Bladder State Classification

In this section, the effect of varying the urine conductivity on bladder state classification with raw EIT voltage data is investigated. Using the datasets described in Section 5.1.3 and summarised in Table 5.1 and Table 5.2, the LOCOCV was used to test on the observations associated with each urine conductivity in the dataset. The classifiers were trained on SNR levels of {40, 60, 80} dB, similar to TC1. The results are given in Table 5.4. With unseen urine conductivities and datasets with high noise, it is still possible to classify not-full and full classes

with an average accuracy over 77%. Both classifiers demonstrated a drop in performance when classifying observations with lower urine conductivities in the dataset as seen in Figure 5.12. These observations with lower urine conductivities have a reduced contrast between the urine conductivity to the background conductivity. For KNN, observations with a urine conductivity of 0.5 S/m were classified with an accuracy of circa 50%. These trends along with the trends of the sensitivity and specificity are similar to those found in the image classification results in Section 4.5.2.

Table 5.4: Average performance of the classifiers for classifying unseen urine conductivities on three different noisy voltage-based datasets.

SNR	Classifier	Accuracy (%)	Sensitivity (%)	Specificity (%)
80 dB	KNN	86.70 ± 16.58	75.96 ± 34.07	97.44 ± 3.79
	Linear SVM	99.33 ± 2.33	98.65 ± 4.66	100.00 ± 0.00
60 dB	KNN	86.92 ± 17.29	78.78 ± 34.74	95.06 ± 3.30
	Linear SVM	95.96 ± 10.03	93.40 ± 20.46	98.53 ± 1.75
40 dB	KNN	77.79 ± 15.91	69.55 ± 40.65	86.03 ± 10.59
	Linear SVM	83.49 ± 9.55	83.46 ± 22.64	83.53 ± 6.51

To potentially explain the trends associated with the sensitivity and specificity for the raw EIT voltage data, more analysis is needed for the 928 individual voltage channels of the measurement frames than in the image data. The images can be more easily explained in terms of the two main components of pixel intensity and spatial information. Such compact representation of data is not possible with the raw EIT voltage data. However, each voltage channel has one single voltage value for each observation and each observation can be further summarised by using a descriptive statistic, such as the mean. Then, each of the mean values of the observations can be grouped together in terms of their respective bladder volume and urine conductivity. This grouping is visualised in Figure 5.13 in order to allow viewing of potential decision rules in 2D for decision boundaries based on the 928 features.

A hypothetical decision rule is considered to demonstrate a possible reason why the sensitivity is reduced for low urine conductivities. For instance, a decision rule can be chosen where all values greater than 17.81 mV (the approximate midpoint of the maximum and minimum mean observation value in the dataset) are classed as not-full, while all equal or below 17.81 mV are classed as full. With this decision rule, all observations for each urine conductivity would be split into two categories of not-full and full (whether correct or not) except for the observations

with the urine conductivities of 0.5 S/m and 0.75 S/m. The mean values of observations with the urine conductivities of 0.5 S/m and 0.75 S/m do not cross the 17.81 mV separation line, so they are all classed as not-full. Thus, this result matches the findings from Figure 5.12. It is also possible to see that not-full bladder volumes around 200-280 ml would be misclassified by this decision rule and would lead to a decrease in specificity as the urine conductivity increases; this effect is seen primarily for the KNN classifier in Figure 5.12.

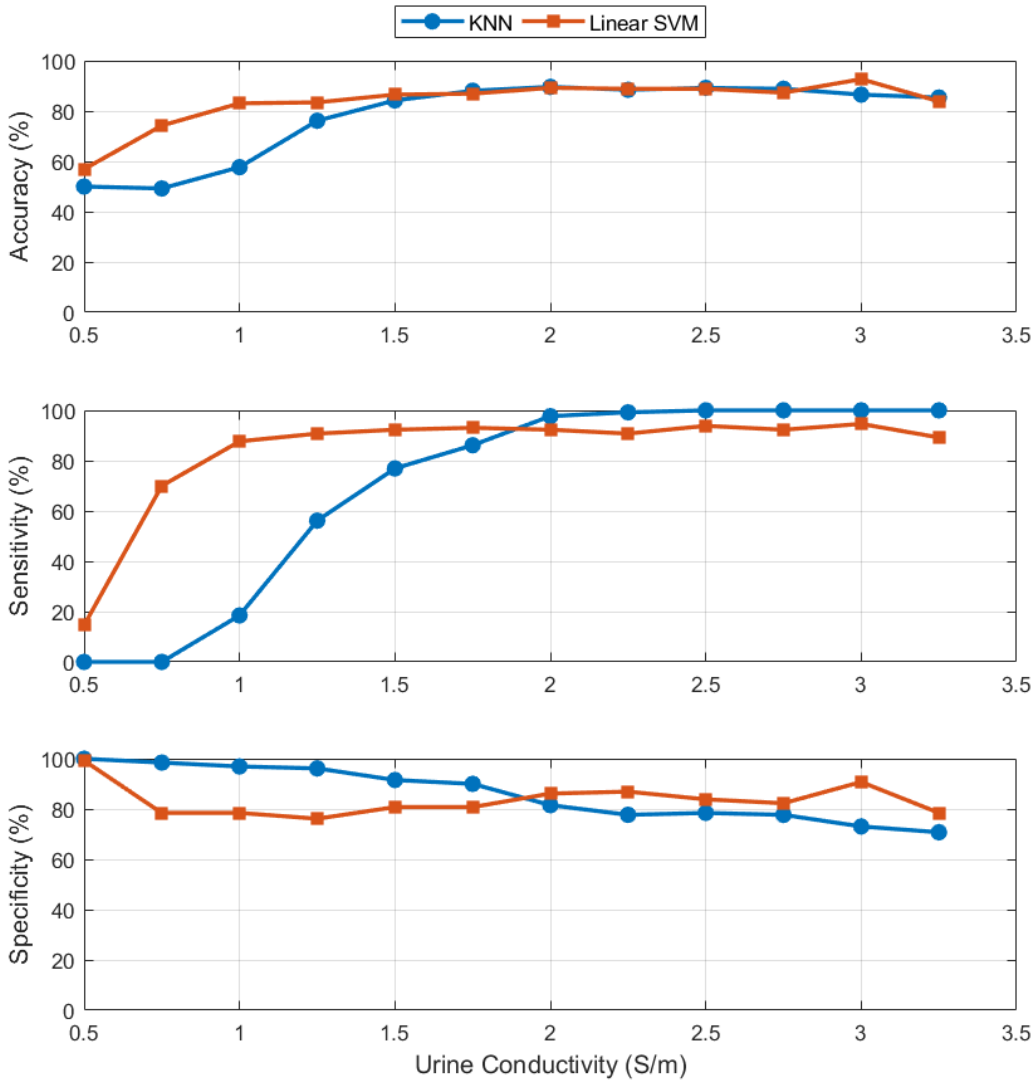

Figure 5.12: Average performance of the classifiers for varying urine conductivities when trained and tested on the 40 dB SNR dataset. The performance of the classifiers in classifying accurately not-full and full bladder volumes using raw EIT voltage data degrades as the contrast between urine conductivity and the background conductivity of the FEM decreases.

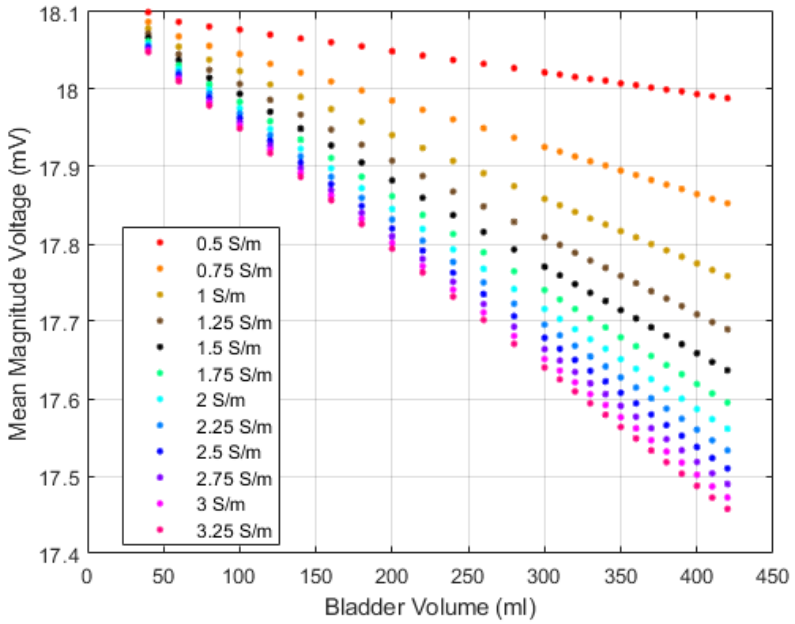

Figure 5.13: Plot of the mean magnitude voltage of each observation in the dataset as a function of bladder volume, presented for the purpose of hypothesising how the decision rules of the classifiers is formed for the 928 feature binary classification 40 dB TC2 dataset. Using a hypothetical decision rule of observations with a mean magnitude voltage greater than 17.81 mV as not-full and observations with a mean magnitude voltage less than or equal to 17.81 mV, it is possible to see how low urine conductivity observations could have a lower sensitivity when classified into not-full and full bladder states. The near zero sensitivity for observations with urine conductivities of 0.5 S/m or 0.75 S/m would be possible as none of the mean values of the observations for these urine conductivities cross the decision boundary. This finding would result in all observations being misclassified as not-full and thus, having a high-rate of false negative classifications.

In this subsection, the effect of urine conductivity was investigated. Findings suggest that it is important to include a range of urine conductivities in the training set in order to have a sufficiently acceptable overall classification performance. In the next subsection, the final condition of the added noise is investigated.

5.3.3 Test-Case 3: Investigating the Effect of Varying Noise on Raw EIT Voltage Data Bladder State Classification

In this section, the effect of varying levels of noise on bladder state classification with raw EIT voltage data is investigated. Using the TC3 dataset designed in Section 5.1.4 and summarised in Table 5.1 and Table 5.2 that had ten different levels of noise specified in terms of SNR, the classifiers were trained and tested on the data using the LOCOCV train-test architecture. The overall performance results are shown in Table 5.5 and the performance of the classifier at each tested SNR is given in Figure 5.14.

Table 5.5: Average performance of the classifiers for classifying bladder fullness with unseen SNR levels.

Classifier	Accuracy (%)	Sensitivity (%)	Specificity (%)
KNN	97.34 ± 4.31	97.56 ± 4.90	97.12 ± 3.88
Linear SVM	93.81 ± 9.21	94.42 ± 9.03	93.21 ± 9.46

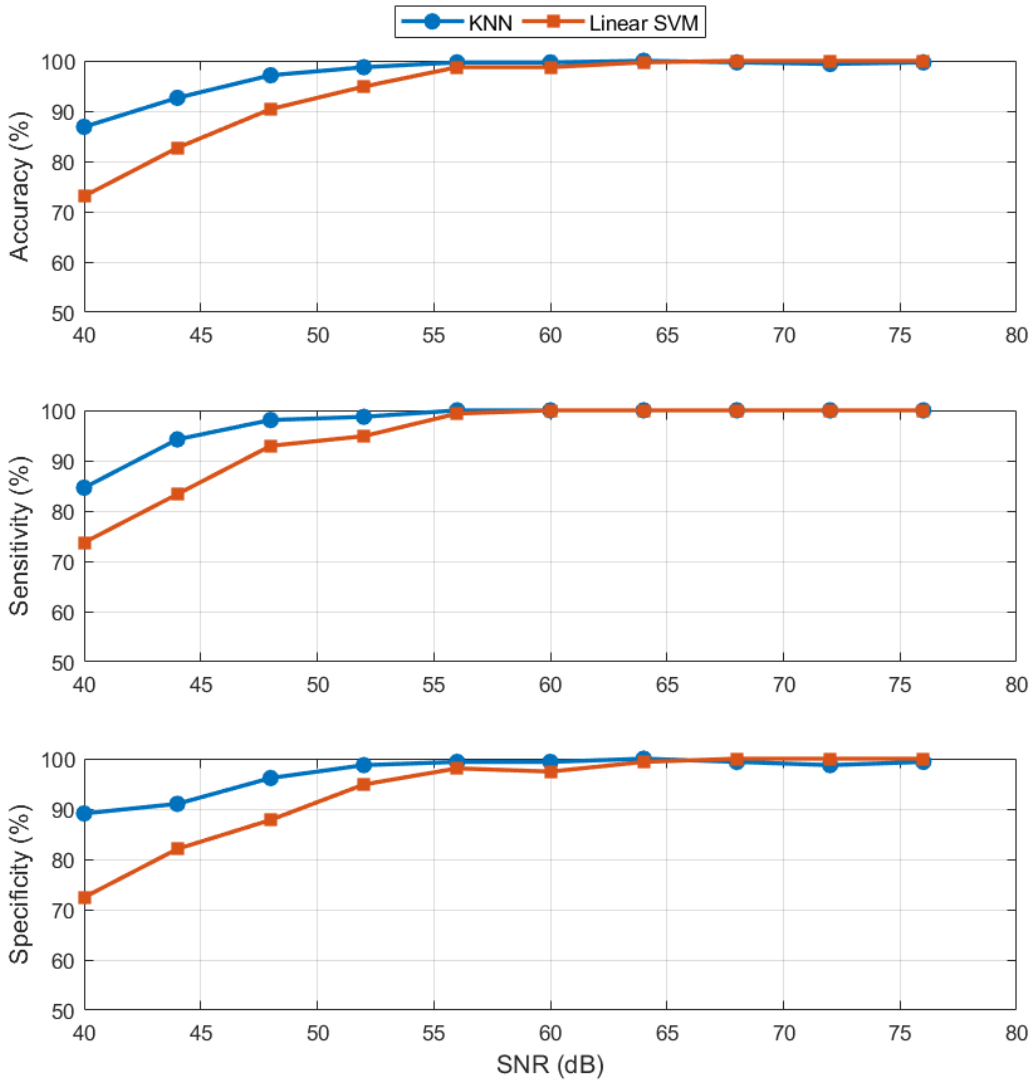

Figure 5.14: Average performance of the classifiers for varying noise level when trained and tested on the 40 dB SNR dataset. As expected, the performance of the classifiers degrades as the SNR decreases, i.e., as the noise level increases.

Overall, the classifiers were able to classify the noisy data with an average accuracy of 93.81% or greater. As expected, the poorest performance was for observations with the lowest SNR of 40 dB (i.e., the highest amount of noise). However, the accuracy for the 40 dB test set was still consistently greater than 70%. This result shows that the classifiers can classify noisy data (in

the case of additive random Gaussian noise), which is important as not all noise may be removed by pre-processing.

5.4 More Realistic Learning Test-Case of All Conditions in the Dataset Varying

In this section, the results of two different realistic test scenarios are presented. First, a realistic learning test-case is performed. This scenario involves the classifiers being trained on data that varies by all three conditions examined in this chapter. The second scenario is then a continual monitoring situation where unseen conditions are given to classifiers to mimic continual monitoring after deployment of the classifiers is investigated.

In the realistic learning test-case, the classifiers are given recordings and class labels without any additional knowledge of what bladder volume and urine conductivity relates to each frame. Much of the noise in data may be removed through pre-processing. However, some unforeseen and unfiltered noise may be present in the observations. Thus, a realistic train-test case is performed here using the stratified 5-repeat 10-fold cross-validation to train and test the classifiers using the TC3 dataset. The TC3 dataset was the most complex dataset devised in this chapter, and included varying bladder volumes, urine conductivities, and measurement frame noise levels. The overall results are given in Table 5.6.

High performance was found with accuracies over 94%. The overall behaviours of the misclassifications around the bladder separation volume, with higher misclassifications at the lower urine conductivities and higher misclassifications at lower SNRs, are similar to what was found in Section 5.3.

Table 5.6: Average performance of the classifiers for classifying bladder fullness for the realistic learning test-case.

Classifier	Accuracy (%)	Sensitivity (%)	Specificity (%)
KNN	97.46 ± 0.89	97.94 ± 1.20	96.97 ± 1.41
Linear SVM	94.29 ± 1.39	94.95 ± 1.73	93.63 ± 1.92

Having demonstrated that the classifiers have a high overall performance as shown in Table 5.6, the classifiers were next retrained using the full dataset. To verify that the full-dataset classifiers performed as expected, the second scenario examined in this section involved using

a continual monitoring dataset to assess whether the trends observed in Section 5.3 were repeated. The results are given in Table 5.7.

Table 5.7: Overall performance of the TC3 dataset trained classifiers on the CM1 dataset.

Classifier	Accuracy (%)	Sensitivity (%)	Specificity (%)
KNN	83.33	90.40	76.26
Linear SVM	83.59	94.70	72.47

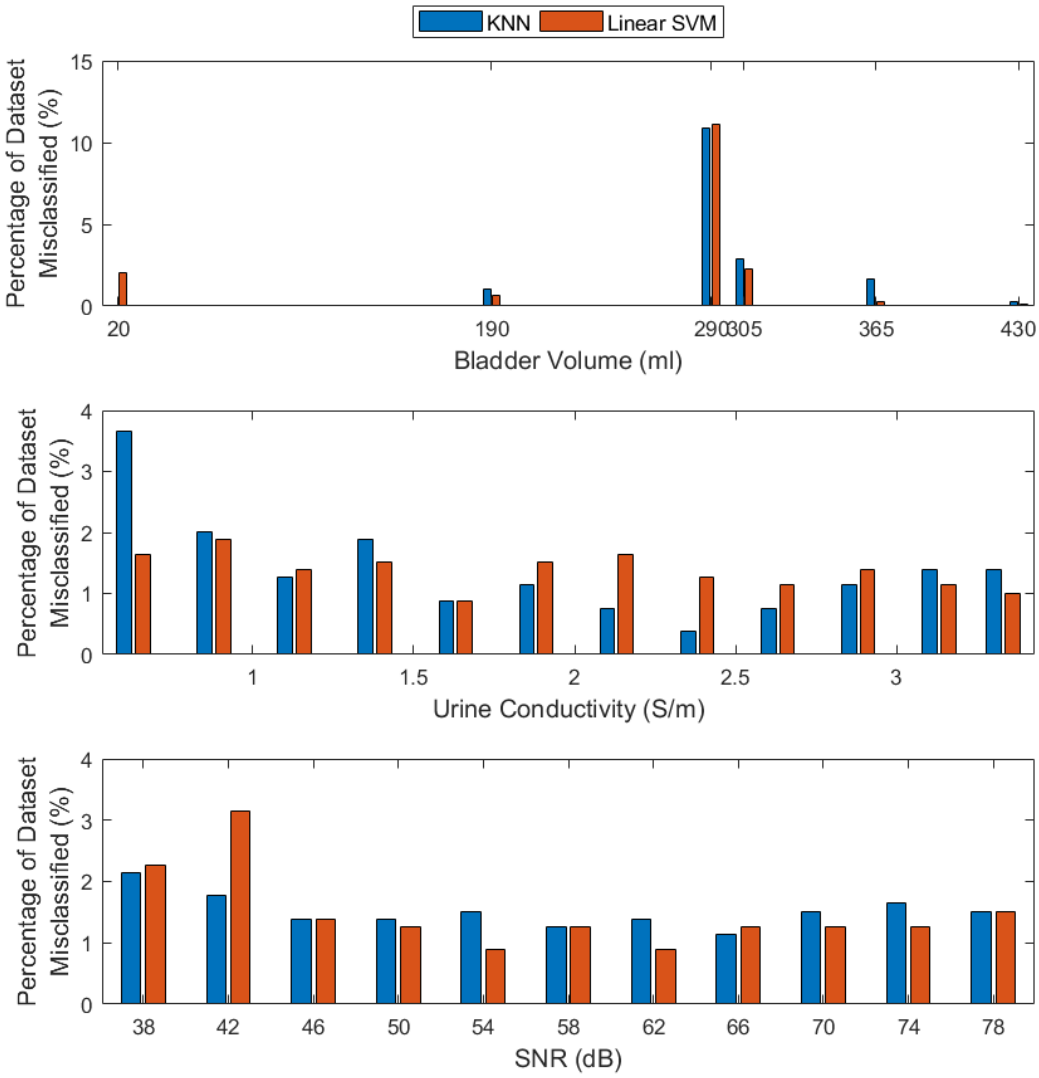

Figure 5.15: Performance of the TC3 dataset trained classifiers on the CM1 dataset. The trends for each condition are similar to the findings in Section 5.3. Thus, the classifiers perform as expected for this example deployment test.

An overall performance was achieved of 83.59% for the linear SVM and 83.33% for the KNN classifiers using the CM1 dataset of six unseen bladder volumes (spread from 20-430 ml),

twelve unseen urine conductivities and eleven unseen noise levels. Importantly, the trends observed in Figure 5.15 are similar to what is expected from Section 5.3 with a higher number of misclassifications around the bladder volume separation of 300 ml, and higher misclassifications at the low urine conductivities and high noise levels.

In summary, two test-cases were examined in this section that were more realistic than the controlled conditions previously examined in Section 5.3. Overall, the trained classifiers performed well having achieved the main trends that have been investigated in Section 5.3 when trained and tested on a dataset with all three conditions varying and when the 'deployable' classifier was given new data to classify in the CM1 dataset.

5.5 Advantages and Disadvantages of EIT Measurement Data for Bladder State Classification

Having determined the feasibility of using raw EIT voltage data as an input source for classification of bladder state using EIT, the advantages and disadvantages of using raw EIT voltage data needs to be assessed.

Raw EIT voltage data is collected by the EIT device from the body of interest before any additional processing to form images. During image reconstruction, assumptions of the *a priori* information are imposed on the data. These assumptions may be incorrect and this mismatch could lead to errors in the resulting images [95], [176], [177]. Also, any assumptions made for image reconstruction could bias any further processing. Thus, use of the raw EIT voltage data has potential to overcome these issues, as the data can be used with minimal processing and assumptions.

However, it is important to note that there are limitations to using raw EIT voltage data. For example, it is more difficult to interpret raw data and the trends are not as obvious as they are in images, unless further analysis such as descriptive statistics is performed. Also, further research is needed to investigate how to apply correction algorithms to the raw EIT voltage data for some of the noise sources outlined in Section 3.6.2, e.g., body movement. Correct finite element method modelling for imaging during movement and modelling of other sources of noise could potentially reduce the effect of these noise sources. Further, research into EIT imaging and FEM modelling is more readily available than work on raw EIT data, and thus could potentially be more suitable for correcting body deformations. One must consider the implications of both images and raw EIT voltage data when choosing between them as inputs

to the classification algorithm. The decision must be weighed against both development and test time, and the resources available.

Comparing the CM test in both Chapter 4 and Chapter 5, the performance achieved with the classifiers using both images and raw EIT voltage data were quite similar. The maximum difference between the accuracy of all the classifiers for both images and raw EIT voltage data was less than 2% in the CM test-case. As outlined in Section 4.4, a higher sensitivity is preferred to a higher specificity when both cannot be equally high. This trade-off ensures fewer false negatives, i.e., the device wearer is told not to go to the toilet when the device wearer should go to the toilet. For both images and raw EIT voltage data, the classifiers do have a higher sensitivity without any calibration before training.

Importantly, the raw EIT voltage data used here did not require a baseline while the time-difference EIT image reconstruction did. A baseline could help compensate for constant noise sources, or the baseline could hinder performance by introducing more noise if the baseline and the newly observed data have different types of noise or levels of noise in each. Further research on how to incorporate baseline data into voltage-based classification is needed. It is important to note that uncorrected raw EIT voltage data performed similarly to the time-difference EIT images for classification of bladder state using machine learning, both in terms of the overall performance results and trends observed in both Chapter 4 and Chapter 5.

From this analysis, there are advantages and disadvantages of using raw EIT voltage data when compared to using EIT Images. However, similar performance with less *a priori* information can be achieved by using the collected voltage data from an EIT system without the processing and assumptions associated with image reconstruction. In future work, a classification approach could be developed with the option of using either data source, then optimise to whichever data source enables the best solution to a bladder monitoring device using EIT. Future work could also involve processing of the raw EIT voltage data to further improve performance of the bladder monitoring EIT device when there are more noise sources and different bladder volume ranges.

5.6 Summary

In this chapter, bladder state classification was performed using raw EIT voltage data, as an alternative data source to pixels from images. Using raw EIT voltage data as the classification input was to overcome some of the limitations of time-difference EIT image reconstruction,

e.g., the requirement of *a priori* information in EIT imaging. The analysis of the raw EIT voltage data was performed in a similar manner to that of the image data in Chapter 4. The key findings from sections within this chapter are highlighted in the following paragraphs.

In Section 5.3, the effect of varying each of the conditions of bladder volume, urine conductivity and noise was investigated. It was found that bladder volumes were primarily misclassified around the bladder separation volume, as expected. However, poorer performance was observed for lower noise datasets than on noisier datasets. For the least noisy dataset (80 dB SNR), there were larger gaps between bladder volumes around the bladder volume separation than on the noisier datasets. This circumstance led to more classification error. The finding suggested that additive Gaussian noise can improve refining the decision boundaries of the classifiers. This improvement occurs when the classifiers are trained on datasets of large bladder volume gaps between the not-full and full bladder volume classes. Where possible, the larger gaps between the bladder volumes could be avoided by collecting more recordings of different bladder volumes close to the bladder separation volume. Findings for the effect of urine conductivity and noise on the bladder state classification using raw EIT voltage data were similar to the investigations of Section 4.5.2 and Section 4.5.3 in Chapter 4. Thus, the findings suggest that the classifiers for using either raw EIT voltage data or images for input require as much variety in urine conductivities as possible to be collected during the training period, particularly at low urine conductivities. Also, it is important to employ strategies to minimise noise where possible. For any remaining noise, samples of various noise levels may be included in the dataset to mitigate the effect on classification.

Section 5.4 presented a realistic train-test case where the classifiers were trained and tested on EIT voltage data collected under all three variable conditions of bladder volume, urine conductivity and noise. High performance was achieved (average accuracies of 94.29% for Linear SVM and 97.46% for KNN on the cross-validation test sets) and a continual monitoring example mimicking real-life deployment was presented. In the CM test-case, the classifiers were trained on the whole dataset and given completely unseen bladder volumes, urine conductivities and noise levels. These results are similar with image classification findings in Section 4.6. The results presented in Section 5.4 indicate that a classifier can be initially trained on a small number of recordings and provide reasonable performance (e.g., classifying the correct state with an accuracy of 80% or greater).

In Section 5.5, the merits of raw EIT voltage data were discussed in comparison to EIT image data. The classifiers using the raw EIT voltage data and the EIT image data had similar performance. However, additional overhead in terms of additional processing and requiring *a priori* information was associated with time-difference EIT image reconstruction. Either approach could be chosen and used to develop an EIT-based enuresis alarm. However, using just the raw EIT voltage data for the initial design reduces complexity and processing, particularly as the data would be collected anyway for image reconstruction.

In summary, this chapter has demonstrated that bladder state classification of not-full and full classes is possible using raw EIT voltage data collected from an adult pelvic model. The use of raw EIT voltage data as the main data input for bladder state classification overcomes some of the limitations of the use of EIT images, and both inputs result in bladder state classifiers of similar classification performance. However, the research now needs to be refined for an EIT-based enuresis device to cater for enuretic children. With children, there are additional limitations such as smaller bladder capacities, reduced pelvic region size for electrodes and the additional complexity of body changes with age. This topic will be investigated in the next chapter. Additionally, specific features can be selected and/or extracted from the collected data that could further enhance classification results (Chapter 7).

6 Numerical Modelling of the Child Pelvic Region

Chapter 4 investigated the feasibility of bladder state classification using machine learning with EIT image data. Promising results for the concept were shown. To overcome some of the limitations of EIT image data, such as requiring *a priori* information, a similar study to Chapter 4 was performed in Chapter 5 using the raw EIT voltage data collected before image reconstruction. Comparable performance in classification of not-full and full bladder volumes was found in terms of performance metrics and trends under the conditions of the varying bladder volumes, urine conductivities and added noise. The performance using raw EIT voltage data was also achieved without using reference data. Removal of the need for reference data reduces the potential of introducing more noise sources into the system due to the mismatch in noise sources between the reference and the observed data.

The findings for both Chapter 4 and Chapter 5 were determined using data from a simplified adult forward model. This forward model facilitated initial feasibility studies with minimum complexity and a large bladder volume range that adults have in comparison to the expected bladder capacity of children [24], [178]. The research for adult applications can be further built on in both simulation and in real-world testing. However, the main target patient group for this research is children with NE. As discussed in Chapter 2, this thesis provides advances towards an EIT-based enuresis alarm device that could support children with bedwetting difficulties. Importantly, any device intended for use with children would likely be tested for safety and functionality in adults before being evaluated on children. Therefore, information gathered from the adult model may be used practically in the development of a device targeting children. However, investigations should also be performed on child models. Notably, child models have additional challenges over those of adults. For example, children have smaller bodies with less room for electrode placement and smaller bladder volume capacities. With smaller bladder capacities, the difference in volume between the full bladder and not-full bladder is also smaller. It would be expected that classification between the two states could be more challenging.

To perform studies for children, a numerical forward model is required. No child forward model has been developed for BVM EIT in the literature to date. Thus, a numerical forward model is devised in the chapter. This numerical forward model builds on the research and knowledge gained in Chapter 3. In Chapter 3, it was deemed appropriate to form a cylindrical-based forward model that was anatomically informed. The reasoning being that the main forward model design in the literature was improved upon and that bladder state classification was in an early stage of development. However, increased complexity in the child forward model may benefit the development of an enuresis alarm device. The increased complexity includes a more realistic boundary based on medical imaging and the inclusion of additional tissue groups other than the bladder. The increased complexity could assist in giving more realistic results and insights.

This chapter is structured as follows: an overview of the realistic numerical forward model for BVM-EIT is discussed in Section 6.1; how CAD files based on raw medical imaging data were gathered is discussed in Section 6.2; modelling of the pelvic boundary for the child forward model is discussed in Section 6.3; modelling of the pelvic background conductivity for the child forward model is presented in Section 6.4; the bladder and urine modelling is discussed in Section 6.5; the additional bone tissues added to the forward model are presented in Section 6.6; the child pelvic model from Section 6.3 to Section 6.6 is summarised in Section 6.7; the forward model is used to simulate example measurement data in Section 6.8; the limitations of the forward model are discussed in Section 6.9; a comparison between the adult and child forward models is performed in Section 6.10; and the chapter is then summarised in Section 6.11.

6.1 Overview of Realistic Numerical Forward Models in BVM-EIT

As outlined in Section 3.1 of Chapter 3, simplified cylindrical forward models have been mainly used to represent the boundary of the pelvic region in BVM EIT simulation. However, there have been some realistic forward model exceptions that should be considered when forming the child pelvic forward model. These exceptions include the use of a single CT slice for 2D simulations [125] and a full body forward model [115]. Single CT slices of the boundary have also been used in BVM EIT for image reconstruction after real-world data collection such as in [13]. The numerical forward models for data generation in these works are discussed in the following paragraphs.

For the 2D simulation by Khambampati et al. [125], the boundary of the pelvic region was extracted from a CT slice for numerical simulation to estimate the size and shape of the bladder. The shape of inner organ region was also extracted and included in the model.

The full-body forward model by Schlebusch [115] was based on male adult data [179]. Schlebusch modelled the body from the ankles to the neck and included the upper part of the arms. The model included internal tissues such as the organs, blood vessels and bone. The organs modelled included the liver, the stomach, the pancreas, the kidneys and the intestines. The bones from the lower femur to the thoracic spine were also included. The blood vessels included were the aorta and the vena cava. The model was used for evaluation of the measurement sensitivity of different electrode measurement arrangements for the bladder [115]. The additional tissues helped determine which electrode configurations had the optimum measurement sensitivity for the bladder. The full-body forward model was used alongside a simplified cylindrical forward model. The simplified cylindrical forward model had a bladder as a sphere. The simplified cylindrical forward model was used for bladder volume data generation and estimating bladder volume using algorithms such as the GI, the neural network, and the equivalent circular diameter.

In this work, a child forward model is developed for the BVM of children. Specifically, the forward model is developed to enable device design for a proactive enuresis alarm to alert the child to go to the toilet before bedwetting. The forward model builds on existing cylindrical bladder volume estimation models by including additional tissue groups beyond the bladder. The forward model also includes a more realistic boundary of the pelvis. The model will capture the ROI (i.e., the pelvic region) to focus on the bladder changes, rather than use a full body model. This use of a specific ROI is similar to what has been completed previously in thorax and head studies [172], [174]. Isolating the forward model to the pelvic region also has the benefit of allowing more elements in pelvic region and, therefore, improving simulation. Also, additional tissues group (e.g., the pelvic girdle) could be included in the 3D model as completed in [123] to determine their impact on classifiers.

Having knowledge of existing research, the child numerical forward model used in this thesis can now be formed. The first step is gathering computer-based physical data of a child to use for the realistic child forward model; this step is presented in the next section.

6.2 Obtaining Raw Medical Imaging Model Data

It can be difficult to obtain publicly available CT or MRI scans of pelvic region of children. However, segmented models of bodies of children do exist for electromagnetic research. Such models are available in the Virtual Population [180] by the IT'IS Foundation (The Foundation for Research on Information Technologies in Society, Zurich, Switzerland, https://itis.swiss/). The Virtual Population contains a variety of adult and children models under different versions. The version 2.0 (V2.0) contains two adults and two children models available in stereolithography (STL) CAD format for finite element modelling use in third-party software.

The two children models consist of a six-year-old boy and an eleven-year-old girl. In this chapter, the boy model (referred to as Thelonious by [180] with DOI of 10.13099/ViP-Thelonious-V2.0 [181]) is used to perform preliminary studies of bladder state classification. One of the primary reasons for choosing the boy model is due to the medical application being NE. Nocturnal enuresis is more prevalent at six years old than at eleven years old [34], [182], [183]. Furthermore, NE affects boys more commonly than girls [1], [34]–[36]. However, the process used to transform the six-year-old boy CAD model to a numerical forward model for BVM stimulation using EIT software could similarly be used to develop a numerical forward model for the eleven-year girl (DOI: 10.13099/ViP-Billie-V2.0 [184]).

The CAD data available for Thelonious in [181] consists of his body divided into several tissues specifically segmented as bladder, gastrointestinal bone and the reproductive system among others. Any non-specified tissues are combined together and categorised as 'other tissue', which includes the outer shape of the body. An accompanying version of Thelonious [181] is a whole-body shell [185] (i.e., the outer boundary of the body only). This shell is appropriate for modelling the boundary in EIT without the need for remeshing all the tissues together, which would have the potential of affecting the topology and introducing unnecessary error. Both sets of data can be used together in this application in order to: 1) model the boundary; 2) add tissues groups beyond the bladder; and 3) obtain anatomical reference measurements such as the top of the pubic symphysis and the intersection of the urethra and the bladder. Thus, a publicly available online data source can in this way be modified to aid in BVM-EIT research and development.

In the following section, the process of creating the boundary of the pelvic model is discussed.

6.3 Modelling of the Pelvic Outer Boundary

The formation of realistic EIT FEMs has been previously investigated in other fields of EIT such as for stroke applications [172], [173]. The overall high-level process generally involves: gathering medical imaging data such as medical imaging scans; segmenting boundary and tissues in the ROIs; extraction of the tissues; then meshing for EIT measurement data simulation and/or image reconstruction. For the child data obtained, extraction of the whole-body shell [185] and tissue groups [181] into CAD files has been performed already. However, additional processing is required to refine the CAD data to the pelvic region only. In this work, the whole-body shell is used as the foundation for the boundary of the forward model and the tissue-groups are added after.

The whole-body shell and the tissue groups were first aligned into the same coordinate space (i.e., the coordinate space of [181]). This alignment allows the additional tissues to be embedded later in the numerical forward model. Also, the alignment helps guide segmentation for the inclusion of the bladder, the urethra, and the pelvic girdle. The alignment was done by using the "snap" function with 3D Builder (3D Builder, Microsoft Corporation). The aligned whole-body shell STL model was then imported into the CAD software Autodesk® Fusion 360® (Autodesk®, www.autodesk.com/products/fusion-360/overview) for further processing of the model. Specifically, this further processing was to determine where to divide the body for the pelvic model and to perform the ROI segmentations. The pelvic boundary was taken just above the genitals to near the rib cage, which is 15 cm along the craniocaudal axis (height). This 15 cm high region contained the bladder, the top of the urethra, and the navel. The region also included the bone from below the pubic symphysis to above the iliac crest (including the upper femur, pelvic girdle and part of the lumber spine), as shown in Figure 6.1. The cut operation was performed with uniform fill to close the CAD body (make 'water-tight') as the whole-body shape was initially hollow inside.

The pelvic boundary model was then extracted from the rest of the CAD model and exported as an STL so that the pelvic boundary model could be further processed by EIDORS, e.g., placing electrodes. This further processing by EIDORS is described in Section 6.8. In the next section, the 'background' conductivity assigned to the pelvic region is discussed.

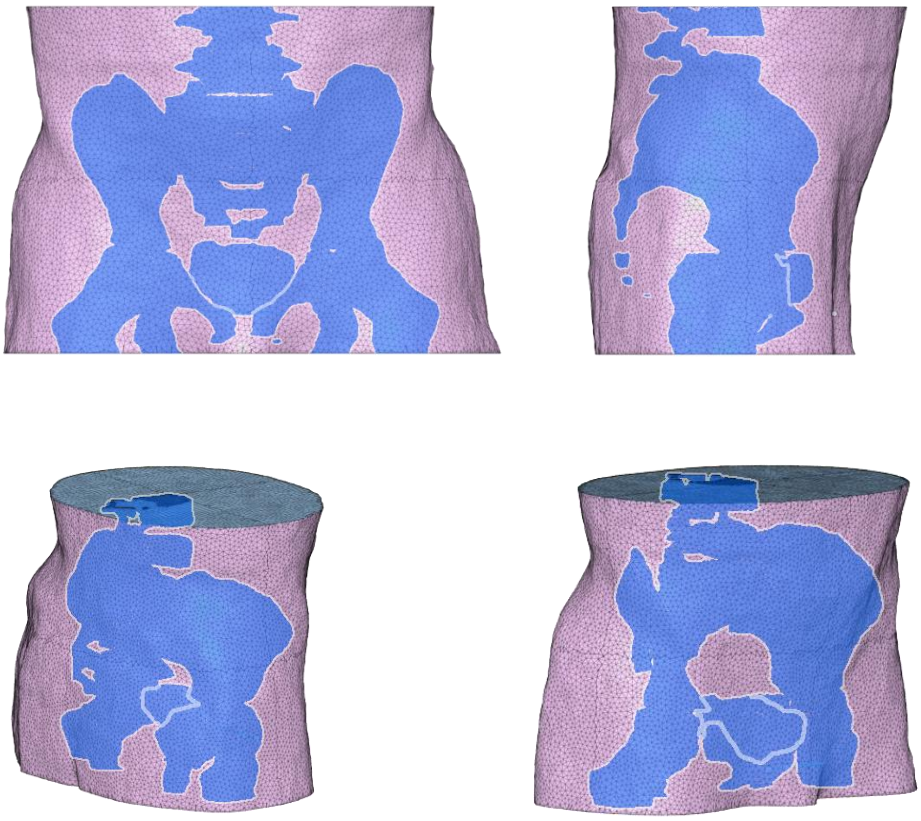

Figure 6.1: Face on and 3D views of the 15 cm high pelvic region: (top-left) front view; (top-right) side view; (bottom-left) 3D view from the posterior; (bottom-right) 3D view from the anterior. The images include bone (upper femur, pelvic girdle and part of the spine), the bladder and the urethra.

6.4 Modelling of the Pelvic Region Background Conductivity

As previously discussed in Section 3.3.2, a single value of conductivity (real or complex) at a single frequency has been assigned to the background of the pelvic boundary for a number of 3D numerical forward models in BVM EIT [114], [117], [123], [124], [126], [136]. Where the conductivity has been related to a tissue, the conductivity of muscle or the intestines at specific frequencies has been used [117], [123], [136].

As discussed in Section 3.3.2, a weighted average may be too specific to a forward model for a given instant in time of a particular person. In Section 3.3.2, this point was particularly relevant as the sample of medical imaging used was for a male cadaver. In living beings, the pelvis contains dynamically changing processes due to the nature of organs and other tissues within this ROI (e.g., the digestion performed by the intestines, the movement of bone and the contraction and the relaxing of muscles). Since this dynamic environment is hard to model, the

background of the numerical forward model is maintained at the conductivity of muscle, similar to previous research [117], [136] and the earlier work in the thesis. The conductivity of muscle used is 0.352 S/m at 50 kHz [104]. By using a background conductivity of muscle instead of a weighted average, other tissues (e.g., the pelvic bone) can be easily added to the forward model without recalculating the background conductivity. While a weighted average may give a better representation of once instant of time, it is accepted that simulation will not ideally model real-life but will give an indication of the expected trends. Thus, a single conductivity value of muscle for the background is considered sufficient.

6.5 Bladder & Urine Modelling

In this section, the bladder is modelled for the six-year-old boy numerical forward model. Also, the bladder volume range for a six-year-old child and the appropriate urine conductivity range are determined.

6.5.1 Bladder Shape within the Pelvic Forward Model

Section 3.4.2 outlined bladder models in 3D numerical studies of BVM EIT to date. The bladder models were spherical-based [114], [123], [124], [126]. These bladder models were used in cylindrical-based numerical forward models (e.g., 30 cm diameter [114], [124], [126]) that are of similar order to cross-sectional area of the adult model in Chapter 3 (both cross-sectional areas greater than 700 cm^2).

Ultrasound bladder volume measurement uses shapes such as the ellipsoid to model the bladder and to determine the bladder volume as discussed in Subsection 3.4.2.1. For children, ultrasound imaging has also been employed for bladder volume estimation. Recently developed ultrasound devices for NE have used ultrasound to measure the anteroposterior size of the bladder of children in order to determine bladder volume during filling [79]. Alongside this work, simplified bladder models such as ellipsoids have been used to model the bladder for bladder volume estimation in previous bladder volume paediatric ultrasound research [186], [187].

Apart from [79], [84]–[86] that reported the single axis anteroposterior measurements during testing of ultrasound bladder monitors, no other studies presenting bladder dimensions for children during bladder filling has been observed by this author. Thus, the ellipsoid bladder model and the corresponding radii relationships developed in Subsection 3.4.2.1 are used to

model the bladder for the child forward model. For expansion of this work, the female bladder model may be formed using the details provided in the footnote[6].

Having determined the bladder shape, the location of the bladder must be decided. This bladder location is detailed in the next subsection.

6.5.2 Bladder Location and Orientation within the Pelvic Forward Model

To determine the bottom of the bladder, the fixed connection of the urethra to the bladder may be the primary option as discussed in Section 3.4.2.2 when clarity in medical imaging allows. In the tissue CAD files given in Thelonious V2.0 [181], both the bladder and the urethra location are present. Thus, intersecting faces and vertices can be determined.

The intersecting faces and vertices were determined using manual inspection in MeshLab software (MeshLab, www.meshlab.net). Ten faces in the urethra STL CAD model were determined to be in contact with the bladder CAD model. The vertices were recorded, and the unique vertices were determined. The mean vertex was calculated and used as the bottom location of the bladder model.

In terms of orientation, the ellipsoid bladder model has three radii specified, each at right angles to each other. The three radii are either oriented along the left-right, anteroposterior or craniocaudal axes, and the choice of axes need to be specified. The same settings for the orientation of the ellipsoid model as discussed in Section 3.4.2.2 are used in this work.

6.5.3 Bladder Volume Range for Simulation

In the literature to date, the expected bladder capacity (EBC) for children based on age has been modelled in mathematical form [22], [23]. The equation in terms of millilitres is defined as:

$$EBC = (1 + age\ in\ years)\ x\ 30\ ml. \tag{6.1}$$

This equation is suitable for estimating bladder capacities of children between the ages of 4-12 years, inclusive [22]. The maximum bladder voiding volumes measured in children can be compared to the EBC using Equation (6.1) as a guide to determining small and large

[6] An ellipsoid for the female model can be created using plotted data from [230] of the female bladder dimensions against normalised capacity. The data is plotted for the three axes of depth, width and height. Data is available for two groups, a control group of 11 women and a group of 11 women with the condition of overactive bladder. The data can be extracted from the plots and then the dimensions can be aligned under the same normalised bladder capacities to form relationships between the dimensions for the ellipsoid volume changes, similar to what was done in Subsection 3.4.2.1.

maximum voided volumes [22]. Thus, in this work the EBC is used to determine the applicable upper limit of the bladder volume. Specifically, Equation (6.1) is applied to calculate the EBC for a 6-year-old child, since this is the age of Thelonious. Thus, the expected upper limit of bladder capacity is considered to be 210 ml in this work.

Similar to adults, children may have residual urine in the bladder. An abnormal quantity of residual urine or incomplete emptying is considered to be greater than 20 ml [178]. The residual urine may be considered in the case of images, as in Chapter 4. In this situation, reference data from after voiding may be used.

However, the full range of bladder volumes from 0 ml to the EBC is considered for the raw EIT voltage-based studies, i.e., 0-210 ml.

6.5.4 Urine Conductivity for Simulation

In Section 3.4.2.4, the literature was reviewed for the electrical conductivity of urine. The scope of the literature exploration was not limited to adults. Thus, the same range of urine conductivities are used for the child model as the adult model. The urine conductivity range is 0.5-3.33 S/m.

Having devised the bladder model (as shown inside the boundary model in Figure 6.2) and the associated bladder volume and urine conductivity ranges, the inclusion of other tissues in the model can be discussed. The modelling of these tissues is described in the next section.

Figure 6.2: The realistic six-year-old model including the ellipsoid model in CAD format. The model is shown with a 60 ml ellipsoidal bladder (shown in blue). The model can be used for EIT data generation once the finite element mesh is created. However, additional tissues could be added to model such as bone.

6.6 Modelling of Bone in the Child Pelvic Forward Model

In several previous BVM and pelvic related EIT studies [113], [115], [123], [154], the pelvic bone has been added to the numerical forward model. The presence of bone and other tissues in the body will affect the current flow from different combination of electrodes. Measurements from certain measurement-injection electrode pairs may be more affected by the presence of these tissues, leading to less informative data for bladder monitoring. Other tissues, such as the intestines, were added to a full-body model by Schlebusch [115] for sensitivity analysis of different measurement setups but not for varying bladder volumes in bladder volume estimation. The presence of many other tissues beyond bone, like the intestines, would require the bladder to be deformable in order for the bladder to fit within the confines of the other tissues. Additionally, modelling deformation would add substantial complexity to the simulation. Therefore, a deformable bladder is not in the scope of this work. Similar to the studies [113], [115], [123], [154], the bone shape in the ROI and conductivity of bone is added to the model along with the bladder model (Section 6.5) and the background conductivity (Section 6.4) for studies based on varying bladder volume. The addition of the bone (upper femurs, pelvic girdle and the lower lumber spine) from Thelonious V2.0 [181] may make the numerical forward model and the outputs more realistic as the current flow will be affected by the different conductivity distributions of tissues within the numerical forward model.

Similar to Section 6.3, the Thelonious V2.0 model [181] was imported into Autodesk® Fusion 360® where the pelvic girdle, the upper femurs and the section of the spine within the 15 cm defined ROI were extracted. The cut operation was performed with uniform fill to make the CAD body closed ('water-tight') as the bone shape was hollow inside. The exported STL model was then further processed to repair holes in the STL mesh using Autodesk® ReCap™ Photo (Autodesk®, www.autodesk.com/products/recap/overview). The prepared model of the bone with the ROI is given in Figure 6.3.

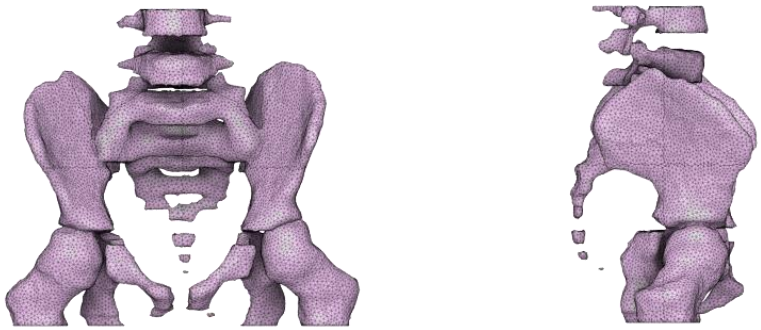

Figure 6.3: Anterior (left) and right side (right) views of the bone included in the 6-year-old pelvic ROI. The bone in the ROI includes the upper femur, the pelvic girdle and a section of the spine (lower lumbar spine).

Next, the STL bone model was added to the pelvic forward model after meshing. This addition is further described in Section 6.7 and Section 6.8. Once the bone is added to the model, conductivities needs to be assigned to the bone tissues.

Bone is composed of a dense outer shell ('cortical bone') and internal spongy structures ('cancellous bone') [16]. Within the bone, there are blood vessels and bone marrow [16]. Different conductivities have been recorded for different parts of the bone [104], [188]. This finding is important when assigning conductivity values in the bone structure. However, only the surface of bone is given in the data obtained from the Thelonious V2.0 [181] model, i.e., there is no distinction made between the type of bone in the model, and only the outer surface is given. Cortical bone forms the outer structure of bone [16]. Thus, the conductivity of cortical bone is assigned to the bone tissue in the child model. The conductivity of cortical bone used in this work is 0.0206 S/m at 50 kHz [104].

6.7 Realistic Pelvic Model of a Six-Year-Old Boy

In this section, the child pelvic model for BVM EIT devised for a six-year-old boy from Section 6.2 to Section 6.6 is demonstrated as an assembled model (Figure 6.4) and the main properties from Section 6.3 to Section 6.6 are summarised in

Table 6.1. The child pelvic model is presented without the elements from discretisation shown (i.e., in ‘solid’ form). The child pelvic model contains conductivities for three tissues (muscle, cortical bone and urine) and the physical structures for bone and the bladder models. Both bone and the bladder are added after meshing (unlike the addition of the bladder in Chapter 3 that was added before meshing), which affects the smoothness of the structures in the numerical forward model. This means the boundary is only meshed once and additional tissues are added afterwards, similar to [189]. This method has the advantages of reducing the number of times required to mesh. Meshing the model only once allows more data to be generated in the same time than by repeatable meshing for each bladder volume change, as was carried out in the adult model of Chapter 3. Further details of the addition of the bladder and bone is given in the next section. Limitations of the approach of adding the bladder and bone to a ‘static’ boundary mesh are further discussed in Section 6.9.

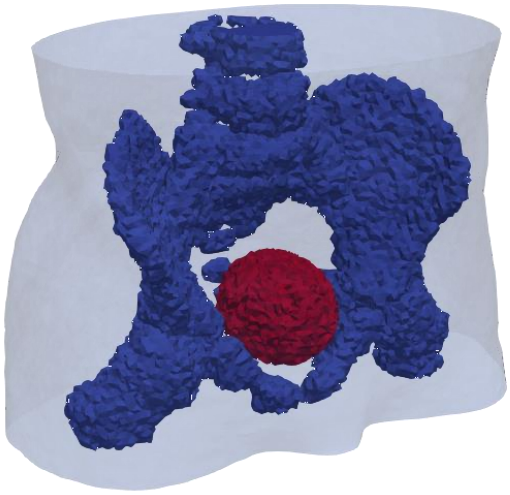

Figure 6.4: ‘Solid’ format of the designed realistic six-year-old pelvic model. The model is shown with a 60 ml ellipsoidal bladder (shown in red) for demonstration. The model also contains the bone of the upper femur, pelvic girdle, and the lower lumber spine (shown in blue).

Table 6.1. Property summary of the designed and developed realistic numerical pelvic model for a six-year-old boy.

Property	Value
Boundary Shape	Modified whole body outer shell from [185] based on MRI images, which has been segmented to capture the 15 cm ROI of the pelvic region
Boundary Maximum Dimensions	21.52 cm along the left-right axis 13.73 cm along the anteroposterior axis 15 cm along the craniocaudal axis
FEM Background Conductivity	0.352 S/m (at 50 kHz)
Bladder Shape	Ellipsoidal
Bladder Location	Left-right axis: -0.59 cm Anteroposterior axis: -3.99 cm Craniocaudal axis: 57.01 cm in the coordinate system of [181]
Realistic Bladder Volume Range	0-210 ml
Realistic Urine Conductivity Range	0.5-3.33 S/m
Bone Conductivity (Cortical)	0.0206 S/m (at 50 kHz)

6.8 Example Data Generation with the Child Pelvic Forward Model

In this section, the addition of the bladder and bone to the forward model is described, along with the electrode configuration employed. Then, the forward model is presented in discretised form. Example data for the forward model with and without the additional bone, with different bladder volumes, and with different urine conductivities is generated. The resulting data is examined to observe the effect of each condition on the raw EIT voltage data produced before classification.

6.8.1 Adding the Bone and Bladder Tissues

Aside from the tissues involved and the child sizing, the forward model presented in this chapter differs from the forward model in Chapter 3 in terms of how the meshes are designed. Specifically, the boundary is only meshed once (‘static’ FEM) in this chapter and then the bladder is added after meshing. In contrast, meshing was performed in Chapter 3 after the bladder was added. The process of meshing the forward model once allows for faster data generation and reduced meshing errors as discussed in Section 3.7. However, the static FEM comes at the cost of a less accurate representation of the bladder due to having to find the elements that the bladder intersects after meshing. This design method means the bladder could

occupy an increased number of elements at the border due to a lack of refinement. To reduce this problem, a weighted average of the conductivities of the bladder and background is used. Explicitly, elements at the border of which the bladder only shares a proportion are assigned a conductivity using a weighted average. The value assigned to the element is a weighted average of the proportion that the bladder occupies and the proportion that the background occupies.

For the addition of bone in the forward model, algorithms from [189], [190] were used to find the intersecting elements between the volume and surface meshes. Then, the bone conductivity was added to the EIDORS forward model using the algorithms. By adding the bone after meshing the FEM, the method for the pelvic boundary has reduced resolution on the border of the bone and background. For each element that contains some bone, the element is assigned the conductivity of bone. While the border of the pelvic bone may be less refined by adding it after meshing, this reduced refinement is considered minor when a high-resolution background mesh of approximately 1.4 million elements is used for the static FEM. Also, the pelvic bone is not changing in the study, unlike the bladder.

Having added the bone tissues, additional care was taken to ensure that the elements of bladder could not overlap with elements of the bone. Due to the simplified design of the bladder models (i.e., ellipsoidal) that cannot deform around the pelvic girdle in the numerical forward model, the range of bladder volumes had to be reduced. Subsequently, the ellipsoid bladder model has a maximum bladder volume range of 0-87 ml. Smaller bladder capacities have been reported for enuretic children, possibly due to the enuretic event occurring before the true bladder capacity has been reached [58]. The compromise of a smaller bladder volume for the increase complexity of simulation is made to determine the effect of bone on bladder state classification as well as to determine how the classifiers perform with a smaller range of potential bladder volumes.

6.8.2 The Forward Model

The forward model consists of a static mesh of approximately 1.4 million elements. As the bladder and bone were added after meshing, no additional elements are used to model them.

In [95], some of the limitations of paediatric EIT gastrointestinal studies that were highlighted included the difficulty in finding enough space for placing sixteen electrodes on the abdomen of children. Thus, the 32-electrode system from Chapter 3 is reduced to a 16-electrode system with a 2x8 electrode ring configuration to adapt to the smaller size of a child. The 2x8 ring

configuration has been previously used in EIT electrode configuration analysis studies in both simulation and on-humans [114], [115], [120]. Research in the field has shown that multilayer configurations have improved advantages for bladder volume estimation [114], [120]. Importantly, current flows in a body in a 3D space rather than a 2D plane. Therefore, a multilayer electrode configuration may be better able to measure 3D volume changes than a single ring of electrodes. This measurement of 3D volume changes is particularly important for this application as the bladder fills upwards (superiorly) into the abdominal as the volume increases. Thus, the two rings of electrodes could potentially better capture the bladder at different volumes (i.e., centred at different heights) than a single ring electrode configuration.

Electrode placements in previous EIT studies of the pelvic region include: starting at just above the pubic symphysis, placing of the electrodes approximate midway point between the pubic symphysis and the navel (approx. 8 cm below the navel), and placing electrodes at the waist [12], [13], [120]. In paediatric bladder ultrasound, the probe is placed "just above the pubic symphysis" [191]. In this work, the bottom electrodes are placed approximately 1 cm above the pubic symphysis (approximately 1.85 cm from the pubic symphysis to the centre of the electrode), which is in line with the definition used in the design of the ultrasound device for NE [79]. The electrodes were placed using the place_elec_on_surf function [148] in EIDORS.

The electrode diameter of 17 mm that was employed in Chapter 3 is also used on the child numerical forward model. The electrode diameter fits in line with other electrode modelling previously used in EIT [151] and is consistent across numerical studies in this thesis. The space between the centre of each electrode is approximately 37 mm along the craniocaudal axis. This spacing leads to an approximate gap of 20 mm between the electrodes along the craniocaudal axis.

The FEM is shown in Figure 6.5 for bladder volumes of 1 ml and 87 ml. The same stimulation protocol outlined in Section 3.6.1 is used in this model, i.e., injection current is 6 mA_{p-p} (approx. 2.12 mA_{rms}) with a Skip of 4. A non-rotational measurement scheme is used, as was outlined in Section 5.1.2. Since the system is a 16-electrode EIT system, there are 208 measurements per frame as there are no measurements from the injection electrodes.

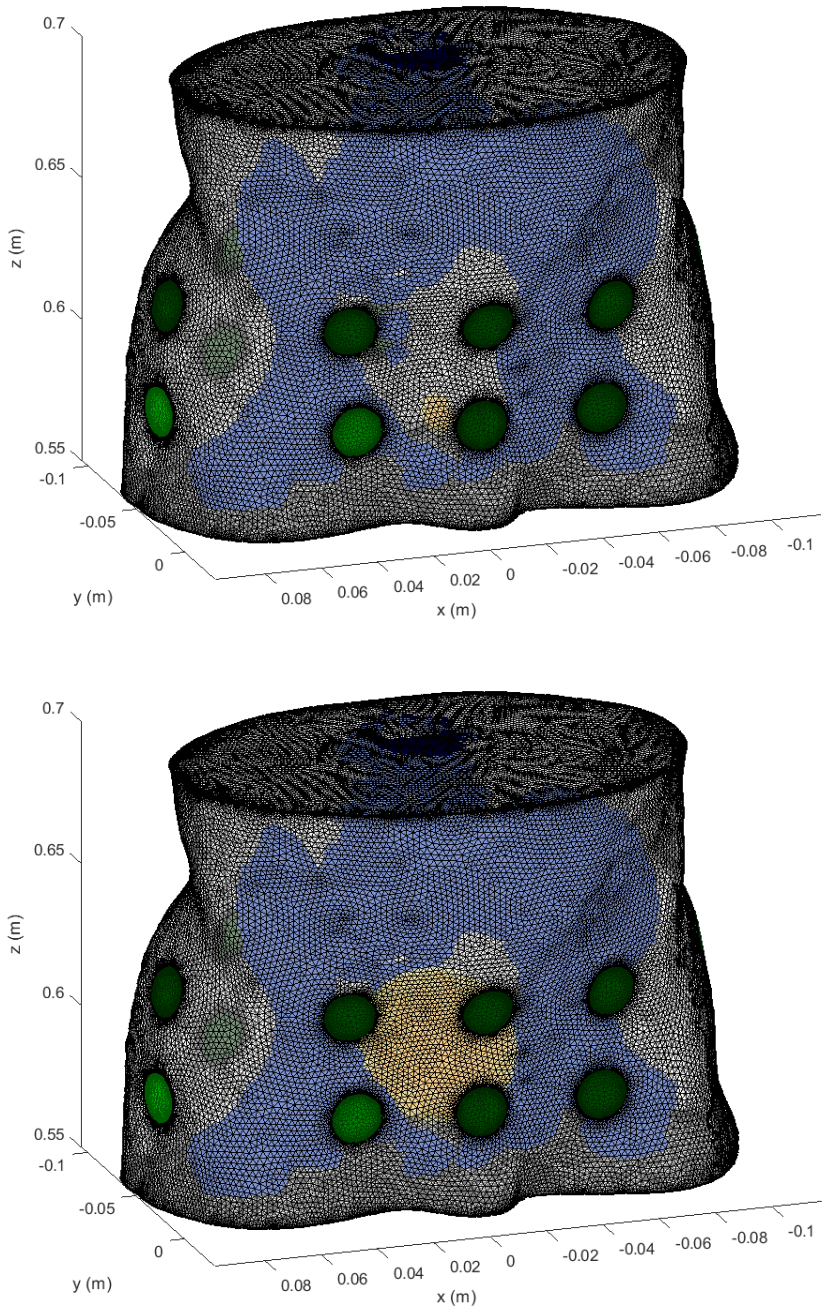

Figure 6.5: The designed realistic forward model of a six-year-old child that can be used to generate EIT measurement data. The forward model is shown with a 1 ml ellipsoidal bladder (top) and an 87 ml ellipsoidal bladder (bottom). The electrodes are shown in green, the bone tissue in blue, and the bladder in yellow.

In the next subsection, this numerical forward model is used to observe the effects of the additional bone and the smaller range of bladder volumes on the raw voltage data.

6.8.3 Data Generation

The findings from Chapter 5 indicated that raw EIT voltage data could be used as an alternative to EIT images as a data source for classification. Using raw EIT voltage data has the advantages

of similar performance to EIT image data, without the need for *a priori* information and correction using a time-difference reference in the classification of not-full and full bladder states. Thus, the use of raw EIT voltage may overcome key challenges with EIT images, and therefore is used in the following work.

Using the child numerical forward model, example data was generated to first show the effect of the addition of bone to the model. Figure 6.6 shows the effect of bone on data collected from the numerical forward model with and without bone. For this example, the bladder was not included. The purpose is purely to examine the impact of the presence of bone tissue on the EIT raw voltage data. The noiseless measurement frame with bone has an overall higher mean magnitude voltage due to the presence of the lower conductivity material of bone (0.0206 S/m) than the background conductivity of muscle (0.352 S/m) in the numerical forward model. This finding is expected. The voltage should be larger when the impedance is greater within a body of interest for a EIT system with a fixed current injection amplitude. The addition of bone has an overall effect of a 25.12% percentage difference between mean magnitude of the noiseless measurement frames of the numerical forward model with and without bone. These results indicate that it might be valuable to include the bone in the modelling for EIT BVM studies, since it seems to have an impact on the results and potential different impacts on certain channels that may be important to the classifiers.

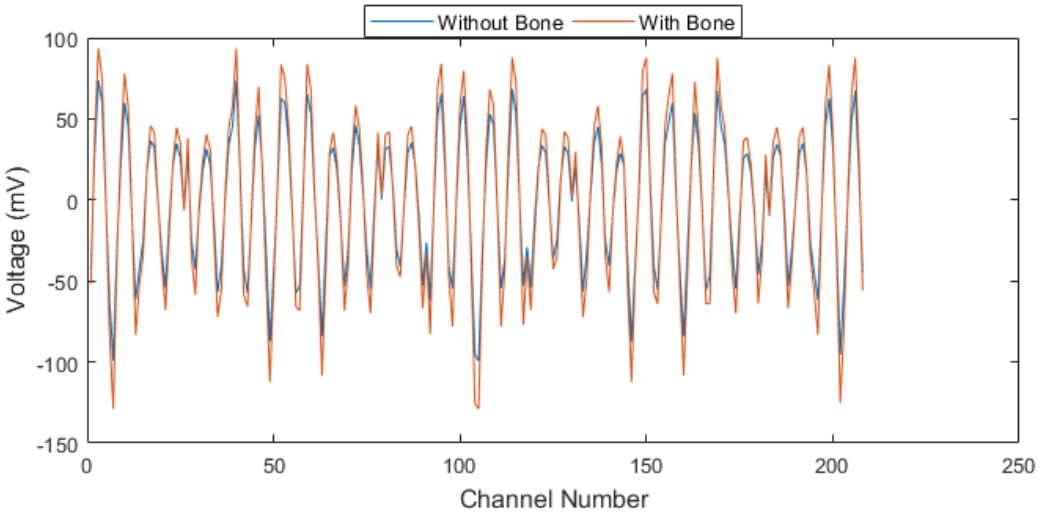

Figure 6.6: Plotted measurement frame voltages for the numerical forward model with and without the bone tissue. The bladder is not present in the numerical forward model. The addition of bone increases the overall measured voltage implying an increase in impedance to current flow in the numerical forward model, as expected.

With the bone included in the forward model, different bladder volume example data was generated with a urine conductivity of 2 S/m. The noiseless measurement frames for 1 ml and

87 ml bladder volumes are given in Figure 6.7. The percentage difference between mean magnitude of the noiseless measurement frames of 1 ml and 87 ml bladder volumes is 11.56% at 2 S/m. For the adult forward model, the percentage difference between mean magnitude of the noiseless measurement frames of 1 ml and 87 was 0.65% at 2 S/m. This finding could be due to: 1) the reduced distance between the electrodes and the bladder in the child model; 2) the multilayer configuration of electrodes in the child model that could improve the separability of the voltage data by capturing the 3D bladder volume change and the 3D current flow.

From Section 5.3.2, it was found that urine conductivity also influences the bladder state classification due to the decreased contrast with the background conductivity.

Table 6.2 presents the mean magnitude of the noiseless measurement frames of 1 ml and 87 ml bladder volumes for the urine conductivities of {0.5, 2, 3.33} S/m. As can be seen from this table, the difference between the bladder volumes ranges from 2.32-14.09%, depending on the urine conductivity.

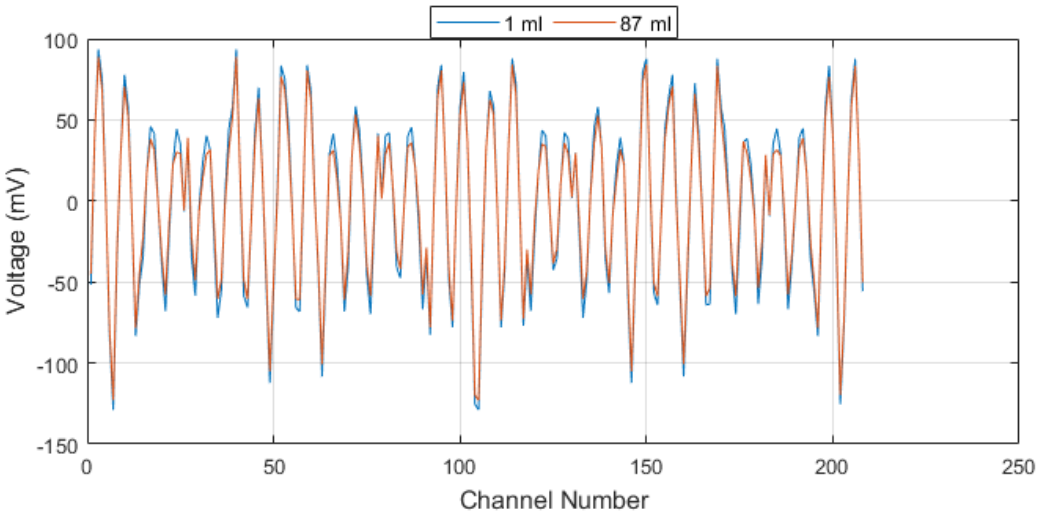

Figure 6.7: Plotted measurement frame voltages for the numerical forward model with bladder volumes of 1 ml and 87 ml and urine conductivity of 2 S/m. As expected, the mean magnitude voltage of the 87 ml bladder volume is less than that of the smaller 1 ml bladder volume.

Table 6.2: Comparing the differences in mean voltage of the measurement frames for the 1 ml and 87 ml bladder volumes at different urine conductivities.

Urine Conductivity	**Percentage Difference between the Mean Voltages of the Measurement Frames of the 1 ml and 87 ml bladder volume**
0.5 S/m	2.32%
2 S/m	11.56%
3.33 S/m	14.09%

Examining the difference in urine conductivity when the bladder volume is held constant, Figure 6.8 shows the measurement frames for the urine conductivities of {0.5, 2, 3.33} S/m with an 87 ml bladder volume. The mean magnitude voltage percentage difference between the 0.5 S/m and 3.33 S/m measurement frames at 87 ml was 11.95%. For 1 ml, the mean magnitude voltage percentage difference between the 0.5 S/m and 3.33 S/m was 0.18%. The exact measurement frame voltages vary for a constant bladder volume, which can impact the bladder state classification.

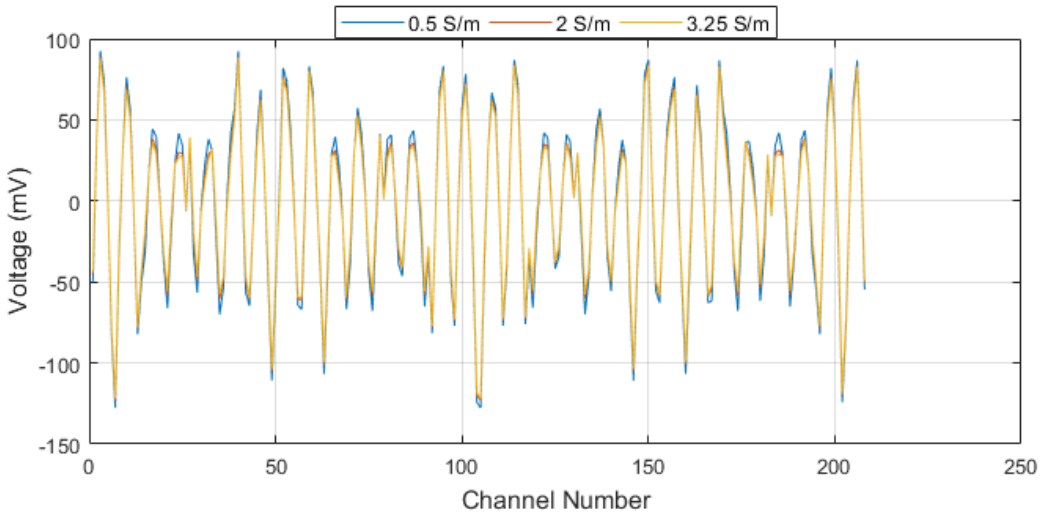

Figure 6.8: Plotted measurement frame voltages for the numerical forward model with a bladder volume of 87 ml and urine conductivities of {0.5, 2, 3.33} S/m. The overall voltage drops as the urine conductivity increases, as expected.

Varying bladder volumes and varying urine conductivities can have similar impacts on the measured voltages, as previously examined in Subsection 3.6.3.1. Therefore, urine conductivity is a form of noise. The machine learning strategies examined in Chapter 4 and Chapter 5 may help extract trends to classify the bladder states in BVM applications for

children. Feature engineering may also help to make a more robust solution by reducing dimensionality, extracting more relevant features, and/or improving overall performance of the classifiers.

In this section, example data was generated to illustrate the effect of adding bone (a less conductive material than muscle or urine) to the model. The child forward model shows similar trends to the adult forward model for varying the bladder volume and urine conductivity on raw EIT measurement frames. The child forward model produces data that has higher voltage differences between bladder volumes and between urine conductivities than the those of adult forward model in Subsection 3.6.3.1. This result may be due to the smaller model size, the bladder location and the electrode configuration differences. Having demonstrated the numerical forward model in action, the limitations of the forward model must now be discussed.

6.9 Limitations of the Child Pelvic Forward Model

In this chapter, a numerical forward model of the pelvic region of a six-year-old boy for BVM EIT was devised, formed, and tested. The forward model was designed to facilitate studies of monitoring bladder volume changes using EIT hardware. To make the forward model more realistic, an anatomically segmented boundary was used along with conductivities of muscle, bone, and urine. Throughout the design, some simplifications/assumptions had to be made. These assumptions include:

- The conductivities of the bladder, bone, and the background are homogeneous;
- The bladder can be sufficiently modelled as an ellipsoid and can be added to the model after meshing without significant effect to the resultant data generated;
- Findings for the bladder volume range of 0-87 ml can be used to infer trends across a greater range of bladder volumes (e.g., 0-210 ml);
- The conductivity of bone can be modelled sufficiently as conductivity of cortical bone.

However, some of these challenges are confined to simulation rather than the real-world. The challenges with remeshing [147] that were experienced with varying bladder volumes for the adult numerical forward model are overcome by meshing the child forward model only once. But the trade-off in meshing only once, is poorer border shape for bladder that changes during data generation. The effect of the poor border shape on the resultant EIT data is potentially minimised by the addition of the element weighted averages and having a highly element dense

mesh. As well as meshing, assumptions made for conductivities such as bone would not be experienced in real-life. However, the assumptions facilitate data generation using only the necessary complexity. Numerical simulation enables controlled study of the effects of varying variables and gaining insight before real-world testing. More advanced studies may be carried out using live subjects such as animal studies like [192] or pilot human studies, after verification of simulation results in phantom studies.

Also, the drop of the bladder volume upper limit from 210 ml to 87 ml may seem large. However, this reduction in the bladder volume range due to the lack of deformation of the bladder around bone can increase the difficulty of the classification problem. The classifiers must determine which bladder volumes belong to which classes, with smaller signal changes in the range of 1-87 ml than in 1-210 ml. Thus, there is strong potential for the classifiers shown if the classifiers can separate bladder volumes in this smaller bladder volume range.

Further improvements can be made to the forward model such as: more refinement of the added bone by including the bone in the initial meshing procedure rather than adding afterwards (such as is done in a number of head studies, e.g., [173]); increased mesh element resolution for more refined bladder volume changes; modelling the bladder so that the bladder can deform around the pelvic girdle; and electrode configuration optimisation to identify the most suitable configuration that is sensitive to changes in bladder volume for children sized bodies.

Importantly, the forward model enables the testing of varying bladder volume in a child size model with the potential to vary key conditions (such as urine conductivity) and increase complexity. The forward model can be discretised again easily to alter electrode configurations arrangements. Additional tissues groups can be added to the model as bone has been. Electrode placements can be varied to give further insight into real-world EIT problems in a controlled fashion [193]. These are studies that may be carried out before or alongside animal and pilot studies for identifying confounders and validating the measurement setups.

6.10 Comparison of Adult and Child Forward Model

In Chapter 3, a simplified 3D cylinder was formed using anatomical information for proportions of the body as well as bladder location and electrical conductivity within the body. These proportions were gathered from medical imaging data for an adult using manual measurement in medical imaging viewing software. The adult forward model was designed to test the potential of bladder state classification with minimal additional complexity beyond the

initial conditions tested such as varying bladder volume, urine conductivities and added noise. The BVM-EIT research to date has been primarily focused on adult applications such as those with urological diseases, spinal cord injury or the elderly [12], [13], [107], [123]. It is also probable that a real-life device solution for children could be required to be evaluated firstly on adults in order to determine reliability and safety of the device.

The anatomical information added to the adult forward model aided in giving insight into the EIT channel voltages expected to be seen from real-life. This level of medical information captured in the adult forward model was considered sufficient at this early stage in design and development. Further research along the adult bladder state classification pathway could include using a realistic boundary to capture a more realistic electrode placement and adding tissues groups for more realistic data generation.

In this chapter, a 6-year-old child forward model was developed to direct the research towards the child monitoring applications such as NE. This forward model was developed to capture the specifics of the child pelvic region, such as smaller girths than adults for electrode placement, different bladder locations and smaller bladder volumes. The relative differences between the adult and child forward models for the size of the model and bladder locations are given in Table 6.3. Notably, the overall bounding box for the child is over 40% smaller than that of the adult along the left-right and anteroposterior axes. The bladder range is much smaller for the child than the adult model. At the specific bladder volumes of 1 ml and 87 ml, the bladder in the child model is positioned closer to anterior along the anteroposterior axis than in the adult case. The bladder also takes up a larger amount of space within the child model compared to the adult model, as shown in the x-y plane of Figure 6.9. Thus, these findings indicate that the child model has greater differences to the adult model designed in Chapter 3 rather than being a scaled down version of an adult.

Also, the number of electrodes has been reduced in the child model due to the decreased size of the child forward model compared to the adult forward model. This reduction in electrodes may lead to less information overall by a reduced number of measurement channels. However, more information may be captured along the craniocaudal plane due to using two rings of electrodes in the child model instead of the single electrode ring in the adult forward model. The height of the rings may also better capture the difference between smaller and larger bladder volumes as the height of the bottom electrode ring in the child forward model is closer to the pubic symphysis along the craniocaudal axis than the ring in the adult model. The

realistic boundary also helps indicate the body curvature that the electrodes may experience and will affect how the current flows from the electrodes for this child forward model compared to the adult cylindrical forward model.

Table 6.3: Quantitative comparison of the adult and child numerical forward models.

Property	Adult	Child
Bounding Box Dimensions	40.74 cm x 23.27 cm x 20 cm	21.52 cm x 13.73 cm x 15 cm
Realistic Bladder Volume Range	0-600 ml	0-210 ml 0-87 ml (with pelvic girdle)
Distance between 1 ml Bladder to Anterior of the Boundary (Anteroposterior Axis at Bladder Midpoint Height)	8.40 cm	3.80 cm
Distance between 87 ml Bladder to Anterior of the Boundary (Anteroposterior Axis at Bladder Midpoint Height)	5.93 cm	4.70 cm
Electrode Configuration	32 Electrode Single Ring	2 Rings of 8 Electrodes Each
Distance between Bottom of Bladder Model to Electrode Centre of Bottom Ring (Craniocaudal Axis)	4.3 cm	1.59 cm

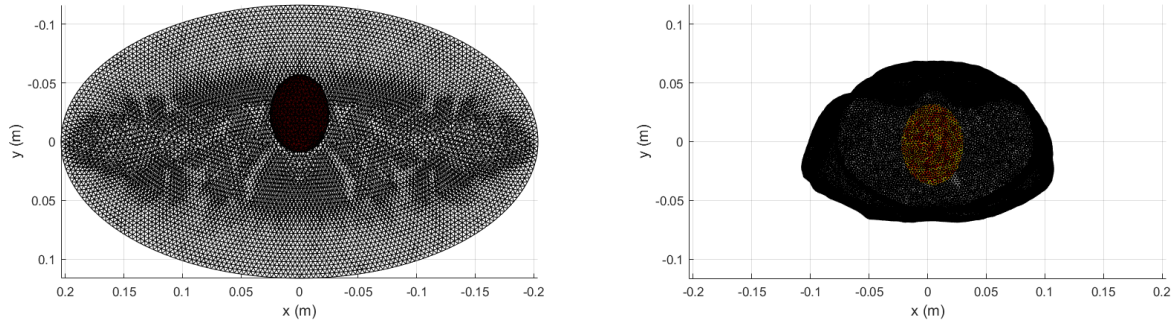

Figure 6.9: Top-down view of the adult (left) and child (right) forward models. Both models are at the same scale and are centred at (0,0) along the x-y plane for comparison. Both models have an 87 ml bladder volume with a urine conductivity of 2 S/m within, shown as red and/or orange. The bone is not shown in the child forward model for clarity. The 87 ml bladder volume takes a considerable amount of space in the child forward model in the x-y plane when compared to the adult forward model.

Bone was added to the child model to make the data generation more realistic, particularly in the form of an increased impedance in the overall body for current flow and resultant measurement voltages. Subsequent effects from design decisions such as a non-deforming bladder model and the bone addition reduced the expected bladder capacity from 210 ml to 87 ml in the child forward model. However, the decreased bladder volume range for the child forward model increases the challenge for the classifiers and gives more confidence in the classifiers working at larger bladder volumes ranges if bladder state can be classified between 1-87 ml.

Importantly, the forward model facilitates capturing measurement data under more realistic conditions for the child due to the anatomically specific considerations applied during the design of the model. This forward model may be used in simulation for controlled testing of conditions that may be difficult to control in the real world such as electrode position.

6.11 Summary

In this chapter, a numerical forward model for a six-year-old boy was developed for BVM-EIT research. The forward model was based on publicly available medical imaging derived CAD files [181], [185][7]. The designed model consisted of three different tissue groups: bone, muscle and urine; as well as realistic structures of the outer pelvic boundary, the bladder and bone. The addition of these tissues in the forward model could give more realistic results and insights at the early prototyping stage of the bladder monitoring device. This chapter outlined a process to create the pelvic region model for BVM-EIT research that could potentially be extended to other models in the Virtual Population [180] (specifically the V2.0 data). The specific content described by each section is summarised below.

Section 6.1 summarised relevant realistic numerical forward models in BVM-EIT. Existing numerical forward models were confined to 2D boundaries from CT or a full adult body. Three-dimensional realistic models in EIT tend to focus on ROIs specifically such as the head. Thus, the need to develop a child pelvic forward model for BVM-EIT was identified.

Section 6.2 highlighted the difficulty in obtaining publicly available medical imaging for paediatric applications. A solution was presented using publicly available CAD files of two children that could be used for paediatric BVM-EIT. Thus, a process could be developed in

[7] The numerical forward model formed is a modified version of the CAD data from the available in [181], [185].

this chapter that could be extended to other similar CAD models that do not require the access to and segmentation of medical imaging files.

Section 6.3 described how the outer boundary can be formed using common CAD operations such as aligning and cutting operations to isolate the pelvic region for EIT simulation. This approach can be used for the other child and adult models available in the virtual population to obtain different body sizes to test a bladder monitor on in simulation or as a basis for phantom creation.

Section 6.4 considered the background conductivity of the numerical forward model. Similar to findings in Section 3.3, a single conductivity value of muscle was selected. While the conductivity outside of the bone or of the bladder is not entirely muscle, the forward model can still give insights into bladder state classification with simulated child EIT data.

Section 6.5 considered the modelling of the bladder. The bladder was considered as an ellipsoid. The bladder was assumed to be composed only of the conductivity of urine. This assumption is similar to previous research in the BVM-EIT field. The realistic six-year-old child bladder volume range of 0-210 ml was determined from the literature. This bladder model facilitates varying bladder volume to gain insight into what raw EIT voltage data may be obtained in reality.

Section 6.6 discussed the addition of bone (upper femurs, pelvic girdle and lower lumber spine). The addition of the less conductive bone (relative to muscle and urine) may provide insight into the effect that the bone in the pelvic region may have on current flow, for example, how electrode channels are impacted in the presence of bone.

Section 6.7 summarised the model designed from Section 6.3 to Section 6.6 and showed the ‘solid’ form of the child pelvic model. The child pelvic model can be used in discretised form with electrodes defined for EIT simulation.

Section 6.8 presented the numerical forward model ready for data generation in EIT software. How the tissues groups were added to the numerical forward model was also discussed. Raw EIT voltage data was generated and the effects of bone, varying bladder volumes and urine conductivities were demonstrated using example noiseless measurement frames. It was found that bone in the numerical forward model led to the expected increase in overall voltage due to an increase in impedance to current flow. For the child forward model, there was improved separation (relative to the adult forward model) between the mean voltages for measurement

frames of different bladder volumes, which could improve bladder state classification. However, there is a similar increase in the difference between mean voltages for measurement frames of different urine conductivities. The variability of urine conductivity is a source of noise for bladder state classification. Thus, the need for machine learning exists in the child application, as it did with the adult application.

Section 6.9 discussed the limitations of the child numerical forward model. The forward model contains assumptions made during the development to simplify the design process. Assumptions are always a part of the numerical forward model design process. However, it is feasible with the forward model to perform BVM studies despite these assumptions. The forward model can complement phantom, animal, or pilot studies in order to test confounders in a controlled fashion.

Section 6.10 discussed the differences in more detail between the adult cylindrical forward model designed in Chapter 3 for early-stage development and the child forward model developed in this chapter. The section highlighted the physical differences between the forward models. Also, these two forward models were developed at different stages in the thesis (initial investigation to more advanced investigations). The child forward model can give more insight into impedance changes within the human body due to added tissues, which can assist in giving results that could be more realistic.

In summary, the first child pelvic forward model for BVM-EIT numerical data generation was created using publicly available CAD models derived from medical imaging data. This process can be used by other researchers in order to reproduce this exact forward model or to develop other child or adult models in the resource [180] for BVM-EIT research. The forward model designed in this chapter has the potential to be used in BVM-EIT child studies investigating the optimisation of electrode configuration in simulation and aiding in phantom development. Importantly, the child forward model can be used to generate raw EIT voltage data to test bladder state classification on the small child size body and on smaller bladder volumes. Machine learning algorithms and feature processing can be applied to perform bladder state classification and to aid in making a robust EIT-based enuresis alarm solution. This topic will be discussed in the next chapter.

7 Bladder State Classification using Machine Learning on Child EIT Measurement Data

In Chapter 5, raw EIT voltage data (also called EIT measurement data) was shown as a promising input to classifiers for bladder state classification. Raw EIT voltage data had the advantage of not requiring the *a priori* information, the assumptions, and the additional computational resources needed by image reconstruction. The research presented in Chapter 5 was implemented on a male adult size forward model. The forward model had a large potential bladder volume range of 0-600 ml, and a large surface area to place 32 electrodes in a single ring configuration.

In Chapter 6, a realistic numerical forward model was devised to support research activities towards child BVM-EIT applications, and to develop relevant EIT data that is in line with the characteristics of bodies of children, e.g., small bladder capacities and reduced body size. The expected bladder capacity for a six-year-old child is 210 ml, but the exact bladder volume can vary greatly between individuals. In this work, the bladder volumes have an upper limit of 87 ml due to the addition of bone within the forward model. Adding this bone to the forward model reduces the expansion space for a non-deformable bladder model. The EIT measurement data generated in Chapter 6 showed a strong difference (11.56%) in the mean EIT voltage between the bladder volumes of 1 ml and 87 ml for a urine conductivity of 2 S/m. However, changes in urine conductivity also affected the mean EIT voltage data. Varying urine conductivities can increase the number of bladder state misclassifications, as shown in Section 5.3.2.

Therefore, bladder state classification is performed in this chapter on data from a child numerical forward model to build on the outcomes from the previous two chapters. Datasets are formed where each observation is different to another based on the combination of bladder volume and urine conductivity. Supervised machine learning is performed using the KNN and SVM classifiers.

In parallel, feature processing and classifier optimisation are also investigated. The aim of using feature processing and classifier optimisation is to determine if the overall performance of the classifier can be enhanced and/or the amount of data stored can be reduced. The feature processing techniques applied in this chapter are all new to the field of BVM using EIT.

Following exploration with different feature processing and model optimisation techniques, the best performing classification model is evaluated against a difficult dataset of misaligned electrode ring positions. The extra error/noise in the measurement data from the misplaced electrode positions is expected in the enuresis alarm application and would be expected to degrade the classification performance. The dataset also contains varying bladder volumes, urine conductivities and added random Gaussian noise.

The remainder of this chapter is divided as follows: the formation of the datasets is discussed in Section 7.1; the classifiers and the optimisation of their hyperparameters are discussed in Section 7.2; the feature processing investigated in this chapter is documented in Section 7.3; the classification architecture is discussed in Section 7.4; the classification results are presented and analysed in Section 7.5; and the chapter is summarised in Section 7.6.

7.1 Formation of Simulated Datasets for EIT Measurement Data Bladder State Classification

In Section 5.1, previous EIT datasets from the literature were discussed along with the design of datasets used in Chapter 5. The datasets in Chapter 5 were used to examine the effect of varying bladder volumes, urine conductivities and added noise on the bladder state classifiers. Also, the datasets of realistic train-test dataset (TC3 dataset) and the continual monitoring dataset (CM1) were designed for observing the classification performance when no condition was specifically excluded for testing.

In this chapter, two datasets similar to TC3 dataset and CM1 are created using child-based numerical data. The first dataset is used for examining classification and feature processing for bladder state classification using raw EIT voltage data. The second dataset is produced for the evaluation of a combined feature processing and trained classifier on an additional unseen noise source., i.e., electrode misalignment. The formation of each of these datasets is discussed in the following subsections.

7.1.1 Dataset Formation for Initial Classification Validation and Feature Processing Investigation

Noiseless measurement frames were generated from the six-year-old boy numerical forward model (designed in Chapter 6) to form unique combinations of bladder volume and urine conductivity for the dataset. Noiseless measurement frames were generated for 86 bladder volumes between 1-86 ml, inclusive. Each bladder volume had 50 different variations of urine conductivity ranging between 0.5-3.33 S/m, inclusive. The resulting dataset contains 4300 unique combinations of bladder volume and urine conductivity. This dataset builds on the findings of Chapters 4 and 5. The analysis in these chapters found that misclassifications can be high, particularly around the separation volume and when there are large variations in urine conductivity values. Therefore, this dataset includes smaller bladder volume gaps around the bladder separation volume (gaps < 10 ml) and more urine conductivities than were included in the datasets of the previous chapters.

Experimental or clinical measurement leads to data that includes noise. While pre-processing may reduce the levels of noise in the EIT measurement data (noise types were previously discussed in Section 3.6.2), it is expected that some noise will be still present in each observation provided to the classifier. Thus, noise is modelled as additive random Gaussian noise (defined in Section 3.6.2). Additive random Gaussian noise is applied to each observation. The noise level is defined by the SNR in decibels. The SNR for each measurement frame is selected by a random uniform distribution. Importantly, each combination of bladder volume and urine conductivity is seen only once in the dataset. Also, the unique combination has a randomly selected level of noise. The range of noise levels considered is {40, 80} dB SNR. This range of SNRs aligns with earlier chapters and previous research in the field, as discussed in Section 3.6.2.

The full bladder volume is considered to start at 44 ml (the bladder separation volume for the child forward model) to enable a balanced dataset. A balanced dataset could be achieved in reality by varying the data collection frequency as a function of time since the last void, as previously discussed in Section 4.1.2 and in Figure 2.14. Note that the first bladder volume associated with the full state also corresponds to the separation volume, i.e., the separation volume between not-full and full is 44 ml.

Figure 7.1 shows example measurement frames for the {1, 44, 86} ml bladder volumes. These frames have a urine conductivity of 0.5 S/m with varying noise levels between 54-73 dB from

the dataset. By visual inspection, the differences between the traces are difficult to determine as the amplitude changes are small. However, the machine learning classifiers could be able to classify the child bladder volume data based on findings in Section 6.8.3. These findings showed that the difference between the bladder volumes of 1 ml and 87 ml with a urine conductivity of 2 S/m was 11.56%. Promising findings were also found in Chapter 5 for bladder state classification on an adult forward model (accuracies over 83.00%).

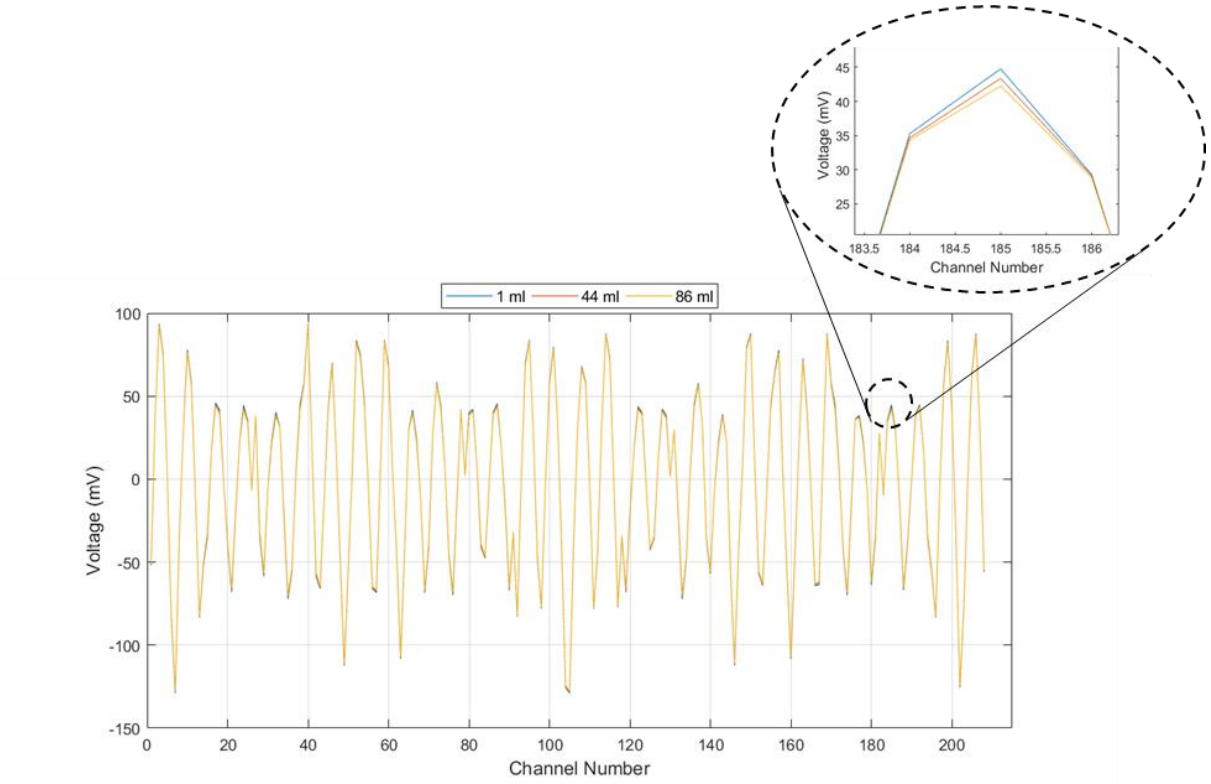

Figure 7.1: Example observations of different bladder volumes (1 ml, 44 ml, and 86 ml) with 0.5 S/m urine conductivity. At this low urine conductivity, amplitude differences between the traces are difficult to discern just by visual inspection.

This dataset is referred to as the Realistic Train Test 2 (RTT2) dataset and is further summarised in Section 7.1.3.

7.1.2 Continual Monitoring Dataset with Misplaced Electrode Locations

A continual monitoring dataset is formed in this subsection to evaluate the robustness of the classifiers developed using the RTT2 dataset. In reality, electrodes may not be placed in the same location each time they are applied. Additionally, electrodes may move slightly between recordings, due to poor contact with the body and body movement. Electrode position errors could have serious effects on electrical impedance measurements when electrodes are placed

in slightly different locations across multiple recordings [194], [195]. Consequently, these errors could affect the reliability of the developed alarm device for children with NE.

Different approaches of examining electrode misplacements in other fields of EIT have been examined in the literature, ranging from moving electrodes individually to moving full electrode rings [195]–[197]. In this work, full electrode ring misplacements are considered. This case models electrode rings embedded in a belt or pyjamas, which allows equal distancing between the electrodes and reduces the risk of individual electrode misplacement errors. Thus, the variations of two electrode rings are considered for use in child-based EIT bladder monitoring. Different scenarios can be analysed: where both electrode rings are misplaced together and when the rings are misplaced differently from each other. The two scenarios then become: 1) both electrode rings are misplaced as a unit; 2) both electrode rings are misplaced, but each ring is misplaced differently. Both scenarios assume that the electrodes are never placed in the exact same locations across different applications of the electrodes. This testing also assumes that the distance between electrodes/relative electrode positions within each ring is fixed, and that the whole ring misplacement is a greater source of error than an individual or subset of electrodes being misplaced.

Four cases are considered in the scenario of the electrode rings misplaced together. The misplacement is performed by shifting the electrode rings along the axial plane by ± 10 mm (referred to as ‘Right10’ and ‘Left10’). Also, vertical misplacement is performed by ± 10 mm along the craniocaudal axis (referred to as ‘Up10’ and ‘Down10’). A snapshot of these misplaced electrode configurations is shown in Figure 7.2, along with correct electrode placements (‘Original’). In the figure, a subset of 6 of the 16 electrodes is shown (three in each ring) for ease of visualisation. However, the misplacements are applied to all electrodes in each ring as discussed above.

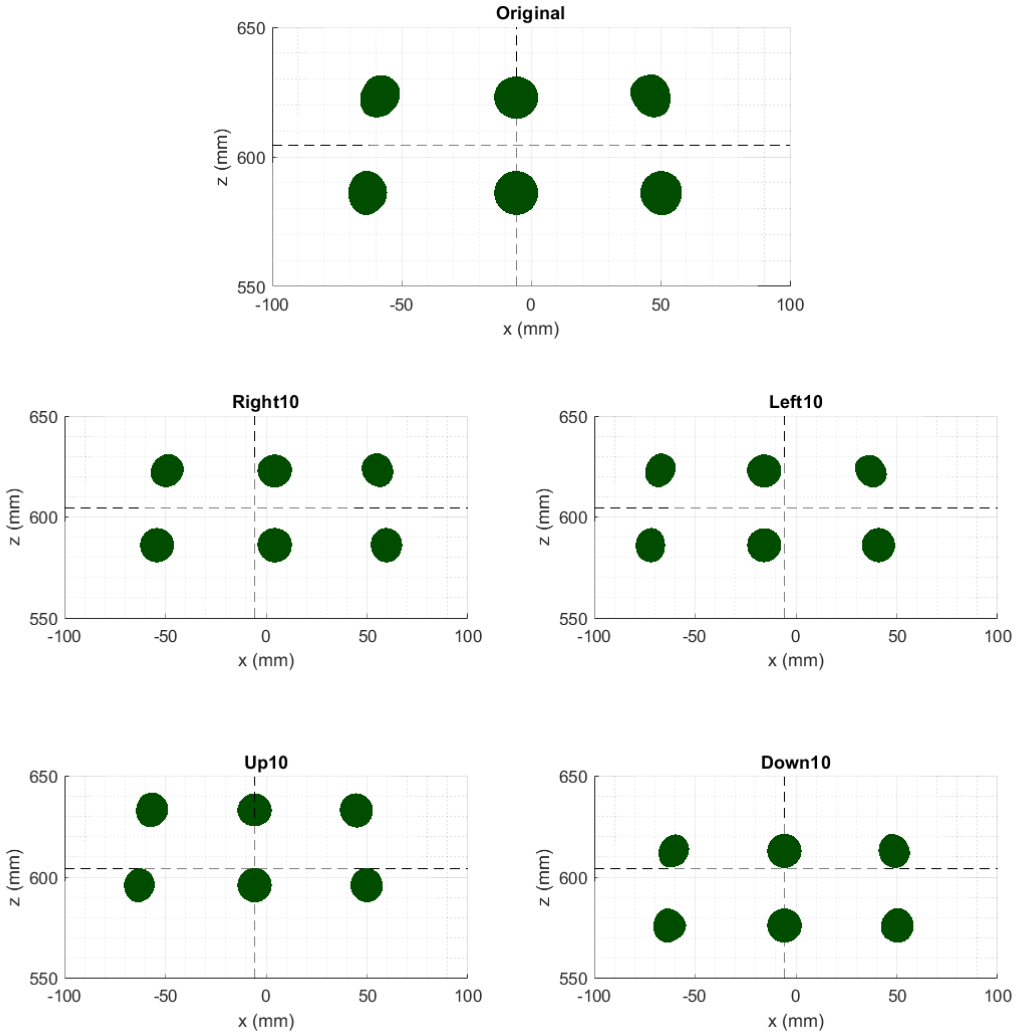

Figure 7.2: Snapshots of the six anterior electrodes for five different electrode configuration positions: electrodes in the correct position ('Original'); electrode rings shifted anterior right by 10 mm ('Right10'); electrode rings shifted anterior left by 10 mm ('Left10'); electrode rings shifted towards the head along the craniocaudal axis by 10 mm ('Up10'); electrode rings shifted down away from the head along the craniocaudal axis by 10 mm ('Down10'). Orthogonal axes with intercepting points of (x = -5.71 mm, z = 604.28 mm) are placed for reference between the snapshots. The shape of each electrode is circular. However, this image is a 2D capture of a 3D space. Thus, some electrodes appear elliptical. The misplacements of electrode rings in this figure mimic the electrodes of both rings acting as a unit on one belt.

The scenario where each ring is misplaced differently is also considered. The cases considered are: i) the two rings moved apart in the craniocaudal (vertical) axis by an extra 20 mm, specifically where each electrode is shifted by 10 mm ('Apart10') as compared to the original case; ii) the rings 10 mm moved closer vertically than the original case ('Together5'); and iii) the rings misplaced from their original centres by 10 mm in the axial plane, with the rings misaligned in opposite directions ('Left Bottom, Right Top' and 'Right Bottom, Left Top').

This results in a total of four different configurations (excluding the original), each considering a specific type of ring misplacement. These configurations consider each ring independently, one step above moving each electrode independently. These cases could be applicable when the electrode rings are embedded in fabric material where twisting and stretching vertically is possible or there are two separate belt rings, but most of the movement impacts each ring as a whole. A snapshot of these misplaced electrode configurations is shown in Figure 7.3. The corresponding subset of electrodes for the correct electrode placements ('Original') are also shown in Figure 7.3 for reference.

Thus, the continual monitoring dataset contains data generated from eight misplaced electrode configurations, as well as data from the original configuration for comparison. The misplaced electrode configurations consist of four misplacement scenarios of both rings moving together, and four misplacement scenarios of the rings moving independently. This dataset is referred to as the continual monitoring 2 (CM2) dataset.

To specifically demonstrate the effect of misplaced electrode rings, noiseless data was generated for a 79 ml bladder volume of urine conductivity 2 S/m, as shown in Figure 7.4. Figure 7.4 shows traces that are visibly highly distorted from each other. The main change between the traces is caused by the electrode misplacement. This finding can be established since each trace results from noiseless simulations on the same bladder volume and the same urine conductivity, but different electrode configuration placements.

To quantify the changes in the traces, the percentage differences of the mean magnitude between each trace and the correct electrode positioned voltage trace were calculated. These percentage difference values are documented in Table 7.1 and range from 0.9-14.63%. The highest percentage differences corresponded with electrode ring misplacement that were altered along the craniocaudal axis (vertical displacements). Large volume changes between the electrodes occur between the vertical misplacements. These volume changes could have a substantially larger effect on the current flow in the body than electrode misplacements along the axial plane. Large changes in current flow will result in large changes in the measured electrical potential. Notably, the percentage difference values are greater than those that were found between different bladder volumes and between different urine conductivities, detailed in Section 6.8.3. Thus, misplacement of electrode rings could negatively influence classification performance by introducing changes in measured voltages that are larger than the changes induced by bladder volume.

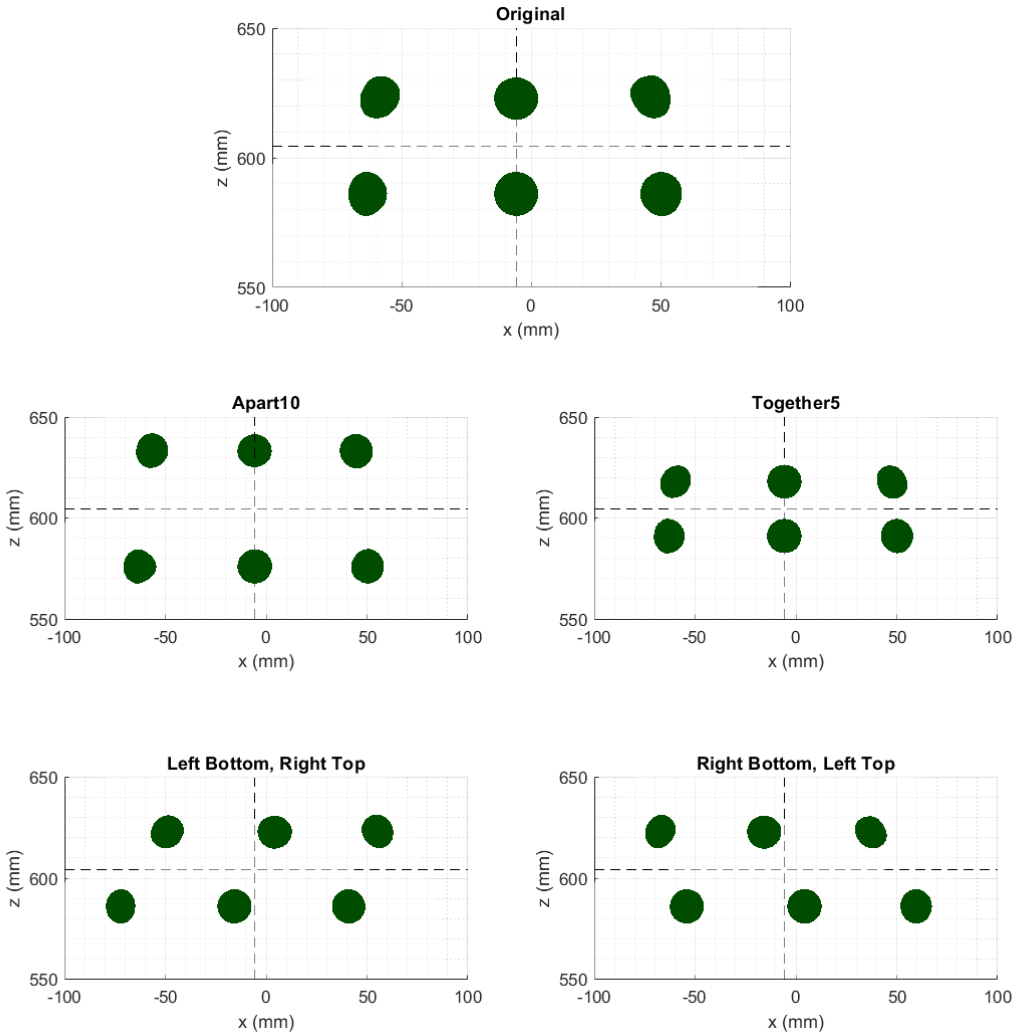

Figure 7.3: Snapshots of the six anterior electrodes for five different electrode configuration positions: electrodes in the correct position ('Original'); electrode rings shifted apart along the craniocaudal axis by an extra 20 mm, each electrode shifted vertically by 10 mm ('Apart10'); electrode rings shifted towards each other along the craniocaudal axis with a minimum vertical distance with the electrode edges of 5 mm ('Together5'); the bottom electrode ring shifted anterior left by 10 mm and the top electrode ring shifted anterior right by 10 mm from their correct electrode positions along the axial plane ('Left Bottom, Right Top'); the bottom electrode ring shifted anterior right by 10 mm and the top electrode ring shifted anterior left by 10 mm from their correct electrode positions along the axial plane ('Right Bottom, Left Top'). Orthogonal Axes with intercepting points of (x = -5.71 mm, z = 604.28 mm) are placed for reference between the snapshots. These misplacements of electrode rings consider each electrode ring acting individually as a unit and the rings misplaced differently.

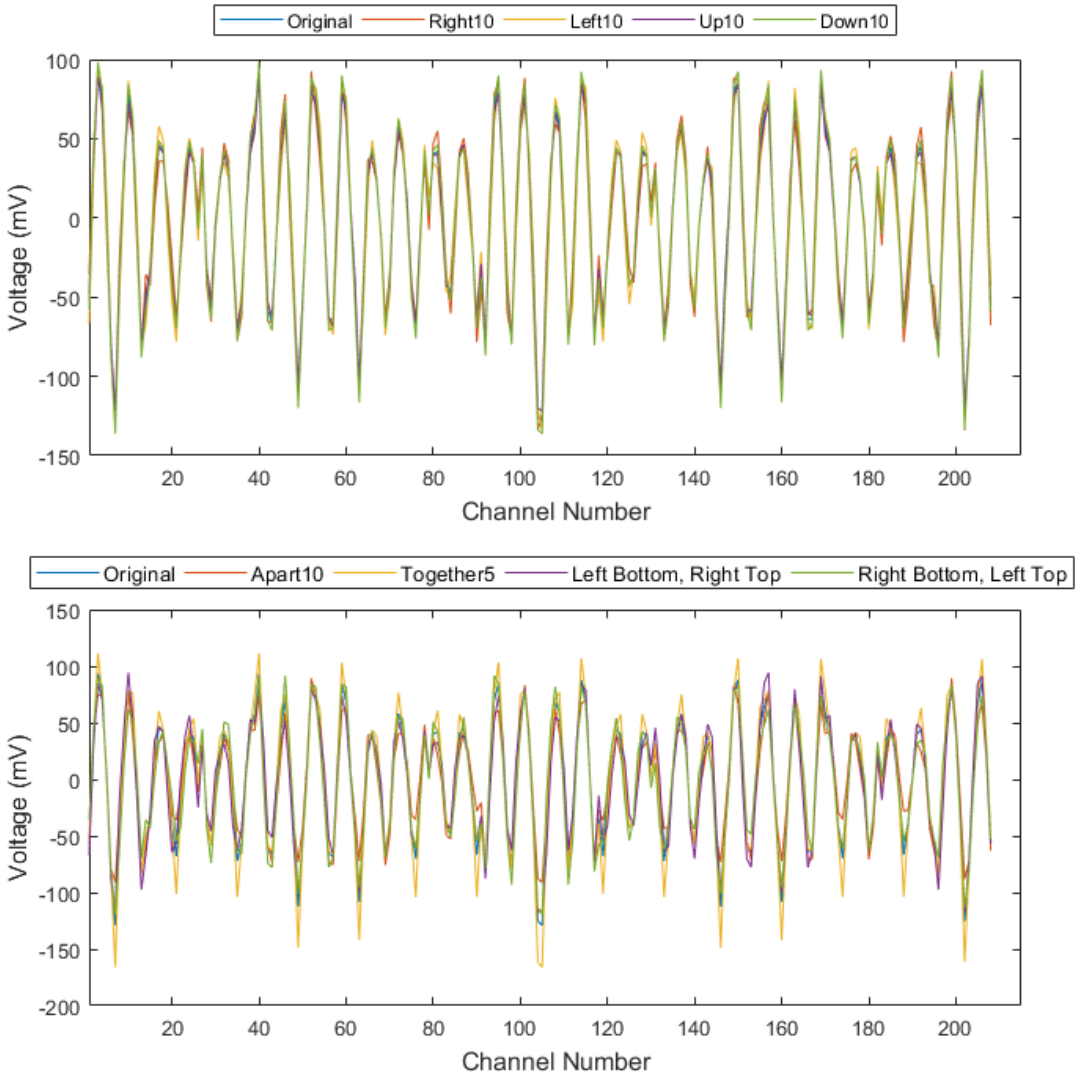

Figure 7.4: Simulated noiseless measurement data from the different misplaced electrode configurations for a 79 ml bladder volume and 2 S/m urine conductivity bladder model. (top) Measurement frame traces for electrode rings misplaced together; (bottom) Measurement frame traces for electrode rings misplaced differently. With the change of electrode ring locations, the measurement frames for the same bladder model are greatly different from the measurement trace of the correct electrode location model ('Original'). The exact differences are quantified in Table 7.1.

Table 7.1: Percentage differences of the mean magnitude between the simulated voltage for each scenario of electrode ring misplacement and the simulated voltage for the correct electrode ring positions ('Original'), calculated from the data plotted in Figure 7.4. In the cells shaded yellow, the electrode rings were moved together. In the cells shaded green, they were moved separately. The "Up10", "Down10", "Apart10", and "Together5" misplacement scenarios involve vertical movements of the rings, while the others involve horizontal movements.

Electrode Misplacement Model	**Percentage Difference**
Right10	1.97%
Left10	1.08%
Up10	3.00%
Down10	5.63%
Apart10	14.63%
Together5	13.27%
Left Bottom, Right Top	0.90%
Right Bottom, Left Top	1.93%

In total, the CM2 dataset contains 900 observations (100 observations for each set of electrode locations). The bladder volumes, the urine conductivity, the level of the added noise vary based on uniform random distributions. Each numerical forward model with differently placed electrodes was randomly assigned to generate one ninth of the dataset. The dataset also contains 100 observations from the correct electrode locations model for comparison.

When adjusting the electrode positions, the forward model needed to be converted from a CAD model to FEM. Differences in the meshing between the nine numerical forward models lead to a maximum bladder volume of to 79 ml rather than 86 ml (to prevent the bladder intersecting the pelvic bone). However, this is a limitation when remeshing the forward model with varying electrode positions and under the same specified mesh resolution. With the change in the upper bladder volume range, there is slight imbalance in the number of the potential bladder volumes (and subsequently the observations) in each of the not-full and full classes ({1, 43} ml and {44, 79} ml, respectively). From findings in Section 5.3.1, the bladder volumes on either extreme of the bladder separation volume are less susceptible to misclassification. The slight

unbalanced of the bladder volume ranges for each class ({1, 43} ml and {44, 79} ml) could be more realistic where less 'full' labelled bladder volumes are captured and balancing the dataset is performed only during training and testing, not continual monitoring. To ensure fairness in assessment for both the randomness in data generation of bladder volumes as well as the not-full and full ranges, the classification accuracy calculation will be performed with the balanced accuracy equation [198]. The equation is defined as:

$$Balanced\ Accuracy = \frac{\frac{TN}{TN+FP}+\frac{TP}{TP+FN}}{2}, \tag{7.1}$$

where *TN*, *FP*, *TP*, and *FN* are the true negative, false positive, true positive and the false negative values, respectively. In other words, the balanced accuracy is the average of the sensitivity and specificity. The exact proportion of not-full labels in this CM2 dataset is 53.78%.

This dataset is referred to as the second continual monitoring dataset or CM2 and the dataset is further summarised in Section 7.1.3.

7.1.3 Summary of the Datasets

Two main datasets are used in this chapter. The first dataset is for forming the classifiers and evaluation (RTT2). The second dataset is for reliability testing when the classifiers are given a new unseen condition that could affect the alarm device in the real-world (CM2), e.g., varying electrode position errors. These datasets are summarised in Table 7.2.

Table 7.2: Characteristics of each condition in the dataset used in Chapter 7.

Dataset	**SNR**	**Bladder Volume**	**Urine Conductivity**	**Misaligned Electrode Positions**
RTT2	4300 SNR Levels from a Random Uniform Distribution over {40, 80} dB	Not-Full: {1 + n} ml Full: {44 + n} ml where n = 0, 1, 2, 3, …, 42	$\{0.5 + \frac{3.33-0.5}{49}p\}$ S/m where p = 0, 1, 2, 3, … 49	None
CM2	900 SNR Levels randomly selected from a Uniform Distribution over {40, 80} dB	900 Bladder Volume from a Random Uniform Distribution of Integers over {1, 79} ml	900 Urine Conductivities from a Random Uniform Distribution over {0.5, 3.33} S/m	Original FEM and 8 Misaligned Electrode Ring Locations

†To two decimal places

7.2 Classifiers and Hyperparameter Optimisation

In the earlier chapters, the classifiers of the KNN and SVM were employed based on the successful use in BVM [92]. From the trends observed in Chapters 4 and 5, both classifiers showed strong potential for bladder state classification and performed similarly in terms of overall classification accuracy. However, both classifiers used pre-set settings in the previous chapters, such as the number of nearest neighbours. The settings of the classifier that are configured prior to training the model (e.g., by the user or an external optimisation tool) are referred to as the hyperparameters [163]. However, these pre-set hyperparameters may be sub-optimal and changing the hyperparameters allows formation of different variants of the same classification algorithm that may have improved classification performance on a specific problem [199]. The hyperparameters for KNN and SVM are discussed in Section 7.2.1 and Section 7.2.2, respectively. Then, methods to select the most suitable hyperparameters are discussed in Section 7.2.3.

7.2.1 Hyperparameters for KNN

The KNN classifier is a lazy-learner algorithm that evaluates at run-time. The algorithm compares test observations to the stored observations based on a distance metric. Based on this comparison, a label is assigned to the observation being classified. In Chapters 4 and 5, the Euclidean distance metric and 9 nearest neighbours was used. However, the distance metric and *k* are hyperparameters of the KNN that can be optimised to help improve the performance of the classification.

In this work, the three-distance metrics evaluated were the Euclidean [167], Manhattan [167] and Chebyshev [200] distances. All three metrics are specific cases of the Minkowski distance ($Dist_{Minkowski}$) [167], [200], which is defined as:

$$Dist_{Minkowski} = \left(\sum_{i=1}^{n} \left|x_{a_i} - x_{b_i}\right|^q\right)^{\frac{1}{q}}, \tag{7.2}$$

where x_{a_i} and x_{b_i} are values for feature *i* in both observations *a* and *b*. The Manhattan distance (q = 1 in Equation (7.2)) takes the sum of the absolute differences between two observations [163]. The Manhattan distance is subsequently a distance option that is less computationally expensive than Euclidean distance (q = 2 in Equation (7.2)), where the Euclidean distance contains a square function and square root function. Chebyshev distance (as q approaches infinity in Equation (7.2)) takes the maximum difference along all the absolute differences for the two observations. These distances are investigated to determine if any one version provides a better fit for the data. Other similarity-based distances metrics (examples listed in [200]) can be investigated in future work.

Typically, *k* is odd for binary classification [167]. Thus, *k* is examined for odd numbers between 1 and 49, inclusive. This range allows exploration of the nearest neighbour values that are not too large, preventing *k* being too large to identify the separating regions [167].

For selection of the label, each of the *k*-nearest neighbours can have an equal vote in the labelling of a new observation. However, the voting step may be refined by giving neighbours closer to the observation more influence in the decision of the new label [201]. To determine if weighting the vote can help improve performance, the following weighting options are considered during optimisation: equal weighting, inverse distance weighting and inverse squared-distance weighting. These are options available in commonly used machine learning packages [202], [203].

The most suitable values of hyperparameters for a classifier are problem specific [167]. In this work, a sample of the possible hyperparameter options are examined. However, future work can examine additional values of hyperparameters if needed to further enhance classification accuracies.

7.2.2 Hyperparameters for SVM

The SVM used in earlier chapters used a linear kernel with a box constraint equal to one, a default set of hyperparameters for SVM. This version of SVM was used to gather initial insights and investigate specific conditions impacting bladder state classification. However, one of the main reasons to use the SVM classifier is due to the 'Kernel Trick' [204]. With the Kernel Trick, the data can be transformed indirectly into a higher dimensional space based on a chosen non-linear kernel [204]. The Kernel Trick is employed to aid in improving the separation of the data by a hyperplane [204]. Non-linear kernels include the radial basis function (RBF) and non-linear polynomials [205], which have been used in other medical applications [206]–[208]. The kernel that best suits the data is also a hyperparameter. Therefore, the kernels examined in this investigation are the linear and RBF kernels, as well as non-linear polynomials.

The four hyperparameters considered for SVM are: the kernel (linear, RBF, or polynomial); the polynomial order (between 2 and 5, inclusive); the box constraint; and Gamma (Gamma applies only for RBF SVM and Gamma controls the spread of the Gaussian function [209], [210]).

To select the optimal hyperparameters, optimisation algorithms are needed to assess the effect of the different combinations of hyperparameters on the classifiers. The optimisation algorithms are discussed in the next subsection.

7.2.3 Classifier Optimisation Tools

In this work, two forms of optimisation techniques are employed: 1) Grid Search; 2) Bayesian optimisation. Both of these algorithms have the potential to find the optimal or near optimal hyperparameters for the given data, which is very useful when the data collected can vary inter- and intra-individual and when the data collected varies over a long period of time, i.e., days.

Grid Search works by evaluating each unique combination of hyperparameters to find the best performing combination for a given evaluation metric. Computing all possible combinations of hyperparameters as in Grid Search can be time and resource consuming, particularly when

there are a large number of hyperparameters (i.e., a large search space) [211]. Where there are a large number of hyperparameters (e.g., four or more), Bayesian optimisation can be used.

Bayesian optimisation [212]–[214] is a black-box optimisation technique that takes account of previous evaluations and their objective score (e.g., cross-validation error) in the optimisation process to choose the next settings (e.g., hyperparameters) to be investigated. Thus, this algorithm more intelligently selects where to investigate the next point in the search space compared to Grid Search.

In this work, Grid Search is used in the cases where the hyperparameter values are discrete and where the unique combinations in the search space are less than or equal to 150 unique combinations (i.e., KNN without any optimisation of the number of input features). The 10-fold cross-validation average accuracy was used as the evaluation metric to be optimised in the Grid Search.

Bayesian Optimisation is then used for both KNN and SVM classifiers where the search space is greater than 150 unique combinations. The number of evaluations for Bayesian Optimisation was constrained to the number of hyperparameters, similar to [215], [216]. In this work, 50 evaluations are performed for each hyperparameter (e.g., optimising the four hyperparameters of the SVM classifier would involve 200 evaluations with Bayesian Optimisation). This constraint may improve the comparison between the trained models that vary in terms of the classification algorithm, the number of hyperparameters, and the optimisation method. Bayesian Optimisation is used to minimise the 10-fold cross-validation average error evaluation metric.

Another way of improving the performance of the classifier is by improving the data provided to the classifier. Feature processing techniques can be applied to remove redundant information or to transform the data to better describe the collected data. Feature processing is described in the next section.

7.3 Feature Processing on EIT Measurement Data

As an alternative to inputting raw EIT measurement data to the classifier, the data in the observations can be further processed before input to the classifier. Processing can include removal of redundant and/or less important features and feature transformation to aid in improved overall classification performance [217], [218]. The main difference between different bladder volumes can be observed in the amplitudes of the voltages in EIT

measurement frames as seen in Figure 7.1. The voltage measurements in a frame are collected at one time (time between measurements in a serial EIT data collection system is neglected) or from a filtered window of frames. Thus, many common time and frequency signal processing and image processing techniques may not be appropriate or help to determine the optimum features in a single measurement frame. However, feature techniques such as feature selection and feature transformation could aid classification by selecting a more relevant subset of features or creating a new set of features that better describe the dataset.

In this work, feature selection algorithms designed for bioimpedance and ranking features based on a specific criteria (termed filter feature selection [217]) are used. In Section 7.3.1, a custom feature reduction algorithm designed for EIT using a Principle of Reciprocity in bioimpedance [97] is discussed. In Section 7.3.2 the supervised filter-based approach is discussed to help select the best channels based on the obtained labels for classification. These channels could be associated with key electrodes such as those nearest the bladder and hence, provide the most relevant information for classification.

Feature transformation algorithms can be used to identify new features that may better summarise the dataset, and therefore be used as input for the classification. In Section 7.3.3, the unsupervised feature transformation Principal Component Analysis (PCA) process is discussed. The use of these feature processing tools is novel for BVM using EIT measurement data.

It is important to note that a hardware dimensionality reduction has occurred between the adult and child models due to the reduction of 32 electrodes to 16 electrodes. Fewer measurements per frame are collected with the child numerical forward model. But, a more optimum electrode configuration is employed, i.e., 2 rings of electrodes to capture 3D current flow and 3D bladder filling, rather than the single ring configuration of the adult model. Thus, classification is performed on 208 voltage features in this chapter rather than the 928 voltage features used in Chapter 5.

7.3.1 Feature Reduction using Reciprocity Principle

In Chapter 5, each measurement in the EIT measurement frame was used as a feature for classification with raw EIT voltage data. This process was similar to the state-of-the-art for bladder volume estimation [115], [124], where the neural network and SVDM were used. However, the Principle of Reciprocity for bioimpedance (also referred to as the voltage-current

reciprocity [219]) indicates that only half of the measurements are independent (i.e., $\frac{n(n-3)}{2}$ for a EIT system with *n* electrodes and no measurements captured or kept from injection electrode pairs) in an ideal scenario (e.g., no noise differences between the electrode pairs such as contact impedance or instrumentation noise mismatches) [124], [219]. Specifically, the Principle of Reciprocity states the data measured for a set of injection and measurement electrode pairs is the same when injection and measurement electrode pairs are switched [97], [219], [220]. This principle is illustrated in Figure 7.5.

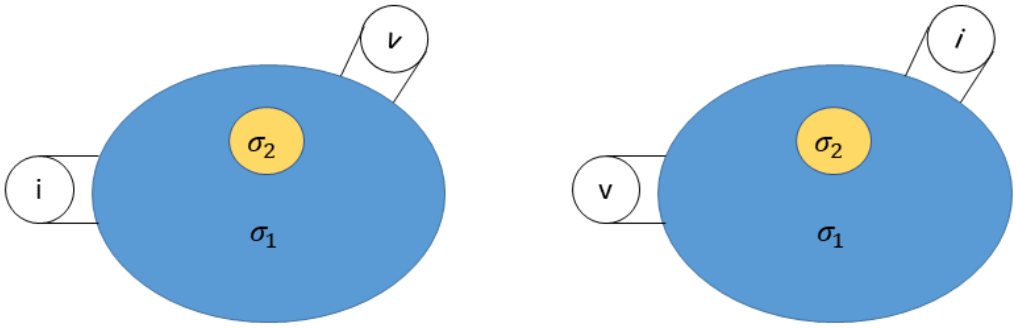

Figure 7.5: Illustration of the bioimpedance Reciprocity Principle. The symbols i, v, σ_1, *and* σ_2 *represent the injection of alternating current, the measuring of the resultant voltage, and the two different conductivity regions, respectively. The measured voltage is the same when the electrode pairs injecting and measuring are swapped in ideal scenarios. Thus, this principle can be used to remove potentially reduntant features and reduce the number of features in the dataset by half.*

Potential breaches of this principle can include noise sources such as non-matching electrode contact impedance and faulty electrodes, as well as physiological changes occurring between the two reciprocal measurements in a serial data collection EIT system [219], [220]. In the case of Chapter 5, noise was added to measurement frames making the observations non-ideal and non-reciprocal.

The Principle of Reciprocity has been used in EIT for determining faulty electrodes [219], in system performance and data quality [100], [220], and in making efficient image reconstruction investigations [221]. In this work, the Reciprocity Principle is used to perform feature reduction in machine learning classification with EIT. An algorithm eliminating reciprocal measurements in the observations could be applied to reduce the potentially highly dependent features in the dataset. This algorithm could be a feature pre-processing step to remove redundant information in the observations before applying stronger feature processing techniques, e.g., Fisher Score Feature Selection and PCA. This process would be akin to using some statistical based feature selection techniques before stronger feature selection tools [217]. The advantage of using an

algorithm to remove reciprocal measurements is that removal of strongly correlated features can reduce redundancy, potentially reducing the storage and computational processing required. Also, the algorithm enables noise removal strategies, such as selecting data from the least noisy reciprocal channel to give to the classifier.

7.3.2 Ranking Features using Fisher Score Feature Selection

In Chapter 5, 928 channels per observation (i.e., 928 features per observation) was used as an entry in the datasets. This large number of channels came from the EIT voltage measurements at 32-electrodes spread in a ring configuration all around the body. For the 16-electrode system used in this chapter, a measurement frame contains 208 measurement voltages. However, certain channels may provide more information relating to bladder volume changes while others may not carry changing bladder volume information at all. Thus, features may be dropped and the overall dimensionality of the dataset reduced.

In this work, the Fisher Score feature selection algorithm is used to rank the features in the dataset. Fisher Score assesses and ranks features based on how values of a feature are similar for one label and how different these values are to values of the feature of the other labels [217], [222]. The algorithm considers each feature independently, i.e., without consideration for feature interaction [222]. Thus, the reciprocal EIT measurements are removed before applying the Fisher Score algorithm to remove potential redundancy. This processing means the Fisher Score is applied on 104 input features.

The top ranked features are chosen as part of the optimisation of the hyperparameters of the classifier. This process tailors the best ranked features for the classifier and avoids a complete search by the classifier over every possible combination of features in a full wrapper feature selection implementation. This empirical selection process is similar to the selection of the number of top ranked-PCA components by the classifier in [92]. The best features for the classifier are then selected by the performance observed rather than by selecting a fixed user defined number of features that may not be optimal.

A feature transformation method is also considered in this work. The PCA algorithm is discussed in the next subsection.

7.3.3 Feature Transformation using Principal Component Analysis

Principal Component Analysis (PCA) is a commonly used unsupervised feature transformation and dimensionality reduction algorithm. Principal Component Analysis transforms a dataset

into linearly independent features referred to as principal components [167]. The algorithm executes this transformation by forming linear combinations of the original features [167] with each linear fit constructed orthogonal to each other [218]. The resultant principal components are subsequently ranked in order of the maximum variance explained by each principal component. Often, most of the original information content can be contained in a subset of top ranked principal components [218]. Thus, a subset of a number of top ranked principal components can then be selected and their values (referred to as 'scores') can be given to the classifier [207].

The PCA algorithm has been used in binary classification tasks of related fields such as microwave breast detection and BVM-microwave applications [92], [223]. The algorithm has been previously used in EIT image studies by the author [224] and in [207] for brain-EIT classification applications using raw EIT voltage data, where strong potential for the use of PCA in improving classification performance has been shown.

The PCA algorithm is investigated for the first time in BVM EIT measurement data classification, and on realistic child-based data to determine if the transformation can help improve performance of the classifiers. The number of top-ranked features is optimised along with the hyperparameters of the classifiers.

7.4 Classification Architecture

In Section 4.3 and Section 5.2, the selection of classification architecture depended on the problem being investigated, as well as the amount of data available. In Chapters 4 and 5, the stratified L2COCV (modified LPCOCV for binary bladder state classification), LOCOCV, and stratified 5-times repeated 10-fold cross-validation were employed. The stratified 5-times repeated 10-fold cross-validation was used for evaluation of the classifiers when no condition was specifically excluded. The advantages of stratified 5-times repeated 10-fold cross-validation was that it further reduced the bias from stratified 10-fold cross-validation of using one random 10-fold split of the dataset. However, this came at the cost of an increased number of evaluations and increased computational power.

In this chapter, the dataset size is larger than used in previous chapters (i.e., 4300 observations in this chapter compared to 3120 observations in Chapters 4 and 5). However, the dimensionality of the dataset has also decreased due to the reduced number of electrodes (a 77.59% reduction from 928 features in previous chapters to 208 features here). Thus, a single

stratified 10-fold cross-validation is considered sufficient for overall evaluation of the model. The architecture allows the generalised performance to be evaluated while reducing the bias of just picking one train-test set from a dataset [167].

With the addition of feature processing and hyperparameter optimisation, nested cross-validation is required. The nested cross-validation is employed so that no data is leaked between the training and test datasets (within nested and outer cross-validation). This process helps eliminates data leakage/contamination, ensuring more reliable results [171]. The overall architecture is given in Figure 7.6. The outer cross-validation uses 10-fold cross-validation for evaluation of the classifier, while the nested cross-validation for hyperparameter selection and feature processing uses 5-fold cross-validation. This architecture allows the exploration of different optimisation methods for the classifiers as is one of the aims of this chapter.

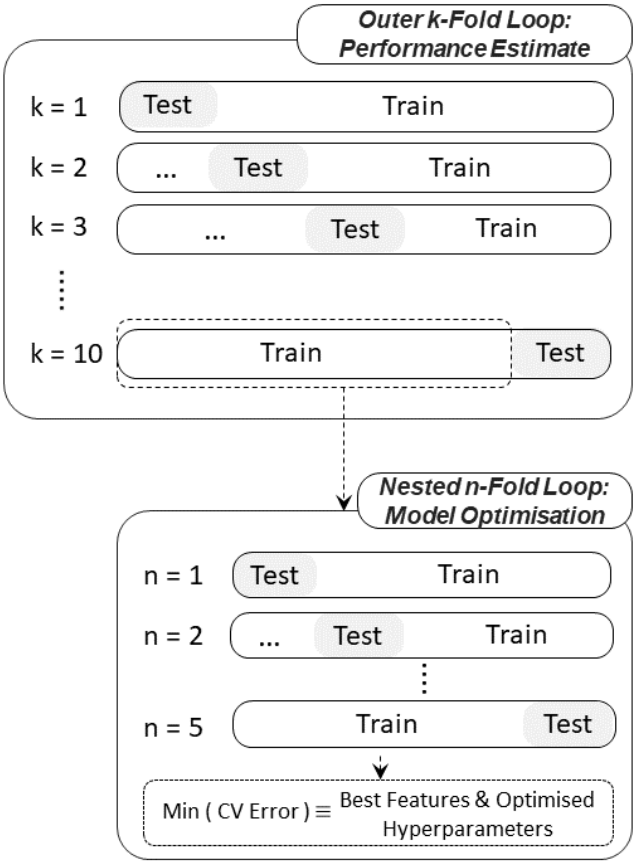

Figure 7.6: Stratified k-fold cross-validation (CV) architecture with nested stratified n-fold cross-validation. The outer stratified k-fold cross-validation architecture is used for fair assessment of the classifiers while the nested stratified n-fold cross-validation architecture is used for model optimisation in terms of both the best features (for feature processing if used) and the optimised hyperparameters for the classifiers. In this chapter, k and n are equal to 10 and 5, respectively. This image has been adapted from Figure 5 in Oliveira et al. [171] *that is licensed under CC BY 4.0* [141].

As a baseline, the pre-set hyperparameters of the classifiers used in Chapter 4 and Chapter 5 are also used in this chapter for comparison. The classification models with pre-set hyperparameters are trained and tested using the stratified 10-fold cross-validation architecture without nested cross-validation (i.e., only the outer loop in Figure 7.6 is needed as the nested cross-validation is not required to select hyperparameters or number of features).

7.4.1 Feature Scaling

For the KNN and SVM classifiers and PCA, feature scaling is used to prevent any feature dominating the classification because of a larger scale than other features in the dataset. Thus, standardisation (previously discussed in Section 4.3.2) is performed. Standardization is performed just before the observations are given to the classifiers except where PCA is used. When PCA is employed, standardisation is performed before applying the PCA algorithm.

Combining all the stages from Section 7.1 to Section 7.4, the next section presents and discusses results from the investigation of the potential of bladder state classification on child EIT measurement data, classifier optimisation and feature processing.

7.5 Investigating Bladder State Classification on Child Raw EIT Voltage Data

In this section, the results for classification are presented and discussed. The results and discussion sections are divided between the classifiers with pre-set hyperparameters, the classifiers with optimisation, and the classifiers with feature processing. Following the BVM raw EIT voltage data domain exploration, the best performing classifier is selected and trained on the dataset. Then, this classifier is tested against the CM2 dataset that contains data from misplacement electrode rings.

7.5.1 Feature Processing and Classifier Optimisation Results and Discussion

7.5.1.1 Classification with Pre-Set Hyperparameters

In this subsection, the classification was performed to observe using the pre-set hyperparameters for the classifiers of KNN and SVM discussed in Section 7.2. These pre-set hyperparameters were used in the bladder state classification investigations in Chapter 4 and Chapter 5 for adult forward model data. Using similar classifier settings allows comparison between the adult and child models that have different body sizes, electrode configurations and

bladder volume ranges. The RTT2 dataset used for training and testing was outlined in Section 7.1 and Table 7.2.

Average accuracies of 97.79% and 96.98% were achieved for KNN and SVM, respectively, as reported in Table 7.3. These performance results are similar to those observed in Section 5.4 for the adult numerical forward model, which had: a bigger cross-sectional area; a deeper bladder within the body; more electrodes; and a single ring of electrodes for data collection. Therefore, high performance in classifying not-full and full bladder states can be achieved in the child body as well as in an adult with the aim of proactively alerting a full bladder. The trends observed in Section 5.3 and Section 5.4 of high misclassification rates around the bladder separation volume, high misclassification rates for low urine conductivity values and increasing misclassifications with higher amounts of measurement frame noise were also observed in this experiment. These findings are important as prototypes may be initially tested on adults before children for better experimental control and reduced risk to vulnerable individuals during device development.

The pre-set hyperparameters used are just one possible combination of hyperparameters. Classification performance can vary based on the hyperparameters chosen. Thus, the classification performance may be improved by selecting a different hyperparameter set using optimisation techniques discussed in Section 7.2. The findings of hyperparameter optimisation are presented in the following subsection.

Table 7.3: Performance results of running classifiers with pre-set hyperparameters on the RTT2 dataset. The Box Constraint is represented by C.

Classifier	Accuracy (%)	Sensitivity (%)	Specificity (%)
Euclidean KNN (k=9)	97.79 ± 0.71	97.54 ± 0.70	98.05 ± 1.20
Linear SVM (C=1)	96.98 ± 0.74	97.12 ± 1.00	96.84 ± 1.35

7.5.1.2 Classification with Hyperparameter Optimisation

Using Grid Search for the KNN algorithm (150 evaluations) and Bayesian Optimisation for SVM (200 evaluations), the hyperparameters discussed in Section 7.2 for each classifier were optimised. The performance metrics are documented in Table 7.4 for the optimised classifiers. For KNN, the average performance did not improve compared to the performance of unoptimized KNN classifier in a previous subsection (7.5.1.1). A small improvement was observed in the standard deviation of the accuracy and the specificity across the ten-fold outer

cross-validation test sets. For SVM, the average accuracy did improve by 0.5%. The average accuracies for the pre-set hyperparameters of SVM used and for the optimised SVM are within one standard deviation of both cases. Thus, the optimal upper limits of the classification performance of the classifiers on the dataset could have been reached.

Several hyperparameters of different values were considered in the optimisation of both classifiers across the 10-fold cross-validation. For SVM, the RBF kernel was chosen during optimisation in the nested cross-validations for evaluation on the ten outer folds. The Box Constraint and Gamma had average values of 699.15 ± 390.56 and 67.21 ± 37.24 respectively. For KNN, the combinations hyperparameters varied for each fold. Euclidean distance was the most consistent hyperparameter selected for KNN. As no one hyperparameter set was consistent, there are many optimal solutions for the dataset.

Table 7.4: Performance results of running classifiers with optimised hyperparameters on the RTT2 dataset.

Classifier	Accuracy (%)	Sensitivity (%)	Specificity (%)
Optimised KNN	97.79 ± 0.53	97.54 ± 0.85	98.05 ± 0.78
Optimised SVM	97.40 ± 0.87	97.54 ± 0.91	97.26 ± 1.77

7.5.1.3 Classification with Reciprocal Feature Processing

Using the Principle of Reciprocity in bioimpedance, the number of features was reduced from 208 to 104 features. This processing may be advantageous where hardware memory is limited and needs to be conserved. However, a high performance was achieved despite the loss of data. The average accuracies of 96.77% for the optimised KNN and 97.65% for the optimised SVM after the feature reduction were achieved, as documented in Table 7.5. Notably, the accuracies of the 208 feature optimised classifiers from Table 7.4 and the 104 feature optimised classifiers in Table 7.5 overlap in terms of their standard deviations. The average accuracy of SVM improved in the removal of highly correlated features when compared with the data in Table 7.3 and Table 7.4.

Thus, pre-processing steps could include choosing the better measurement of the reciprocal pairs (e.g., the pair that has the lowest channel noise, chosen by the calculated SNR of each channel). Then, only the better-quality measurements in the reduced frame can be used in classification. This processing step could have benefits in terms of increasing the amount of data that can be stored in the enuresis alarm as well as removing redundant measurements that are highly correlated. The main benefit of the reciprocal feature processing is that more options are available for error handling, e.g., selecting the best reciprocal channel or averaging

reciprocal measurements to reduce noise. Removing redundant features may be necessary for additional processing algorithms that do not consider feature interaction like Fisher Score. The results for Fisher Score are presented in the next subsection.

Table 7.5: Performance results of running classifiers with optimised hyperparameters on the RTT2 dataset using the Reciprocal Feature Processing.

Classifier	Accuracy (%)	Sensitivity (%)	Specificity (%)
Optimised KNN	96.77 ± 0.84	95.95 ± 1.52	97.58 ± 1.47
Optimised SVM	97.65 ± 0.73	97.58 ± 1.16	97.72 ± 1.34

7.5.1.4 Classification with Fisher and Reciprocal Feature Selection

The Fisher Score feature selection algorithm was applied to the nested training data after the reciprocal measurements were removed. The performance metrics are documented in Table 7.6. The process improved the performance for KNN when compared to the reciprocal removal only results in Table 7.5. However, the average accuracy of SVM did not improve. The improvement for KNN was within one standard deviation of the KNN average accuracy results in Subsection 7.5.1.3. Thus, the improvement is marginal, which could be expected when high performance is already being achieved by both classifiers.

The number of top ranked features was either 101 of 104 fisher score ranked features for KNN (average 103.70 ± 0.95) and varied from 82 to 104 fisher score ranked features for SVM (average 95.20 ± 7.27). The added noise employed over the range of 40-80 dB affects each individual channel/feature in the observations given to the classifier to learn from. Therefore, the classifiers may require all the possible features in the current simulation scenario in order to obtain best classification performance. Also, another potential reason for why most features were kept is that only one main dynamic process was present in the forward model, i.e., changing of bladder volume and urine conductivity. Many dynamic changes may occur in the pelvic region in reality, such as flatulence and muscle contractions. These dynamic changes may be captured in certain voltage channels rather than the bladder volume changes. A supervised feature selection algorithm like Fisher Score may be able to remove these irrelevant features before classification. Therefore, this supervised feature selection strategy could be valuable in future research and be better assessed when pilot volunteer data is available for classification.

Table 7.6: Performance results of running classifiers with optimised hyperparameters on the RTT2 dataset using the Fisher Feature Selection and the Reciprocal Feature Pre-processing.

Classifier	Accuracy (%)	Sensitivity (%)	Specificity (%)
Optimised KNN	96.86 ± 0.99	96.37 ± 1.43	97.35 ± 1.30
Optimised SVM	97.63 ± 0.45	97.54 ± 1.26	97.72 ± 1.06

7.5.1.5 Classification with PCA

The performance results for PCA with both classification algorithms and Bayesian Optimisation is given in Table 7.7. The PCA transformation technique created 208 linear independent features to be selected by the optimisation technique for the classifier. Thus, the exact number of principal components used is based on the optimal combination of the number of first *n* principal components and the optimised hyperparameters for the classifier (200 evaluations for KNN with Bayesian Optimisation). The average number of principal components chosen for KNN over the ten evaluation test folds were 35.40 ± 58.13 principal components. This reduction is the largest reduction in the number of features given to the classifier observed in this section. For SVM, the average accuracy decreased in comparison to the optimised results in Table 7.4. The number of top-ranked PCA components were 118.4 ± 85.21. While the number of features used by the classifier was greatly reduced, the performance of the classifiers did not increase. Thus, PCA may help in cases where the Curse of Dimensionality [225] is problematic, e.g., a large electrode array and a lower number of measurement frames collected. The findings so far are summarised in the next subsection.

Table 7.7: Performance results of running classifiers with optimised hyperparameters on the RTT2 dataset using the feature transformation PCA.

Classifier	Accuracy (%)	Sensitivity (%)	Specificity (%)
Optimised KNN	97.72 ± 0.97	97.44 ± 0.88	98.00 ± 1.46
Optimised SVM	97.16 ± 0.86	97.30 ± 0.72	97.02 ± 1.60

7.5.1.6 Summary of Feature Processing and Classifier Optimisation Techniques

In this subsection, feature processing and classifier optimisation were performed using the KNN and SVM classification algorithms. This work provides the first set of investigations of different feature processing algorithm and classifier optimisation for BVM with EIT measurement data. A summary of the best performing algorithms in each investigation is

provided in Table 7.8. Classification using child data for bladder state classification has a strong potential due to very high performance (accuracies above 95%) in simulations that include varying bladder volumes, varying urine conductivities and varying measurement frame noise. The best performer was KNN with Bayesian Optimisation. This optimised classifier had the highest accuracy and lowest variance in classification performance combination of all the test cases. Thus, this algorithm can be used in the final investigations of this thesis: the effect of new, unseen misaligned electrode placements on the bladder state classifier.

Table 7.8: Summary of the best performing combinations from Subsection 7.5.1.1 to Subsection 7.5.1.5. The grey shaded region highlights the best overall performing classifier.

Investigation	Feature Processing	Best Classification Algorithm	Optimisation Algorithm	Generalised Accuracy (%)
Baseline Performance with Pre-set Classifiers	Standardisation	KNN	None	97.79 ± 0.71
Classifier Optimisation	Standardisation	KNN	Grid Search	97.79 ± 0.53
Feature Reduction with Principle of Reciprocity	Standardisation & Removing Reciprocal Measurements	SVM	Bayesian Optimisation	96.77 ± 0.84
Feature Selection with Fisher Score	Standardisation & Fisher Score	SVM	Bayesian Optimisation	97.63 ± 0.45
Feature Transformation with PCA	Standardisation & PCA	KNN	Bayesian Optimisation	97.72 ± 0.97

7.5.2 Continual Monitoring Dataset 2: Results, Discussion and Further Exploration for Electrode Position Errors

For further analysis of how a classifier would perform with measurement frame data when electrode position errors are present, one classification model was selected to be tested against the CM2 dataset presented in Section 7.1.2. The optimised KNN was selected. This classification model obtained the highest generalised accuracy and the lowest variance in classification performance across all the ten test sets in Section 7.5.1. In reality, it would be expected that only one classification model would be used after training and testing when a suitable generalised performance was obtained (e.g., greater than 80%). This classification model would then be trained on the whole dataset to form one classifier to deploy rather than ten classifiers from ten-fold cross-validation that were trained on only a proportion of the dataset.

The optimised KNN was trained on the whole RTT2 dataset from Section 7.1.1. The trained KNN classifier had the following hyperparameters: Euclidean distance; fifteen nearest neighbours; and equal distance weighting. After training, the resultant classifier was evaluated on the CM2 dataset, which consisted of 100 observations for each configuration in the dataset. The configurations included the correct electrode position model for comparison as well as eight misplaced electrode configurations (four electrode rings misplaced equally, and four electrode rings misplaced in opposed directions). These configurations have been discussed previously in detail in Section 7.1.2.

The performance metric values on the whole CM2 dataset were 62.96%, 62.50%, and 63.43% for the balanced accuracy (Equation (7.1)), the sensitivity and the specificity, respectively. With the added condition of eight misaligned electrode rings in the CM2 dataset, the performance of the classifiers greatly degraded in terms of magnitude (over 90% to below 70%), as compared to the scenario without any electrode misplacement errors in the previous subsection (Section 7.5.1). To determine why the performance degraded greatly, the misclassifications for the misplaced electrode configurations in the CM2 dataset were analysed.

The breakdown in performance in terms of the performance metrics is presented in Figure 7.7 for the misaligned electrode ring configurations. As expected, the least number of misclassifications was for the 100 observations generated from the numerical forward model with the correct electrode positions. The performance metrics for the data on the correct electrode ring locations were 95.06%, 92.16%, and 97.96% for the balanced accuracy, the sensitivity and the specificity, respectively. These values are in similar magnitude as the values in Table 7.7.

The two misplaced electrode configurations with the least effect were those that were shifted left or right by 10 mm together. Unlike with the vertical shifted electrode misplacements, the body volume between the electrode rings is the same for electrode misplacements horizontally. The electrode positions relative to each other have also changed the least out of all the misplaced electrode configurations as the two rings are misplaced in unison. This finding suggests that large misplacements (as much as 1 cm) of the electrodes along the axial plane are tolerable by the trained classifier when the electrode rings are misplaced equally.

However, greater misclassification was observed for the other misplaced electrode configurations. In fact, the misplaced configurations {‘Up10’, ‘Apart10’, ‘Right Bottom, Left

Top', 'Together5'} either had 100% sensitivity or 100% specificity (i.e., balanced accuracies of 50%).

The classifier does not seem to extrapolate well for measurement data from misplaced electrodes. The scenario examined here is an extreme one. The classifier is trained on data from ideally placed electrodes and then must extrapolate to large variants of the trained data. This scenario may only occur in reality if the family were very careful at the start when the device is learning and as time passed, became less careful with placing the electrodes without retraining the classifier.

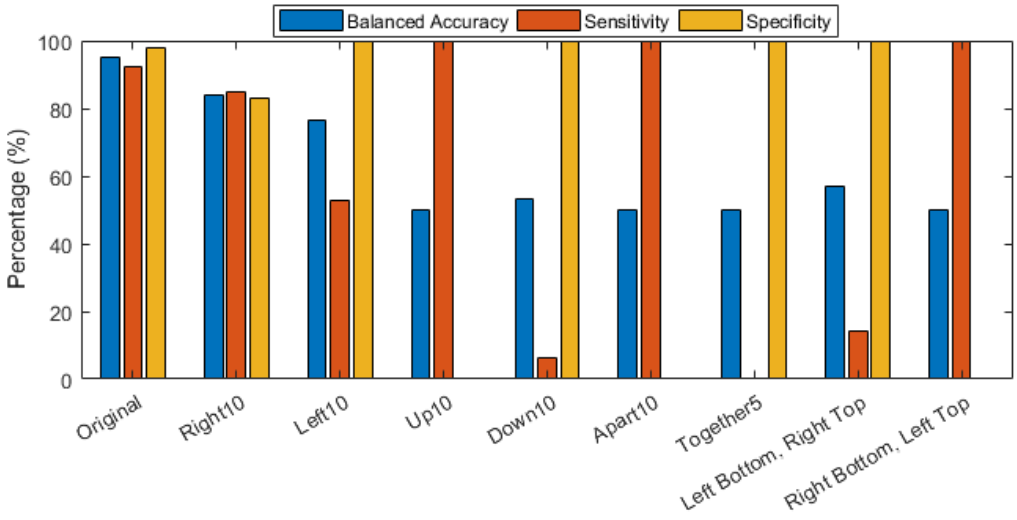

Figure 7.7: Performance of the optimised KNN classifier on each misaligned electrode configuration from the CM2 dataset. As expected, the best performance is from the correct electrode placements and performance degrades with misplaced electrodes. However, four configurations have accuracies circa 50% (worst case for binary classification). Thus, electrode ring misplacement needs to be captured in the training dataset or efforts need to be undertaken to maintain control over positioning.

To further determine if there is any tolerability of the classifier to small electrode misplacements, the misplacement configurations with balanced accuracies around 50% were further analysed in smaller misplaced displacements of {1, 2, 4, 6, 8} mm. Each configuration had 100 observations of randomly generated bladder volumes, urine conductivities and SNRs as per the CM2 setup described in Section 7.1.2. The performance metric curves for displacements of 1-8 mm (1-5 mm for the 'Together' misplacement) are given in Figure 7.8. *Please note:* in the case of the 'Together' electrode misplacement configuration, the 79 ml could not be constructed due to mesh intersection with the bone. Thus, the two observations that had randomly generated bladder volumes of 79 ml were manually changed to 78 ml. This reduction of the bladder volume range did not affect the proportion of labels in each class as

was randomly generated. Only the upper bladder volume for this electrode misplacement was reduced by 1 ml and this change is therefore expected to have minimal impact.

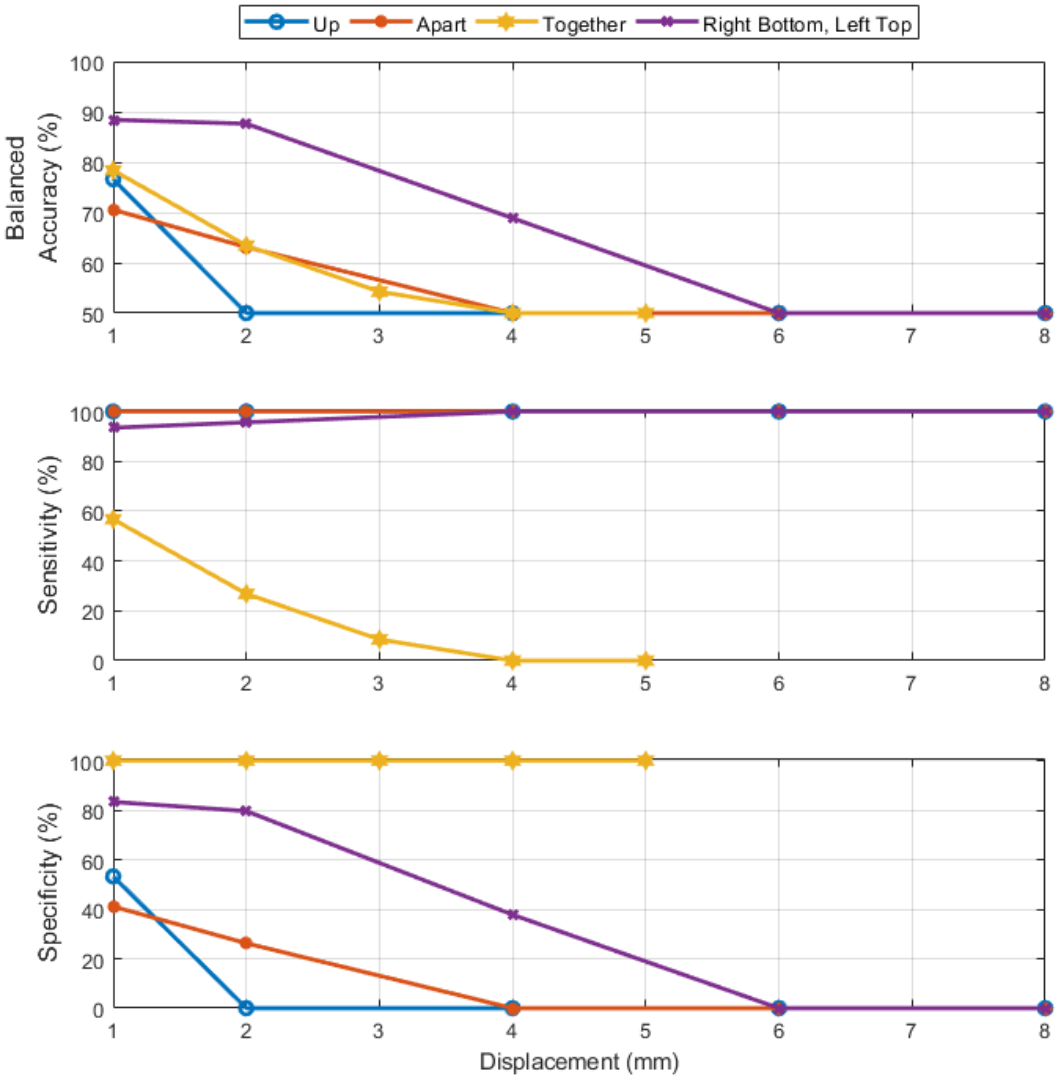

Figure 7.8: Investigating the tolerance of the KNN classifier to electrode misplacement for the four worst electrode misplacement configurations in Figure 7.7. The tolerance of the misplaced electrode configurations in the craniocaudal axis is less than 2 mm before the prediction accuracy is less than 70%. For the axial misplaced electrode configuration, the tolerance is better at less than 4 mm.

In the scenario of misplaced electrode rings axially but the rings misplaced differently, 2 mm displacements can be tolerated for classifications accuracies around 80%. For misplacements of both rings along the craniocaudal axis, the tolerance is less than 2 mm as larger displacements result in the accuracy of the classifier being close or around 50% (worst case for a binary decision). Therefore, the classifier struggles to extrapolate to misplaced configurations that are affected along the craniocaudal axis. This is a condition that has to be considered in

device design. This problem not only affects EIT, but technologies such as Ultra-Wide Band Radar and Ultrasound as highlighted in Section 2.3.4. To alleviate the problem for EIT, the user may be guided to ensure the electrode positions are as accurately placed as possible and data from a variety of misplacements over time needs to be captured in the dataset. To capture a variety of data from different electrode ring positions, the user may be asked to reposition the electrodes after each voiding cycle during the initial data collection. For a device worn at night, the electrodes may only be placed once per night.

To verify that this solution shows promise, data used in Figure 7.8 with displacements of {1, 2, 4, 6, 8} mm were all combined into one dataset (termed 'RTT3' and contains 2000 observations). The LOCOCV with nested LOCOCV was used to train and test the KNN classifier under the condition that all the data for one electrode misplacement be left out. This training case would be similar to training on multiple nights of recordings and testing the classifier against data for an untrained night. The number of observations in the test set at any one time was 100 observations. The generalised performances of the classifier were 86.75 ± 4.38%, 78.40 ± 9.68% and 93.05 ± 8.65% for the balanced accuracy, sensitivity and specificity, respectively. The minimum observed accuracy was 77.00%. This performance is much improved compared to the results presented in Figure 7.8. The maximum unseen displacements in the RTT3 dataset was 2 mm. The majority of the accuracies of 2 mm displacements in Figure 7.8 were below 65%. Thus, when a variety of electrode misplacements are included in the training, the classifier can better extrapolate data outputs based on new electrode misplacements.

In this section, the effect of electrode misplacements was examined, the tolerability of the classifiers determined for the worst affected electrode misplacements and a potential solution of remedying the problem was investigated. In the next section, the chapter is summarised based on the overall objectives and findings.

7.6 Summary

In this chapter, bladder state classification was performed using raw EIT voltage data from a child forward model. The analysis of the raw EIT voltage data was performed using realistic train-test strategies. The key findings from sections within this chapter are highlighted in the following paragraphs.

In Section 7.1, the RTT2 dataset was formed for validation of bladder volume classification trends on child raw EIT data as well as domain exploration using different feature processing techniques. The most unique dataset in the thesis was formed where each observation differs by a combination of bladder volume and urine conductivity. Along with this dataset, a continual monitoring dataset (CM2) was formed with the additional condition of misaligned electrode ring locations (four misaligned electrode configurations where the rings were misaligned in unison and four where the rings were misaligned differently). This condition could be expected with a device in clinical use, as electrodes are unlikely to be placed in the same exact physical location each time. It was found that data generated from these different electrode locations have large effects on measurement data and thus, could strongly affect the classification performance.

In Section 7.2, a selection of hyperparameters for the chosen classifiers was discussed along with optimisation methods to help identify the optimum hyperparameter sets. A more optimum hyperparameter set may help improve the overall classification results on the dataset.

In Section 7.3, feature processing algorithms were designed and/or selected to be investigated for this application on EIT measurement data. These algorithms could have the potential to reduce the volume of data stored, to reduce redundancy in the dataset, and/or to improve classification performance.

In Section 7.4, an architecture for training the machine learning algorithms and evaluating their performance was discussed. Importantly, the architecture enables no data contamination during training or testing ensuring more accurate classification performance results.

In Section 7.5, classification was performed using the various optimisation and feature processing methods from the previous sections, and results were analysed and compared. High classification performance of over 96% was achieved by classifiers, with both pre-set and optimised hyperparameter settings. The high classification performance validates the potential for BVM using raw EIT voltage data and machine learning for child-based applications. Alongside validation of the potential of EIT measurement data classification for BVM monitoring, feature processing was examined to determine if performance could be improved by: reducing the number of features given to the classifier; decreasing dataset storage; and/or by improving accuracy. Different strategies based on a principle for bioimpedance, feature selection and feature transformation were examined. The feature transformation technique PCA along with the KNN classifier provided the best average accuracy of the feature

processing algorithms, as well as the lowest reduction in the number of features used by the classifier, reducing unnecessary information given to the classifier. However, the best overall performance was by the optimised KNN classifier using all 208 features. This finding indicates that the reciprocal features do provide useful information to the classifier when there is noise present in the dataset.

In the second part of Section 7.5, the KNN classifier using Grid Search was trained on the whole dataset and subjected to new data with the new condition of misaligned electrode ring locations. While the classifier was able to extrapolate for electrodes misaligned along the axial plane in unison, the performance severely degraded for changes in the electrodes in the craniocaudal axis (where accuracies of only 50% were observed). An approach to overcome this problem was investigated by including misplaced electrode locations in the training dataset. The overall performance greatly improved (accuracy improvement > 10%). Thus, strategies to capture a variety of data from different electrode configuration misplacements in the dataset needs to be executed if this condition is not sufficiently handled by guiding the user on careful electrode placement. Future work can investigate feature processing and classifier optimisation on the datasets with electrode misplacements to determine if the classification performance can be further improved.

Having investigated the concept of BVM using machine learning classification with both images and raw EIT voltage data on a number of real-world conditions in the controlled environment of simulation, the thesis is next concluded and future work outlined in Chapter 8.

8 Conclusions and Future Work

In this chapter, the need and the motivation for this thesis are summarised. Next, each chapter is summarised in terms of the overall findings and the key contributions. Then, avenues for future work are proposed to further advance the design and development of a proactive, EIT-based bedwetting alarm for children with NE.

8.1 Summary and Conclusions

Nocturnal enuresis is the loss of bladder control during sleep and can be a troubling condition for both the child and the parents/guardians. Mental health and social interactions are adversely impacted when children suffer from NE. The condition is financially costly for the family and also places a significant burden on health systems.

When treating NE, it is essential to identify any comorbidities and underlying causes. These comorbidities and underlying causes are treated first before considering NE directly. Primary treatment options for NE include the enuresis alarm device and the pharmacological drug Desmopressin. The enuresis alarm is often the preferred option due to the relatively high long-term success rates compared to Desmopressin. However, the enuresis alarm has significant limitations. These limitations created a need for research that was critically reviewed in Chapter 2.

Specifically, the underlying anatomy of the bladder was presented in Chapter 2 and the clinical need of NE was introduced. The chapter established that the current treatment options for NE are reactive in operation or chemically alter bodily functions. The current preferred treatment of alarm therapy takes time to provide a response to bedwetting. Also, the enuresis alarm can often be discontinued by the child and family before successful treatment of NE has occurred. An ideal treatment option would be proactive and would have a high long-term success rate. A proactive solution would also have an immediate bedwetting reduction response. One potential technology that could provide such a solution is EIT. Electrical impedance tomography is a low-cost and wearable medical imaging technology. The technology has been shown to be capable of monitoring bladder filling over time in adult volunteer studies. However, no studies have investigated BVM for child-specific applications such as a proactive bedwetting alarm using NE. Also, the primary research for bladder fullness monitoring has been for bladder

volume estimation rather than predicting the "state" of the bladder. Classification of not-full and full bladder states would be more suitable for an NE alarm system, rather that requiring an exact estimate of bladder volume. Therefore, a technology gap (EIT bladder state monitoring and classification) was found and addressed in this thesis. However, a numerical forward model was needed to generate EIT measurement data. The first step in answering these needs is the creation of anatomically-informed numerical forward models of the pelvis and the bladder.

In Chapter 3, numerical forward models previously used in EIT BVM applications were critically reviewed. Numerical forward models presented in the literature were all adult sized, as the research in the field has not focused on any child-specific applications. Most forward models included cylindrical boundaries representing the pelvic and abdominal regions, while the bladder was modelled as either a sphere or a cylinder. These forward models lacked anatomical information that could provide more realistic results and guide better optimisation of electrode position and key electrode channels to improve classification. For this reason, a simplified 3D pelvic numerical forward model was developed early in this thesis using anatomical information from MRI images of the human body. The numerical forward model was adult size, in line with the current literature. Typically, an adult has a wider girth and a deeper bladder within the pelvic cavity compared to a child; thus, presenting a more challenging EIT scenario for bladder state classification. Also, it would be expected that the findings for any new medical device would have to be verified on healthy adult volunteers before ethically assessing the EIT bedwetting device with enuretic children. Therefore, it is important to determine how the bladder state classification would perform on adult size models early in the research process. By comparing the separability of EIT voltage and image data generated from the forward model for not-full and full bladder volumes, it was found that images offered a strong potential of separating empty and full bladder volumes by descriptive statistics alone. It was also found that using images as the input source for a classifier would be a strong starting point for bladder state classification.

In Chapter 4, the bladder state classification using machine learning was performed for the first time on EIT image data. The classifiers were evaluated under the conditions of varying bladder volumes, varying urine conductivities and added measurement frame noise, using the numerical forward model formed in Chapter 3. When varying the bladder volume, it was found that observations of bladder volumes nearest the decision boundary of not-full and full experienced the highest misclassification rate. When urine conductivities varied, the classifiers faced considerable difficulty in classifying observations with urine conductivities on the low

range of the expected urine conductivity range (< 1.5 S/m), with accuracies dropping from above 80% to circa 50% in the extreme case (0.5 S/m). At low urine conductivities, the contrast between the urine conductivity and the surrounding background conductivity is at the lowest. This reduced contrast led to a reduced difference between the bladder volume EIT measurements. These condition deviations (to what was mainly observed in the training data) challenged the classifiers to determine the bladder state for observations with low urine conductivity. When faced with varying levels of random Gaussian noise, the performance of the classifiers degraded gradually with increasing levels of noise (decreasing SNR), as would be expected. Accuracies remained greater than 70% at the most difficult SNR level tested of 40 dB, having decreased gradually from greater than 95% at 80 dB SNR. When the classifiers were trained on all conditions and subjected to new unseen data, high classification performance of over 83% was observed. Therefore, bladder state classification has potential when image data is used as input to the classifiers. However, reliable image reconstruction can require a large amount of accurate *a priori* information. Obtaining accurate *a priori* information may be difficult in this application where noise sources such as body movement, body deformation from different lying positions, and electrode contact and position may vary over the course of a night. Therefore, the measured EIT voltage data could be used as an alternative input to the classifiers instead of image data.

In Chapter 5, the feasibility of EIT voltage data as an alternative input for bladder state classification using machine learning was investigated for the first time. The methodology was chosen to match that of the work in Chapter 4, allowing for direct comparison between classification accuracies with voltage data and image data as inputs. Similar results to Chapter 4 were found here when voltage was used as classifier input: high amounts of misclassifications occurred around the bladder volume separation volume, at the low end of the urine conductivity range, and with the presence of high noise levels. Importantly, comparable classification performance of using the EIT voltage data and the EIT image data as classifier inputs was found for bladder state classification. The findings suggest that voltage data can be used in place of image data to reduce the additional overhead of additional processing and the *a priori* information required for time-difference EIT image reconstruction. Feasibility of bladder state classification using machine learning has been demonstrated in the thesis so far and the tolerance levels of the classifiers have been assessed for varying bladder volumes, urine conductivities, and added measurement frame noise. At this stage, the research needed to be directed towards the specific challenges associated with bladder monitoring within a child

cohort. These specific challenges for children include smaller bladder capacities, reduced pelvic region size for electrodes, and the unique anatomy of a growing child.

In Chapter 6, the first realistic child pelvic forward model for EIT was designed and developed. The numerical forward model consisted of an anatomically correct boundary extracted from medical imaging, along with the pelvic bone. The bladder volume range was greatly reduced from that of the adult model, from 0-420 ml to 0-210 ml. The reduced body surface area of the child model limited the number of electrodes that could be placed around the pelvic region. Thus, a 16-electrode system was used with two parallel rings of eight electrodes each. This numerical forward model presented in this chapter can be employed to help evaluate bladder state classification using machine learning on child EIT data.

In Chapter 7, the findings from Chapter 5 were verified on child data. This investigation was the first-time child EIT data was used for a EIT bladder fullness application. High generalised classification accuracies of over 95% were achieved on the dataset. The dataset contained varying bladder volumes, urine conductivities, and added random Gaussian noise. In parallel, optimisation techniques and feature processing for this application were implemented to determine if the performance of the machine learning classifier system could be further optimised. The techniques examined in this chapter improved the performance of the system by: reducing the need to store data for retraining by half; reducing the number of features needed by the classifier if there was high dimensionality in the dataset; and by reducing the variance of the classification performance.

In the second part of Chapter 7, the best observed classification model of KNN with Grid Search Optimisation was tested against the scenario of varying electrode positions when trained on data from ideal electrode positions. Specifically, the electrode positions were misplaced rings on a ring-by-ring basis. This scenario considered two electrode rings being firstly misplaced in unison and secondly individually. The misplacements occurred in both the axial plane and in the craniocaudal axis. Overall, the most difficult scenario for the classifier was electrode positions varying in the craniocaudal axis. In this scenario, the classification accuracies dropped below 65% in most cases, with only 2 mm electrode misplacements. Sensor misplacement is a shared source of error in technologies such as Ultrasound and UWB Radar. However, this problem was remedied in the EIT simulations by including a range of electrode misplacements in the training dataset. A designer must account for electrode position errors

and the other noise sources (varying urine conductivity, a random source of noise, and varying body sizes) when designing the EIT-based bedwetting alarm.

Overall, this thesis has made significant strides towards the design and development of a non-invasive, proactive bladder monitor for children with NE based on EIT. More research is needed in this area to further the development of an EIT-based bedwetting alarm, as outlined in the next section.

8.2 Future Work

To further the design and development of an EIT-based bedwetting alarm, a number of steps ranging from device design to clinical validation need to be performed.

First, the work in this thesis can be extended by performing the feature processing and classifier optimisation in Chapter 7 on a dataset containing data from a variety of different electrode misplacements (as initially examined in Section 7.5) in simulation using realistic child forward models that can be developed using the protocol in Chapter 6. Also, the work in this thesis can be extended by determining if it is possible to develop specific feature processing algorithms to overcome this source of measurement error.

After selecting the EIT hardware and the development of a reusable, comfortable, and quick deployable electrode interface, the simulation results for bladder state classification need to be validated in the presence of real-world noise from an EIT device worn on-body. This work could be completed in a carefully designed pilot patient study. A small sample of volunteers (e.g., five/six adults) could be monitored over multiple bladder filling periods, similar to the study by Abbey & Close [107]. A sufficiently large number of observations for multiple individual volunteers may be obtained by recording frequently during the bladder fillings. If possible, voiding should also be recorded to determine if the rapid change in impedance due to bladder emptying can be used as a marker to help label observations automatically.

This pilot study work may also help investigate whether patient specific classifier training is required. If not required, a classification algorithm could be pre-trained on data already obtained from other individuals before giving the device to a new user (e.g., pilot data with large variations of urine conductivities and placement of electrodes). The device could then be used immediately rather than having a training period before the device can be employed. The classifier can then be retrained and refined as data is gathered from the specific user over multiple nights.

More advance pilot studies could then be performed with adults or children wearing the device at night-time. A small cohort could be given the device to use to monitor bladder filling during the night. This cohort would include volunteers who wake to go to the toilet at night due to a full bladder or those with NE. An alert may be used to awaken the device wearer, or the device wearer may be asked to note the time they wake to determine if the classifier is working. Previous ultrasound studies that could help in designing the study protocol are Kuru et al. [47] and Kwinten et al. [84].

Throughout each pilot study, noise sources negatively impacting the classification performance need to be identified. Suitable filters to handle noise should be devised to reduce the need to collect large amounts of data for the classifiers to mitigate all noise sources. For example, a low-pass filter may help reduce the effect of high-frequency electronic noise or mean/median filter for breathing artefacts [192]. Other noise sources that may arise include body movement and loss of sensor contact. The system will need to monitor changes that affect the recorded voltages. Noisy/errored channels could be identified by analysing the noise in the channels or by estimating electrode-contact impedance from the injection electrodes. These channels may be ignored if reciprocal feature processing is being used or the values may be replaced with the average values for each of these noisy channels in the frame. Additional sensors, like an inertial motion unit (IMU), could be employed to identify when the child is changing body position during sleep or to identify when there are high vibrations. During these times, the EIT system could delay recording or fail-safe by alerting early. An updated future vision of the device is captured in the Figure 8.1 that fits into the overall system layout in Figure 2.13. The flowchart of the signal processing that could be used in the system is given in Figure 8.2. Future work could also determine if any additional sensors could be of benefit, such as electromyography to monitor muscle activity in the region.

One of the benefits of using measured EIT voltage data for the classifiers was that time-differencing subtraction was not required for the correction of mismatches between the recording scenario and the *a priori* information. Time-difference subtraction could still be used for future designs of the classifiers using measured EIT voltage data to improve standardising data from different recording periods, i.e., remove any variation of the initial voltages between recording (e.g., caused by contact impedances variations).

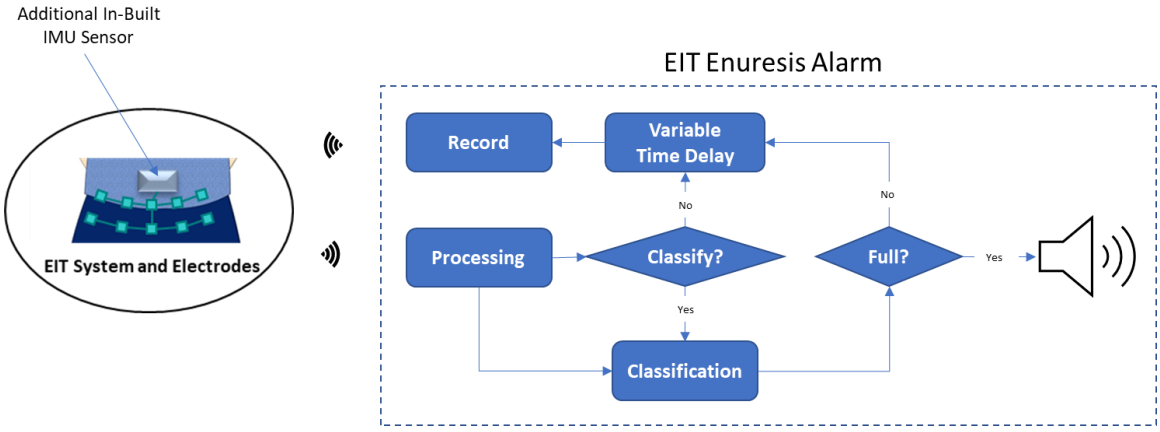

Figure 8.1: Updated illustration from Figure 2.14 of a simplified EIT monitoring system with a machine learning classifier to determine whether the processed frame is for a not-full or full bladder. The alarm box communicates back and forth with the EIT recording system wirelessly. Processing cleans the EIT data received as a time-series and forms a single frame to be given to the classifier to determine the bladder state. An additional IMU sensor can be used to determine if there is high body movement, in which classifying is skipped until the next recording period. A variable delay can be employed where the recording should be infrequent just after voiding, but more frequent as time passes. On classification of a 'full' state, the alarm sounds.

The system design can also be refined further in simulation, phantom, and volunteer studies. System enhancements include examining the most suitable number of electrodes and electrode configurations for varying body shapes of growing male and female children and varying body mass indexes. Different interfaces may be needed based on age and/or body shape. The electrode configuration could also be analysed to assess how resilient to body movement the electrode configuration is, and how comfortable the electrode placement and electrode type is for the wearer.

To optimize the device functionality in disciplines beyond electrical and electronic engineering, the ergonomics of the device and creation of an appealing device need to be considered. Designing an appealing device is important to encourage uptake and compliance. The interface should be comfortable to wear overnight and easily positioned by the child. The alarm needs to be tailored to wake the child but not cause trauma, e.g., alarm types using familiar voices, music or waking by increasing light in the room. Maintenance also needs to be assessed, including cleaning.

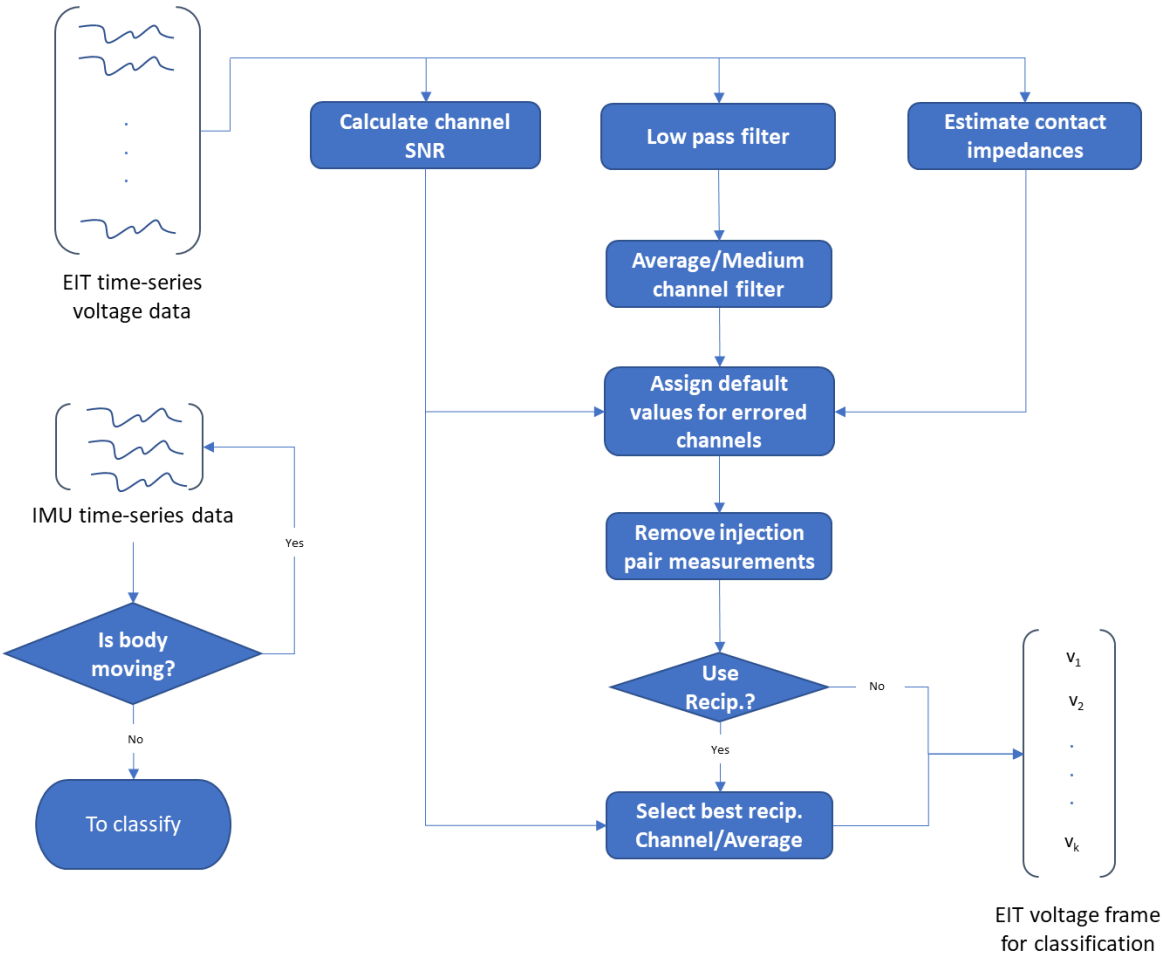

Figure 8.2: A flowchart of the processing that a proactive EIT enuresis alarm could use to extract the voltage frame to classify from a window of EIT measurement data (multiple frames). Reciprocal (Recip.) feature processing could be used to average out noise or replace errored channels. The additional sensor of an IMU unit could allow detection of high body movement so that the device avoids classifying potentially errored EIT data (e.g., if it is not suitable to classify EIT data, data collection should be repeated).

Further work (as outlined in this section) is needed before bringing an EIT-based device for treating NE to market. Medical device design can take many years. However, this work is required to develop a final prototype that can be certified as safe by regulatory bodies and performance tested against the commonly prescribed bedwetting alarms. With all of this research, a low-cost proactive bedwetting alarm solution may be possible for children with NE.

Bibliography

[1] B. S. Buckley and M. C. M. Lapitan, “Prevalence of Urinary Incontinence in Men, Women, and Children—Current Evidence: Findings of the Fourth International Consultation on Incontinence,” *Urology*, vol. 76, no. 2, pp. 265–270, Aug. 2010, doi: 10.1016/j.urology.2009.11.078.

[2] M. Theunis, E. Van Hoecke, S. Paesbrugge, P. Hoebeke, and J. Vande Walle, “Self-Image and Performance in Children with Nocturnal Enuresis,” *Eur. Urol.*, vol. 41, no. 6, pp. 660–667, Jun. 2002, doi: 10.1016/S0302-2838(02)00127-6.

[3] J. P. Nørgaard, J. C. Djurhuus, H. Watanabe, A. Stenberg, and B. Lettgen, “Experience and current status of research into the pathophysiology of nocturnal enuresis,” *Br. J. Urol.*, vol. 79, no. 6, pp. 825–35, Jun. 1997, doi: 10.1046/j.1464-410x.1997.00207.x.

[4] T. Schulpen, “The burden of nocturnal enuresis,” *Acta Paediatr.*, vol. 86, no. 9, pp. 981–984, Sep. 1997, doi: 10.1111/j.1651-2227.1997.tb15183.x.

[5] G. B. Mesibov, C. S. Schroeder, and L. Wesson, “Parental Concerns About Their Children,” *J. Pediatr. Psychol.*, vol. 2, no. 1, pp. 13–17, Jan. 1977, doi: 10.1093/jpepsy/2.1.13.

[6] National Institute for Health and Care Excellence, “Bedwetting in under 19s Clinical guideline [CG111],” 2010. https://www.nice.org.uk/guidance/cg111.

[7] A.-F. A.-M. Ahmed, M. M. Amin, M. M. Ali, and E. A.-M. Shalaby, “Efficacy of an Enuresis Alarm, Desmopressin, and Combination Therapy in the Treatment of Saudi Children With Primary Monosymptomatic Nocturnal Enuresis,” *Korean J. Urol.*, vol. 54, no. 11, pp. 783–790, 2013, doi: 10.4111/kju.2013.54.11.783.

[8] T. Nevéus, “Nocturnal enuresis—theoretic background and practical guidelines,” *Pediatr. Nephrol.*, vol. 26, no. 8, pp. 1207–1214, Aug. 2011, doi: 10.1007/s00467-011-1762-8.

[9] E. Prince and M. Heys, “Nocturnal enuresis: an update on management,” *Drug Ther. Bull.*, vol. 58, no. 2, pp. 25–29, Feb. 2020, doi: 10.1136/dtb.2018.000034.

[10] C. M. Glazener and J. H. Evans, “Desmopressin for nocturnal enuresis in children,” *Cochrane database Syst. Rev.*, no. 3, p. CD002112, Jul. 2002, doi: 10.1002/14651858.CD002112.

[11] I. Frerichs *et al.*, “Chest electrical impedance tomography examination, data analysis, terminology, clinical use and recommendations: consensus statement of the TRanslational EIT developmeNt stuDy group,” *Thorax*, vol. 72, no. 1, pp. 83–93, Jan. 2017, doi: 10.1136/thoraxjnl-2016-208357.

[12] S. Leonhardt *et al.*, “Electric impedance tomography for monitoring volume and size of the urinary bladder,” *Biomed. Tech. (Berl).*, vol. 56, no. 6, pp. 301–7, Dec. 2011, doi: 10.1515/BMT.2011.022.

[13] R. Li, J. Gao, Y. Li, J. Wu, Z. Zhao, and Y. Liu, “Preliminary Study of Assessing Bladder Urinary Volume Using Electrical Impedance Tomography,” *J. Med. Biol. Eng.*, vol. 36, no. 1, pp. 71–79, Feb. 2016, doi: 10.1007/s40846-016-0108-1.

[14] Springhouse, “Urinary system,” in *Lippincott Professional Guides: Anatomy & Physiology*, 2nd ed., Philadelphia: Lippincott Williams & Wilkins, 2002, pp. 157–163.

[15] J. Chambers, Ed., “The Urinary System,” in *The Facts On File Encyclopedia of Health and Medicine, Volume 3*, 1st ed., New York: Infobase Publishing, 2007, pp. 169–233.

[16] R. Drake, A. W. Vogl, and A. W. M. Mitchell, *Gray’s anatomy for students*, 3rd ed. Saint Louis: Elsevier, 2014.

[17] R. Lawson and Otago Polytechnic, “Anatomy and physiology of animals Urinary system.jpg.” https://commons.wikimedia.org/wiki/File:Anatomy_and_physiology_of_animals_Urinary_system.jpg (accessed Sep. 10, 2020).

[18] “Creative Commons — Attribution 3.0 Unported — CC BY 3.0.” https://creativecommons.org/licenses/by/3.0/deed.en (accessed Sep. 10, 2020).

[19] andrybak, “Male and female anatomy.svg.” https://commons.wikimedia.org/wiki/File:Male_and_female_anatomy.svg (accessed Sep. 10, 2020).

[20] “Creative Commons — Attribution-ShareAlike 3.0 Unported — CC BY-SA 3.0.” https://creativecommons.org/licenses/by-sa/3.0/deed.en (accessed Sep. 10, 2020).

[21] W. C. de Groat, D. Griffiths, and N. Yoshimura, “Neural Control of the Lower Urinary Tract,” *Compr. Physiol.*, vol. 5, no. 1, pp. 327–396, Jan. 2015, doi: 10.1002/cphy.c130056.

[22] P. F. Austin *et al.*, “The standardization of terminology of lower urinary tract function in children and adolescents: Update report from the standardization committee of the International Children’s Continence Society,” *Neurourol. Urodyn.*, vol. 35, no. 4, pp. 471–481, Apr. 2016, doi: 10.1002/nau.22751.

[23] S. A. Koff, “Estimating bladder capacity in children,” *Urology*, vol. 21, no. 3, p. 248, Mar. 1983, doi: 10.1016/0090-4295(83)90079-1.

[24] E. S. Lukacz *et al.*, “A healthy bladder: a consensus statement,” *Int. J. Clin. Pract.*, vol. 65, no. 10, pp. 1026–1036, Oct. 2011, doi: 10.1111/j.1742-1241.2011.02763.x.

[25] J. J. Wyndaele, “Normality in urodynamics studied in healthy adults,” *J. Urol.*, vol. 161, no. 3, pp. 899–902, Mar. 1999, doi: 10.1016/S0022-5347(01)61801-9.

[26] G. A. Demaagd and T. C. Davenport, “Management of urinary incontinence,” *P T*, vol. 37, no. 6, pp. 345–361, Jun. 2012.

[27] P. Shadpour and M. Shiehmorteza, “Enuresis persisting into adulthood,” *Urol. J.*, vol. 3, no. 3, pp. 117–29, 2006.

[28] C. P. George, F. H. Messerli, J. Genest, W. Nowaczynski, R. Boucher, and M. Kuchel Orofo-Oftega, “Diurnal variation of plasma vasopressin in man,” *J. Clin. Endocrinol. Metab.*, vol. 41, no. 2, pp. 332–8, Aug. 1975, doi: 10.1210/jcem-41-2-332.

[29] J. P. Nørgaard, E. B. Pedersen, and J. C. Djurhuus, “Diurnal Anti-Diuretic-Hormone Levels in Enuretics,” *J. Urol.*, vol. 134, no. 5, pp. 1029–1031, Nov. 1985, doi: 10.1016/S0022-5347(17)47581-1.

[30] N. Stanley, “The Underestimated Impact of Nocturia on Quality of Life,” *Eur. Urol. Suppl.*, vol. 4, no. 7, pp. 17–19, Oct. 2005, doi: 10.1016/j.eursup.2005.07.002.

[31] J. P. Weiss, “Nocturia: focus on etiology and consequences,” *Rev. Urol.*, vol. 14, no. 3–4, pp. 48–55, 2012, doi: 10.3909/riu0576.

[32] J. Jhaveri, M. Gauthier-Loiselle, P. Gagnon-Sanschagrin, and E. Q. Wu, “The Economic Burden of Nocturia on the U.S. Health Care System and Society: A National Health and Nutrition Examination Survey Analysis,” *J. Manag. Care Spec. Pharm.*, vol. 25, no. 12, pp. 1398–1408, Dec. 2019, doi: 10.18553/jmcp.2019.19191.

[33] A. J. Wright, “Childhood enuresis,” *Paediatr. Child Health (Oxford).*, vol. 26, no. 8, pp. 353–359, Aug. 2016, doi: 10.1016/j.paed.2016.04.008.

[34] H. Sarici, O. Telli, B. C. Ozgur, A. Demirbas, S. Ozgur, and M. A. Karagoz, “Prevalence of nocturnal enuresis and its influence on quality of life in school-aged children,” *J. Pediatr. Urol.*, vol. 12, no. 3, pp. 159.e1-159.e6, Jun. 2016, doi: 10.1016/j.jpurol.2015.11.011.

[35] M. S. Su, A. M. Li, H. K. So, C. T. Au, C. Ho, and Y. K. Wing, “Nocturnal Enuresis in Children: Prevalence, Correlates, and Relationship with Obstructive Sleep Apnea,” *J. Pediatr.*, vol. 159, no. 2, pp. 238-242.e1, Aug. 2011, doi: 10.1016/j.jpeds.2011.01.036.

[36] H.-M. Huang *et al.*, “Prevalence and risk factors of nocturnal enuresis among children ages 5–12 years in Xi’an, China: a cross-sectional study,” *BMC Pediatr.*, vol. 20, no. 1, p. 305, Jun. 2020, doi: 10.1186/s12887-020-02202-w.

[37] S. Yucel, O. Kutlu, E. Kukul, and M. Baykara, “Impact of urodynamics in treatment of primary nocturnal enuresis persisting into adulthood,” *Urology*, vol. 64, no. 5, pp. 1020–1025, Nov. 2004, doi: 10.1016/j.urology.2004.06.067.

[38] C. K. Yeung, J. D. Y. Sihoe, F. K. Y. Sit, W. Bower, B. Sreedhar, and J. Lau, “Characteristics of primary nocturnal enuresis in adults: an epidemiological study,” *BJU Int.*, vol. 93, no. 3, pp. 341–345, Feb. 2004, doi: 10.1111/j.1464-410X.2003.04612.x.

[39] A. G. Kilicoglu *et al.*, “Impact of enuresis nocturna on health-related quality of life in children and their mothers,” *J. Pediatr. Urol.*, vol. 10, no. 6, pp. 1261–1266, Dec. 2014, doi: 10.1016/j.jpurol.2014.07.005.

[40] O. Koca *et al.*, “Evaluation of depression and self-esteem in children with monosymptomatic nocturnal enuresis: A controlled trial,” *Arch. Ital. di Urol. e Androl.*, vol. 86, no. 3, p. 212, Sep. 2014, doi: 10.4081/aiua.2014.3.212.

[41] J. Wootton and S. Norfolk, “Nocturnal enuresis: assessing and treating children and young people,” *Community Pract.*, vol. 83, no. 12, pp. 37–9, Dec. 2010.

[42] R. J. Butler, E. J. Redfern, and W. I. Forsythe, “The Child’s Construing of Nocturnal Enuresis: A Method of Inquiry and Prediction of Outcome,” *J. Child Psychol. Psychiatry*, vol. 31, no. 3, pp. 447–454, Mar. 1990, doi: 10.1111/j.1469-7610.1990.tb01581.x.

[43] H. B. Lottmann and I. Alova, “Primary monosymptomatic nocturnal enuresis in children and adolescents,” *Int. J. Clin. Pract.*, vol. 61, no. 155, pp. 8–16, Aug. 2007, doi: 10.1111/j.1742-1241.2007.01464.x.

[44] E. A. Meydan, M. Civilibal, M. Elevli, N. S. Duru, and N. Civilibal, “The quality of life of mothers of children with monosymptomatic enuresis nocturna,” *Int. Urol. Nephrol.*, vol. 44, no. 3, pp. 655–659, Jun. 2012, doi: 10.1007/s11255-011-0087-7.

[45] S. Nascimento Fagundes *et al.*, “Impact of a multidisciplinary evaluation in pediatric patients with nocturnal monosymptomatic enuresis,” *Pediatr. Nephrol.*, vol. 31, no. 8, pp. 1295–1303, Aug. 2016, doi: 10.1007/s00467-016-3316-6.

[46] T. Neveus *et al.*, “Evaluation of and Treatment for Monosymptomatic Enuresis: A Standardization Document From the International Children’s Continence Society,” *J. Urol.*, vol. 183, no. 2, pp. 441–447, Feb. 2010, doi: 10.1016/j.juro.2009.10.043.

[47] K. Kuru, D. Ansell, M. Jones, C. De Goede, and P. Leather, “Feasibility study of intelligent autonomous determination of the bladder voiding need to treat bedwetting using ultrasound and smartphone ML techniques,” *Med. Biol. Eng. Comput.*, vol. 57, no. 5, pp. 1079–1097, May 2019, doi: 10.1007/s11517-018-1942-9.

[48] E. Kuwertz-Bröking and A. von Gontard, “Clinical management of nocturnal enuresis,” *Pediatr. Nephrol.*, vol. 33, no. 7, pp. 1145–1154, Jul. 2018, doi: 10.1007/s00467-017-3778-1.

[49] R. Sinha and S. Raut, “Management of nocturnal enuresis - myths and facts,” *World J. Nephrol.*, vol. 5, no. 4, pp. 328–38, Jul. 2016, doi: 10.5527/wjn.v5.i4.328.

[50] National Clinical Guideline Centre, *Nocturnal enuresis: The management of bedwetting in children and young people*. London: National Clinical Guideline Centre, 2010.

[51] M. R. Järvelin, L. Vikeväinen-Tervonen, I. Moilanen, and N. P. Huttunen, “Enuresis in seven-year-old children,” *Acta Paediatr. Scand.*, vol. 77, no. 1, pp. 148–53, Jan. 1988, doi: 10.1111/j.1651-2227.1988.tb10614.x.

[52] A. von Gontard, J. Heron, and C. Joinson, “Family History of Nocturnal Enuresis and Urinary Incontinence: Results From a Large Epidemiological Study,” *J. Urol.*, vol. 185, no. 6, pp. 2303–2307, Jun. 2011, doi: 10.1016/j.juro.2011.02.040.

[53] H. Bakwin, “Enuresis in twins,” *Am. J. Dis. Child.*, vol. 121, no. 3, pp. 222–5, Mar. 1971, doi: 10.1001/archpedi.1971.02100140088007.

[54] C. Hublin, J. Kaprio, M. Partinen, and M. Koskenvuo, “Nocturnal enuresis in a nationwide twin cohort,” *Sleep*, vol. 21, no. 6, pp. 579–85, Sep. 1998, doi: 10.1093/sleep/21.6.579.

[55] H. Arnell *et al.*, “The genetics of primary nocturnal enuresis: inheritance and suggestion of a second major gene on chromosome 12q,” *J. Med. Genet.*, vol. 34, no. 5, pp. 360–5, May 1997, doi: 10.1136/jmg.34.5.360.

[56] H. Eiberg, I. Berendt, and J. Mohr, “Assignment of dominant inherited nocturnal enuresis (ENUR1) to chromosome 13q,” *Nat. Genet.*, vol. 10, no. 3, pp. 354–6, Jul. 1995, doi: 10.1038/ng0795-354.

[57] S. Rittig, U. B. Knudsen, J. P. Norgaard, E. B. Pedersen, and J. C. Djurhuus, “Abnormal diurnal rhythm of plasma vasopressin and urinary output in patients with enuresis,” *Am. J. Physiol. Physiol.*, vol. 256, no. 4, pp. F664–F671, Apr. 1989, doi: 10.1152/ajprenal.1989.256.4.F664.

[58] T. Nevéus, “Pathogenesis of enuresis: Towards a new understanding,” *Int. J. Urol.*, vol. 24, no. 3, pp. 174–182, Mar. 2017, doi: 10.1111/iju.13310.

[59] M. Maternik, K. Krzeminska, and A. Zurowska, “The management of childhood urinary incontinence,” *Pediatr. Nephrol.*, vol. 30, no. 1, pp. 41–50, Jan. 2015, doi: 10.1007/s00467-014-2791-x.

[60] N. Wolfish, R. Pivik, and K. Busby, “Elevated sleep arousal thresholds in enuretic boys: clinical implications,” *Acta Paediatr.*, vol. 86, no. 4, pp. 381–384, Apr. 1997, doi: 10.1111/j.1651-2227.1997.tb09027.x.

[61] M. S. Su, L. Xu, W. F. Pan, and C. C. Li, “Current perspectives on the correlation of nocturnal enuresis with obstructive sleep apnea in children,” *World J. Pediatr.*, vol. 15, no. 2, pp. 109–116, 2019, doi: 10.1007/s12519-018-0199-6.

[62] L. Borch, S. Hagstroem, W. F. Bower, C. Siggaard Rittig, and S. Rittig, “Bladder and bowel dysfunction and the resolution of urinary incontinence with successful management of bowel symptoms in children,” *Acta Paediatr.*, vol. 102, no. 5, pp. e215-20, May 2013, doi: 10.1111/apa.12158.

[63] S. Yazbeck, E. Schick, and S. O’Regan, “Relevance of constipation to enuresis, urinary tract infection and reflux. A review,” *European Urology*, vol. 13, no. 5. Eur Urol, pp. 318–321, 1987, doi: 10.1159/000472809.

[64] J. Vande Walle, S. Rittig, S. Bauer, P. Eggert, D. Marschall-Kehrel, and S. Tekgul, “Practical consensus guidelines for the management of enuresis,” *Eur. J. Pediatr.*, vol. 171, no. 6, pp. 971–983, Jun. 2012, doi: 10.1007/s00431-012-1687-7.

[65] P. H. Caldwell, M. Codarini, F. Stewart, D. Hahn, and P. Sureshkumar, “Alarm interventions for nocturnal enuresis in children,” *Cochrane database Syst. Rev.*, vol. 5, no. 47, p. CD002911, May 2020, doi: 10.1002/14651858.CD002911.pub3.

[66] P. H. Y. Caldwell *et al.*, “A randomised controlled trial of a code-word enuresis alarm,” *Arch. Dis. Child.*, vol. 101, no. 4, pp. 326–31, Apr. 2016, doi: 10.1136/archdischild-2015-308564.

[67] Kiwianaa, “DRIsleeper-Wireless-Alarm.gif.” https://commons.wikimedia.org/wiki/File:DRIsleeper-Wireless-Alarm.gif (accessed Sep. 10, 2020).

[68] J. Vande Walle, M. Stockner, A. Raes, and J. Norgaard, “Desmopressin 30 Years in Clinical Use: A Safety Review,” *Curr. Drug Saf.*, vol. 2, no. 3, pp. 232–238, Sep. 2007, doi: 10.2174/157488607781668891.

[69] G. Nankivell and P. H. Caldwell, “Paediatric urinary incontinence,” *Aust. Prescr.*, vol. 37, no. 6, pp. 192–195, Dec. 2014, doi: 10.18773/austprescr.2014.075.

[70] C. J. Hillary and C. Chapple, “The Evaluation and Treatment of Adult Nocturnal Enuresis,” *Curr. Bladder Dysfunct. Rep.*, vol. 9, no. 2, pp. 84–89, Jun. 2014, doi: 10.1007/s11884-014-0237-8.

[71] P. H. Y. Caldwell, P. Sureshkumar, and W. C. F. Wong, “Tricyclic and related drugs for nocturnal enuresis in children,” *Cochrane database Syst. Rev.*, vol. 2016, no. 1, Jan. 2016, doi: 10.1002/14651858.CD002117.pub2.

[72] C. M. A. Glazener, J. H. C. Evans, and R. E. Peto, “Treating Nocturnal Enuresis in Children,” *J. Wound, Ostomy Cont. Nurs.*, vol. 31, no. 4, pp. 223–234, Jul. 2004, doi: 10.1097/00152192-200407000-00013.

[73] C. C.-H. Peng, S. S.-D. Yang, P. F. Austin, and S.-J. Chang, “Systematic Review and Meta-analysis of Alarm versus Desmopressin Therapy for Pediatric Monosymptomatic Enuresis,” *Sci. Rep.*, vol. 8, no. 1, p. 16755, Nov. 2018, doi: 10.1038/s41598-018-34935-1.

[74] N. Perrin, L. Sayer, and A. While, “The efficacy of alarm therapy versus desmopressin therapy in the treatment of primary mono-symptomatic nocturnal enuresis: a systematic review,” *Prim. Health Care Res. Dev.*, vol. 16, no. 01, pp. 21–31, Jan. 2015, doi: 10.1017/S146342361300042X.

[75] J. Evans, B. Malmsten, A. Maddocks, H. S. Popli, and H. Lottmann, “Randomized comparison of long-term desmopressin and alarm treatment for bedwetting,” *J. Pediatr. Urol.*, vol. 7, no. 1, pp. 21–29, 2011, doi: 10.1016/j.jpurol.2010.04.018.

[76] C. F. N. Ng *et al.*, “Comparing alarms, desmopressin, and combined treatment in Chinese enuretic children,” *Pediatr. Nephrol.*, vol. 20, no. 2, pp. 163–169, 2005, doi: 10.1007/s00467-004-1708-5.

[77] C. Glazener, J. Evans, and R. Peto, “Alarm interventions for nocturnal enuresis in children,” *Evidence-Based Child Heal. A Cochrane Rev. J.*, vol. 1, no. 1, pp. 9–97, Mar. 2006, doi: 10.1002/ebch.4.

[78] P. Petrican and M. A. Sawan, “Design of a miniaturized ultrasonic bladder volume monitor and subsequent preliminary evaluation on 41 enuretic patients,” *IEEE Trans. Rehabil. Eng.*, vol. 6, no. 1, pp. 66–74, Mar. 1998, doi: 10.1109/86.662622.

[79] P. G. van Leuteren, A. J. Klijn, T. P. V. M. de Jong, and P. Dik, “SENS-U: validation of a wearable ultrasonic bladder monitor in children during urodynamic studies,” *J. Pediatr. Urol.*, vol. 14, no. 6, pp. 569.e1-569.e6, Dec. 2018, doi: 10.1016/j.jpurol.2018.07.018.

[80] N. K. Kristiansen, J. C. Djurhuus, and H. Nygaard, “Design and evaluation of an ultrasound-based bladder volume monitor,” *Med. Biol. Eng. Comput.*, vol. 42, no. 6, pp. 762–769, Nov. 2004, doi: 10.1007/BF02345209.

[81] H. Niu *et al.*, “Design of an Ultrasound Bladder Volume Measurement and Alarm System,” in *2011 5th Int. Conf. Bioinformatics Biomed. Eng.*, May 2011, vol. M, no. 1, pp. 1–4, doi: 10.1109/icbbe.2011.5781498.

[82] N. K. Kristiansen, H. Nygaard, and J. C. Djurhuus, “Clinical evaluation of a novel ultrasound-based bladder volume monitor,” *Scand. J. Urol. Nephrol.*, vol. 39, no. 4, pp. 321–8, 2005, doi: 10.1080/00365590510031165.

[83] A. Carovac, F. Smajlovic, and D. Junuzovic, “Application of ultrasound in medicine,” *Acta Inform. Med.*, vol. 19, no. 3, pp. 168–71, Sep. 2011, doi: 10.5455/aim.2011.19.168-171.

[84] W. M. J. Kwinten, P. G. van Leuteren, M. van Duren – van Iersel, P. Dik, and P. E. Jira, “SENS-U: continuous home monitoring of natural nocturnal bladder filling in children with nocturnal enuresis – a feasibility study,” *J. Pediatr. Urol.*, vol. 16, no. 2, pp. 196.e1-196.e6, Apr. 2020, doi: 10.1016/j.jpurol.2020.01.012.

[85] P. G. van Leuteren, A. J. Nieuwhof-Leppink, and P. Dik, “SENS-U: clinical evaluation of a full-bladder notification – a pilot study,” *J. Pediatr. Urol.*, vol. 15, no. 4, pp. 381.e1-381.e5, Aug. 2019, doi: 10.1016/j.jpurol.2019.04.006.

[86] P. G. van Leuteren, B. A. de Vries, G. C. J. de Joode-Smink, B. ten Haken, T. P. V. M. de Jong, and P. Dik, “URIKA, continuous ultrasound monitoring for the detection of a full bladder in children with dysfunctional voiding: a feasibility study,” *Biomed. Phys. Eng. Express*, vol. 3, no. 1, pp. 1–7, Feb. 2017, doi: 10.1088/2057-1976/aa589f.

[87] L. Vallozzi, C. Hertleer, and H. Rogier, “Latest developments in the field of textile antennas,” in *Smart Textiles and their Applications*, Elsevier, 2016, pp. 599–626.

[88] X. Li, G. Adamiuk, E. Pancera, and T. Zwick, “Physics-based propagation characterisations of UWB signals for the urine detection in human bladder,” *Int. J. Ultra Wideband Commun. Syst.*, vol. 2, no. 2, pp. 94–103, Dec. 2011, doi: 10.1504/IJUWBCS.2011.044601.

[89] E. Pancera, T. Zwick, and W. Wiesbeck, “Ultra Wideband Radar Imaging: An Approach to Monitor the Water Accumulation in the Human Body,” in *2010 IEEE Int. Conf. Wirel. Inform. Tech. Syst.*, Aug. 2010, no. 1, pp. 1–4, doi: 10.1109/ICWITS.2010.5611899.

[90] E. Pancera, X. Li, L. Zwirello, and T. Zwick, “Performance of ultra wideband antennas for monitoring water accumulation in human bodies,” in *Proc. 4th European Conf. Antennas Propag.*, Apr. 2010, pp. 1–5.

[91] M. O’Halloran, F. Morgan, D. Flores-Tapia, D. Byrne, M. Glavin, and E. Jones, “Prototype Ultra Wideband Radar System for Bladder Monitoring Applications,” *Prog. Electromagn. Res. C*, vol. 33, pp. 17–28, 2012, doi: 10.2528/PIERC12080805.

[92] F. Krewer, F. Morgan, E. Jones, M. Glavin, and M. O’Halloran, “Development of a wearable microwave bladder monitor for the management and treatment of urinary incontinence,” in *Radar Sensor Technology XVIII*, May 2014, vol. 9077, p. 90770X, doi: 10.1117/12.2049689.

[93] “TECHSHEET,” *Novioscan.com*. https://novioscan.com/wp-content/uploads/2019/06/Techsheet-SENS-U-KIDS.pdf (accessed Sep. 21, 2020).

[94] A. Santorelli, E. Porter, E. Kang, T. Piske, M. Popovic, and J. D. Schwartz, “A Time-Domain Microwave System for Breast Cancer Detection Using a Flexible Circuit Board,” *IEEE Trans. Instrum. Meas.*, vol. 64, no. 11, pp. 2986–2994, Nov. 2015, doi: 10.1109/TIM.2015.2440565.

[95] D. S. Holder, *Electrical Impedance Tomography: Methods, History and Applications*. CRC Press, 2004.

[96] J. F. Edd, L. Horowitz, and B. Rubinsky, “Temperature dependence of tissue impedivity in electrical impedance tomography of cryosurgery,” *IEEE Trans. Biomed. Eng.*, vol. 52, no. 4, pp. 695–701, 2005, doi: 10.1109/TBME.2005.844042.

[97] S. Grimnes and Ø. G. Martinsen, *Bioimpedance and bioelectricity basics*, 2nd ed. Academic Press, 2008.

[98] M. Rahal, J. M. Khor, A. Demosthenous, A. Tizzard, and R. Bayford, “A comparison study of electrodes for neonate electrical impedance tomography,” *Physiol. Meas.*, vol. 30, no. 6, pp. S73–S84, Jun. 2009, doi: 10.1088/0967-3334/30/6/S05.

[99] A. Adler and A. Boyle, “Electrical Impedance Tomography: Tissue Properties to Image Measures,” *IEEE Trans. Biomed. Eng.*, vol. 64, no. 11, pp. 2494–2504, Nov. 2017, doi: 10.1109/TBME.2017.2728323.

[100] J. Avery, T. Dowrick, M. Faulkner, N. Goren, and D. Holder, “A Versatile and Reproducible Multi-Frequency Electrical Impedance Tomography System,” *Sensors*, vol. 17, no. 2, p. 280, Jan. 2017, doi: 10.3390/s17020280.

[101] B. Brown, “Electrical impedance tomography (EIT): a review,” *J. Med. Eng. Technol.*, vol. 27, no. 3, pp. 97–108, Jan. 2003, doi: 10.1080/0309190021000059687.

[102] T. A. Khan and S. H. Ling, “Review on Electrical Impedance Tomography: Artificial Intelligence Methods and its Applications,” *Algorithms*, vol. 12, no. 5, p. 88, Apr. 2019, doi: 10.3390/a12050088.

[103] A. Adler and W. R. B. Lionheart, “Uses and abuses of EIDORS: an extensible software base for EIT,” *Physiol. Meas.*, vol. 27, no. 5, pp. S25–S42, May 2006, doi: 10.1088/0967-3334/27/5/S03.

[104] P. A. Hasgall *et al.*, “IT’IS Database for thermal and electromagnetic parameters of biological tissues,” 2018. itis.swiss/database (accessed Aug. 31, 2020).

[105] J. C. Denniston and L. E. Baker, “Measurement of urinary bladder emptying using electrical impedance,” *Med. Biol. Eng.*, vol. 13, no. 2, pp. 305–306, Mar. 1975, doi: 10.1007/BF02477745.

[106] P. T. Doyle and D. W. Hill, “The measurement of residual urine volume by electrical impedance in man,” *Med. Biol. Eng.*, vol. 13, no. 2, pp. 307–308, Mar. 1975, doi: 10.1007/BF02477746.

[107] J. C. Abbey and L. Close, “Electrical Impedance Measurement of Urinary Bladder Fullness,” *J. Microw. Power*, vol. 18, no. 3, pp. 305–309, Jan. 1983, doi: 10.1080/16070658.1983.11689335.

[108] C. T. Kim, T. A. Linsenmeyer, H. Kim, and H. Yoon, “Bladder volume measurement with electrical impedance analysis in spinal cord-injured patients,” *Am. J. Phys. Med. Rehabil.*, vol. 77, no. 6, pp. 498–502, Nov. 1998, doi: 10.1097/00002060-199811000-00009.

[109] A. Yamada, M. Fuse, T. Aoyagi, H. Hosaka, H. Toma, and H. Yanagisawa, “Preventive equipment for urinary incontinence: a device employing lower abdominal impendance changes,” *Int. J. Artif. Organs*, vol. 17, no. 3, pp. 146–50, Mar. 1994, doi: 10.1177/039139889401700304.

[110] W.-C. Liao and F.-S. Jaw, “Noninvasive electrical impedance analysis to measure human urinary bladder volume,” *J. Obstet. Gynaecol. Res.*, vol. 37, no. 8, pp. 1071–5, Aug. 2011, doi: 10.1111/j.1447-0756.2010.01487.x.

[111] A. Palla, S. Rossi, and L. Fanucci, “Bioimpedance based monitoring system for people with neurogenic dysfunction of the urinary bladder,” *Stud. Health Technol. Inform.*, vol. 217, pp. 892–6, 2015, doi: 10.3233/978-1-61499-566-1-892.

[112] K. Shida and S. Yagami, “A Non-Invasive Urination-Desire Sensing System based on Four-Electrodes Impedance Measurement Method,” in *IECON 2006 - 32nd Annu. Conf. IEEE Industrial Electronics*, Nov. 2006, pp. 2975–2978, doi: 10.1109/IECON.2006.347460.

[113] P. Hua, E. J. Woo, J. G. Webster, and W. J. Tompkins, “Bladder fullness detection using multiple electrodes,” in *Proc. Annu. Int. Conf. IEEE Eng. Med. Biol. Soc.*, 1988, pp. 290–291, doi: 10.1109/IEMBS.1988.94522.

[114] T. Schlebusch and S. Leonhardt, “Effect of electrode arrangements on bladder volume estimation by electrical impedance tomography,” *J. Phys. Conf. Ser.*, vol. 434, pp. 1–4, Apr. 2013, doi: 10.1088/1742-6596/434/1/012080.

[115] T. Schlebusch, “Impedanz-Zystovolumetrie,” Ph. D. dissertation, Electr. Eng. Inform. Tech., RWTH Aachen, Aachen, North Rhine-Westphalia, Germany, 2015. [Online]. Available: http://publications.rwth-aachen.de/record/480158.

[116] W. He, P. Ran, Z. Xu, B. Li, and S. Li, “A 3D Visualization Method for Bladder Filling Examination Based on EIT,” *Comput. Math. Methods Med.*, vol. 2012, pp. 1–9, 2012, doi: 10.1155/2012/528096.

[117] T. Schlebusch *et al.*, “Impedance Ratio Method for Urine Conductivity-Invariant Estimation of Bladder Volume,” *J. Electr. Bioimpedance*, vol. 5, no. 1, pp. 48–54, Sep. 2014, doi: 10.5617/jeb.895.

[118] A. Palla, C. Crema, L. Fanucci, and P. Bellagente, “Kalman-Based Approach to Bladder Volume Estimation for People with Neurogenic Dysfunction of the Urinary Bladder,” in *Int. Conf. Computers Helping People w. Special Needs (ICCHP 2016)*, K. Miesenberger, C. Bühler, and P. Penaz, Eds. Cham: Springer, Cham, 2016, pp. 521–528.

[119] Y. Li *et al.*, “Analysis of measurement electrode location in bladder urine monitoring using electrical impedance,” *Biomed. Eng. Online*, vol. 18, no. 1, p. 34, Mar. 2019, doi: 10.1186/s12938-019-0651-4.

[120] D. Leonhäuser *et al.*, “Evaluation of electrical impedance tomography for determination of urinary bladder volume: comparison with standard ultrasound methods in healthy volunteers,” *Biomed. Eng. Online*, vol. 17, no. 1, p. 95, Jul. 2018, doi: 10.1186/s12938-018-0526-0.

[121] R. Li, J. Gao, H. Wang, and Q. Jiang, “Design of a Noninvasive Bladder Urinary Volume Monitoring System Based on Bio-Impedance,” *Engineering*, vol. 5, no. 10, pp. 321–325, Oct. 2013, doi: 10.4236/eng.2013.510B065.

[122] A. Yamada, M. Fuse, T. Aoyagi, H. Hosaka, H. Yanagisawa, and H. Toma, “Preventive equipment of urinary incontinence: A device employing lower abdominal impedance changes,” *Jinko Zoki*, vol. 22, no. 4, pp. 1162–1167, 1993, doi: 10.11392/jsao1972.22.1162.

[123] T. Schlebusch, S. Nienke, S. A. Santos, and S. Leonhardt, “Bladder volume estimation from electrical impedance tomography,” in *2013 35th Annu. Int. Conf. IEEE Eng. Med. Biol. Soc. (EMBC)*, Jul. 2013, vol. 2013, pp. 6441–6444, doi: 10.1109/EMBC.2013.6611029.

[124] T. Schlebusch, S. Nienke, S. Leonhardt, and M. Walter, “Bladder volume estimation from electrical impedance tomography,” *Physiol. Meas.*, vol. 35, no. 9, pp. 1813–1823, Sep. 2014, doi: 10.1088/0967-3334/35/9/1813.

[125] A. K. Khambampati, S. K. Konki, Y. J. Han, S. K. Sharma, and K. Y. Kim, “An Efficient Method to Determine the Size of Bladder Using Electrical Impedance Tomography,” in *TENCON 2018 - 2018 IEEE Region 10 Conf.*, Oct. 2018, pp. 1933–1936, doi: 10.1109/TENCON.2018.8650499.

[126] T. Schlebusch, S. Leonhardt, and B. Grychtol, “Parametric Reconstruction for Impedance Cystovolumetry,” in *Proc. 15th Int. Conf. Biomed. Appl. Electr. Impedance Tomography*, Apr. 2014, p. 13, doi: 10.5281/zenodo.17749.

[127] S. Shin, J. Moon, S. Kye, K. Lee, Y. S. Lee, and H.-G. Kang, “Continuous bladder volume monitoring system for wearable applications,” in *2017 39th Annu. Int. Conf. IEEE Eng. Med. Biol. Soc. (EMBC)*, Jul. 2017, pp. 4435–4438, doi: 10.1109/EMBC.2017.8037840.

[128] J.-J. Huang, Y.-H. Hung, J.-J. Wang, and B.-S. Lin, “Design of wearable and wireless electrical impedance tomography system,” *Measurement*, vol. 78, pp. 9–17, Jan. 2016, doi: 10.1016/j.measurement.2015.09.031.

[129] Y. Zhang and C. Harrison, “Tomo: Wearable, Low-Cost, Electrical Impedance Tomography for Hand Gesture Recognition,” in *Proc. 28th Annu. ACM Symp. User Interface Softw. & Tech. - UIST ’15*, 2015, pp. 167–173, doi: 10.1145/2807442.2807480.

[130] Y. Zhang, R. Xiao, and C. Harrison, “Advancing Hand Gesture Recognition with High Resolution Electrical Impedance Tomography,” in *Proc. 29th Annu. ACM Symp. User Interface Softw. & Tech*, Oct. 2016, pp. 843–850, doi: 10.1145/2984511.2984574.

[131] M. J. Ackerman, “The Visible Human Project,” *Proc. IEEE*, vol. 86, no. 3, pp. 504–511, Mar. 1998, doi: 10.1109/5.662875.

[132] “MR Research Facility: Visible Human Project Datasets.” https://mri.radiology.uiowa.edu/visible_human_datasets.html (accessed Nov. 11, 2019).

[133] Edoarado, “File:Anatomical Planes-en.svg - Wikimedia Commons,” *Wikimedia Commons*, 2011. https://commons.wikimedia.org/wiki/File:Anatomical_Planes-en.svg (accessed Nov. 06, 2020).

[134] Bladder and Bowel Nursing Team, “Procedure for bladder scanning,” NHS Lothian, Lothian, 2016.

[135] Senior Continence Specialist Sister, “Portable Bladder Scanner Use Procedure (BVI 3000/Cubescan 700) (Continence Manual),” Rotherham Doncaster & South Humber NHS Foundation Trust, 2019.

[136] J. Orschulik, T. Schlebusch, and S. Leonhardt, “Impedance-Cystovolumetry from Multifrequency Electrical Impedance Tomography,” in *15th Int. Conf. Biomed. Appl. Electr. Impedance Tomography*, Apr. 2014, p. 44, doi: 10.5281/zenodo.17749.

[137] SenTec, “SenTec EIT Pioneer Set - SenTec.” https://www.sentec.com/products/eit/pioneer-set/ (accessed Nov. 06, 2020).

[138] H. Hvarness, B. Skjoldbye, and H. Jakobsen, “Urinary Bladder Volume Measurements: Comparison of Three Ultrasound Calculation Methods,” *Scand. J. Urol. Nephrol.*, vol. 36, no. 3, pp. 177–181, Jan. 2002, doi: 10.1080/003655902320131839.

[139] N. Hirahara *et al.*, “Four-dimensional ultrasonography for dynamic bladder shape visualization and analysis during voiding,” *J. Ultrasound Med.*, vol. 25, no. 3, pp. 307–13, Mar. 2006, doi: 10.7863/jum.2006.25.3.307.

[140] E. Dunne, A. Santorelli, B. McGinley, G. Leader, M. O'Halloran, and E. Porter, "Supervised Learning Classifiers for Electrical Impedance-based Bladder State Detection," *Sci. Rep.*, vol. 8, no. 1, pp. 1–12, Mar. 2018, doi: 10.1038/s41598-018-23786-5.

[141] "Creative Commons — Attribution 4.0 International — CC BY 4.0." https://creativecommons.org/licenses/by/4.0/ (accessed Nov. 06, 2020).

[142] N. F. Wasserman, B. Spilseth, J. Golzarian, and G. J. Metzger, "Use of MRI for Lobar Classification of Benign Prostatic Hyperplasia: Potential Phenotypic Biomarkers for Research on Treatment Strategies," *Am. J. Roentgenol.*, vol. 205, no. 3, pp. 564–571, Sep. 2015, doi: 10.2214/AJR.14.13602.

[143] N. K. Kristiansen, S. Ringgaard, H. Nygaard, and J. C. Djurhuus, "Effect of Bladder Volume, Gender and Body Position on the Shape and Position of the Urinary Bladder," *Scand. J. Urol. Nephrol.*, vol. 38, no. 6, pp. 462–468, Jan. 2004, doi: 10.1080/00365590410018693.

[144] C. E. Kelly, "Evaluation of voiding dysfunction and measurement of bladder volume," *Rev. Urol.*, vol. 6 Suppl 1, no. Suppl 1, pp. S32-7, 2004.

[145] C. Gabriel, A. Peyman, and E. H. Grant, "Electrical conductivity of tissue at frequencies below 1 MHz," *Phys. Med. Biol.*, vol. 54, no. 16, pp. 4863–4878, Aug. 2009, doi: 10.1088/0031-9155/54/16/002.

[146] F. A. Duck, *Physical Properties of Tissues: A Comprehensive Reference Book*, 1st ed. Academic Press, 1990.

[147] A. Adler and W. R. B. Lionheart, "Minimizing EIT image artefacts from mesh variability in finite element models," *Physiol. Meas.*, vol. 32, no. 7, pp. 823–834, Jul. 2011, doi: 10.1088/0967-3334/32/7/S07.

[148] B. Grychtol and A. Adler, "FEM electrode refinement for electrical impedance tomography," in *2013 35th Annu. Int. Conf. IEEE Eng. Med. Biol. Soc. (EMBC)*, Jul. 2013, pp. 6429–6432, doi: 10.1109/EMBC.2013.6611026.

[149] International Electrotechnical Commission, *Medical electrical equipment-Part 1: General requirements for basic safety and essential performance*, 3rd ed. IEC 60601-1:2005(E), 2005.

[150] O. Gilad, L. Horesh, and D. S. Holder, "Design of electrodes and current limits for low frequency electrical impedance tomography of the brain," *Med. Biol. Eng. Comput.*, vol. 45, no. 7, pp. 621–33, Jul. 2007, doi: 10.1007/s11517-007-0209-7.

[151] A. Adler *et al.*, "GREIT: a unified approach to 2D linear EIT reconstruction of lung images," *Physiol. Meas.*, vol. 30, no. 6, pp. S35–S55, Jun. 2009, doi: 10.1088/0967-3334/30/6/S03.

[152] A. Adler, B. Grychtol, and R. Bayford, "Why is EIT so hard, and what are we doing about it?," *Physiol. Meas.*, vol. 36, no. 6, pp. 1067–73, Jun. 2015, doi: 10.1088/0967-3334/36/6/1067.

[153] F. Braun, M. Proenca, J. Sola, J.-P. Thiran, and A. Adler, "A Versatile Noise Performance Metric for Electrical Impedance Tomography Algorithms," *IEEE Trans. Biomed. Eng.*, vol. 64, no. 10, pp. 2321–2330, 2017, doi: 10.1109/TBME.2017.2659540.

[154] S. Meeson, A. L. Killingback, and B. H. Blott, "The dependence of EIT images on the assumed initial conductivity distribution: a study of pelvic imaging," *Phys. Med. Biol.*, vol. 40, no. 4, pp. 643–57, Apr. 1995, doi: 10.1088/0031-9155/40/4/010.

[155] A. Adler, "add_noise," *EIDORS*, 2010. http://eidors3d.sourceforge.net/doc/index.html?eidors/models/add_noise.html (accessed Aug. 29, 2019).

[156] M. Yasin, S. Böhm, P. O. Gaggero, and A. Adler, "Evaluation of EIT system performance," *Physiol. Meas.*, vol. 32, no. 7, pp. 851–865, Jul. 2011, doi: 10.1088/0967-3334/32/7/S09.

[157] B. Grychtol, G. Elke, P. Meybohm, N. Weiler, I. Frerichs, and A. Adler, "Functional validation and comparison framework for EIT lung imaging," *PLoS One*, vol. 9, no. 8, pp. 1–13, Aug. 2014, doi: 10.1371/journal.pone.0103045.

[158] S. de Gelidi *et al.*, “Torso shape detection to improve lung monitoring,” *Physiol. Meas.*, vol. 39, no. 7, p. 074001, 2018, doi: 10.1088/1361-6579/aacc1c.

[159] S. Leonhardt and B. Lachmann, “Electrical impedance tomography: The holy grail of ventilation and perfusion monitoring?,” *Intensive Care Med.*, vol. 38, no. 12, pp. 1917–1929, 2012, doi: 10.1007/s00134-012-2684-z.

[160] M. Vartak *et al.*, “ModelDB: A system for machine learning model management,” Jun. 2016, doi: 10.1145/2939502.2939516.

[161] A. Rajan, G. P. Ramesh, and J. Yuvaraj, “Glaucomatous image Classification using Wavelet Transform,” in *2014 IEEE Int. Conf. Advanced Commun., Control and Computing Tech.*, May 2014, no. 978, pp. 1398–1402, doi: 10.1109/ICACCCT.2014.7019330.

[162] R. Ebrahimzadeh and M. Jampour, “Efficient Handwritten Digit Recognition based on Histogram of Oriented Gradients and SVM,” *Int. J. Comput. Appl.*, vol. 104, no. 9, pp. 10–13, Oct. 2014, doi: 10.5120/18229-9167.

[163] I. H. Witten, E. Frank, M. A. Hall, and C. J. Pal, *Data Mining: Practical Machine Learning Tools and Techniques*, 4th ed. Morgan Kaufmann, 2016.

[164] R. C. Conceicao, M. O’Halloran, M. Glavin, and E. Jones, “Support Vector Machines for the Classification of Early-Stage Breast Cancer Based on Radar Target Signatures,” *Prog. Electromagn. Res. B*, vol. 23, pp. 311–327, 2010, doi: 10.2528/PIERB10062407.

[165] S. B. Kotsiantis, “Supervised Machine Learning: A Review of Classification Techniques,” *Informatica*, vol. 31, no. 3, pp. 249–268, Oct. 2007.

[166] C. Campbell and Y. Ying, “Learning with Support Vector Machines,” *Synth. Lect. Artif. Intell. Mach. Learn.*, vol. 5, no. 1, pp. 1–95, Feb. 2011, doi: 10.2200/S00324ED1V01Y201102AIM010.

[167] M. Kuhn and K. Johnson, *Applied Predictive Modeling*. New York, NY: Springer-Verlag New York, 2013.

[168] M. Esterman, B. J. Tamber-Rosenau, Y.-C. Chiu, and S. Yantis, “Avoiding non-independence in fMRI data analysis: Leave one subject out,” *Neuroimage*, vol. 50, no. 2, pp. 572–576, Apr. 2010, doi: 10.1016/j.neuroimage.2009.10.092.

[169] C. Setz, B. Arnrich, J. Schumm, R. La Marca, G. Troster, and U. Ehlert, “Discriminating Stress From Cognitive Load Using a Wearable EDA Device,” *IEEE Trans. Inf. Technol. Biomed.*, vol. 14, no. 2, pp. 410–417, Mar. 2010, doi: 10.1109/TITB.2009.2036164.

[170] M. Antal and G. Nemes, “Gender recognition from mobile biometric data,” in *2016 IEEE 11th International Symposium on Applied Computational Intelligence and Informatics (SACI)*, May 2016, pp. 243–248, doi: 10.1109/SACI.2016.7507379.

[171] B. Oliveira, D. Godinho, M. O’Halloran, M. Glavin, E. Jones, and R. Conceição, “Diagnosing Breast Cancer with Microwave Technology: remaining challenges and potential solutions with machine learning,” *Diagnostics*, vol. 8, no. 2, p. 36, 2018, doi: 10.3390/diagnostics8020036.

[172] M. Jehl, K. Aristovich, M. Faulkner, and D. Holder, “Are patient specific meshes required for EIT head imaging?,” *Physiol. Meas.*, vol. 37, no. 6, pp. 879–892, Jun. 2016, doi: 10.1088/0967-3334/37/6/879.

[173] A. Tizzard, L. Horesh, R. J. Yerworth, D. S. Holder, and R. H. Bayford, “Generating accurate finite element meshes for the forward model of the human head in EIT,” *Physiol. Meas.*, vol. 26, no. 2, pp. S251–S261, 2005, doi: 10.1088/0967-3334/26/2/024.

[174] B. Grychtol, B. Müller, and A. Adler, “3D EIT image reconstruction with GREIT,” *Physiol. Meas.*, vol. 37, no. 6, pp. 785–800, Jun. 2016, doi: 10.1088/0967-3334/37/6/785.

[175] A. Biguri, B. Grychtol, A. Adler, and M. Soleimani, “Tracking boundary movement and exterior shape modelling in lung EIT imaging,” *Physiol. Meas.*, vol. 36, no. 6, pp. 1119–1135, Jun. 2015, doi: 10.1088/0967-3334/36/6/1119.

[176] B. Grychtol, W. R. B. Lionheart, M. Bodenstein, G. K. Wolf, and A. Adler, “Impact of Model Shape Mismatch on Reconstruction Quality in Electrical Impedance Tomography,” *IEEE Trans. Med. Imaging*, vol. 31, no. 9, pp. 1754–1760, Sep. 2012, doi: 10.1109/TMI.2012.2200904.

[177] M. Jehl, J. Avery, E. Malone, D. Holder, and T. Betcke, “Correcting electrode modelling errors in EIT on realistic 3D head models,” *Physiol. Meas.*, vol. 36, no. 12, pp. 2423–2442, 2015, doi: 10.1088/0967-3334/36/12/2423.

[178] T. Nevéus *et al.*, “The Standardization of Terminology of Lower Urinary Tract Function in Children and Adolescents: Report from the Standardisation Committee of the International Children’s Continence Society,” *J. Urol.*, vol. 176, no. 1, pp. 314–324, Jul. 2006, doi: 10.1016/S0022-5347(06)00305-3.

[179] N. Mitsuhashi, K. Fujieda, T. Tamura, S. Kawamoto, T. Takagi, and K. Okubo, “BodyParts3D: 3D structure database for anatomical concepts,” *Nucleic Acids Res.*, vol. 37, no. Database issue, pp. D782-5, Jan. 2009, doi: 10.1093/nar/gkn613.

[180] M.-C. Gosselin *et al.*, “Development of a new generation of high-resolution anatomical models for medical device evaluation: the Virtual Population 3.0,” *Phys. Med. Biol.*, vol. 59, no. 18, pp. 5287–5303, Sep. 2014, doi: 10.1088/0031-9155/59/18/5287.

[181] IT’IS Foundation, “Thelonious V2.0,” 2015, doi: 10.13099/ViP-Thelonious-V2.0.

[182] R. S. Byrd, M. Weitzman, N. E. Lanphear, and P. Auinger, “Bed-wetting in US children: epidemiology and related behavior problems,” *Pediatrics*, vol. 98, no. 3 Pt 1, pp. 414–9, Sep. 1996.

[183] M. L. Chiozza *et al.*, “An Italian epidemiological multicentre study of nocturnal enuresis,” *Br. J. Urol.*, vol. 81 Suppl 3, pp. 86–9, May 1998, doi: 10.1046/j.1464-410x.1998.00015.x.

[184] IT’IS Foundation, “Billie V2.0,” 2015, doi: 10.13099/ViP-Billie-V2.0.

[185] IT’IS Foundation, “Thelonious Whole-Body Shell V2.0,” Oct. 30, 2015. https://itis.swiss/virtual-population/virtual-population/vip2/thelonious/thelonious-whole-body-shell-v2-0/ (accessed Apr. 29, 2020).

[186] A. C. Kuzmic, B. Brkljacic, and D. Ivankovic, “The impact of bladder shape on the ultrasonographic measurement of bladder volume in children,” *Pediatr. Radiol.*, vol. 33, no. 8, pp. 530–534, Aug. 2003, doi: 10.1007/s00247-003-0945-2.

[187] U. Erasmie and K.-J. Lidefelt, “Accuracy of ultrasonic assessment of residual urine in children,” *Pediatr. Radiol.*, vol. 19, no. 6–7, pp. 388–390, Jul. 1989, doi: 10.1007/BF02387634.

[188] C. Gabriel, S. Gabriel, and E. Corthout, “The dielectric properties of biological tissues: I. Literature survey,” *Phys. Med. Biol.*, vol. 41, no. 11, pp. 2231–2249, Nov. 1996, doi: 10.1088/0031-9155/41/11/001.

[189] B. McDermott, M. O’Halloran, E. Porter, and A. Santorelli, “Brain haemorrhage detection using a SVM classifier with electrical impedance tomography measurement frames,” *PLoS One*, vol. 13, no. 7, pp. 1–26, Jul. 2018, doi: 10.1371/journal.pone.0200469.

[190] J. Korsawe, “intriangulation(vertices,faces,testp,heavytest),” *MATLAB Central File Exchange*, 2020. https://www.mathworks.com/matlabcentral/fileexchange/43381-intriangulation-vertices-faces-testp-heavytest (accessed May 22, 2020).

[191] A. Snow, C. Estrada, and J. S. Chow, “Ultrasonography of the Pediatric Bladder,” *Ultrasound Clin.*, vol. 8, no. 3, pp. 423–439, Jul. 2013, doi: 10.1016/j.cult.2013.03.004.

[192] E. Dunne *et al.*, “Detection of Vesicoureteral Reflux Using Electrical Impedance Tomography,” *IEEE Trans. Biomed. Eng.*, vol. 66, no. 8, pp. 2279–2286, Aug. 2019, doi: 10.1109/TBME.2018.2886830.

[193] A. Boyle and A. Adler, “The impact of electrode area, contact impedance and boundary shape on EIT images,” *Physiol. Meas.*, vol. 32, no. 7, pp. 745–54, Jul. 2011, doi: 10.1088/0967-3334/32/7/S02.

[194] A. Lozano, J. Rosell, and R. Pallas-Areny, “Errors in prolonged electrical impedance measurements due to electrode repositioning and postural changes,” *Physiol. Meas.*, vol. 16, no. 2, pp. 121–130, May 1995, doi: 10.1088/0967-3334/16/2/004.

[195] T. Ouypornkochagorn, “Influence of electrode placement error and contact impedance error to scalp voltage in electrical impedance tomography application,” *iEECON 2019 - 7th Int. Electr. Eng. Congr. Proc.*, pp. 50–53, 2019, doi: 10.1109/iEECON45304.2019.8939016.

[196] B. M. Graham and A. Adler, “Electrode placement configurations for 3D EIT,” *Physiol. Meas.*, vol. 28, no. 7, pp. S29–S44, Jul. 2007, doi: 10.1088/0967-3334/28/7/S03.

[197] B. McDermott, M. O’Halloran, J. Avery, and E. Porter, “Bi-Frequency Symmetry Difference EIT—Feasibility and Limitations of Application to Stroke Diagnosis,” *IEEE J. Biomed. Heal. Informatics*, vol. 24, no. 8, pp. 2407–2419, Aug. 2020, doi: 10.1109/JBHI.2019.2960862.

[198] K. H. Brodersen, C. S. Ong, K. E. Stephan, and J. M. Buhmann, “The Balanced Accuracy and Its Posterior Distribution,” in *2010 20th Int. Conf. Pattern Recognition*, Aug. 2010, pp. 3121–3124, doi: 10.1109/ICPR.2010.764.

[199] C. Thornton, F. Hutter, H. H. Hoos, and K. Leyton-Brown, “Auto-WEKA: combined selection and hyperparameter optimization of classification algorithms,” in *Proc. 19th ACM SIGKDD Int. Conf. on Knowl. Discovery Data Mining - KDD ’13*, Aug. 2013, p. 847, doi: 10.1145/2487575.2487629.

[200] H. A. Abu Alfeilat *et al.*, “Effects of Distance Measure Choice on K-Nearest Neighbor Classifier Performance: A Review,” *Big Data*, vol. 7, no. 4, pp. 221–248, Dec. 2019, doi: 10.1089/big.2018.0175.

[201] Z. Geler, V. Kurbalija, M. Radovanović, and M. Ivanović, “Comparison of different weighting schemes for the kNN classifier on time-series data,” *Knowl. Inf. Syst.*, vol. 48, no. 2, pp. 331–378, Aug. 2016, doi: 10.1007/s10115-015-0881-0.

[202] E. Frank, M. A. Hall, and I. H. Witten, *Online Appendix for “Data Mining: Practical Machine Learning Tools and Techniques,”* 4th ed. Morgan Kaufmann, 2016.

[203] F. Pedregosa *et al.*, “Scikit-learn: Machine Learning in Python,” *J. Mach. Learn. Res.*, vol. 12, pp. 2825–2830, Oct. 2011.

[204] B. Schölkopf and A. J. Smola, *Learning With Kernels: Support Vector Machines, Regularization, Optimization, and Beyond*. MIT Press, 2002.

[205] T. Hastie, R. Tibshirani, and J. Friedman, *The Elements of Statistical Learning: Data Mining, Inference, and Prediction*, 2nd ed. New York, NY: Springer-Verlag New York, 2009.

[206] A. Santorelli, Y. Li, E. Porter, M. Popovic, and M. Coates, “Investigation of classification algorithms for a prototype microwave breast cancer monitor,” in *The 8th European Conf. Antennas Propag. (EuCAP 2014)*, Apr. 2014, no. EuCAP, pp. 320–324, doi: 10.1109/EuCAP.2014.6901757.

[207] B. McDermott, E. Dunne, M. O’Halloran, E. Porter, and A. Santorelli, “Brain Haemorrhage Detection Through SVM Classification of Electrical Impedance Tomography Measurements,” in *Brain and Human Body Modeling: Computational Human Modeling at EMBC 2018*, Cham: Springer International Publishing, 2019, pp. 211–244.

[208] N. V. S. Natteshan and J. Angel Arul Jothi, “Automatic Classification of Brain MRI Images Using SVM and Neural Network Classifiers,” in *Advances in Intelligent Informatics*, E.-S. M. El-Alfy, S. M. Thampi, H. Takagi, S. Piramuthu, and T. Hanne, Eds. Springer, Cham, 2015, pp. 19–30.

[209] A. Ben-Hur and J. Weston, “A User’s Guide to Support Vector Machines,” in *Data Mining Techniques for the Life Sciences.*, O. Carugo and F. Eisenhaber, Eds. Humana Press, 2010, pp. 223–239.

[210] M. Amer, M. Goldstein, and S. Abdennadher, “Enhancing one-class support vector machines for unsupervised anomaly detection,” in *Proc. ACM SIGKDD Workshop Outlier Detection Description - ODD ’13*, 2013, pp. 8–15, doi: 10.1145/2500853.2500857.

[211] J. Bergstra and Y. Bengio, “Random search for hyper-parameter optimization,” *J. Mach. Learn. Res.*, vol. 13, pp. 281–305, Feb. 2012.

[212] A. D. Bull, “Convergence rates of efficient global optimization algorithms,” *J. Mach. Learn. Res.*, vol. 12, pp. 2879–2904, Oct. 2011.

[213] J. Snoek, H. Larochelle, and R. P. Adams, “Practical Bayesian Optimization of Machine Learning Algorithms,” in *NIPS’ 12: Proceedings of the 25th International Conference on Neural Information*, Dec. 2012, vol. 2, pp. 2951–2959, doi: 10.5555/2999325.2999464.

[214] M. A. Gelbart, J. Snoek, and R. P. Adams, “Bayesian Optimization with Unknown Constraints,” in *UAI’14: Proc. 30th Conf. Uncertainty Artificial Intell.*, 2014, pp. 250–259.

[215] G. Malkomes and R. Garnett, “Automating Bayesian optimization with Bayesian optimization,” in *NIPS’18: Proc. 32nd Int. Conf. Neural Inform.*, 2018, pp. 5988–5997.

[216] J. González, M. Osborne, and N. D. Lawrence, “GLASSES: Relieving the myopia of Bayesian optimisation,” in *Proc. 19th Int.Conf. Artificial Intell. Statistics*, 2016, vol. 51, pp. 790–799.

[217] J. Li *et al.*, “Feature Selection,” *ACM Comput. Surv.*, vol. 50, no. 6, pp. 1–45, Jan. 2018, doi: 10.1145/3136625.

[218] T. Howley, M. G. Madden, M.-L. O’Connell, and A. G. Ryder, “The effect of principal component analysis on machine learning accuracy with high-dimensional spectral data,” *Knowledge-Based Syst.*, vol. 19, no. 5, pp. 363–370, Sep. 2006, doi: 10.1016/j.knosys.2005.11.014.

[219] A. E. Hartinger, R. Guardo, A. Adler, and H. Gagnon, “Real-Time Management of Faulty Electrodes in Electrical Impedance Tomography,” *IEEE Trans. Biomed. Eng.*, vol. 56, no. 2, pp. 369–377, Feb. 2009, doi: 10.1109/TBME.2008.2003103.

[220] R. J. Yerworth, I. Frerichs, and R. Bayford, “Analysis and compensation for errors in electrical impedance tomography images and ventilation-related measures due to serial data collection,” *J. Clin. Monit. Comput.*, vol. 31, no. 5, pp. 1093–1101, Oct. 2017, doi: 10.1007/s10877-016-9920-y.

[221] B. Brandstätter, “Jacobian calculation for electrical impedance tomography based on the reciprocity principle,” *IEEE Trans. Magn.*, vol. 39, no. 3, pp. 1309–1312, May 2003, doi: 10.1109/TMAG.2003.810390.

[222] J. Tang, S. Alelyani, and H. Liu, “Feature Selection for Classification: A Review,” in *Data Classification: Algorithms and Applications*, C. C. Aggarwal, Ed. CRC Press, 2014, pp. 37–64.

[223] A. Santorelli, E. Porter, E. Kirshin, Y. J. Liu, and M. Popovic, “Investigation of classifiers for tumor detection with an experimental time-domain breast screening system,” *Prog. Electromagn. Res.*, vol. 144, pp. 45–57, 2014, doi: 10.2528/PIER13110709.

[224] E. Dunne, A. Santorelli, B. McGinley, G. Leader, M. O’Halloran, and E. Porter, “Image-based classification of bladder state using electrical impedance tomography,” *Physiol. Meas.*, vol. 39, no. 12, pp. 1–13, Dec. 2018, doi: 10.1088/1361-6579/aae6ed.

[225] E. Keogh and A. Mueen, “Curse of Dimensionality,” in *Encyclopedia of Machine Learning and Data Mining*, Boston, MA: Springer US, 2017, pp. 314–315.

[226] “Adhesive patches - Novioscan,” *Novioscan.com*, 2020. https://novioscan.com/product/adhesive-patches/ (accessed Sep. 21, 2020).

[227] “Ultrasound gel - Novioscan,” *Novioscan.com*. https://novioscan.com/product/ultrasound-gel/ (accessed Sep. 21, 2020).

[228] “Alcohol swabs - Novioscan,” *Novioscan.com*. https://novioscan.com/product/alcohol-swabs/ (accessed Sep. 21, 2020).

[229] “The National Library of Medicine’s Visible Human Project.” https://www.nlm.nih.gov/research/visible/visible_human.html (accessed Nov. 09, 2020).

[230] S. Glass Clark *et al.*, “Use of Ultrasound Urodynamics to Identify Differences in Bladder Shape Between Individuals With and Without Overactive Bladder,” *Female Pelvic Med. Reconstr. Surg.*, vol. 26, no. 10, pp. 635–639, Oct. 2020, doi: 10.1097/SPV.0000000000000638.